

# **Synthesis and Characterization of Transition Metal based Nanocatalysts for Energy Efficient Electrochemical H<sub>2</sub> Production**



Thesis submitted in partial fulfillment

for the award of the degree

**Doctor of Philosophy**

by

**SANTOSH SEMWAL**

**RAJIV GANDHI INSTITUTE OF PETROLEUM TECHNOLOGY**

**JAIS, INDIA – 229304**

**21BS0013**

**2024**



---

## CERTIFICATE

It is certified that the work contained in the thesis titled "*Synthesis and Characterization of Transition Metal based Nanocatalysts for Energy Efficient Electrochemical H<sub>2</sub> Production*" by "*Santosh Semwal*" has been carried out under our supervision and this work has not been submitted elsewhere for a degree.

It is further certified that the student has fulfilled all the requirements of Comprehensive, Candidacy, SOTA, and Open Seminar.

---

(Supervisor)

**Prof. A. S. K. Sinha**

---

(Co-Supervisor)

**Prof. Umapasana Ojha**

---

---

## DECLARATION BY THE CANDIDATE

I, "*Santosh Semwal*", certify that the work embodied in this thesis is my own bonafide work and was carried out by me under the supervision of "*Prof. A. S. K. Sinha*" and co-supervision of "*Prof. Umapasana Ojha*" from "*August 2021*" to "*November 2024*", at Rajiv Gandhi Institute of Petroleum Technology, Jais, India. The matter embodied in this thesis has not been submitted for the award of any other degree. I further declare that I have faithfully acknowledged and given credit to the researchers and research community wherever their works have been cited in my work in this thesis. I further declare that I have not willfully copied any other's work, paragraphs, text, data, results, etc., reported in journals, books, magazines, reports dissertations, theses, etc., or available at websites and have not included them in this thesis and have not cited as my own work.

Date:

**Santosh Semwal**

Place: RGIPT Jais

Roll No.: 21BS0013

---



---

## CERTIFICATE BY THE SUPERVISOR (S)

It is certified that the above statement made by the student is correct to the best of our knowledge.

---

(Supervisor)

**Prof. A. S. K. Sinha**

---

(Co-Supervisor)

**Prof. Umapasana Ojha**

---

Signature & Seal of Head of Department

---

## CERTIFICATE

CERTIFIED that the work contained in the thesis titled “*Synthesis and Characterization of Transition Metal based Nanocatalysts for Energy Efficient Electrochemical H<sub>2</sub> Production*” by **Mr. Santosh Semwal** has been carried out under our supervision. It is also certified that he fulfilled the mandatory requirement of TWO quality publications arose out of his thesis work.

It is further certified that the two publications (copies enclosed) of the aforesaid **Mr. Santosh Semwal** have been published in the Journals indexed by –

- a) SCI
- b) SCI Extended
- c) SCOPUS
- d) \*Non-indexed Journals-(only in special cases)(\*Please enclose DPGC resolution in this regard)

---

**Prof. A. S. K. Sinha**

(Supervisor)

---

**Prof. Umapasana Ojha**

(Co-Supervisor)

---

**Dr. P. K. Srivastava**

(Convener, DPGC)

---

N.B.: Please strike out the category (a, b, c, d) that is not applicable.



---

## **COPYRIGHT TRANSFER CERTIFICATE**

**Title of the thesis:** *Synthesis and Characterization of Transition Metal based Nanocatalysts for Energy Efficient Electrochemical H<sub>2</sub> Production*

**Name of the student:** *Santosh Semwal*

### **Copyright Transfer**

The undersigned hereby assigns to the Rajiv Gandhi Institute of Petroleum Technology, Jais all rights under copyright that may exist in and for the above thesis submitted for the award of the "Doctor of Philosophy".

Date:

Place: RGIPT Jais

---

**Santosh Semwal**

Roll No.: 21BS0013

---

Note: However, the author may reproduce or authorize others to reproduce material extracted verbatim from the thesis or derivative of the thesis for the author's personal use provided that the source and the Institute's copyright notice are indicated.



*Dedicated to my beloved parents...*



# Acknowledgment

*Arise, awake, and stop not till the goal is reached.*

*\_ Swami Vivekananda*

I would like to express my sincere gratitude to the Almighty for bestowing his blessings upon me throughout my academic journey. His divine grace has been the guiding light that has illuminated my path and enabled me to reach this milestone.

I am deeply indebted to my research supervisor, **Prof. A. S. K. Sinha**, for his invaluable guidance, unwavering support, and constant encouragement. His insightful advice, patience, and expertise have been instrumental in shaping my research and academic growth. I am truly fortunate to have had the opportunity to learn from such a brilliant and inspiring mentor.

I would also like to extend my wholehearted thanks to my co-supervisor, **Prof. Umapasana Ojha**, for his significant contributions to my research. He constantly pushed me to improve as a researcher and uphold my moral principles. Additionally, I want to express my gratitude for his insightful conversations and recommendations, which were always freely given when needed. Prof. Ojha continued to be dedicated to my development even after he moved to IIT Bhubaneswar, frequently holding late-night meetings to work around our schedules. It is quite admirable that he is always willing to engage in intelligent conversation. Every discussion I've had with him has helped me become a more capable researcher. Prof. Ojha's mentorship went beyond academic advice; he taught me the value of determination, critical thinking, and upholding high standards in research. His patient mentorship and encouragement have inspired me to

strive for excellence. I am truly grateful for his unwavering belief in my abilities and his commitment to my academic growth.

I am thankful to my Research Progress Evolution Committee members, **Dr. Debashish Panda** and **Dr. Gunjan Kumar Agrahari**, for their valuable guidance, constructive feedback, and continuous support throughout my research journey. Their insightful suggestions and expertise have significantly enhanced the quality of my work. I would also like to express my sincere gratitude to **Dr. Shikha Singh** for her assistance in coordinating and arranging my RPEC meeting and open seminar. I extend my heartfelt appreciation to **Dr. Arshad Aijaz** for his prompt support with document signing requirements, which helped ensure smooth administrative proceedings.

I would also like to thank the entire department, especially Head of Department's **Prof. Atul Sharma**, for providing a conducive research environment and necessary facilities.

I am grateful to my senior researchers and labmates **Dr. Subhankar Mandal**, **Dr. Niharika Pandey**, **Dr. Chandan Upadhyay**, **Dr. Arpan Tewary**, **Shrinkhala Anand** and **Yukti Setia** for their valuable insights, constructive criticism, and unwavering support. I would like to extend a special thanks to Dr. Chandan Upadhyay and Dr. Arpan Tewary for their constant support and encouragement. His friendly behavior and willingness to help made my research journey much more enjoyable.

I would like to express my sincere gratitude to our collaborators Prof. Saroj Kumar Nayak (IIT Bhubaneswar), Dr Karthikeyan Jeyakumar (NIT Durgapur), Dr Rajashri Urkude (BARC), Aiswarya Samal (IIT Bhubaneswar), and Renna Shakir (RGIPT) for their valuable contributions to this research. Their expertise, insights, and dedicated support were instrumental in bringing this work to fruition.

I would like to acknowledge the financial support provided by Rajiv Gandhi Institute of Petroleum Technology Jais, Amethi, Uttar Pradesh, and I am thankful to the Central Instrumental Facility of RGIPT for instrumental facilities. This support has been crucial in enabling me to conduct my research and complete my PhD. I am also grateful to the technical staff of the department for their assistance in various aspects of my research, including equipment maintenance, software support, and chemical suppliers.

From my earliest days in school through this doctoral journey, I've been fortunate to have extraordinary people lighting my path. I am also deeply grateful to my school teachers, college professors and friends Naveen Semwal, Rahul Bisht, Sandeep Rawat, Sandeep, Neelam Raturi, Sushil Joshi, Prashant, Priya Mata, Abhishek Panwar, Ashish Tariyal, Saurabh Pandey, Utsav Mishra, Arvind, Rajesh, Aditiya, Swati, Pooja Saurabh Mishra and Sidharth Atal for their unwavering encouragement, emotional support, and for always being there to lend a listening ear when I needed it most.

I extend my heartfelt gratitude to my M.Sc. seniors who played a pivotal role in guiding me through my NET and GATE preparation journey. I am particularly indebted to Krishna, Kamlesh Rawat, Amit, Deepak, Dr. Parul Sani, Dr. Shivam Rawat, Deepti, Dr. Shashi and Vikas Pundir for their unwavering support and mentorship. Their encouragement and guidance have not only helped me in exam preparation but also provided me with a clearer perspective on research opportunities.

Finally, I owe a heartfelt thanks to my family members, my father- Ramesh Prasad Semwal, mother- Chandrakala Devi, brother- Yogesh, Sachin, sister-in-law- Kiran Semwal and sisters- Santoshi and Preeti for their unconditional love, understanding, and steadfast belief in me. Your continuous support and encouragement have been the foundation upon which I have been able to achieve this milestone.

I dedicate this thesis to my beloved family, whose love and support have been my constant source of strength and inspiration.

# Table of Contents

Acknowledgment.....	i
Table of Contents .....	v
List of Figures.....	ix
List of Scheme .....	xv
List of Abbreviations.....	xvii
Preface .....	xix
Chapter 1.....	1
<b>Introduction and Literature Survey .....</b>	<b>1</b>
1.1 Abstract .....	1
1.2 Hybrid Water Electrolysis Process for Green Hydrogen Production .....	2
1.2.1 Background of Water Electrolysis.....	4
1.2.2 Statement of the Problems.....	4
1.2.3 Half-Cell reactions in water electrolysis .....	6
1.2.4 Hydrogen Production Coupled with Sulfion Oxidation Reaction (SOR)..	9
1.2.4.1 Claus process for sulfur recovery .....	10
1.2.5 H <sub>2</sub> Production Coupled with Methanol Oxidation Reaction (MOR).....	12
1.2.6 Natural Gas:.....	12
1.2.7 Biomass .....	13
1.2.8 Fermentation.....	13
1.2.9 Hydrogen production coupled with urea oxidation reaction .....	16
1.2.10 Mechanism of UOR .....	18
1.3 Why transition Metal-based catalyst? .....	18
1.4 Criteria for electrocatalytic performance .....	22
1.4.1 Overpotential ( $\eta$ ).....	23
1.4.2 Electrochemical Surface Area (ECSA).....	23
1.4.3 Tafel Slope .....	24

1.4.4	Faradaic Efficiency .....	24
1.4.5	Stability .....	25
1.5	Future possibilities and worldwide markets for hydrogen-based energy.....	26
1.6	Conclusion .....	28
<b>Chapter 2.....</b>		<b>31</b>
2.1	Abstract .....	31
2.2	Introduction .....	32
2.3	Experimental Section .....	35
2.3.1	Materials.....	35
2.3.2	Characterization .....	35
2.3.3	Fabrication of Electrode.....	36
2.3.4	Electrochemical Evaluation.....	37
2.3.5	Quantification of H <sub>2</sub> Gas.....	38
2.3.6	ECSA Measurement.....	38
2.3.7	Recovery of Sulfur.....	39
2.3.8	Computational method.....	39
2.4	Calculation for power consumption.....	40
2.5	Synthetic Process of Ni-Co <sub>9</sub> S <sub>8</sub> and Ni-FeOOH.....	41
2.6	Results & Discussion .....	42
2.7	Conclusion.....	59
<b>Chapter 3.....</b>		<b>61</b>
3.1	Abstract .....	61
3.2	Introduction .....	62
3.3	Experimental Section .....	65
3.3.1	Material Required .....	65
3.3.2	Material Characterization:.....	65
3.3.3	Synthesis of NF-PAHz-Co <sub>3</sub> O <sub>4</sub> @NiCu.....	66
3.3.4	Synthesis of NF-PAHz-NiCu .....	66
3.3.5	Synthesis of PAHz-Cu .....	67
3.3.6	Electrochemical Measurements .....	67
3.3.7	Fabrication of PAHz-Cu Electrode:.....	68

3.3.8	Fabrication of IrO <sub>2</sub> and Pt/C electrode.....	68
3.3.9	Computational methods .....	68
3.3.10	Detailed MOR activity calculation: .....	70
3.3.10.1	Step I: CH <sub>3</sub> OH adsorption:.....	70
3.3.10.2	Step II: CH <sub>3</sub> OH→CH <sub>3</sub> O: .....	70
3.3.10.3	Step III: CH <sub>3</sub> O→CH <sub>2</sub> O:.....	71
3.3.10.4	Step IV: CH <sub>2</sub> O→HCO:.....	71
3.3.10.5	Step V: HCO→HCOOH: .....	71
3.3.11	Electrochemical Measurements: .....	71
3.3.11.1	Quantification of H <sub>2</sub> Gas:.....	71
3.3.12	ECSA Measurement.....	72
3.3.13	Product Analysis .....	72
3.4	Result and Discussion .....	72
3.5	Conclusion.....	88
<b>Chapter 4</b>	<b>.....</b>	<b>91</b>
	<b>In situ Growth of CeFe doped CeO<sub>2</sub>/Ni<sub>3</sub>S<sub>2</sub> nanorod as highly stable bifunctional electrocatalyst for effective urea oxidation reaction. ....</b>	<b>91</b>
4.1	Abstract .....	91
4.2	Introduction .....	92
4.3	Experimental Section .....	94
4.3.1	Material Requires:.....	94
4.3.2	Material Characterization:.....	94
4.3.3	Electrochemical Measurements:.....	94
4.3.4	Synthesis of CoFe doped CeO <sub>2</sub> @Ni <sub>3</sub> S <sub>2</sub> .....	95
4.3.5	Synthesis of Ni <sub>3</sub> S <sub>2</sub> /NF.....	95
4.4	Result and discussion .....	96
4.5	Conclusion.....	104
<b>Chapter 5</b>	<b>.....</b>	<b>107</b>
5.1	Summary .....	107
5.2	Future Scope.....	110
<b>Appendix</b>	<b>.....</b>	<b>113</b>

<b>References .....</b>	<b>141</b>
<b>List of Publications.....</b>	<b>179</b>
<b>Conferences/Workshops/Webinars.....</b>	<b>181</b>

# List of Figures

<b>Figure 1.1:</b> (a) Polarization curve schematic design for the HER and other low-onset potential available potential oxidation processes, including the oxygen evolution reaction (OER), urea oxidation reaction (UOR), the alcohol oxidation reaction (AOR), the sulfion oxidation reaction (SOR), and the hydrozine oxidation reaction (HzOR). Reproduced with permission from ref. [33]. Copyright 2023 Royal Society of Chemistry.....	3
<b>Figure 1.2:</b> Major problems occurred in water electrolysis.....	5
<b>Figure 1.3:</b> Electrolytic cell assembly of SOR coupled with HER.....	11
<b>Figure 1.4:</b> Major Sources of methanol production. ....	12
<b>Figure 1.5:</b> Schematic illustrating energy-efficient H <sub>2</sub> production coupled with MOR electrolyzer/devices.....	14
<b>Figure 1.6:</b> A electrocatalytic MOR mechanism with two pathways, where the adsorption site on the catalyst surface is denoted by the symbol *, the CO route by the red arrows, and the CO-free pathway by the others. Reproduced with permission from ref. [173]. Copyright 2023 Wiley-VCH .....	16
<b>Figure 1.7:</b> Important properties of transition metal-based catalyst. ....	20
<b>Figure 1.8:</b> An outline of hydrogen fuel's future and its potential applications. Reproduced with permission from ref. [129]. Copyright 2020 Royal Society of Chemistry .....	27
<b>Figure 2.1:</b> Peaks highlighted with "#" and "*" correspond to FeOOH and Co <sub>9</sub> S <sub>8</sub> , respectively, according to the NiFeOOH-Co <sub>9</sub> S <sub>8</sub> -21 electrode's (A) Fe 2p, (B) Ni 2p, (C) Co 2p, (D) S 2p, (E) O 1s XPS data, (F) the electrode surface's XRD trace, and (G) the Raman spectra for the different compositions of NiFeOOH-Co <sub>9</sub> S <sub>8</sub> -n. ....	43
<b>Figure 2.2:</b> The FE-SEM pictures of (A1 and A2) NiFeOOH-Co <sub>9</sub> S <sub>8</sub> -11, (B1 & B2) NiFeOOH-Co <sub>9</sub> S <sub>8</sub> -21, (C1 & C2) NiFeOOH-Co <sub>9</sub> S <sub>8</sub> -12, and (D1 & D2) NiFeOOH-Co <sub>9</sub> S <sub>8</sub> -	

13 at various magnifications; (E) the FeOOH-Co<sub>9</sub>S<sub>8</sub>-21 TEM image; (F) the d spacing values matching to FeOOH and Co<sub>9</sub>S<sub>8</sub> determined from digital micrographs software, inset SAED spectra of FeOOH-Co<sub>9</sub>S<sub>8</sub>-21, showing the lattice planes, (G) the corresponding IFFT plot display the d spacing values, and the HAADF-STEM image of FeOOH-Co<sub>9</sub>S<sub>8</sub>-21 for the various elements merged (H1) and for single elements (H2-H5), respectively ..... 45

**Figure 2.3:** Plots of the various catalyst compositions include: (A) SOR and (B) HER plots, (C) the potential required to realize various j values for the electrodes, (D) Tafel plot obtained from SOR traces of various electrodes, (E) EIS Nyquist plots of various electrodes and bare Ni Foam, (F) the SOR chronoamperometry data of the NiFeOOH-Co<sub>9</sub>S<sub>8</sub>-21 recorded in 1.0 M NaOH + 1.0 M Na<sub>2</sub>S solution, and (F) the SOR and (H) traces for NiFeOOH-Co<sub>9</sub>S<sub>8</sub>-21 recorded in 1.0 to 4.0 M Na<sub>2</sub>S solution, and (I) the V<sub>RHE</sub> corresponding to j values of 100, 500, and 1000 mA/cm<sup>2</sup> for different Na<sub>2</sub>S concentration. In each case, the reference electrode was made of graphite, while the counter electrode was made of Hg/HgO. The data was collected using an H-cell configuration with an inter-electrode spacing of 7 cm. .... 48

**Figure 2.4:** The LSV polarization traces (A) SOR and (B) HER of NiFeOOH-Co<sub>9</sub>S<sub>8</sub>-21 recorded under various temperature (C) The V<sub>RHE</sub> values corresponding to various j<sub>SOR</sub> and j<sub>HER</sub> values recorded under various temperature situations for NiFeOOH-Co<sub>9</sub>S<sub>8</sub>-21, (D) [S<sup>2</sup>] vs. time plots documented under various temperature conditions using NiFeOOH-Co<sub>9</sub>S<sub>8</sub>-21 as both counter and working electrodes, (E) the Tafel plots obtained from SOR traces of NiFeOOH-Co<sub>9</sub>S<sub>8</sub>-21 under various temperature conditions, (F) the Arrhenius plot for SOR using NiFeOOH-Co<sub>9</sub>S<sub>8</sub>-21 in 1.0 M Na<sub>2</sub>S + 1.0 M NaOH. .... 51

**Figure 2.5:** (A) pictures of the H-type cell and single-cell electrochemical setups used for the SOR and HER traces, (B) SOR and (C) HER profiles recorded with graphite and NiFeOOH-Co<sub>9</sub>S<sub>8</sub>-21 as the counter electrodes (D) SOR LSV traces recorded in an H-type electrochemical cell with various interelectrode distances (E) HER and (F) SOR LSV traces recorded in a single cell electrochemical setup with graphite and NiFeOOH-Co<sub>9</sub>S<sub>8</sub>-21 as the counter electrodes, the potential values corresponding to different j values achieved in a (G) single cell and (H) H-type electrochemical cell, (I) the stability

(i-t) data recorded in an H-type electrochemical cell with a 2 cm interelectrode distance using NiFeOOH-Co<sub>9</sub>S<sub>8</sub>-21 as both counter and working electrodes..... 53

**Figure 2.6:** The NiFeOOH-Co<sub>9</sub>S<sub>8</sub>-n (a: n = 21, b: n = 12, c: n = 13, d: n = 11) (A) OER and (B) HER polarization traces recorded in single cell electrochemical setup using 1.0 M NaOH electrolyte , (C) the bar graph shows the potential ( $V_{RHE}$ ) values related with different j values found during the HER and OER process, (D) the NiFeOOH-Co<sub>9</sub>S<sub>8</sub>-21 SOR (H-type electrochemical cell) and OER (single cell) polarization traces illustrating the potential ( $V_{RHE}$ ) requirements to reach certain j values, (E) the HER-SOR (1.0 M Na<sub>2</sub>S+1.0 M NaOH ) and HER-OER (1.0 M NaOH) polarization traces depict the total potential needed to realize H<sub>2</sub> production at j values of 100 mA/cm<sup>2</sup>, (F) the stability traces of HER activity recorded in absence and presence of 1.0 M NaOH in 1.0 M Na<sub>2</sub>S ..... 54

**Figure 2.7:** (A) Diagram of the H-type two-electrode electrochemical setup used to produce H<sub>2</sub> (B) evaluation of the LSV traces recorded in an H-type and single cell with NiFeOOH-Co<sub>9</sub>S<sub>8</sub>-21 as the working and counter electrodes; (C) the LSV traces documented in a two-electrode setup using an H-type electrochemical cell with a 2 cm inter-electrode distance, the electrodes used were NiFeOOH-Co<sub>9</sub>S<sub>8</sub>-21/NiFeOOH-Co<sub>9</sub>S<sub>8</sub>-21 and NiFeOOH-Co<sub>9</sub>S<sub>8</sub>-21/graphite, (D) chronoamperometry traces of the SOR conducted under two-electrode electrochemical set up in an single cell (0.8 V), and H-type (0.7 V), (E) the plot showing the faradaic efficiency with theoretical and experimental H<sub>2</sub> production over time in an H-type cell electrochemical cell, (F) a comparison of the power consumption of the current electrode and systems that have been reported for the production of 1 kg of H<sub>2</sub>, (G) the UV-Vis spectra of the electrolyte, which were obtained at different time intervals during chronoamperometry experiment, (H) the XRD data, and (I) the FE-SEM data of the Sn that was extracted from the anodic solution following H<sub>2</sub>SO<sub>4</sub> neutralization..... 56

**Figure 2.8:** The findings of the DFT analysis (A) the energy levels of Co<sub>9</sub>S<sub>8</sub> and O-doped Co<sub>9</sub>S<sub>8</sub> for the HER process, and (B) the free energy levels of the final product and intermediate as calculated utilizing a step by step SOR procedure on the 200 facet of Co<sub>9</sub>S<sub>8</sub>. ..... 58

**Figure 3.1:** (A) The NF-PAHz-Co<sub>3</sub>O<sub>4</sub>@NiCu XRD data and the associated JCPDS traces, (B) the XRD traces in "A" magnified in the 42-46° 2θ region; (C) the Cu 2p, (D) Ni 2p, (E) Co 2p, and (F) N 1s XPS spectra of NF-PAHz-Co<sub>3</sub>O<sub>4</sub>@NiCu, (G) the UPS spectra of NF-PAHz-Co<sub>3</sub>O<sub>4</sub>@NiCu, the Cu K-edge (H) XANES and (I) Fourier transformed (FT)-EXAFS spectra; the Ni K-edge (J) XANES and (K) FT-EXAFS spectra; the Co K-edge (L) XANES and (M) FT-EXAFS spectra. .... 75

**Figure 3.2:** (A & B) NF-PAHz-Co<sub>3</sub>O<sub>4</sub>@NiCu FESEM images at various magnifications, (C) NF-PAHz-NiCu & (D) PAHz-Cu FESEM images, (E & F) NF-PAHz-Co<sub>3</sub>O<sub>4</sub>@NiCu TEM images at various magnifications, (G) the d spacing value of PAHz-Co<sub>3</sub>O<sub>4</sub>@NiCu and (H) the corresponding inverse fast fourier transform (IFFT) data, (I) the TEM diffraction pattern of PAHz-Co<sub>3</sub>O<sub>4</sub>@NiCu, and (J to P) the HAADF-STEM elemental mapping of PAHz-Co<sub>3</sub>O<sub>4</sub>@NiCu..... 79

**Figure 3.3:** (A) The MOR and (B) OER lsv traces of NF-PAHz-Co<sub>3</sub>O<sub>4</sub>@NiCu, control, and reference electrodes, (C) the overall water splitting curves of NF-PAHz-Co<sub>3</sub>O<sub>4</sub>@NiCu MOR and OER-based processes, (D) the comparison of the MOR j value at 1.5 V<sub>RHE</sub> of NF-PAHz-Co<sub>3</sub>O<sub>4</sub>@NiCu with that of the recently reported systems, (E) the chronoamperometry traces of NF-PAHz-Co<sub>3</sub>O<sub>4</sub>@NiCu demonstrating the stability of MOR and OER; (F) the Tafel slope values of NF-PAHz-Co<sub>3</sub>O<sub>4</sub>@NiCu and controls recorded for MOR process, (G) the Nyquist fits of NF-PAHz-Co<sub>3</sub>O<sub>4</sub>@NiCu obtained during MOR and OER operation; and (H) the comparison of j and potential values between MOR and OER operations for NF-PAHz-Co<sub>3</sub>O<sub>4</sub>@NiCu..... 83

**Figure 3.4:** (A) The schematics of the two-electrode electrochemical setup for MOR coupled H<sub>2</sub> production using NF-PAHz-Co<sub>3</sub>O<sub>4</sub>@NiCu as the working and counter electrodes, (B) the linear sweep voltammetry (LSV) for OER and MOR based procedures in the two-electrode setup, (C) the chronoamperometry trace of the MOR based process recorded at 1.62 V and (D) the OER based process recorded at 1.76 and 2.10 V in the two-electrode setup, (G) the electrolyte solution's <sup>1</sup>H NMR and (H) FT-IR spectra recorded after regular intervals during MOR operation..... 85

**Figure 3.5:** Diagrams of the OER activity of the Co-O doped on the (A) Cu and (B) Ni sites of Co-O@NiCu, Gibb's free energy diagrams for the OER activities of NiCu,

Co@NiCu, and Co-O@NiCu calculated for (C) Cu site and (D) Ni site, respectively, PDOS of NiCu, Co@NiCu, and Co-O@NiCu obtained for (E) Cu site and (F) Ni site, (G) illustrating the different steps of MOR activity on the Co-O@NiCu operated at Cu site, and (H) the Gibb's free energy diagrams for the MOR activities on Co-O@NiCu calculated on Cu site. The catalyst's active site is denoted by the symbol \*, and the species adsorbed on it are represented by the symbols \*CH<sub>3</sub>OH, \*CH<sub>3</sub>O, \*CH<sub>2</sub>O, \*HCO, and \*HCOOH. .... 86

**Figure 4.1:** The XRD spectra of (A) CF-CeO<sub>2</sub>/Ni<sub>3</sub>S<sub>2</sub> and Ni<sub>3</sub>S<sub>2</sub>/NF with JCPDS correlations, the raman spectra of (B) CF-CeO<sub>2</sub>/Ni<sub>3</sub>S<sub>2</sub> and Ni<sub>3</sub>S<sub>2</sub>/NF, the xps spectra (C) Ni 2p, (D) Ce 3d, (E) Fe 2p, (F) Co 2p and (G) S 2p of CF-CeO<sub>2</sub>/Ni<sub>3</sub>S<sub>2</sub>. .... 98

**Figure 4.2:** The FE-SEM images of (A & B) CF-CeO<sub>2</sub>/Ni<sub>3</sub>S<sub>2</sub> and (B1 & B2) Ni<sub>3</sub>S<sub>2</sub>/NF at various magnifications, (E & F) TEM image of CF-CeO<sub>2</sub>/Ni<sub>3</sub>S<sub>2</sub>; (G) the d spacing values matching with Ni<sub>3</sub>S<sub>2</sub> and CeO<sub>2</sub> computed from digital micrographs software, the inset displays the SAED spectra of CF-CeO<sub>2</sub>/Ni<sub>3</sub>S<sub>2</sub> displaying the lattice planes, and (G) IFFT plot displaying the d spacing values, the (I-P) HAADF-STEM elemental mapping of CF-CeO<sub>2</sub>/Ni<sub>3</sub>S<sub>2</sub>. .... 100

**Figure 4.3:** The LSV polarisation traces for (A) UOR, (B) HER, the overall (UOR+HER) LSV traces of CF-CeO<sub>2</sub>/Ni<sub>3</sub>S<sub>2</sub>, (D) Tafel slope, (E) EIS plot and (H) chronoamperometry trace of CF-CeO<sub>2</sub>/Ni<sub>3</sub>S<sub>2</sub>. .... 102

**Figure 4.4:** The (A) Schematic representation of two electrode device, (B) LSV polarisation traces of CF-CeO<sub>2</sub>/Ni<sub>3</sub>S<sub>2</sub> and Ni<sub>3</sub>S<sub>2</sub>, and (C) chronoamperometry trace of CF-CeO<sub>2</sub>/Ni<sub>3</sub>S<sub>2</sub>. .... 103

This page was initially left blank.

## List of Scheme

- Scheme 2.1:** (A) The NiFeOOH-Co<sub>9</sub>S<sub>8</sub>-n heterostructure is formed in a one-pot synthetic technique, as seen in the synthetic scheme. (B) The table displays the sample code and matching Fe<sup>3+</sup>: Co<sup>2+</sup> ratios taken in the precursor solution. .... 42
- Scheme 3.1:** The synthesis of different nanostructures with and without NF is shown in the schematic method. .... 73
- Scheme 4.1:** Synthetic scheme showing the formation of CoFe doped CeO<sub>2</sub>@Ni<sub>3</sub>S<sub>2</sub>. . 97

This page was initially left blank.

## List of Abbreviations

<b>OER</b>	Oxygen Evolution Reaction
<b>HER</b>	Hydrogen Evolution Reaction
<b>SOR</b>	Sulfion Oxidation Reaction
<b>DFT</b>	Density Functional Theory
<b>NF</b>	Nickel Foam
<b>PAHz</b>	Polyacryloyl Hydrazide
<b>XRD</b>	X-ray diffraction
<b>FT-IR</b>	Fourier Transform-Infrared
<b>THF</b>	Tetrahydrofuran
<b>NMR</b>	Nuclear Magnetic Resonance
<b>DSC</b>	Differential Scanning Calorimetry
<b>XPS</b>	X-Ray photoelectron spectroscopy
<b>UPS</b>	Ultraviolet photoelectron spectroscopy
<b>SEM</b>	Scanning electron microscopy
<b>XANES</b>	X-ray absorption near edge structure
<b>FT-EXAFS</b>	Fourier transformed-Extended X-ray absorption fine structure
<b>HR-TEM</b>	High resolution transmission electron microscopy
<b>SAED</b>	Selected Area Electron Diffraction
<b>LSV</b>	Linear Sweep Voltammetry

<b>R<sub>s</sub></b>	Solution Resistance
<b>CV</b>	Cyclic Voltammetry
<b>TM</b>	Transition Metal
<b>HMF</b>	5-hydroxymethylfurfural
<b>AOR</b>	Alcohol Oxidation Reaction
<b>H<sub>2</sub>OR</b>	Hydrozine Oxidation Reaction
<b>TOF</b>	Turnover frequency
<b>ECSA</b>	Electrochemically Active Surface Area
<b>η</b>	Overpotential
<b>NC</b>	Nitrogen-doped Carbon
<b>DFT</b>	Density Functional Theory
<b>DI</b>	Deionized
<b>IFFT</b>	Inverse Fast Fourier Transform
<b>HAADF-STEM</b>	High-Angle Annular Dark-Field Scanning Transmission Electron Microscopy
<b>PDOS</b>	Partial Density of States

# Preface

The development of efficient and durable catalysts for hydrogen production from oxidation reactions is crucial for enabling clean and sustainable hydrogen energy technologies. Transition metal (TM) compounds have emerged as promising heterogeneous catalysts for oxidizing sulfur compounds, water, methanol and urea to generate hydrogen gas and valuable chemicals via thermochemical and electrochemical routes. Hydrogen has emerged as a promising energy carrier for a sustainable and low-carbon future. However, the development of economical and scalable production methods from abundant feedstocks remains a significant challenge. The electrochemical oxidation of sulfur-based compounds is a crucial process in various industrial applications, such as the desulfurization of fuels, production of sulfuric acid, elemental sulfur, and hydrogen. TM-based catalysts have been extensively studied for Sulfur Oxidation Reaction (SOR) due to their unique electronic properties, high conductivity, and ability to facilitate electron transfer reactions. These catalysts can significantly enhance the reaction kinetics, selectivity, and overall efficiency of the SOR process. The choice of TM, its composition, nanostructure, and support material play a vital role in determining the catalytic performance. The electrochemical water oxidation reaction is a key half-cell reaction in many nonconventional energy conversion and storage technologies, such as electrochemical water splitting is a pollution free approach to produce hydrogen fuel and used in metal-air batteries. But the sluggish kinetics a significant bottleneck that requires effective catalysts to facilitate the multi-electron transfer process. TM-based heterogeneous catalysts have emerged as promising candidates due to their high activity, stability, and earth abundance compared to noble metal catalysts. The electrochemical conversion of methanol to value-added chemicals has gained significant attention due to the increasing demand for sustainable energy

storage and chemical production. Among the potential products, formate ( $\text{HCOO}^-$ ) is a valuable chemical feedstock with applications in various industries, including agriculture, pharmaceuticals, and energy storage. The electrocatalytic oxidation of methanol to formate offers an attractive alternative to traditional chemical processes, as it can be conducted under mild conditions and potentially utilize renewable electricity. TM-based catalysts have shown great promise in facilitating the selective oxidation of methanol to formate. These catalysts can be designed and tailored to achieve high activity, selectivity, and stability through careful selection of metal centers, ligand environments, and nanostructured architectures.

Chapter 1: In this chapter, we have elaborated the detailed introduction of TM-based catalyst for sulfion, water and methanol oxidation reaction. TM-based catalysts have high electrocatalytic activity, high surface area with more active sites for MOR, OER, OER, UOR and HER.

Chapter 2: In this chapter, the synthesis of the  $\text{NiFeOOH-Co}_9\text{S}_8$  heterojunction catalyst represents a promising approach for sustainable hydrogen production and waste valorization. This bifunctional catalyst leverages the synergy between the nickel-iron oxyhydroxide ( $\text{NiFeOOH}$ ) and cobalt sulfide ( $\text{Co}_9\text{S}_8$ ) components to facilitate the sulfur oxidation reaction (SOR) coupled with the hydrogen evolution reaction (HER). SOR involves the oxidation of sulfur-containing compounds, such as sulfion (a mixture of sulfur-containing waste from industrial processes and petroleum refining), to produce valuable chemicals like sulfuric acid and elemental sulfur. Simultaneously, the HER occurs, generating hydrogen gas as a clean energy carrier.

Chapter 3: In this chapter, the  $\text{Co}_3\text{O}_4@ \text{NiCu}$ -Polymer nano cubes synthesized using polyacryloyl hydrazide as a reducing and capping agent on a nickel foam surface

represent a versatile and efficient catalyst system for both methanol oxidation and water oxidation reactions. The selective production of formate from methanol and the ability to operate without a membrane system make this catalyst promising for various energy-related applications, such as fuel cells, chemical synthesis, and water splitting processes.

Chapter 4: In this Chapter, the CoFe doped CeO<sub>2</sub>/Ni<sub>3</sub>S<sub>2</sub> catalyst was synthesized via a hydrothermal method using reducing sugar, likely involving the reduction of metal precursors by carbohydrate like glucose to form the mixed metal oxide/sulfide nanoparticles. This catalyst is being explored for the urea oxidation reaction, which produces hydrogen gas as a clean fuel. Here we used cerium with Co and Fe because cerium itself can act as both a catalyst and a catalyst promoter. Its flexible coordination environments and excellent redox properties (ability to cycle between Ce<sup>3+</sup> and Ce<sup>4+</sup> oxidation states) make it advantageous. The redox cycle of Ce can facilitate charge transfer processes involved in catalytic cycles.

Chapter 5: In this chapter, we have concluded the important aspects of TM based nano catalyst for efficient anode half-cell. Future perspectives on the work are also discussed, along with some key recommendations.

This page was initially left blank.

# Chapter 1

## Introduction and Literature Survey

### 1.1 Abstract

Hydrogen has become an attractive choice in the search for sustainable energy solutions due to its high energy density and renewability. A viable method for producing hydrogen ( $H_2$ ) sustainably is electrocatalytic water splitting, however, the anodic oxygen evolution reaction (OER) limits the process. The water-splitting cell's efficiency is diminished by the sluggish kinetics and high energy consumption. Using more thermodynamically advantageous substrate oxidation processes in place of the anodic OER to get around this restriction. These different reactions may result in "hybrid" or "assisted" water electrolysis configurations, where the anodic oxidation step offers flexibility in process design and output while simultaneously increasing energy efficiency and producing value-added products. The use of sacrificial oxidants in hybrid water electrolysis systems has been the focus of recent developments, these oxidants are chosen such that their oxidation produces useful byproducts, improving the process's overall sustainability and economics. Another crucial area of study is the development of transition metal-based catalysts. The inherent catalytic activity and stability may be improved by carefully adjusting the chemical and electrical conditions. Studies of these systems involve determining active catalytic sites, clarifying interactions with reaction intermediates, and comprehending how adding different materials influences the overall reaction dynamics. Many tactics, such as the creation of nanostructures, the addition of conductive support materials, and the introduction of foreign elements, have been used to improve the performance of electrocatalysts. To solve the worldwide challenges of pollution and energy scarcity, hydrogen is a viable clean energy carrier.

## 1.2 Hybrid Water Electrolysis Process for Green Hydrogen Production

The potential of hydrogen as a replacement for conventional fossil fuels like natural gas and gasoline is becoming more widely recognized. Its potential for zero carbon emissions and high energy density (120-142 MJ kg<sup>-1</sup>) makes it a desirable alternative for sustainable energy. [1,2] Therefore, creating effective and eco-friendly processes to create "green" hydrogen has taken center stage in the energy industry. [3] Hydrogen generation using water electrolysis using renewable energy sources has shown promise. The HER at the cathode and OER at the anode are the two half-reactions involved in the electrolysis of water.[4,5] Under conventional circumstances (25°C and 1 atm), the thermodynamic voltage needed for water electrolysis is 1.23 V, however, in real-world applications, larger cell voltages are usually needed, often surpassing 1.8 V.[6,7] In particular, this is true the high current densities required in industrial environments.[8,9] The slow kinetics of the four-electron oxygen evolution process, which results in a high activation barrier, provide the biggest obstacle to water electrolysis.[10,11] Removing this obstacle is essential to increasing the scalability and efficiency of hydrogen generation by water electrolysis. Significant progress has been achieved recently in creating anode and cathode electrocatalysts that are more effective in lowering overpotentials and total cell voltage during the electrolysis of water. Traditional water electrolysis still has a number of drawbacks, such as the anode's generation of non-valuable oxygen, the necessity for a membrane to keep hydrogen and oxygen from mixing, and the high energy costs. [12,13] Novel electrochemical approaches have been suggested by researchers as solutions to these problems. Using solid redox anodes in a decoupled water-splitting system avoids the requirement for a membrane and lowers the possibility of gas mixing. [14,15] Nevertheless, this technique still uses a lot of energy at the anode for the oxygen evolution process (OER). Hybrid water electrolysis has drawn interest as a more potential alternative. By using a different electrolyte at the anode, this system may substitute the



transition metal-based catalyst. These reactions are beneficial due to hydrogen production on the cathode side and valuable chemicals on the anode side.

### **1.2.1 Background of Water Electrolysis**

Nicholson and Carlisle made the first discovery of water electrolysis in 1800, marking the beginning of the first industrial revolution and the history of the process.[34] The next several decades saw further advancements in the technique, with the first large-scale 10,000 Nm<sup>3</sup>/h plant operating in 1939 and more than 400 industrial water electrolysis units operating by 1902.[35] General Electric was developed the first solid polymer electrolyte (SPE) system in 1966, the first solid oxide water electrolysis unit was created in 1972, and Zdansky/Lonza developed the first pressurized commercial electrolyzer in 1948 were all noteworthy turning points in the 20<sup>th</sup> century. Cutting-edge alkaline systems first appeared in the late 1970s. [36] Recent advancements in high-temperature solid oxide technology, together with the rebuilding and optimization of alkaline water electrolyzers, have allowed for the creation of proton exchange membranes for fuel cells and water electrolysis units, further revolutionizing the industry. Advancements in water electrolysis capabilities and applications across sectors have been made possible by this continuous stream of breakthroughs over the last 200 years. [37]

### **1.2.2 Statement of the Problems**

Water electrolysis is a potential technique for creating clean hydrogen fuel, but to be effective and economically feasible, it must overcome several important obstacles. These difficulties include a wide range of electrolysis-related topics, including reaction kinetics, material constraints, and safety issues. The possible mixing of hydrogen and oxygen gases generated at the cathode and anode, respectively, is one of the main safety issues with water electrolysis. If this combination is lit on fire, there might be serious threats to people's safety. Since gas crossing lowers the quality of the hydrogen generated,

preventing it is essential for efficiency as well as safety. [38] The cathode and anode compartments are kept apart by membranes, which also enable the selective movement of ions and prevent gas mixing. Finding membrane materials that can withstand the severe conditions of electrolysis and are also highly conductive is still a difficult task. It is necessary to overcome problems including fouling, membrane deterioration, and excessive costs. [39] Noble metal catalysts, namely platinum for the HER and iridium for the OER, are essential to many effective electrolyzers. Due to their scarcity and high cost, these materials greatly raise the total cost of electrolyzers. The development of stable, affordable, and active substitutes for noble metal catalysts is a primary area of scientific interest. Catalyst deterioration may eventually result from the rigorous working conditions of water electrolysis, which include high potential and very high pH settings. Enhancing the catalysts' long-term stability under working circumstances is essential to the water electrolysis systems potential to be commercially successful. [40] While the HER prefers acidic environments, the OER usually occurs more effectively in alkaline conditions.

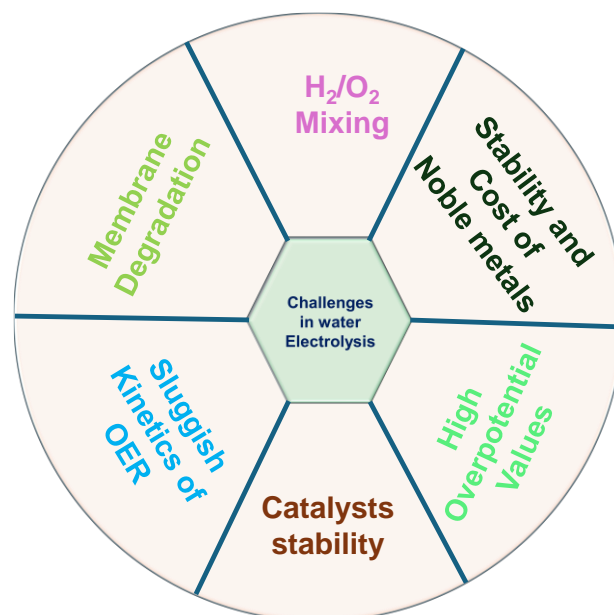


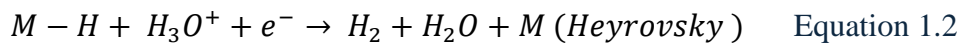
**Figure 1.2:** Major problems occurred in water electrolysis.

The issue in building effective electrolyzers that can function ideally for both half-reactions at the same time is the pH mismatch. Developing pH-neutral electrolytes or coming up with innovative cell designs that can adapt to various pH conditions might be two ways to solve this problem. [41] In comparison to the HER, the OER is kinetically slower. Efficiency losses and elevated overpotentials result from this disparity in response rates. Improving the reaction kinetics of electrode designs and creating more active OER catalysts are essential for raising system efficiency. [42] The overall lifetime of electrolyzers is a significant factor in their economic feasibility. Components such as catalysts, membranes, and electrodes can degrade over time, leading to decreased efficiency and eventual failure. Extending the operational lifetime of electrolyzers is essential for reducing the levelized cost of hydrogen production. [43]

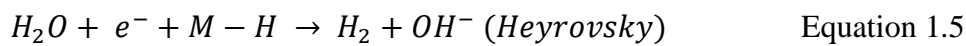
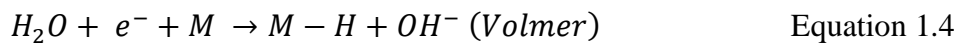
### **1.2.3 Half-Cell reactions in water electrolysis**

Two different electrochemical reactions take place at different electrodes during the process of water electrolysis. The HER occurs at the cathode and hydrogen gas is formed when water molecules are reduced and acquire electrons. Concurrently, the OER takes place at the anode where water molecules get oxidized and lose electrons during this half-reaction, releasing oxygen gas. The total water electrolysis process, which separates water into its individual components of hydrogen and oxygen, is made up of these two half-cell processes. In water electrolysis, HER usually takes place on the cathode surface. [44] Multiple processes are involved in this process in acidic conditions. First, a hydronium ion ( $\text{H}_3\text{O}^+$ ) contacts with an open site (represented by M) on the electrocatalyst surface to initiate the Volmer reaction. The hydronium ion is released as a result of this interaction, and an adsorbed hydrogen atom (M-H) forms on the catalyst surface. After that, one of two processes, the chemical Tafel step or the electrochemical Heyrovsky step, can lead to the creation of molecular hydrogen ( $\text{H}_2$ ). In the Heyrovsky

step, the adsorbed hydrogen and another hydronium ion combine to make H<sub>2</sub> and replenish the catalyst site. As an alternative, two nearby adsorbed hydrogen atoms combine to generate H<sub>2</sub> in the Tafel step, which also frees up the catalyst sites. [45] The composition of the electrocatalyst, the electrode voltage, and the reaction circumstances are some of the variables that affect the specific route and efficiency of H<sub>2</sub> synthesis.

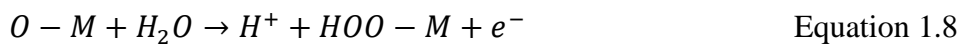


In contrast to acidic medium, the hydrogen HER mechanism is different in alkaline/neutral environments. The Tafel step is unchanged in alkaline or neutral conditions, however the Heyrovsky and Volmer processes include hydroxide ions. [46]

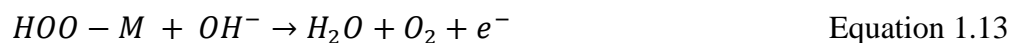
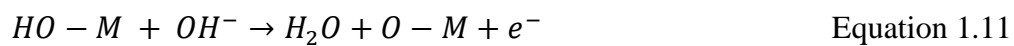


The main difference is that instead of proton reduction, water dissociation forms the metal-hydrogen (M-H) intermediates under alkaline/neutral circumstances.[47] For all electrocatalysts, the HER kinetics are largely dependent on the strength of these M-H bonds.[48] According to Sabatier's principle, the M-H bond strength should be balanced, that is, neither too strong nor too weak for maximum HER activity to occur. Both the construction of M-H intermediates and the eventual release of hydrogen gas are aided by this equilibrium. Consequently, hydrogen binding energy is often used as a HER activity descriptor. [49] It's crucial to remember that Sabatier's concept by itself is unable to account for the fact that metal electrocatalysts often show less HER activity in alkaline environments as opposed to acidic ones. This explanatory power limit emphasizes the

intricacy of the HER process and the need to take extra factors into account when evaluating the performance of electrocatalysts in various pH ranges. At the anode OER is a crucial step in the electrolysis of water. Water molecules immediately undergo oxidation in acidic media. The procedure starts with the adsorption of water onto the electrode surface and proceeds through many stages of electron transfer that are related to protons. [50] The steps are the following:



The action is identical in alkaline conditions, but instead of using water molecules, it uses hydroxide ions. Adsorbed hydroxyl species are created throughout the process, which begins with the oxidation of hydroxide ions. Oxygen evolution is the result of subsequent stages that entail the production of oxo and peroxy intermediates. [51] The mechanism is given below:



Compared to acidic medium, the use of less costly, non-noble metal catalysts is often permitted in alkaline environments. The total performance of water splitting in both

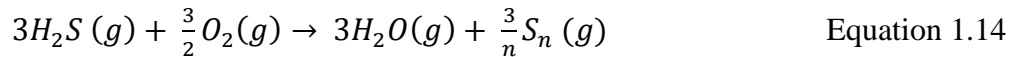
scenarios depends heavily on the OER's efficiency, which is often constrained by the large overpotential needed to drive the reaction.

#### **1.2.4 Hydrogen Production Coupled with Sulfion Oxidation Reaction (SOR)**

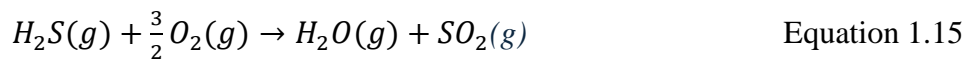
Sulfion oxidation reaction (SOR) is essential to many significant applications in a wide range of sectors. This procedure is crucial for the creation of sulfur-based batteries, [52] hydrogen sulfide recovery [53] and electrochemical desulfurization. [54,55] When dealing with the problems caused by sulfides, which are common in both residential and commercial wastewater from a variety of sources including tanneries, [56] paper mills, [57] and petrochemical industries, [58] the need of SOR becomes clearer. Since these sulfides often have strong corrosive properties, [59] disagreeable scents, [60] and are hazardous, [61] effectively eliminating them by SOR is essential for both improving human health and safety and protecting the environment. Even if they work well, traditional sulfide abatement technologies including biological and chemical oxidation, catalytic conversion, and precipitation approaches have several disadvantages. [62,63] These methods usually have high operating costs because they need significant energy inputs and depend largely on chemical additions. To address the broad problem of sulfide pollution across multiple industries, it is imperative that more effective and affordable SOR technologies be developed, combining environmental considerations with practicality. For hydrogen production mainly electrochemical water splitting is used but the OER at the anode has a high energy barrier, which makes it difficult to electrolyze water to create hydrogen.[64] This process includes complicated, multi-step, slow-kinetic proton and electron transfers and necessitates a substantial voltage of 1.23 V vs. RHE.[65] Large, applied potentials are required because to the thermodynamic limits of the OER, which despite advances in catalyst design, results in poor energy efficiency and high energy consumption for hydrogen production.[66]

#### 1.2.4.1 Claus Process for Sulfur Recovery

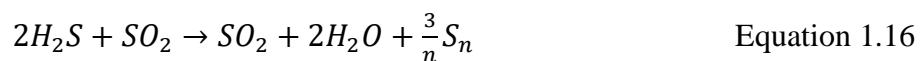
The most popular technique for turning hydrogen sulfide (H<sub>2</sub>S) into elemental sulfur (S<sub>8</sub>) is the Claus process, especially for acid gas streams that include more than 20% H<sub>2</sub>S. [67,68,69]



This procedure entails a two-step reaction sequence. Equation 1.15 describes the first stage, which takes place in a high-temperature thermal reactor. Here, around one-third of the H<sub>2</sub>S is oxidized with oxygen to create water vapor and sulfur dioxide (SO<sub>2</sub>). Even with oxygen enrichment, the process is restricted to acid gas streams containing at least 20 mol% H<sub>2</sub>S since this reaction needs a steady flame.



After this first oxidation, in the thermal reactor (fitted with a waste heat boiler) and later catalytic reactors, the remaining two-thirds of the H<sub>2</sub>S react with the freshly generated SO<sub>2</sub>. Equation 1.16 depicts this second process, which produces extra water vapor and elemental sulfur. Together, these two procedures efficiently transform hydrogen sulfide into elemental sulfur, optimize sulfur recovery, and control the heat produced by the exothermic processes.



Although the Claus process is often used in industry to handle H<sub>2</sub>S, certain serious issues have not yet been properly resolved. The significant expense of controlling the tail gas, which needs extra processing to satisfy environmental regulations, is one of the main issues. Furthermore, certain organizations may find it difficult to enter the market due to the significant upfront costs associated with putting the Claus method into practice.

Fundamental to the process is the chemistry of oxidative reactions, which naturally provide water as a byproduct. Due to its low worth, this water represents a lost chance to use resources more effectively. The Claus method is still the industry standard because it can properly dispose of  $\text{H}_2\text{S}$  without harming the environment, even with these drawbacks. This procedure efficiently transforms the dangerous gas into sulfur compounds that are easier to handle and comply with stricter environmental standards. [70]

The electrocatalytic SOR provides a more effective way, without the need for extra oxidants or intricate separation procedures, to transform sulfide ions into useful elemental sulfur at ambient temperature.[71] The SOR's oxidation potential ( $\text{S}^{2-} \rightarrow \text{S} + 2e^-$ ) is a remarkable  $-0.48 \text{ V}$  Vs SHE, which is much lower than the OER.[22] An anode-based SOR and cathode-based HER may be combined to form a hybrid water electrolysis system.[72]

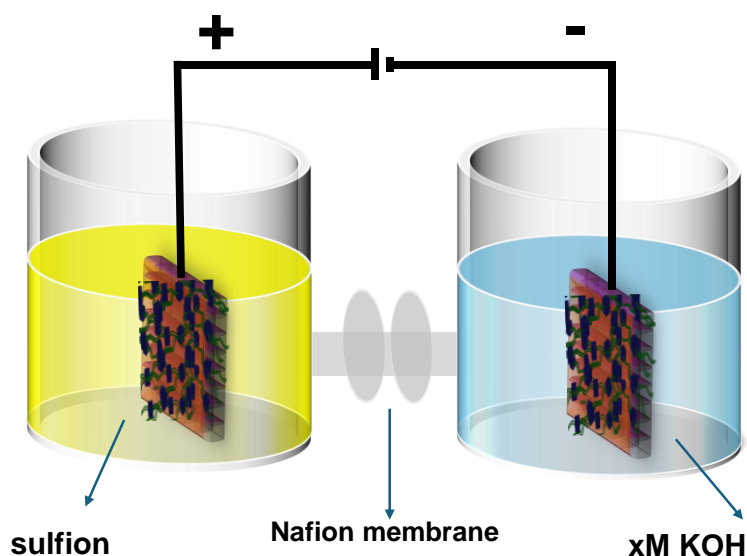


**Figure 1.3:** Electrolytic cell assembly of SOR coupled with HER

In comparison to conventional water splitting techniques, this technology offers significant economic and environmental benefits by recovering sulfur and producing hydrogen concurrently. It also lowers the total cell voltage.

### 1.2.5 H<sub>2</sub> Production Coupled with Methanol Oxidation Reaction (MOR)

Methanol (CH<sub>3</sub>OH) stands out as a particularly advantageous biomass derivative due to its simple C1 molecular structure, comparatively low theoretical oxidation potential, and high theoretical scale hydrogen coproduction during the oxidation of biomass and related chemicals. [73] The major sources of methanol are the following:

### 1.2.6 Natural Gas

Natural gas, which mostly consists of methane, is the most often utilized feedstock for the synthesis of methanol. The conversion of methane to synthesis gas, which is a blend of hydrogen and carbon monoxide, is known as steam reforming. After that, the synthesis gas is catalytically transformed into methanol. [74]

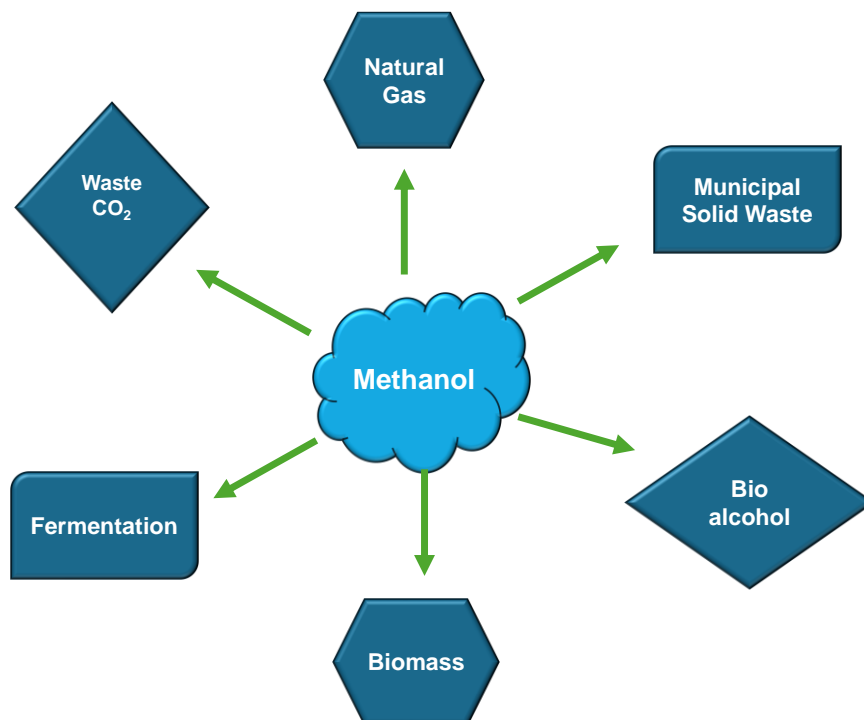


**Figure 1.4:** Major Sources of methanol production.

### **1.2.7 Biomass**

Gasification and other catalytic conversion procedures may be utilized to create methanol from renewable biomass sources, such as wood waste, energy crops, and agricultural wastes. [75]

### **1.2.8 Fermentation**

Methanol may be directly produced by fermenting biomass feedstocks, such as agricultural wastes and municipal solid wastes, using certain microorganisms, such as yeasts or bacteria that have been genetically modified. [76]

Biomass and its derivatives represent the most rich and renewable carbon resources on Earth. Thermodynamically referred to as the conversion of methanol to formate is more advantageous than water oxidation and uses less energy. Methanol upgrading is the process of electrochemically reforming methanol to create hydrogen as well as perhaps valuable formate. In several industrial areas, such as printing, fabric dyeing, and pharmaceutical manufacture, formate is an essential middleman. One million tons or more of formic acid are produced each year, making it a major chemical product. Nowadays, the production of formate involves two steps: first, methanol and carbon monoxide react at high temperatures and pressures. The resultant methyl formate is then hydrolyzed. [77] Due to its high demand and energy-intensive production method, formate is four times more expensive per metric ton than methanol. Methanol is a more desirable choice than other alcohols due to its higher capacity for producing hydrogen and other advantageous qualities. Together, these elements draw attention to the importance of methanol in relation to chemical production, renewable energy sources, and possible industrial uses. They also underline the role that methanol will play in the shift towards more environmentally friendly and productive chemical processes. [78] Formate synthesis from alcohols by electrocatalysis is an exciting new route in

sustainable chemical synthesis. Although C2 alcohols such as glycerol and ethylene glycol have been investigated for this purpose, their effectiveness has been hindered by the increased energy needed for the breakage of carbon-carbon bonds and their reduced selectivity with respect to the formation of formate.[79,80] On the other hand, it seems like a more practical and promising approach to convert C1 methanol to formate. By using the benefits of electrocatalysis, this methanol-to-formate method enables conversion at room temperature and ambient situations. In alkaline media, the electrochemical setup combines the MOR at the anode with the HER at the cathode to produce formate and hydrogen concurrently. [81]

Enhanced hydrogen evolution, less reliance on fossil fuels, and possible improvement of commercial formate synthesis methods are only a few advantages of this approach.

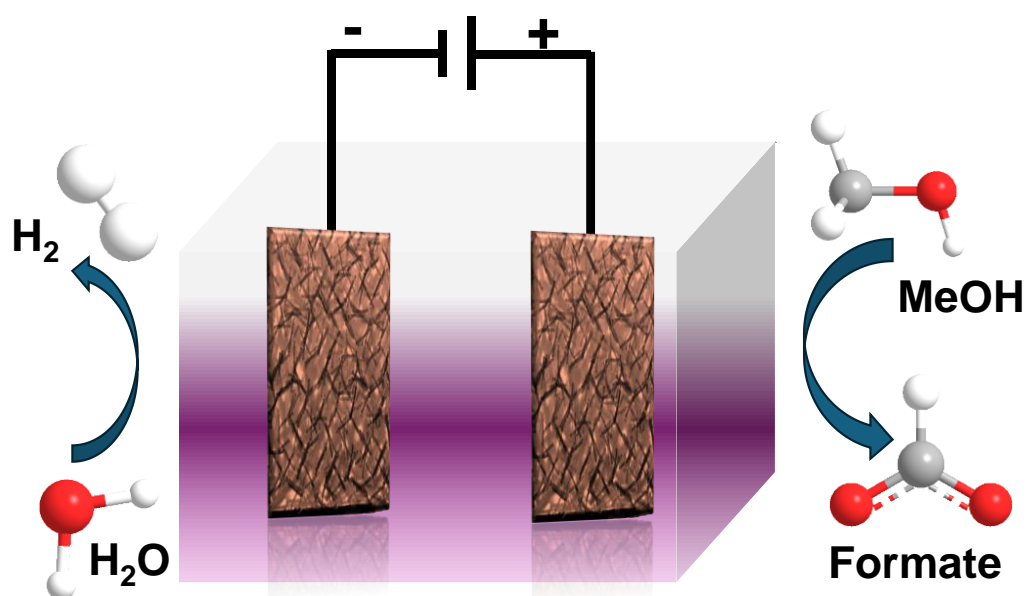


**Figure 1.5:** Schematic illustrating energy-efficient H<sub>2</sub> production coupled with MOR electrolyzer/devices.

These elements work together to make the electrocatalytic conversion of methanol to formate a desirable and ecologically responsible method of producing chemicals and converting energy, which is in line with the chemical industry's increasing need for sustainable solutions.

A major area of concentration in the study of electrocatalysis has been the development of effective and affordable catalysts for the MOR and HER in water electrolysis systems. Although platinum nanoparticles and ruthenium/iridium oxides were the main components of earlier catalysts for these reactions, their high cost and unavailability have prevented them from being widely used in industry. [82,83] To tackle these obstacles, focus on creating dual-function catalysts made of elements that are readily available on Earth, which have high activity and long-term stability for both MOR and HER. Nanomaterials based on nickel have become attractive options because of their availability and high intrinsic activity. Numerous compounds containing nickel, such as NiCu alloy, [84] Cu/NiCu,[85] CNFs@NiSe/CC,[86] NiO/NF[87] Fe-Ni NPs,[88] Ni/N-C@500,[89] CuNi NPs[90] Ni(OH)<sub>2</sub>/MnCO<sub>3</sub>[91] have shown significant promise in this area. Researchers have used techniques including heteroatom doping and morphological design to further improve the performance of these materials, to increase MOR/HER electrocatalysts' longevity and activity. These techniques have created new opportunities for the development of highly effective and financially feasible hybrid water electrolysis systems, which may pave the way for more environmentally friendly energy generation techniques.

The full oxidation of methanol by precious metal catalysts usually results in the production of carbon dioxide (CO<sub>2</sub>) and water (H<sub>2</sub>O) as byproducts. When the objective is to create useful chemical intermediates, this total oxidation is often undesired. On the other hand, non-precious metal catalysts provide a more focused method. These catalysts

can promote incomplete methanol oxidation reactions, or i-MORs. The main benefit of MOR is that it produces formic acid as opposed to completely oxidized compounds. The synthesis of high-value compounds from methanol may now be done effectively and sustainably using a selective oxidation process. Rather than using the less valuable byproducts of full oxidation, these non-precious metal catalysts provide for a more cost-effective and ecologically responsible method of generating critical chemical intermediates by halting the process at the formic acid stage. [92,93] The Possible mechanism of the methanol oxidation reaction is given below:

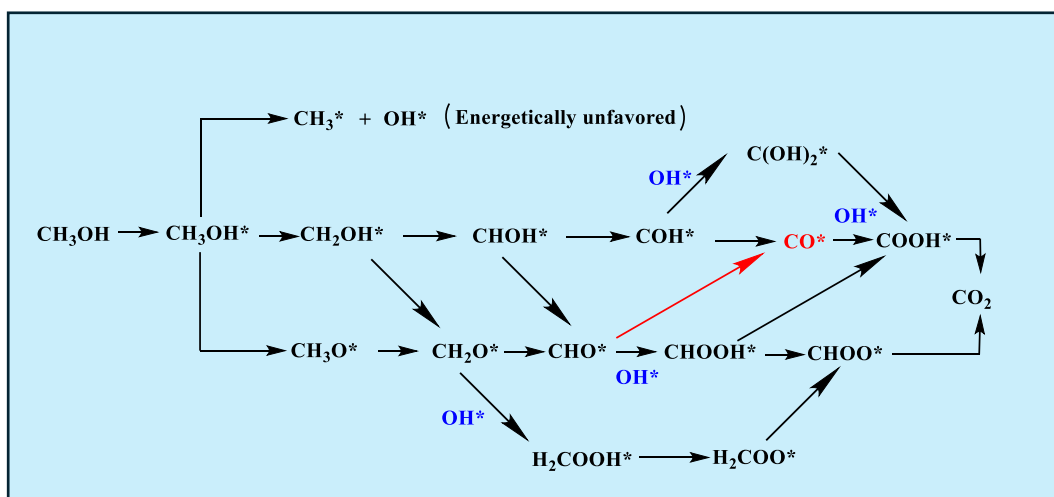


**Figure 1.6:** An electrocatalytic MOR mechanism with two pathways, where the adsorption site on the catalyst surface is denoted by the symbol \*, the CO route by the red arrows, and the CO-free pathway by the others. Reproduced with permission from ref. [187]. Copyright 2023 Wiley-VCH

### 1.2.9 Hydrogen production coupled with urea oxidation reaction

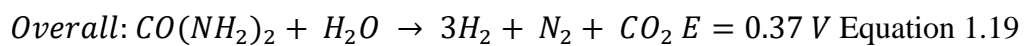
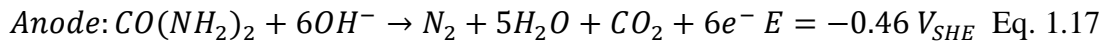
Urea is biologically broken down into ammonia by urease enzymes found in certain microbes. [94] Because of its enzymatic beginnings, this process first seems to be non-toxic and ecologically benign. However, if the resulting ammonia is left untreated, it can undergo additional reactions to form environmentally harmful compounds like nitrites and ammonium sulfate, which can seriously harm human health, disrupt soil chemistry,

and affect air quality. [95,96] As a substitute strategy that completely avoids ammonia production, electrochemical urea oxidation has been thoroughly investigated to overcome these environmental issues. In addition to reducing environmental risks, this electrochemical technique shows promise for use in sustainable energy production, especially in systems that generate hydrogen. The urea oxidation reaction (UOR) has attracted a lot of interest, since the theoretical potential need for urea-assisted water splitting is strikingly lower at 0.37 V than the much greater 1.23 V required for traditional water splitting. [97]

There are many uses of urea electro-oxidation in fuel cells, urea wastewater treatment, and hydrogen production.[98,99] The procedure is very intricate, requiring a complicated mechanism that uses four protons and six electrons, which makes it kinetically slow and needs extremely effective catalysts to reach realistic reaction rates.[100] The traditional catalysts for this process have historically been noble metals including iridium, platinum, and ruthenium. Nevertheless, they are not viable for extensive industrial applications because of their high cost and restricted supply. [101,102] Because of this financial limitation, research attention is now being directed on more prevalent transition metals and their oxides as substitute catalysts. [103] Since they are inexpensive and have a respectable catalytic activity, nickel and its hybrid compounds have become very attractive options. The catalytic mechanism of nickel-based materials is a two-step process: first, high-valence nickel species are produced by electrochemical oxidation, and then these activated nickel species oxidize urea molecules in a chemical oxidation step. This mechanistic knowledge has been essential in creating nickel-based catalytic devices for urea electro-oxidation that are more effective.

### 1.2.10 Mechanism of UOR

Similar to water splitting, two simultaneous processes take place at separate electrodes in urea-assisted electrochemical devices: the HER at the cathode and UOR at the anode. Usually, an alkaline electrolyte environment is used for this procedure. The mechanism is given below: [104]



### 1.3 Why transition Metal-based catalyst?

The advancement of water electrolysis and hybrid water electrolysis technologies depends on the creation of effective electrocatalysts for HER, OER, MOR, UOR and SOR. Although Pt, Ru, Ir, Rh, Pd and Ru based catalysts are now thought to be state-of-the-art catalysts. [105,106] These include inadequate stability, especially for OER catalysts, high prices, poor adherence to substrate significant overpotentials during large-scale operations, and scarcity. [107] Therefore, the development of non-precious, transition metal-based substitutes are urgently needed. Chalcogenides, [108] carbides, [109] sulfide, [110] phosphides [111] (oxy)hydroxide, [112] borides [81] and oxides [113] are among the attractive options for hybrid water electrolysis, these compounds usually exhibit superior performance in acidic and alkaline environments. To improve the gas-solid-liquid triple phase interface characteristics performance and lifetime of these noble metal-free catalysts, particularly at high current densities. This method entails a thorough approach that targets three crucial areas:

1. Boosting mass transfer and from the catalytic surface within the electrolyte.

2. Improving transport charges from the conducting support to redox intermediates and active sites.
3. Optimizing surface conversion processes, such as reactant adsorption, the desorption of intermediates, and interfacial charge transfer and products from active centers.

Recently, advances in the science of water electrolysis have been made by creating extremely stable and active electrocatalysts that can overcome the drawbacks of existing noble metal-based systems via the careful integration of these components. Many tactics have been used to maximize charge transfer and improve active site exposure to improve electrocatalyst performance. With the creation of various morphologies such as microspheres,[114] nanowires,[115] nanosheets,[116] nanorods,[117] nanocubes[84] and nanoarrays,[118] nanostructuring has shown to be an important strategy. The accessibility and surface area of active areas are enhanced by these nanostructures. Composition engineering has been used to improve inherent catalytic activity and provide synergistic effects, especially when creating multi-component systems. Metal (alloy) core electrocatalysts, [119] binder-free electrocatalysts, [120] and the use of highly conductive substrates including carbon cloth, [121] carbon fiber, [122] Ni foam, [123] and Cu foam [124] increase charge transmission. Larger surface areas for catalyst development and dispersion, improved conductivity overall, faster electron transfer rates, and improved accessibility to active. This all-encompassing method reduces electrochemical polarization, which lowers overpotentials. Furthermore, direct metal sources for the fabrication of electrocatalysts with different morphologies may be provided via metal-based support.

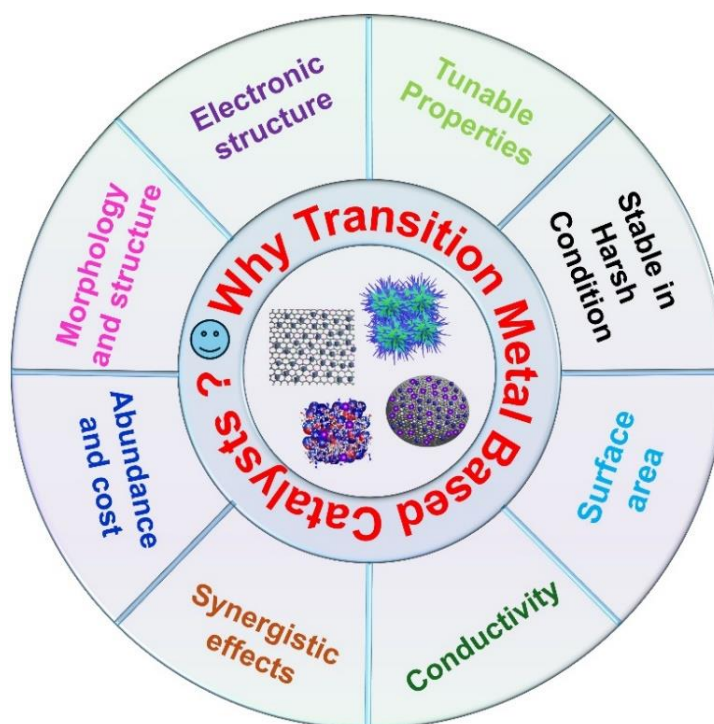


**Figure 1.7:** Important properties of transition metal-based catalyst.

Through the integration of nanostructuring, composition engineering, and optimum support materials, scientists hope to increase the performance of electrocatalysts for a range of applications by increasing the utilization efficiency of active sites and improving overall conductivity.

#### **1.4 Transforming Waste into Sustainable Energy: The Role of Sulfion, Methanol and Methanol Oxidation Reactions-**

Sulfion Oxidation Reaction – One possible technique for producing clean hydrogen ( $H_2$ ) from hazardous waste, such as hydrogen sulfide ( $H_2S$ ), is the sulfion oxidation reaction (SOR). This technique recycles environmental contaminants in addition to creating  $H_2$  that uses less energy. For example, a CoNi@NGs catalyst that efficiently converted poisonous  $H_2S$  into useful  $H_2$  and sulfur, achieving a low SOR onset potential of 0.25 V and a high faradaic efficiency (FE) of almost 98% at  $100\text{ mA cm}^{-2}$ .<sup>[53]</sup> This strategy demonstrates how industrial by-products may be used to promote the hydrogen economy.

Urea Oxidation Reaction- Another cutting-edge method for producing sustainable energy is urea electrolysis. Compared to conventional water splitting, it can theoretically save almost 70% of the energy by lowering the thermodynamic potential from 1.23 V to 0.37 V. [125] This procedure may efficiently use urea-rich wastewater, which is frequently encountered in residential and commercial sites, to solve the problems of water pollution and energy generation. The efficiency of urea oxidation has been further increased by the invention of non-precious transition metal catalysts, making it a feasible substitute for the creation of hydrogen.

Methanol Oxidation Reaction- Methanol's low cost and high energy density make it a desirable fuel for the generation of sustainable energy. It is a good substitute for fossil fuels since it can be made from renewable resources. By converting methanol into hydrogen ( $H_2$ ) and formate the electrochemical methanol oxidation reaction (MOR) promotes the hydrogen economy by offering a greener energy source. Using methanol, which may be produced from waste materials or biomass, aids in resolving environmental issues related to waste disposal.

### **1.5 The potential environmental benefits of producing hydrogen from Sulfion, Methanol and Urea oxidation reactions**

There are various environmental advantages to producing hydrogen by oxidizing sulfion, methanol, and urea, especially when considering waste management and sustainable energy. The following are the main benefits:

**Reduction of Greenhouse Gas Emissions:** When hydrogen is produced using these oxidation processes instead of conventional fossil fuel techniques, carbon emissions can be greatly reduced. Since hydrogen only produces water when it burns, it is a clean fuel that helps to lower greenhouse gas emissions.

**Utilization of Waste Materials:** Hydrogen sulfide ( $\text{H}_2\text{S}$ ), a hazardous byproduct from the extraction of oil and gas, may be electrocatalytically broken down by the sulfion oxidation reaction (SOR). In addition to producing hydrogen, this method recycles environmental contaminants, lessening their detrimental effects on the ecosystem. Urea, a frequent contaminant present in wastewater, may be used, especially through urea oxidation. The process of turning urea into hydrogen not only produces energy but also aids in wastewater treatment, which lowers pollution levels in the environment. Using methanol, which may be produced from waste materials or biomass, aids in resolving environmental issues related to waste disposal. In addition to producing hydrogen, the electrochemical conversion of methanol lowers greenhouse gas emissions, fostering a more sustainable energy environment.

**Lower Energy Consumption:** In water electrolysis, the oxygen evolution process (OER) has higher theoretical equilibrium potentials than the methanol, sulfion and urea oxidation reactions. As a result, the process of producing hydrogen is more environmentally friendly and energy-efficient overall since less energy is needed for these reactions.

**Production of Value-Added Chemicals:** Small molecules like methanol can undergo oxidation to produce formate and sulfion undergo to produce sulfur which is useful compounds with a wide range of commercial uses. The process's sustainability is improved by the combined advantage of creating hydrogen and valuable byproducts.

## 1.6 Criteria for Electrocatalytic Performance

Several crucial factors need to be computed and thoroughly examined to evaluate the electrocatalytic performance of catalysts for the OER, MOR, SOR, UOR and HER. Included in these are the onset potential, overpotential ( $\eta$ ),  $iR$ -correction, the

electrochemically active surface area (ECSA), Tafel slope, Turnover frequency (TOF), stability tests, and Faradaic efficiency. Combining these factors provides a thorough knowledge of an electrocatalyst's performance, allowing for insightful material comparisons and directing future advancements in the area of electrocatalysis. [41,126,127,128,129]

### 1.6.1 Overpotential ( $\eta$ )

One important parameter for evaluating a system's electrocatalytic activity is the overpotential ( $\eta$ ). It measures the extra potential needed to drive an electrochemical reaction at a given current density, over and above the thermodynamic equilibrium value.

The overpotential may be stated mathematically as-

$$\eta = E_{\text{applied}} - E_0 - iR \quad \text{Equation 1.20}$$

Where  $E_0$  is the theoretical equilibrium potential,  $iR$  is the ohmic correction under the specified circumstances, and  $E_{\text{applied}}$  is the actual potential applied to the system. This correction factor makes up for the voltage drop caused by the electrolyte's resistance as well as that of the other electrochemical cell components. Better electrocatalytic efficiency is shown by a lower overpotential, which means that the process can progress more efficiently and get closer to its thermodynamic potential.

### 1.6.2 Electrochemical Surface Area (ECSA)

The connection between double layer capacitance ( $C_{\text{dl}}$ ) and specific capacitance ( $C_s$ ) of electrode materials is used to determine electrochemically active surface area (ECSA), as shown by equation (1.21).

$$ECSA = \frac{C_{\text{dl}}}{C_s} \quad \text{Equation 1.21}$$

Although exact  $C_s$  evaluation has been identified as a major problem in determining ECSA, and typically results in the usage of a single  $C_s$  value across different materials.

$C_{dl}$  is calculated using scan rate-dependent cyclic voltammetry measurement in non-faradaic regions.

### 1.6.3 Tafel Slope

In electrochemistry, the Tafel plot is an essential tool for examining the kinetics of electrode reactions, especially when electrocatalysis is involved. The Tafel plot's basic premise is the logarithmic relationship between the current density ( $j$ ) and overpotential ( $\eta$ ). The Tafel equation is given below-

$$\eta = a + b \log j \quad \text{Equation 1.22}$$

Where 'b' denotes the Tafel slope. This equation may obtain two important quantities, the exchange current density ( $j_0$ ) and the Tafel slope (b). With varying slope values denoting distinct rate-determining stages or reaction routes, the Tafel slope, b, sheds light on the electrode reaction's catalytic mechanism. Conversely, the linear part of the Tafel plot is extended to the y-axis intercept (where  $\eta$  is zero) to estimate the exchange current density. A lowest Tafel slope (b) and a high exchange current density ( $j_0$ ) are characteristics of an ideal catalytic material in practical applications. For effective electrocatalysis, a high  $j_0$  denotes fast electron transfer kinetics at equilibrium and a modest b denotes a gradual rise in overpotential with current density.

### 1.7 Faradaic Efficiency

One of the most important measurements in hybrid water electrolysis is faradaic efficiency (FE), which measures how well charges are used to produce oxygen ( $O_2$ ) or hydrogen ( $H_2$ ). It may be defined as the ratio of the quantity of gas generated that is measured to the amount theoretically computed under the assumption that all passed charge is utilized for gas creation. Faradaic efficiency is defined as-

$$FE(\%) = \frac{n_{gas,measured}}{n_{gas,theoretical}} = \frac{n_{gas,measured}}{It \times (N \times F)^{-1}} \times 100 \quad \text{Equation 1.23}$$

Where  $n_{\text{gas,measured}}$  is the measured gas production rate in moles per second and  $n_{\text{gas,theoretical}}$  is determined by the formula  $It / (N \times F)$ , where  $F$  is Faraday's constant (96,485.3 coulombs per mole),  $I$  is the current in amperes,  $t$  is time in second and  $N$  is the number of electrons transferred (2 for  $\text{H}_2$  and 4 for  $\text{O}_2$ ).

In practical experiments, the total charge transferred over a given time frame is monitored using an electrochemical workstation, while the quantity of  $\text{H}_2$  or  $\text{O}_2$  generated is usually evaluated using gas chromatography (GC) analysis or the water-gas displacement technique.

### **1.7.1 Stability**

An electrocatalyst's stability plays a crucial role in evaluating its viability for large-scale commercial applications as it measures the catalyst's capacity to sustain its activity over time. High stability may sometimes be sacrificed for less activity, even if it is necessary for real-world applications. To assess the stability of an electrocatalyst, many techniques are often used. A popular approach is the accelerated durability test, which entails hundreds to thousands of cyclic voltammetry (CV) cycles at a high scan rate. Before and after fast CV cycling, linear sweep voltammetry (LSV) is used to measure the overpotential shift at a given current density (usually  $10 \text{ mA cm}^{-2}$ ), a lower shift denotes more stability. Two more widely used techniques are the potential-time (E-t) curve recording at a set current density using chronopotentiometry and the current-time (I-t) curve measuring at a constant potential using chronoamperometry. When an electrocatalyst maintains a constant current density during chronoamperometry or exhibits a small overpotential rise during chronopotentiometry, it is deemed stable and appropriate for scaling up in water electrolyzers. These stability assessment methods are essential for figuring out the long-term sustainability and effectiveness of electrocatalysts in large-scale applications.

## **1.8 Future possibilities and worldwide markets for hydrogen-based energy**

Natural gas reforming and coal gasification are two methods that rely heavily on fossil fuels for the manufacture of commercial hydrogen. On the other hand, biomass feedstocks for hydrogen production may be treated similarly. Although water electrolysis has been used for decades in certain industrial applications, new developments in technology and the expansion of reasonably priced electrical supply have rekindled interest in this method. The generation of hydrogen is expected to mostly rely on electrolysis in the future, although other technologies such as thermolysis and photolysis may make better use of solar or thermal energy. The creation of "green hydrogen" using water electrolysis driven by renewable energy sources that are less harmful to the environment is becoming more popular. The rising cost of energy from renewable sources including solar, wind, hydroelectric, and tidal power is expected to make this technology more economical than typical industrial manufacturing. The creation of hydrogen from biomass, algae, and biotransformation processes is the subject of continuing research and development, and some nations have developed national hydrogen programs and allocated funds for their implementation. Most people agree that fuel cells and hydrogen technologies are essential to a future sustainable energy source. According to projections, the percentage of hydrogen produced by renewable energy sources will be 11% in 2025 and 34% in 2050, accounting for 36% and 69% of the total energy demand, respectively. The shift to a hydrogen economy requires a comprehensive reorganization of current human activities and infrastructure to the revolutionary effects of the oil and gas economy. As a result of this change in the production paradigm away from the conventional exploration and exploitation of fossil fuels, new systems for the storage, distribution, and transportation of hydrogen must be developed to fulfill demand. The development of novel engine designs that are especially suited to effectively use hydrogen will be necessary when hydrogen becomes the dominant energy source. The

requirement for the big, continuous supply of hydrogen exerts tremendous strain on production capacity and infrastructure development, which is why hydrogen fuel is becoming more popular in heavy sectors like machine making and metallurgy.

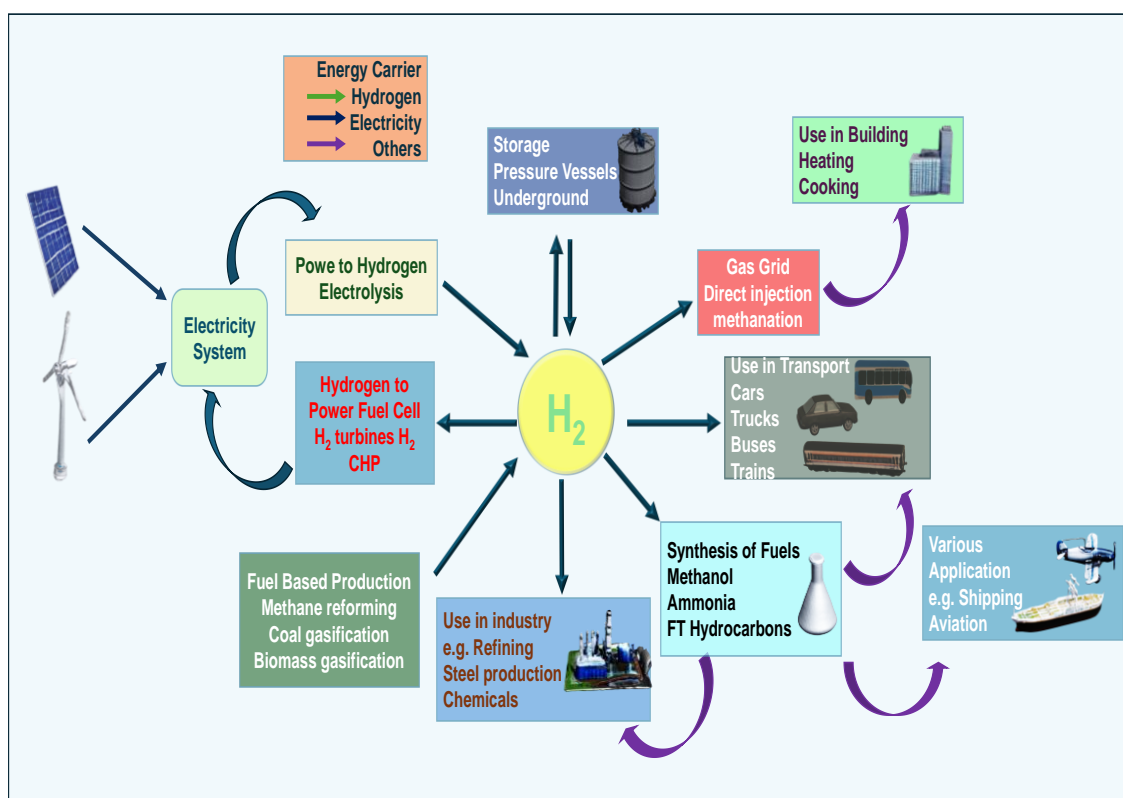


**Figure 1.8:** An outline of hydrogen fuel's future and its potential applications. Reproduced with permission from ref. [130]. Copyright 2020 Royal Society of Chemistry

Concurrently, clean hydrogen is becoming more and more important for a variety of uses in light sectors like food and medicine. Hydrogen is essential to the food industry because it allows  $H_2$  molecules to be incorporated into unsaturated vegetable oils and fats. It also has the potential to be used to create fertilizers that are more environmentally friendly. Hydrogen's medicinal qualities have been acknowledged by the medical community, with uses ranging from treating illnesses to relieving stress via inhalation therapy. A consistent source of high-purity hydrogen gas is essential for the medical use

of hydrogen, which is delivered by facemasks, nasal cannulas, or ventilator circuits. The vast range of industries for which hydrogen is being used highlights how crucial it is to build a stable, effective, clean infrastructure for hydrogen generation and delivery to sustain the growing hydrogen economy and all of its implications for all spheres of human endeavor.

## **1.9 Conclusion**

The energy density of hydrogen ( $H_2$ ) is much greater than that of traditional fossil fuels like natural gas and gasoline, and it has the potential to produce zero carbon emissions. Therefore, it is essential to create efficient and sustainable processes for producing green hydrogen. Water electrolysis driven by renewable energy has become a desirable alternative for producing  $H_2$ , since it eliminates the carbon emissions linked to manufacturing techniques based on fossil fuels. Nevertheless, slow kinetics and large overpotentials provide problems for the oxygen evolution process (OER) in water electrolysis. Despite its present limitations in kinetic overpotentials, hybrid water electrolysis is an alternative of OER to overcome this. This technique offers a sustainable way to upgrade organic compounds at the anode while generating hydrogen at the cathode. It includes the electrooxidation of tiny organic molecules such as alcohols, aldehydes, amines, and biomass. Reactive oxygen species and explosive  $H_2/O_2$  combinations are reduced by using this method. In electrolyzers, these coupling mechanisms improve atom/electron usage while drastically lowering cell voltage. These technologies are still in the early phases of development and have an inadequate transformation efficiency, despite their benefits. Nonetheless, it is anticipated that more developments in the design of electrolyzers and electrodes will result in useful uses in chemical manufacturing. It is essential to create new transition metal-based electrocatalysts from materials that are readily available on Earth. Because of their unique

physiochemical characteristics and flexible compositions and architecture, TM-based electrocatalysts have drawn a lot of interest in the area of hybrid water electrolysis. Numerous approaches, such as surface engineering, mixing multiple transition metals, and adding heteroatom dopants, have been effectively used to improve the electrocatalytic efficacy of these catalysts. These methods raise the electrochemically active surface area of the catalysts and boost their efficiency, making them more appropriate for use in industrial surroundings. The development of TM-based catalysts is largely dependent on the integration of theoretical calculations with practical data, especially considering the speed at which computational chemistry is developing. Enhancing TM-based electrocatalysts' performance and applicability in the larger context of electrocatalysis calls for a multimodal strategy. Key techniques in catalyst engineering and design include surface modification, alloying, and nano-structuring. These techniques are crucial for improving stability and activity, particularly in alkaline environments where it is essential to overcome sluggish behavior. Energy-efficient hydrogen generation requires addressing many important concerns, including the logical design of high-performance electrodes, the clarification of reaction processes, the investigation of new reactions, the optimization of electrolyzer systems, and a thorough economic analysis.

This page was initially left blank.

## Chapter 2

# Effective Sulfion Oxidation Reaction Combined with H<sub>2</sub> Production at High Current Density Using NiFeOOH-Co<sub>9</sub>S<sub>8</sub>-Intercalated Nanostructure

(Adapted from DOI:10.1021/acsanm.3c03438, Copyright 2023, American Chemical Society)

### 2.1 Abstract

Hydrogen (H<sub>2</sub>) evolution and electrocatalytic sulfion (S<sup>2-</sup>) recycling are essential for transforming waste into sustainable energy and advancing the hydrogen economy. While there are electrocatalysts in the literature that demonstrate effectiveness in either the SOR (sulfion oxidation reaction) or the HER (hydrogen evolution reaction), it is preferable to have systems that demonstrate competence in both SOR and HER together to produce H<sub>2</sub> in a highly energy-efficient manner. The NiFeOOH-Co<sub>9</sub>S<sub>8</sub>-n intercalated nano array is developed using a salt [Co(NO<sub>3</sub>)<sub>2</sub>] and Lewis acid (FeCl<sub>3</sub>) with the various Co:Fe proportions on NF (Ni foam) in a one-step hydrothermal method at a minimal temperature of 50 °C. The NiFeOOH-Co<sub>9</sub>S<sub>8</sub>-n demonstrates bifunctionality, and despite the relatively large *j* value of 1000 mA/cm<sup>2</sup>, H<sub>2</sub> production is obtained at a low overall potential (SOR + HER) value of 0.84 V in (1.0 M) NaOH + (1.0 M) Na<sub>2</sub>S. The effectiveness of the electrode in a 1.0 M Na<sub>2</sub>S solution allowed the SOR *j* value to surpass 1000 mA/cm<sup>2</sup> at 0.72 V without the presence of NaOH. The FeOOH-Co<sub>9</sub>S<sub>8</sub> intercalation allowed for the oxide doping of Co<sub>9</sub>S<sub>8</sub>, which increased the electrocatalytic activity, according to the DFT analysis. The nanocatalyst encourages extremely energy-efficient and sustainable H<sub>2</sub> production with SOR in electrolyzer mode realized *j* values of 100 mA/cm<sup>2</sup> at 0.44 V (without iR corrected) and shows the ultralow power utilization (11.8 kWh/kg H<sub>2</sub>). This is the smallest value amongst reported systems proposing its feasibility towards industrial production of valuable chemicals and H<sub>2</sub> in the future.

## 2.2 Introduction

Green hydrogen ( $H_2$ ) has the potential to be an energy source with no carbon emissions. [131,132,133] There has been an increase in interest in recent years in technologies to create high current densities. Currently investigating commercially feasible methods for producing green hydrogen from diverse sources. [134,135] Numerous intriguing strategies are being thoroughly researched, such as Pyrolysis of plasma, [136] Gasification of biomass, [137] electrolysis of water, [138] the use of photocatalysis, [139,140] conversion of microbial biomass. The extraction of  $H_2$  from industrial waste is one particularly interesting route. This strategy provides two advantages: it solves the problem of handling hazardous waste and generates a useful energy source at the same time. One of the primary gaseous byproducts of refining natural gas and crude oil is hydrogen sulfide ( $H_2S$ ), which is extremely harmful to living things. [141] The development of effective processes to convert  $H_2$  from  $H_2S$  is essential for energy sustainability and environmental preservation. Now, industries mostly handle  $H_2S$  via Claus thermal and catalytic techniques. [142] Under high temperatures, these processes transform  $H_2S$  into elemental sulfur ( $S_n$ ) and water ( $H_2O$ ). These procedures, however, result in byproducts that are not practical for commercial use, demand sophisticated systems, and consume a lot of energy. Due to these limitations, we are currently concentrating on several strategies for splitting  $H_2S$  with the goal of extracting both elemental sulfur and  $H_2$ . This method appears to be a more practical and cost-effective alternative than the conventional  $H_2S$  treatment procedures.

There are possible methods to convert hydrogen sulfide ( $H_2S$ ) into sulfur ( $S$ ) and hydrogen ( $H_2$ ) via photocatalysis or electrocatalysis.[143] Even though photocatalytic techniques like employing  $Ca^{2+}$  modified cadmium sulfide nanocrystals in the presence of  $Na_2SO_3$  have been extensively studied, there are still difficulties with this technique.[144] These include the light absorption by sulfide ions and the sulfur buildup

on catalytic sites, both of which lower efficiency.[145] H<sub>2</sub>S splitting by electrocatalysis has benefits in terms of energy economy. Compared to oxygen evolution, which requires a thermodynamical potential of 1.23 V<sub>RHE</sub>, the sulfur oxidation process (SOR) requires a much lower potential (-0.48 V<sub>SHE</sub>). [146,22] Future hydrogen sources seem bright because of this and the creation of sustainable and active catalysts that can achieve elevated current densities at low potentials. Prospective outcomes for H<sub>2</sub>S splitting at low potentials have been demonstrated by recent developments in nanocatalyst systems.[147,8] For example, an embedded cobalt-nickel nanoalloy in nitrogen-doped graphene showed a long-term stability of 1200 hours and a low overpotential ( $\eta$ ) of 0.25 V.[53] With a  $j$  of 100 mA/cm<sup>2</sup>, bifunctional cobalt sulfide (Co<sub>3</sub>S<sub>4</sub>) nanowires produced hydrogen at an overall potential (SOR+HER) of only 0.47 V.[148] A cobalt-iron sulfide (CoFeS<sub>2</sub>) catalyst produced hydrogen with a high Faradaic efficiency of 97.8% and a low onset potential of 0.23 V<sub>RHE</sub>. [149] At a  $j$  value of 100 mA/cm<sup>2</sup>, iron carbides captured in N-doped carbon nanotubes had a high sulfur yield of 33.76 mg h<sup>-1</sup>. [67] Even with these developments, further study is required to create catalytic systems that can function in an industrially feasible manner, such as reaching long-term stability and current densities of 1000 mA/cm<sup>2</sup> below at 1.0 V overall potentials. Furthermore, there aren't many catalyst systems available that can effectively carry out HER and SOR at the same time, which would significantly increase energy efficiency. Improving the commercial viability of H<sub>2</sub>S splitting requires the development of multifunctional catalyst systems that can produce hydrogen at low cell voltages (less than 1.0 V). These systems have the potential to revolutionize the use of H<sub>2</sub>S as a hydrogen source and eliminate the shortcomings in present research.

One major obstacle in the development of nanocatalyst-coated electrodes for the sulfur oxidation reaction (SOR) is shielding the surface from deposits of elemental

sulfur ( $S_n$ ) that occur during the anodic process.[150] To create more robust catalyst systems tackled this problem by encasing active catalysts in conductive coatings.[151] For example,  $FeN_4$  enclosed in porous carbon nitride demonstrated resistance towards  $S_n$  toxic conditions and continued to be effective for as long as 270 hours.[152] By employing atomically dispersed cobalt in nitrogen-doped carbon (NC) with  $CoN_4$  sites, even more remarkable outcomes were obtained, increasing durability to 460 hours.[153] It has been discovered that adding sulfur as a dopant increases SOR efficiency. For instance, with a  $j$  of  $10 \text{ mA/cm}^2$ ,  $WS_2$  nanosheets demonstrated a potential of 0.48 V for SOR.[72] Self-cleaning electrodes are developed to retain SOR activity for 100 hours with a superior desulfurization efficacy of 89.3% by utilizing the sulfophobic characteristics of metal sulfides.[71] The literature reports suggest that transition metal (TM) sulfides have the potential for long-term SOR activity when paired with an active intercalating layer. [154,155] Among catalyst systems, oxyhydroxides stand out for their strong electro-oxidation capabilities and stability in alkaline medium.[156,157] They have performed exceptionally well in alkaline HER procedures, in particular.[158,159] These results led to the hypothesis that long-term stability might be preserved while SOR and HER activity were increased by including active metal sulfides into an oxyhydroxide matrix. Research already conducted has demonstrated that metal hydroxide-sulfide hybrid structures can be effectively utilized to increase the durability and performance of the oxygen evolution process (HER/OER) in alkaline environments. [160,161] The capacity to build and integrate several catalytic systems at the nanoscale simultaneously, while also fine-tuning their composition, is still a major difficulty. This is usually a multi-step, intricate process that is challenging to optimize.

In this work,  $NiFeOOH$  and  $Co_9S_8$  nanostructures on NF are combined to create a novel electrode material that has an efficient bi-functional activity for both the HER and SOR.

The synthesis uses a novel one-step, low-temperature (50°C) method that grows and intercalates Ni/FeOOH and Co<sub>9</sub>S<sub>8</sub> layers on the NF substrate concurrently by making use of the distinct reactivity of FeCl<sub>3</sub> and Co(NO<sub>3</sub>)<sub>2</sub> with Na<sub>2</sub>S<sub>2</sub>O<sub>5</sub>. The work intends to improve the efficacy of SOR by purposefully adding oxide to the Co<sub>9</sub>S<sub>8</sub> layer to form an intercalating layer. By modifying the Fe<sup>3+</sup> to Co<sup>2+</sup> ratio in the precursor solution, control the nanostructure shape and dimensions to solve potential problems with sulfur deposition on the anode surface and enhance its self-cleaning properties.

The study assesses the performance of several NiFeOOH-Co<sub>9</sub>S<sub>8</sub>-n compositions in terms of SOR and HER. The work investigates the effects of electrode spacing and cell architecture to optimize power usage. To evaluate the electrodes' practical application and also evaluate how well they work in a two-electrode setup. The density functional theory (DFT) models provide deeper insights into the impact of oxide doping in Co<sub>9</sub>S<sub>8</sub> on SOR activity. With this all-encompassing method, advanced bi-functional electrode material for electrochemical applications is developed and understood through performance testing, theoretical modeling, and experimental synthesis.

## **2.3 Experimental Section**

### **2.3.1 Materials**

Cobalt (II) nitrate hexahydrate (Sigma Aldrich, 98%), hydrochloric acid (SDFCL, 99%), iron (III) chloride hexahydrate (Molychem, 98%), sodium metabisulfite (Avra, 97%), nafion 117 membrane (Kanopy Techno Solutions), Ni Foam (Goodfellow, thickness 1.6 mm, 99%), sodium hydroxide (Qualigens, 98%), ethanol (Changshu HFCL, 99%), sodium sulfide (Molychem, 98%), H<sub>2</sub> gas (Sigma Aldrich, 99.9%), The purified DI water was used for experiment.

### **2.3.2 Characterization**

Several analytical techniques were used to characterize the material. An Autolab M204 PGSTAT workstation was used for electrochemical measurements. Utilizing copper K-

alpha radiation, a PANanalytical Empyrean XRD Diffractometer was used to study the crystal structure, scanning from 5° to 90° (2θ) at a rate of 2° per minute. The elemental chemical states were investigated using a Thermo Scientific XPS machine operational with a monochromatic aluminum K-alpha source. A JEOL JSM-7900F field-emission scanning electron microscope (FESEM) was used to study surface characteristics, and energy-dispersive X-ray spectroscopy (EDS) was used to map elements. High-resolution imaging of particle morphology and SAED pattern was obtained using a JEOL JEM-F200 transmission electron microscope (TEM). Using an EDS detector, STEM-HAADF studies were performed, and the generated images were analyzed using ImageJ software. We evaluated optical characteristics with an Agilent Cary 5000 UV-Vis spectrometer. Hydrogen purity was evaluated using a NUCON GL 5765 gas chromatograph. An Elementar UNICUBE analyzer was used to determine elemental makeup. A Utech Thermo Fisher pH meter was used to track the pH of the solution. The Raman spectroscopy data were recorded using a Jobin-Yvon HR-800 Raman Microprobe at 24 mW and 632 nm excitation. Thermal behavior was investigated using differential scanning calorimetry (Hitachi DSC7020) from 30°C to 250°C at 5°C/min and thermogravimetric analysis was performed using Linseis TGA PT1000 from 30°C to 800°C at 10°C/min.

### **2.3.3 Fabrication of Electrode**

A 1.5 x 2.5 cm<sup>2</sup> Ni foam (NF) substrate was cleaned using ethanol, deionized (DI) water, and hydrochloric acid to remove surface impurities. In 15 mL of DI water, sodium metabisulfite, iron (III) chloride hexahydrate, and cobalt (II) nitrate hexahydrate were combined and stirred until a homogenous mixture was achieved. After the mixture was moved, the cleaned NF was put inside an autoclave. After that, the sealed autoclave was heated for three hours at 50 °C in a hot air oven to encourage homogenous nanoparticle

development on the Ni foam surface. Following the heating cycle, the autoclave was taken out and allowed to cool at room temperature. After being extracted, the NF was thoroughly cleaned with DI water three to four times, and it was left to dry overnight at 50°C in a vacuum oven. Four different electrodes were made by repeating this technique, each with a different molar ratio of Fe<sup>3+</sup> to Co<sup>2+</sup>. The electrodes that emerged were given the following names: Fe<sup>3+</sup>:Co<sup>2+</sup> in NiFeOOH-Co<sub>9</sub>S<sub>8</sub>-11 is 0.37:0.34 mmol, Fe<sup>3+</sup>:Co<sup>2+</sup> in NiFeOOH-Co<sub>9</sub>S<sub>8</sub>-12 is 0.37:0.68 mmol, Fe<sup>3+</sup>:Co<sup>2+</sup> in NiFeOOH-Co<sub>9</sub>S<sub>8</sub>-13 is 0.37:1.00 mmol, Fe<sup>3+</sup>:Co<sup>2+</sup> in NiFeOOH-Co<sub>9</sub>S<sub>8</sub>-21 is 0.74:0.34 mmol.

### 2.3.4 Electrochemical Evaluation

The two setups were used to conduct electrochemical experiments: a mini gas-tight cell and an H-type electrochemical cell with 50 mL compartments divided by a Nafion 117 membrane. To measure electrode performance a three-electrode setup was used. NiFeOOH-Co<sub>9</sub>S<sub>8</sub>-n was the working electrode (WE), Hg/HgO (1.0 M NaOH) electrode was the reference electrode and a 10 mm graphite rod or NiFeOOH-Co<sub>9</sub>S<sub>8</sub>-n as the counter electrode. 1 M NaOH was used for the HER and OER. The cathodic side of SOR comprised 1 M NaOH for HER, while the anodic electrolyte was 1 M NaOH + 1 M Na<sub>2</sub>S in case of H-Cell. The linear sweep voltammetry (LSV) data were recorded with a scan rate of 5 mV/s while stirring continuously at 700 rpm. Measurements of electrochemical impedance were conducted between 10 Hz and 10 MHz in frequency. The Nernst equation was exploited to convert results to the reversible hydrogen electrode (RHE) scale to standardize potential measurements:

$$E_{RHE} = E_{Hg/HgO}^0 + E_{Hg/HgO} + 0.0591 \times pH \quad \text{Equation 2.1}$$

On the basis of the geometric area (0.25 cm<sup>2</sup>) of the WE, current was standardized to current density. To depict the conversion of sulfide to polysulfide over time, UV-Vis spectroscopic data were recorded at interval of 4 to 24 h concentrating on changes in

absorbance at a wavelength of 300 nm using chronoamperometry testing measurements at 100 mA/cm<sup>2</sup>.

### 2.3.5 Quantification of H<sub>2</sub> Gas

Using a water displacement approach, the amount of H<sub>2</sub> gas generated in a 30-minute chronoamperometric (i-t) experiment at a constant potential in an H-type cell setup was measured. In this process, 1 M NaOH solution was put into an inverted burette and replaced by the H<sub>2</sub> gas produced at the cathode during the reaction. Using the following formula, Faraday's law was utilized to ascertain the faradaic efficiency of H<sub>2</sub> production:

$$\text{Faradaic Efficiency (\%)} = nF \times \frac{m}{Q} \times 100 \quad \text{Equation 2.2}$$

Within this formula:

Q = overall electrical charge

n = no. of electrons involved in the chemical reaction

F = Faraday's constant,

M = moles of hydrogen gas (H<sub>2</sub>) produced

Using gas chromatography, the hydrogen gas quality was evaluated. In a dual-compartment H-cell, the H<sub>2</sub> was extracted from the cathode using a three-electrode arrangement. This formula was used to determine the hydrogen purity:

$$\text{Hydrogen purity (\%)} = \frac{\text{Area of Sample Hydrogen}}{\text{Area of Pure Hydrogen}} \times 100 \quad \text{Equation 2.3}$$

### 2.3.6 ECSA Measurement

The three electrodes in a single cell were used to measure the catalyst's electrochemically active surface area (ECSA) using 1.0 M NaOH + 1.0 M Na<sub>2</sub>S electrolyte. In the non-faradaic area, cyclic voltammetry was carried out using applied voltages between 0 and

0.29 V with different scan rates of 10, 30, 50, 70, and 90 mV/s, respectively. The average current density was plotted against the scan rate to determine the double-layer capacitance (C<sub>dl</sub>). The resultant C<sub>dl</sub> value was then divided by the electrode material's specific capacitance to determine the ECSA. The standard specific capacitance (C<sub>s</sub>) values 40 μF cm<sup>-2</sup> in this instance.

ECSA can be calculated using the following formula:

$$ECSA = \frac{C_{dl}}{C_s} \quad \text{Equation 2.4}$$

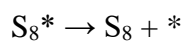
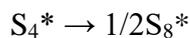
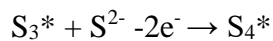
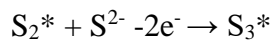
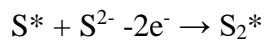
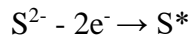
### 2.3.7 Recovery of Sulfur

Sulfur was extracted using a chronoamperometry technique, which produced polysulfide compounds when a constant voltage was applied at 0.4 V for 24 hours. A controlled acidification process was used to convert these polysulfides into elemental sulfur. This was chilling the solution in an ice bath while sulfuric acid (H<sub>2</sub>SO<sub>4</sub>) was added gradually. Drop by drop, the acid was added to the solution until the pH hit 1.0, which is extremely acidic. A yellow precipitate that had formed as a result of this acidity was subsequently separated via filtration. To get rid of any contaminants, the recovered material was carefully cleaned with deionized water. The sample was then dried in a hot air oven for a duration of 12 h. To confirm sulfur's purity, two analytical methods were applied. To ascertain the elemental composition, CHNS elemental analysis was first carried out. To further evaluate the sample's purity and elemental composition, Energy Dispersive X-ray Spectroscopy (EDS) was carried out in conjunction with Scanning Electron Microscopy (SEM).

### 2.3.8 Computational method

The VASP algorithm was used to perform spin-polarized density functional theory (DFT) computations. The projector-augmented wave (PAW) approach was used to characterize

electron-ion interactions, and the generalized gradient approximation (GGA) with the Perdew-Burke-Ernzerhof (PBE) functional was employed to quantify the exchange-correlation energy.[162] Density functional theory calculations were used in the investigation, using a plane wave energy cut-off of 500 eV and convergence thresholds of 0.01 eV/Å for force and  $10^{-6}$  eV for energy. Using the Grimme method and the DFT-D3 correction, van der Waals interactions were included. After optimizing the equilibrium lattice constant of the  $\text{Co}_9\text{S}_8$  cubic unit cell using a  $2 \times 2 \times 2$  Monkhorst-Pack k-point grid, the  $\text{Co}_9\text{S}_8$  200 surface model was constructed. A  $4 \times 4 \times 1$  Monkhorst-Pack grid was used for Brillouin zone sampling in surface calculations, with a fixed vacuum spacing of 10 Å perpendicular to the plane of the structure. Gibbs free energy changes were calculated for each electron transfer step using the computational standard hydrogen electrode (CHE) model by Nørskov et al. [163] ( $\Delta G = \Delta H + \Delta \text{ZPE} - T\Delta S$ ), where  $\Delta H$  is the enthalpy change from DFT calculations, T is the temperature (set at 298.15 K),  $\Delta S$  is entropy change, and  $\Delta \text{ZPE}$  is the zero-point energy change. Entropy and ZPE values for free gas molecules were derived from the NIST database, but for adsorbed species, these parameters were computed using vibrational frequencies, considering only vibrational entropy calculations for the S adsorbed species. The SOR to  $\text{S}_8$  moves through the following series of basic phases in order:



## 2.4 Calculation for power consumption

One kilogram of hydrogen requires the following charge (Q) to be generated:

$$Q = \frac{1000 \times N_A \times 2e}{M_{H_2}} = \frac{1000 \times 2 \times 6.023 \times 10^{23} \times 1.602 \times 10^{-19}}{2.016}$$

$$= 95706785.7 \text{ C}$$

Where  $M_{H_2}$  = Relative molecular mass of hydrogen ( $H_2$ )

$N_A$  = Avogadro Number

$e$  = Charge of an electron

For the SOR + HER, the applied voltage (V) is 0.444 V at a current density of 100 mA/cm<sup>2</sup>.

The amount of electricity (W) needed to produce one kilogram of hydrogen is:

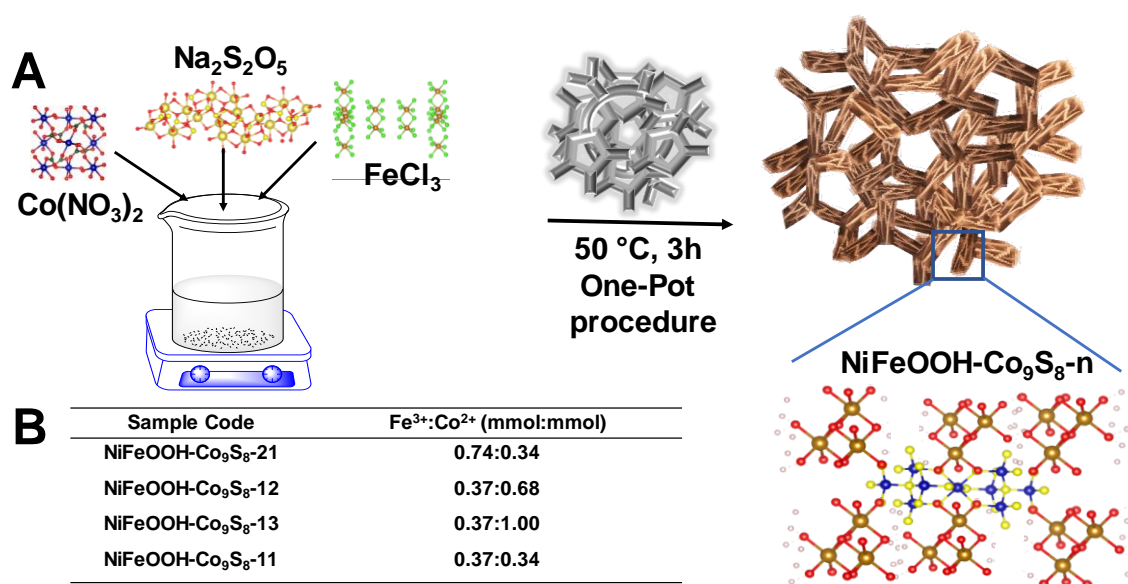
$$W = Q \times V = 95706785.7 \times 0.444 = 42493812.9 \text{ J} = 11.80 \text{ kW.h}$$

## 2.5 Synthetic Process of Ni-Co<sub>9</sub>S<sub>8</sub> and Ni-FeOOH

To get rid of surface contaminants, HCl, ethanol, and DI water were used to clean the 1.5 x 2.5 cm<sup>2</sup> Ni foam. The nickel foam substrate supported the growth of the cobalt sulfide (Co<sub>9</sub>S<sub>8</sub>) and metal oxide-hydroxide (FeOOH). In 15 milliliters of DI water, 0.21 milligrams of sodium metabisulfite and 0.34 milligrams of cobalt (II) nitrate hexahydrate were combined to grow Co<sub>9</sub>S<sub>8</sub> nanoparticles. Likewise, 15 milliliters of DI water were combined with 0.21 mL of sodium metabisulfite and 0.74 milligrams of iron (III) chloride hexahydrate to form the FeOOH nanonaoparticle. Ni Foam was then retained inside the hydrothermal autoclave reactor once the mixture had been transferred there. To obtain consistent nanoparticle formation on the Ni Foam surface, the hydrothermal autoclave reactor was then put in a hot air oven set to 50 °C for three hours. The hydrothermal autoclave reactor was removed from the oven and allowed to come to room temperature. The Ni Foam was removed and dried in a vacuum oven at 50 °C for the whole night after being cleaned three or four times with DI water.

## 2.6 Results & Discussion

NiFeOOH-Co<sub>9</sub>S<sub>8</sub> intercalated nanostructures were grown on the Ni foam surface in the presence of Na<sub>2</sub>S<sub>2</sub>O<sub>5</sub> using a one-pot process at a moderate temperature of 50 °C, employing FeCl<sub>3</sub>·6H<sub>2</sub>O and Co(NO<sub>3</sub>)<sub>2</sub>·6H<sub>2</sub>O as precursors (**Scheme 2.1**). Under the given circumstances, it is possible that the responsiveness preferences of FeCl<sub>3</sub> (Lewis acid) and Co(NO<sub>3</sub>)<sub>2</sub> (salt) towards Na<sub>2</sub>S<sub>2</sub>O<sub>5</sub> allowed the FeOOH and Co<sub>9</sub>S<sub>8</sub> nanostructures to develop and intercalate simultaneously.



**Scheme 2.1:** (A) The NiFeOOH-Co<sub>9</sub>S<sub>8</sub>-n heterostructure is formed in a one-pot synthetic technique, as seen in the synthetic scheme. (B) The table displays the sample code and matching Fe<sup>3+</sup>: Co<sup>2+</sup> ratios taken in the precursor solution.

The component elements present in the heterostructure were shown to have peaks in the NiFeOOH-Co<sub>9</sub>S<sub>8</sub>-n XPS survey spectra (**Figure A1**). FeOOH was depicted in the heterostructure, as shown by the Fe 2p XPS spectra, which also showed a satellite peak at 716.9 eV and a significant peak at 711.5 eV (**Figure 2.1A**). [164] A distinctive peak at 856.0 eV was identified by XPS investigation of the Ni 2p spectra. This suggests that the nickel on the Ni foam (NF) surface underwent oxidation, leading to the formation of nickel oxyhydroxide species (**Figure 2.1B**). [165]

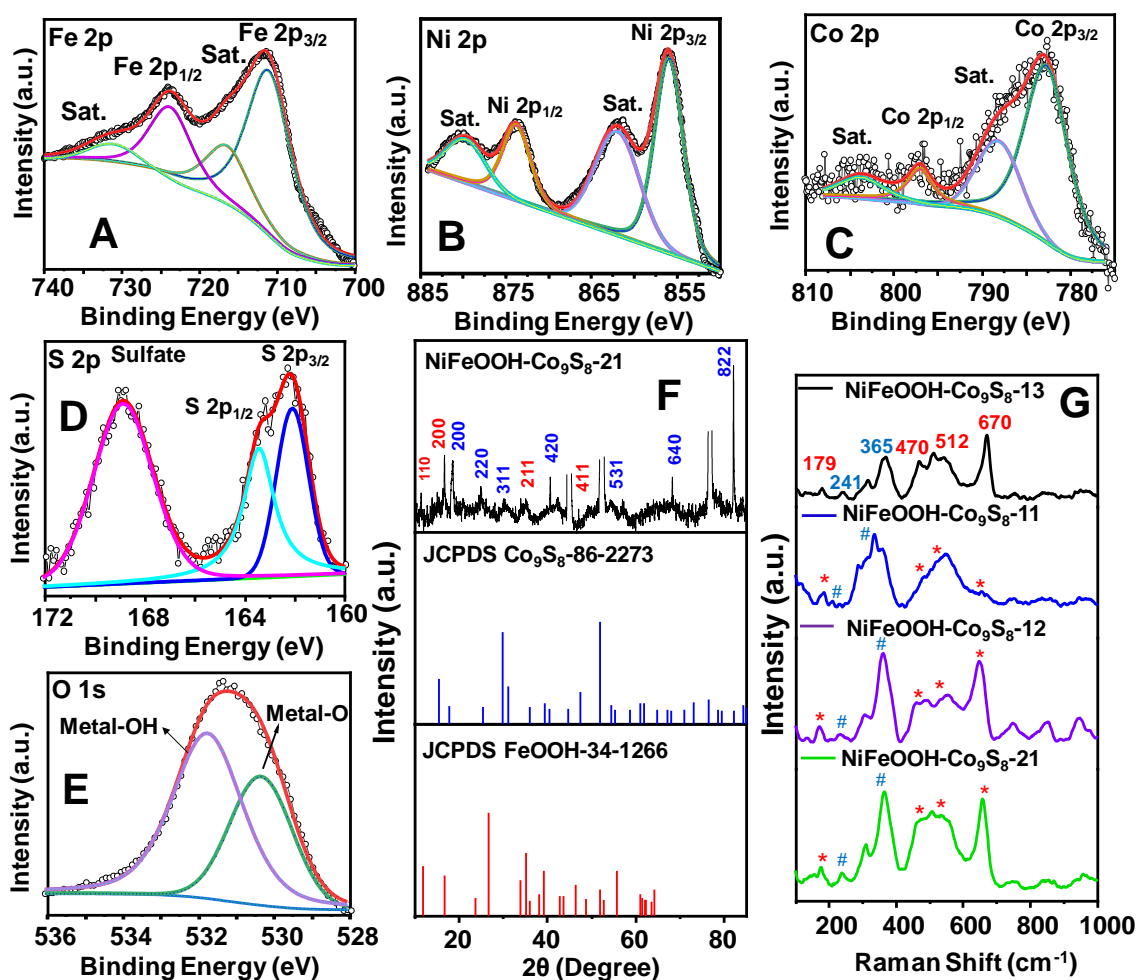


**Figure 2.1:** Peaks highlighted with "#" and "\*" correspond to FeOOH and Co<sub>9</sub>S<sub>8</sub>, respectively, according to the NiFeOOH-Co<sub>9</sub>S<sub>8</sub>-21 electrode's (A) Fe 2p, (B) Ni 2p, (C) Co 2p, (D) S 2p, (E) O 1s XPS data, (F) the electrode surface's XRD trace, and (G) the Raman spectra for the different compositions of NiFeOOH-Co<sub>9</sub>S<sub>8</sub>-n.

Co 2p peak at 782.8 eV and its satellite peak at 788.3 eV, were detected by XPS analysis, which verified the existence of Co<sub>9</sub>S<sub>8</sub> in the synthesized material. (**Figure 2.1C**). Literature reports suggest that the Co 2p peak for Co<sub>9</sub>S<sub>8</sub> may be observed at around 781.5 eV. [166] The interaction between Co<sub>9</sub>S<sub>8</sub> and NiFeOOH in their heterostructure configuration and the oxide doping that took place in the Co<sub>9</sub>S<sub>8</sub> are probably the two main causes of the observed mild upfield shift of 1.3 eV in the peak. [167] The foregoing

finding was further supported by the Co 2p peak in XPS spectra at 781.5 eV seen in the control sample (Ni-Co<sub>9</sub>S<sub>8</sub>), which was produced without FeOOH (**Figure A1**). According to published reports, CoS<sub>x</sub> oxide doping raises the Co 2p peak to around 2.7 eV. [168] The existence of Co<sub>9</sub>S<sub>8</sub> in the catalyst layer was confirmed by the S 2p signal at 162.1 eV (**Figure 2.1D**). [169] Interestingly, the S 2p spectra also showed a peak at 168.8 eV that was associated with sulfate functionality. This peak may be explained by the partial oxidation of the resultant sulfide in the presence of air. When sulfides are exposed to the environment, they are known to generate the equivalent sulfate.[170,171] Significantly, the absence of peaks between 163.7 and 164.9 eV indicated that there was no elemental Sulfur present in the sample.[172] The heterostructure's Ni/Fe-OH and Ni/Fe-O moieties had peaked in the O 1s XPS spectra at 531.8 and 530.4 eV respectively, confirming the aforementioned position (**Figure 2.1E**).[173] All four samples, which were created with varying molar ratios of Fe<sup>3+</sup> to Co<sup>2+</sup> in the reaction mixture, had comparable peak locations for Ni 2p, Fe 2p, Co 2p and S 2p (**Figures A2-A4**). The XPS elemental analysis yielded atomic ratios of Co to S ranging from 1.10 to 1.28, indicating the production of Co<sub>9</sub>S<sub>8</sub> inside the nanostructure (**Table A1**). To determine the degree of intercalation between FeOOH and Co<sub>9</sub>S<sub>8</sub> layers, XPS data was gathered after various etching times. Two important conclusions are strongly supported by the constant Co:Fe atomic ratio seen in all measurements: first, that the intercalation method produced the desired result, and second, that cobalt is uniformly distributed throughout the iron oxyhydroxide (FeOOH) matrix at all depths. (**Figure A5**). In XRD spectra, the planes 110, 200, 211, and 411 were responsible for FeOOH associated with JCPDS correlations. Similarly, the XRD data of NiFeOOH-Co<sub>9</sub>S<sub>8</sub>-21 also showed the 200, 220, 311, 420, 640, and 822 planes for Co<sub>9</sub>S<sub>8</sub> (**Figure 2.1F**). The XRD measurements of the other NiFeOOH-

Co<sub>9</sub>S<sub>8-n</sub> showed the FeOOH and Co<sub>9</sub>S<sub>8</sub> lattice planes, indicating that heterostructure formation occurred in each instance (**Figures A6-A7**).

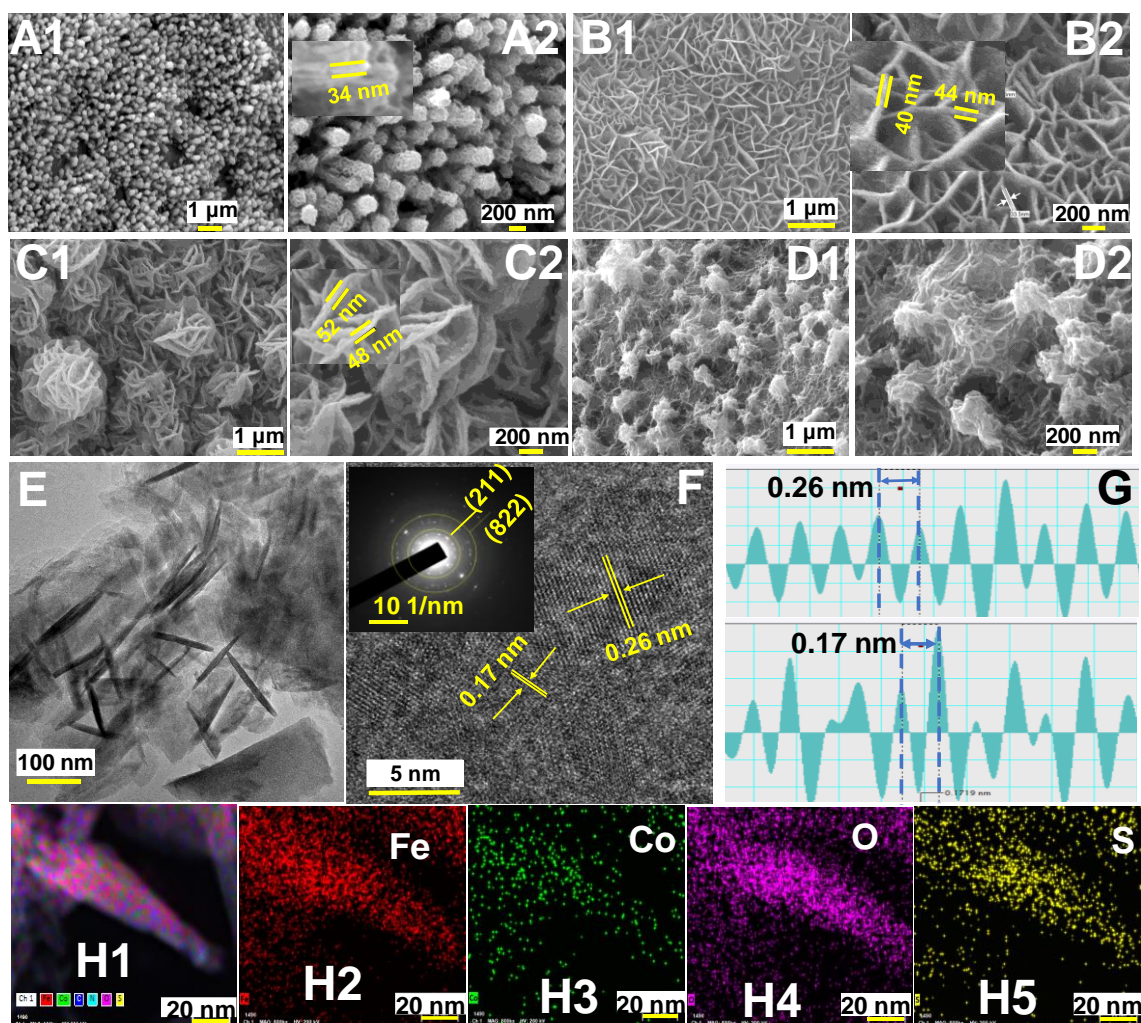


**Figure 2.2:** The FE-SEM pictures of (A1 and A2) NiFeOOH-Co<sub>9</sub>S<sub>8-11</sub>, (B1 & B2) NiFeOOH-Co<sub>9</sub>S<sub>8-21</sub>, (C1 & C2) NiFeOOH-Co<sub>9</sub>S<sub>8-12</sub>, and (D1 & D2) NiFeOOH-Co<sub>9</sub>S<sub>8-13</sub> at various magnifications; (E) the FeOOH-Co<sub>9</sub>S<sub>8-21</sub> TEM image; (F) the d spacing values matching to FeOOH and Co<sub>9</sub>S<sub>8</sub> determined from digital micrographs software, inset SAED spectra of FeOOH-Co<sub>9</sub>S<sub>8-21</sub>, showing the lattice planes, (G) the corresponding IFFT plot display the d spacing values, and the HAADF-STEM image of FeOOH-Co<sub>9</sub>S<sub>8-21</sub> for the various elements merged (H1) and for single elements (H2-H5), respectively.

Raman spectra showed the peaks at 470, 512, and 670  $\text{cm}^{-1}$ , which correspond to the Eg, F2g, and A1g modes of  $\text{Co}_9\text{S}_8$  (**Figure 2.1G**). [174,175] Similarly, peaks for the FeOOH at 241 and 365  $\text{cm}^{-1}$  emerged, indicating that NiFeOOH- $\text{Co}_9\text{S}_8$ -n heterostructures were forming. [176]

The FE-SEM data of the NiFeOOH- $\text{Co}_9\text{S}_8$ -n surface showed the lateral proliferation of nanostructures on the Ni Foam surface (**Figures 2.2A1-D2**). It's interesting to note that the precursor solution's  $\text{Fe}^{3+}$  to  $\text{Co}^{2+}$  ratio affected the nanostructure's sizes and growth. In NiFeOOH- $\text{Co}_9\text{S}_8$ -11, cylindrical rods with consistent dimensions and an average thickness of about 34 nm were seen to develop laterally (**Figure 2.2A and 2.2A2**). Micro flakes with a regular thickness of 44 nm were seen to develop in the NiFeOOH- $\text{Co}_9\text{S}_8$ -21 (**Figures 2.2B1-B2, A8**). On the surface of NiFeOOH- $\text{Co}_9\text{S}_8$ -12, lateral growth microflowers were evident (**Figure 2.2C**). Petal thickness average was found to be around 56 nm (**Figure A9**). The microstructures of NiFeOOH- $\text{Co}_9\text{S}_8$ -13 were octopus-shaped, having an average width of 221 nm (**Figure 2.2D**). The atomic ratio of Co:Fe in the heterostructures ranged from 1:0.22 to 1.0:2.3, according to the SEM-EDS study (**Table A 2**). Microstructure formation on the NF surface was inhibited by a subsequent increase in the quantity of  $\text{Fe}^{3+}$  ( $\text{Fe}^{3+}:\text{Co}^{2+} = 1.1:0.34$ , mmol:mmol) in the precursor solution (**Figure A10**). The XPS study and the production of  $\text{Co}_9\text{S}_8$  were corroborated by the atomic ratio ( $\sim 1.12$ ) among Co and S determined from the EDS spectra (**Table A 1**). Overall, according to the FE-SEM data, the process permits control over the sizes and forms of nanostructures based on NiFeOOH- $\text{Co}_9\text{S}_8$ -n on the electrode surface, which might be required to customize the electrochemical activity.

The HR-TEM data of the FeOOH- $\text{Co}_9\text{S}_8$ -21 nanostructure developed on glass substrate were recorded since etching the nanostructure from the Ni foam surface was

not practical. This showed the existence of nanorods with an average size in the range of 8 to 20 nm (**Figure 2.2E**). The existence of both elements in the heterostructure is supported by the d spacing values of 0.26 and 0.17 nm found in the HR-TEM data, which matched to the 211 planes of FeOOH and the 822 plane of Co<sub>9</sub>S<sub>8</sub>, respectively (**Figures 2.2F-2.2H**).<sup>[177]</sup> To learn more about the composition of one of the nanorods, the HAADF-STEM data was gathered. The sample showed that Fe and O were the primary elements, followed by Co and S, confirming the expected distribution of Co<sub>9</sub>S<sub>8</sub> in the FeOOH matrix (**Figures 2.2H2-2.2H5**). The existence of 211 and 822 planes, respectively, further supported the presence of FeOOH and Co<sub>9</sub>S<sub>8</sub> in the heterostructure, according to the SAED patterns that were also generated from the TEM diffraction data (**Figure 2.2F**). The intercalation was supported by the intertwining of the lattice fringes of FeOOH and Co<sub>9</sub>S<sub>8</sub> (**Figure A11**). All things considered, the evidence from Raman, XRD, XPS, HR-TEM, and FE-SEM confirmed the emergence and development of FeOOH-Co<sub>9</sub>S<sub>8</sub>-21 intercalated nanostructures on Ni Foam. To understand the temperature behavior, the nanocatalyst's DSC and TGA data were acquired (**Figure A12**). Up to 250 °C, no discernible thermal transition could be seen in the DSC heating and cooling traces. The TGA trace showed that up to 800 °C, there is very little total weight loss (~10%). The catalyst's adventitious moisture loss may be the cause of a little weight loss of up to 6% till 100 °C. An additional ~4% weight loss that happened between 300 and 500 °C might be attributed to the trace amounts of unreacted salts that were perhaps confined in the catalyst matrix throughout the development phase.

Utilizing a three-electrode setup, the electrocatalytic effectiveness of the NiFeOOH-Co<sub>9</sub>S<sub>8</sub>-n electrodes was assessed by logging linear sweep voltammetry (LSV) data with 1.0 M NaOH and 1.0 M Na<sub>2</sub>S in an aqueous electrolyte.

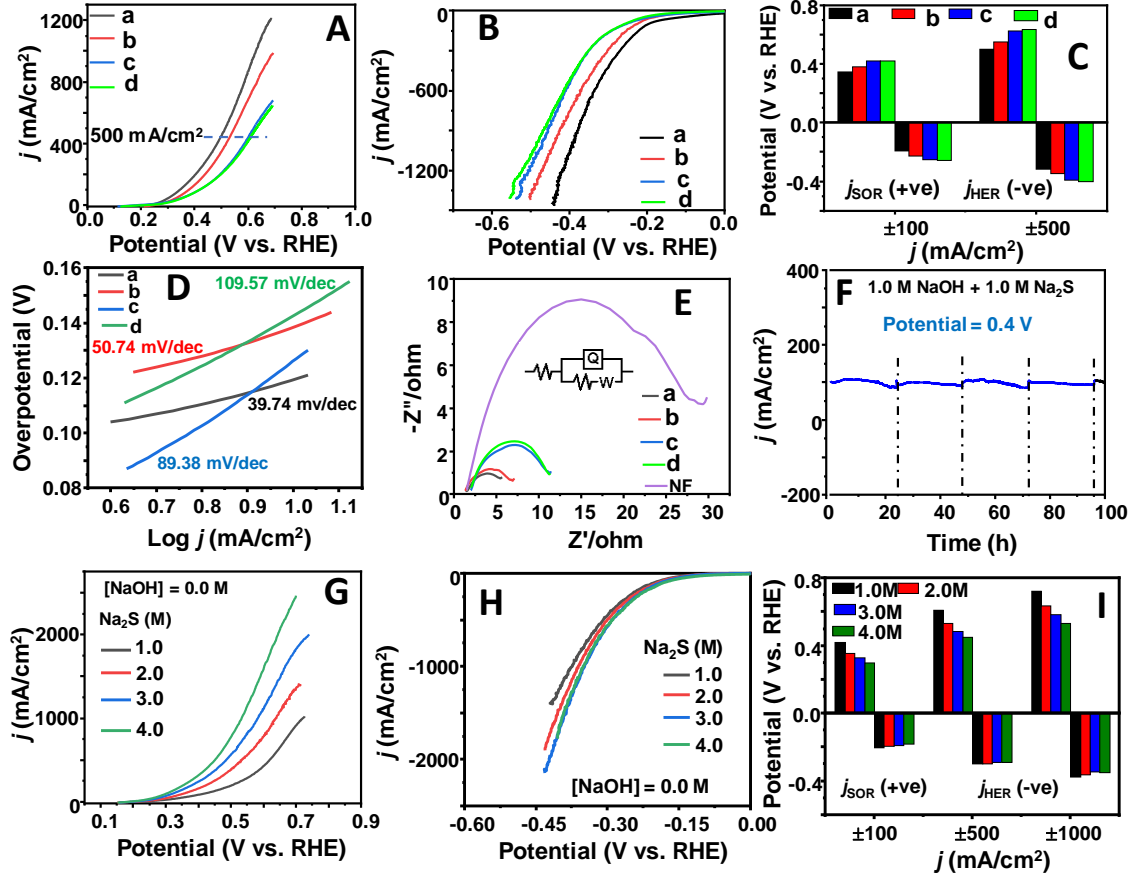


**Figure 2.3:** Plots of the various catalyst compositions include: (A) SOR and (B) HER plots, (C) the potential required to realize various  $j$  values for the electrodes, (D) Tafel plot obtained from SOR traces of various electrodes, (E) EIS Nyquist plots of various electrodes and bare Ni Foam, (F) the SOR chronoamperometry data of the NiFeOOH-CO<sub>9</sub>S<sub>8</sub>-21 recorded in 1.0 M NaOH + 1.0 M Na<sub>2</sub>S solution, and (G) the SOR and (H) the HER traces for NiFeOOH-CO<sub>9</sub>S<sub>8</sub>-21 recorded in 1.0 to 4.0 M Na<sub>2</sub>S solution with 5 mV/s scan rate and electrode area of 0.25 cm<sup>2</sup> and (I) the  $V_{\text{RHE}}$  corresponding to  $j$  values of 100, 500, and 1000 mA/cm<sup>2</sup> for different Na<sub>2</sub>S concentration. In each case, the reference electrode was made of graphite, while the counter electrode was made of Hg/HgO. The data was collected using an H-cell configuration with an inter-electrode spacing of 7 cm.

The  $j$  value of 500 mA/cm<sup>2</sup> was attained in the potential range of 0.50 to 0.62  $V_{\text{RHE}}$ , indicating that the composition of the electrodes had a significant impact on their

SOR efficiency (**Figure 3.3A**). The NiFeOOH-Co<sub>9</sub>S<sub>8</sub>-21 achieved  $j$  values of 500 and 1183 mA/cm<sup>2</sup> at 0.50 and 0.65 V<sub>RHE</sub>, respectively (**Figure 3.3C**). The  $j$  value attained by the aforementioned electrode could be comparable or better than the other electrode systems for SOR activities documented in the literature (**Table A3**). Notably, the electrodes demonstrated efficient HER performance as well, and for the various compositions, a  $j$  value of 500 mA/cm<sup>2</sup> was realized between -0.32 and -0.39 V<sub>RHE</sub> (**Figure 3.3B**). The values of the SOR Tafel slope were calculated between 39.74 and 109.57 mV/dec (**Figure 3.3D**). The composition with the smallest Tafel value among those indicating its high efficiency was NiFeOOH-Co<sub>9</sub>S<sub>8</sub>-21 (39.74 mV/dec). Ni-FeOOH and Ni-Co<sub>9</sub>S<sub>8</sub> control electrodes showed significantly lower SOR and HER activities, indicating the significance of oxide doping the Co<sub>9</sub>S<sub>8</sub> component by intercalating both components for efficient catalysis (**Figure A13A-D**).

The NiFeOOH-Co<sub>9</sub>S<sub>8</sub>-n electrochemical impedance spectra were fitted to an analogous circuit model. The solution resistance ( $R_s$ ) values (1.45  $\Omega$ ) of the electrolyte for the electrodes were found to be comparable by the EIS plots corresponding to the SOR activity, where the curves came from similar positions (**Figure 3.3E**). Significantly, compared to the other compositions, the charge transfer resistance ( $R_{CT}$ ) value for NiFeOOH-Co<sub>9</sub>S<sub>8</sub>-21, as indicated by the diameter of the plot's semicircle, was minimal. This could have facilitated charge transfer during the electrode half-cell reactions and increased SOR and HER activity. NiFeOOH-Co<sub>9</sub>S<sub>8</sub>-21 had the lowest work function value (6.77 eV) based on UPS spectra, which supports the above even more (**Figure A14**). The capacitance plots' values for the electrochemical surface area (ECSA) showed that the electrodes' SOR activity is proportionate. The ECSA of the several compositions examined, NiFeOOH-Co<sub>9</sub>S<sub>8</sub>-21, most likely showed the highest ECSA (65.8 cm<sup>2</sup>) (**Figures A15-A18, Table A4**). Then, the NiFeOOH-Co<sub>9</sub>S<sub>8</sub>-21 chronoamperometry data

were obtained at 0.4 V<sub>RHE</sub> with a matching  $j$  value of 100 mA/cm<sup>2</sup>. Throughout the 100-h period, there was no discernible change in the  $j$  value, indicating that the electrode's endurance was satisfactory (**Figure 3.3F**).

The NiFeOOH-Co<sub>9</sub>S<sub>8</sub>-21 exhibited better activity in terms of SOR and HER activities, leading to the measurement of the electrode's SOR and HER efficiencies without the presence of NaOH. The  $j$  values of 500 and 100 mA/cm<sup>2</sup> were found at 0.61 and 0.42 V<sub>RHE</sub>, respectively, in the presence of 1.0 M Na<sub>2</sub>S. As the [Na<sub>2</sub>S] increased to 4.0 M, the values further fell to 0.45 V and 0.30 V (**Figures 3.3G & 3.3I**). There may not be many reports in the literature of electrodes that can achieve the aforesaid SOR  $j$  value without a base. Additionally, in 1.0 M Na<sub>2</sub>S, the electrodes showed HER  $j$  values of 500 and 100 mA/cm<sup>2</sup> at -0.30 and -0.20 V<sub>RHE</sub> (**Figures 3.3H & 3.3I**). The rate of [S<sup>2-</sup>] consumption was then investigated using NiFeOOH-Co<sub>9</sub>S<sub>8</sub>-21 in 1.0 M Na<sub>2</sub>S and 1.0 M NaOH solution at several temperatures. As the electrolyte temperature rose, there was a noticeable rise in the SOR and HER activity. As the temperature increased from 30 to 60 °C, the potential to reach a SOR  $j$  value of 500 mA/cm<sup>2</sup> fell from 0.53 to 0.45 V (**Figures 2.4A–2.4C**). At 60 °C, a low potential of 0.67 V was achieved, leading to a very high SOR  $j$  value of 3000 mA/cm<sup>2</sup>. By monitoring the electrolyte's UV-Vis spectra at regular intervals and keeping the SOR  $j$  value of 100 mA/cm<sup>2</sup> at 0.4 V<sub>RHE</sub>, the rate of consumption of S<sup>2-</sup> was determined (**Figure A19**). A non-linear route was followed by the change in [S<sup>2-</sup>] with time, and the non-linearity was more noticeable for reactions carried out at high temperatures (**Figure 2.4D**). This indicated that the conversion deviates somewhat from first-order behavior, maybe because of the intermediate adsorption and desorption phases on the catalyst surface during electrolysis. For NiFeOOH-Co<sub>9</sub>S<sub>8</sub>-21, the SOR Tafel slopes at various temperatures were obtained from LSV traces. As the temperature increased, the value slightly dropped from 44.0 to 34.4

mV/dec, indicating a rise in SOR activity (**Figure 2.4E**). The exchange current density ( $j_0$ ) value at each temperature was then calculated by extrapolating the Tafel slopes to 0.0 V. Using  $j_0$  and electrolysis temperature, the Arrhenius plot for the SOR activity with NiFeOOH-Co<sub>9</sub>S<sub>8</sub>-21 in 1.0 M Na<sub>2</sub>S + 1.0 M NaOH was created.

The following formula was used to calculate the  $E_a$  value based on the slope of the Arrhenius plot: [178]

$$\log j_0 = \log A - \frac{E_a}{2.303RT} \quad \text{Equation 2.5}$$

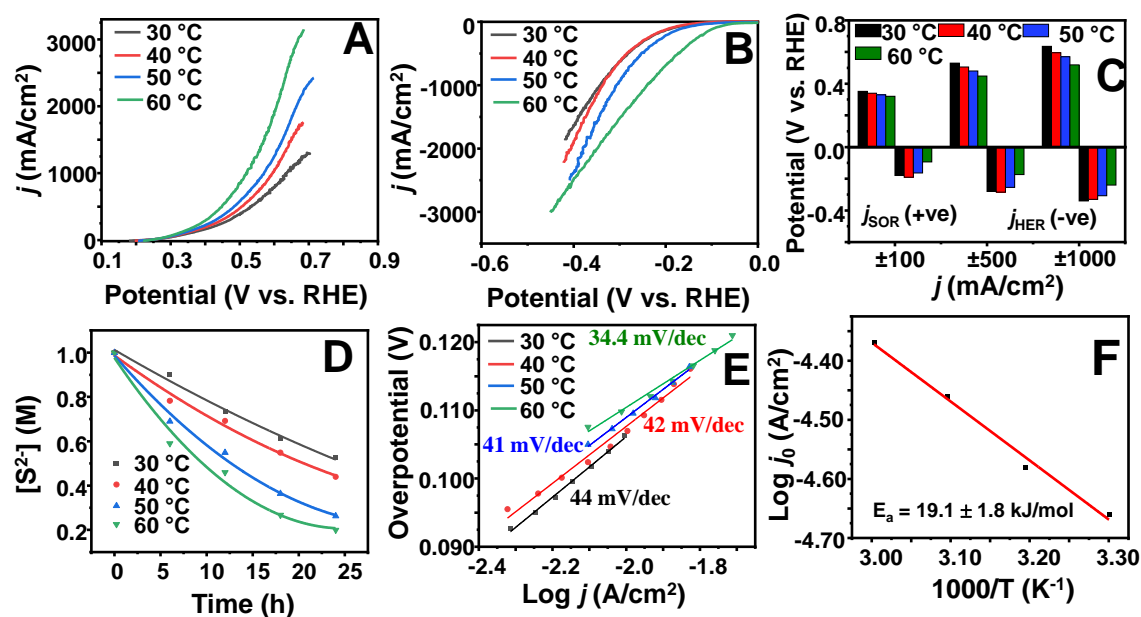


**Figure 2.4:** The LSV polarization traces (A) SOR and (B) HER of NiFeOOH-Co<sub>9</sub>S<sub>8</sub>-21 recorded under various temperature (C) The  $V_{\text{RHE}}$  values corresponding to various  $j_{\text{SOR}}$  and  $j_{\text{HER}}$  values recorded under various temperature situations for NiFeOOH-Co<sub>9</sub>S<sub>8</sub>-21, (D)  $[S^{2-}]$  vs. time plots documented under various temperature conditions using NiFeOOH-Co<sub>9</sub>S<sub>8</sub>-21 as both counter and working electrodes, (E) the Tafel plots obtained from SOR traces of NiFeOOH-Co<sub>9</sub>S<sub>8</sub>-21 under various temperature conditions, (F) the Arrhenius plot for SOR using NiFeOOH-Co<sub>9</sub>S<sub>8</sub>-21 in 1.0 M Na<sub>2</sub>S + 1.0 M NaOH with 5 mV/s scan rate and electrode area of 0.25 cm<sup>2</sup>

The quick activity of the NiFeOOH-Co<sub>9</sub>S<sub>8</sub>-21 towards SOR activity and the R<sub>CT</sub> results was further supported by the low E<sub>a</sub> value (19.1 kJ/mol) for S<sup>2-</sup> to Sn<sup>2-</sup> under electrochemical conditions in comparison to the OER (67 kJ/mol) reported in the literature(**Figure 2.4F**).[179] Although a variety of variables, including the average surface area, the number of active sites, and the ease with which bubbles may be detached from the electrode surface, may influence the E<sub>a</sub> value, the research confirmed the simplicity of the SOR with the current electrodes.

It's interesting to note that NiFeOOH-Co<sub>9</sub>S<sub>8</sub>-n electrodes worked well for both HER and SOR activities as bi-functional electrodes (**Figure 2.5A**). When NiFeOOH-Co<sub>9</sub>S<sub>8</sub>-21 was used in place of graphite as the cathode, the SOR *j* value at 0.4 V<sub>RHE</sub> (without iR corrected) improved from 100 to 150 mA/cm<sup>2</sup> (**Figure 2.5B**). These electrodes may be used as bi-functional electrodes for both HER and SOR processes, as shown by the HER *j* value at -0.4 V<sub>RHE</sub> (without iR corrected) increasing from 700 to 860 mA/cm<sup>2</sup> (**Figure 2.5C**). Above the *j* value of 500 mA/cm<sup>2</sup>, the performance was presumably further enhanced by the distance between the electrodes (**Figure 2.5D**). A 0.14 V drop in potential was seen when the inter-electrode spacing was reduced from 6 to 2 cm. This corresponds to a *j* value of 1000 mA/cm<sup>2</sup>. Since graphite, the counter electrode, compromises SOR activity in a single cell, the majority of SOR experiments that have been published in the literature to date employ H-type cells (**Figures 2.5E – 2.5F**). Using graphite as the cathode, the highest SOR *j* value in a single cell was achieved at 0.60 V, around 500 mA/cm<sup>2</sup>. It's interesting to note that the *j* value increased to 760 mA/cm<sup>2</sup> at the same voltage when NiFeOOH-Co<sub>9</sub>S<sub>8</sub>-21 was present as the anode and cathode. The bi-functional electrodes seem to have allowed the HER/SOR activities to be conducted in a single cell, as shown by the HER and SOR *j* values of 500 and 100 mA/cm<sup>2</sup> that were realized at iR uncorrected potentials of -0.37 & 0.69 and -0.20 & 0.36

$V_{\text{RHE}}$ , respectively (Figures 2.5G-2.5H). Since the  $j$  value of 143 mA/cm<sup>2</sup> was maintained for up to 100 hours at 0.4 V<sub>RHE</sub> for SOR, the chronoamperometry data collected using NiFeOOH-Co<sub>9</sub>S<sub>8</sub>-21 as both the cathode and anode demonstrated acceptable durability (Figure 2.5I).

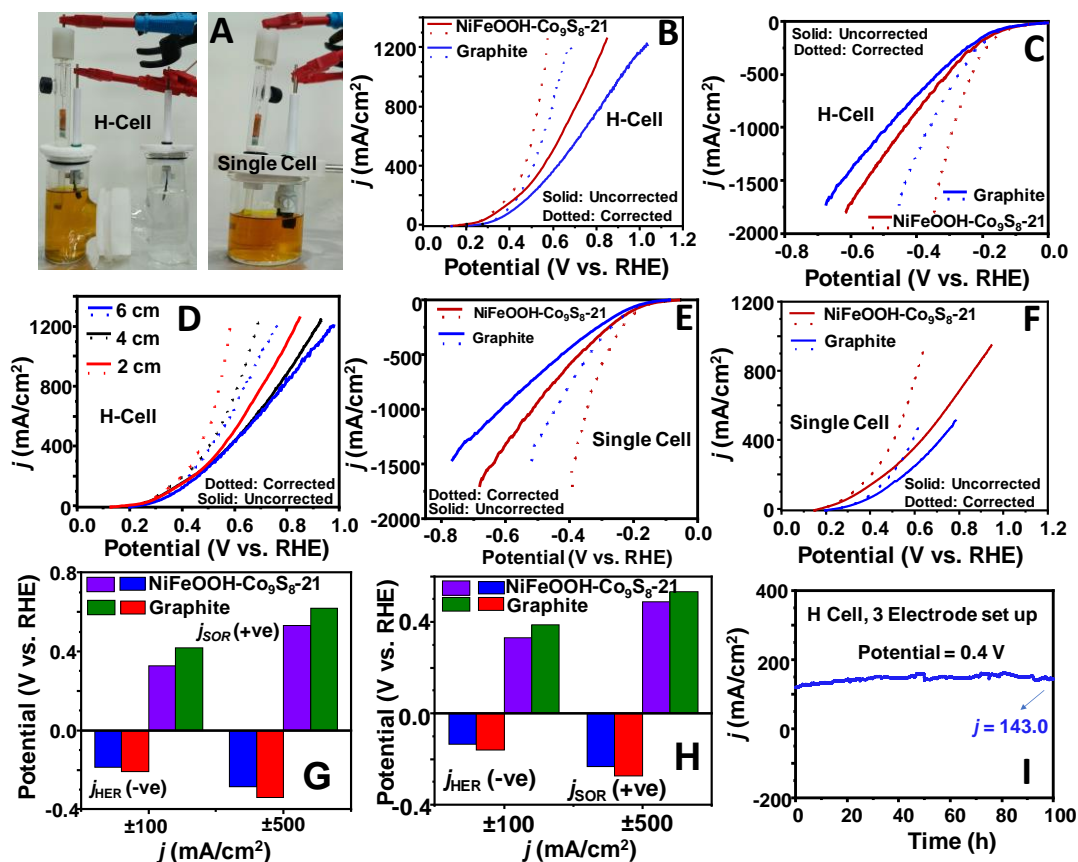


**Figure 2.5:** (A) Pictures of the H-type cell and single-cell electrochemical setups used for the SOR and HER traces, (B) SOR and (C) HER profiles recorded with graphite and NiFeOOH-Co<sub>9</sub>S<sub>8</sub>-21 as the counter electrodes (D) SOR LSV traces recorded in an H-type electrochemical cell with various interelectrode distances (E) HER and (F) SOR LSV traces recorded in a single cell electrochemical setup with graphite and NiFeOOH-Co<sub>9</sub>S<sub>8</sub>-21 as the counter electrodes, the potential values corresponding to different  $j$  values achieved in a (G) single cell and (H) H-type electrochemical cell, (I) the stability (i-t) data recorded in an H-type electrochemical cell with a 2 cm interelectrode distance using NiFeOOH-Co<sub>9</sub>S<sub>8</sub>-21 as both counter and working electrodes.

The energy efficiency of the present process for producing H<sub>2</sub> was then compared to that of the conventional water-splitting method utilizing NiFeOOH-Co<sub>9</sub>S<sub>8</sub>-21. NiFeOOH-Co<sub>9</sub>S<sub>8</sub>-21 obtained HER and OER *j* values of 100 mA/cm<sup>2</sup> at -0.33 and 1.48 V<sub>RHE</sub> potential in the presence of 1.0 M NaOH, and the electrodes demonstrated sufficient OER activity (Figures 2.6A-2.6C).

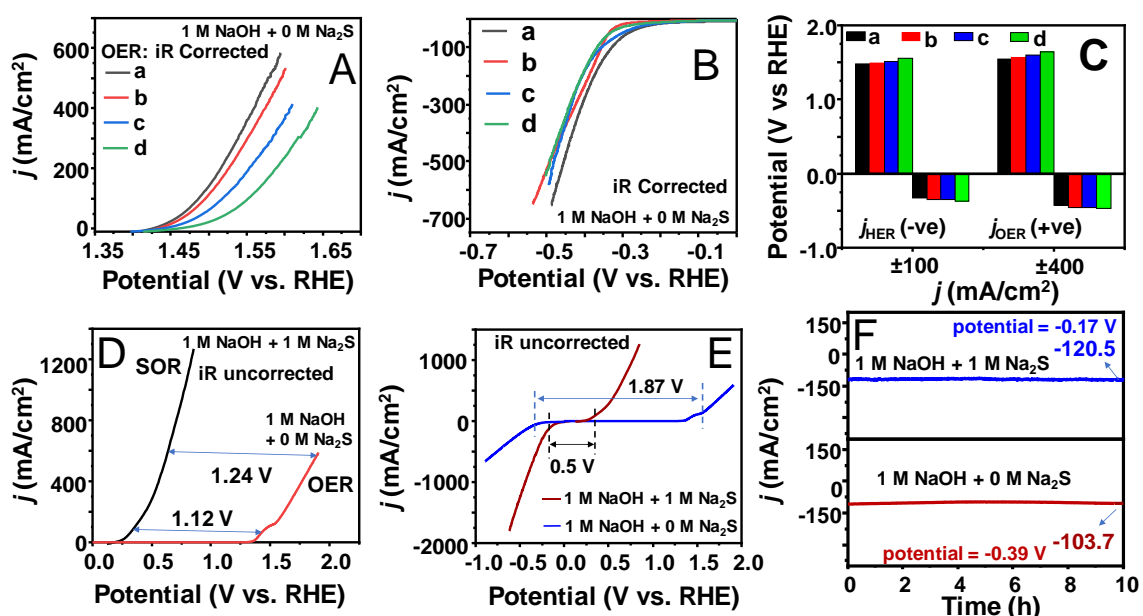


**Figure 2.6:** The NiFeOOH-Co<sub>9</sub>S<sub>8</sub>-*n* (a: *n* = 21, b: *n* = 12, c: *n* = 13, d: *n* = 11) (A) OER and (B) HER polarization traces recorded in single cell electrochemical setup using 1.0 M NaOH electrolyte, (C) the bar graph shows the potential (V<sub>RHE</sub>) values related with different *j* values found during the HER and OER process, (D) the NiFeOOH-Co<sub>9</sub>S<sub>8</sub>-21 SOR (H-type electrochemical cell) and OER (single cell) polarization traces illustrating the potential (V<sub>RHE</sub>) requirements to reach certain *j* values, (E) the HER-SOR (1.0 M Na<sub>2</sub>S+1.0 M NaOH) and HER-OER (1.0 M NaOH) polarization traces with 5 mV/s scan rate and electrode area of 0.25 cm<sup>2</sup> depict the total potential needed to realize H<sub>2</sub> production at *j* values of 100 mA/cm<sup>2</sup>, (F) the stability traces of HER activity recorded in absence and presence of 1.0 M NaOH in 1.0 M Na<sub>2</sub>S.

Importantly, without  $iR$  corrected potential in SOR to attain  $j$  values of 500 and 100 mA/cm<sup>2</sup> was 1.24 and 1.12 V lower respectively, than that of the OER activity, indicating a much superior energy proficiency in the former instance (**Figure 2.6D**). To our knowledge, NiFeOOH-Co<sub>9</sub>S<sub>8</sub>-21 is more proficient than other catalyst systems described in the literature for both HER and SOR, allowing to produce H<sub>2</sub> at  $j$  values of 1000 and 100 mA/cm<sup>2</sup> at total potential values of 0.84 and 0.46 V, respectively (**Figure 2.6E, Table A5**). The electrodes provide a useful power-saving substitute with the SOR process, as seen by the much lower total potential value (1.87 V) required to get a  $j$  value of 100 mA/cm<sup>2</sup> utilizing the conventional electrolysis approach via OER and HER activity. (**Figure 2.6E**). The HER chronoamperometry data also showed a similar pattern, with the  $j$  value of 120.5 mA/cm<sup>2</sup> being kept at -0.17 V while Na<sub>2</sub>S was present and increasing to -0.39 V when it wasn't to sustain the  $j$  value of 103.7 mA/cm<sup>2</sup> for 10 hours. (**Figure 2.6F**).

A two-electrode setup was used to study the oxidation of sulfion and the production of H<sub>2</sub> to assess the feasibility of industrial application. The H-type cell's anode chamber contained 1.0 M Na<sub>2</sub>S and 1.0 M NaOH, while the cathode chamber contained 1.0 M NaOH. (**Figure 2.7A**). With  $j$  values of 500 and 100 mA/cm<sup>2</sup> attainable at an uncorrected cell voltage of 1.14 and 0.69 V, respectively, the LSV traces demonstrated the advantages of using NiFeOOH-Co<sub>9</sub>S<sub>8</sub>-21 as both the anode and cathode. However, the value rose to 1.13 V (100 mA/cm<sup>2</sup>) and 1.58 V (500 mA/cm<sup>2</sup>), respectively, when graphite was used as the counter electrode. (**Figure 2.7B**) Interestingly, a single cell configuration using NiFeOOH-Co<sub>9</sub>S<sub>8</sub>-21 as the counter and working electrodes achieved a phenomenal uncorrected voltage of 0.44 and 1.0 V to get the  $j$  values of 100 and 500 mA/cm<sup>2</sup>, indicating that this system could be the most effective one yet reported. (**Figure 2.7C**).

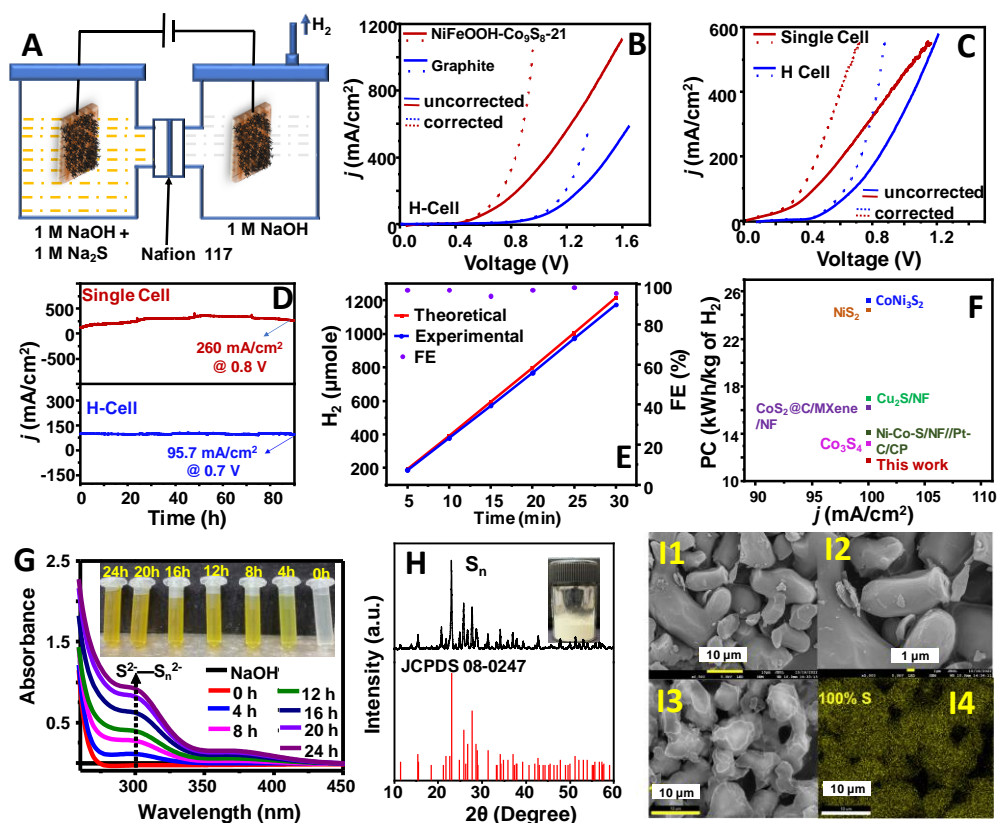


**Figure 2.7:** (A) Diagram of the H-type two-electrode electrochemical setup used to produce  $\text{H}_2$  (B) evaluation of the LSV traces recorded in an H-type and single cell with  $\text{NiFeOOH-Co}_9\text{S}_8\text{-21}$  as the working and counter electrodes; (C) the LSV traces documented in a two-electrode setup using an H-type electrochemical cell with a 2 cm inter-electrode distance, the electrodes used were  $\text{NiFeOOH-Co}_9\text{S}_8\text{-21/NiFeOOH-Co}_9\text{S}_8\text{-21}$  and  $\text{NiFeOOH-Co}_9\text{S}_8\text{-21/graphite}$ , (D) chronoamperometry traces of the SOR conducted under two-electrode electrochemical set up in an single cell (0.8 V), and H-type (0.7 V), (E) the plot showing the faradaic efficiency with theoretical and experimental  $\text{H}_2$  production over time in an H-type cell electrochemical cell, (F) a comparison of the power consumption of the current electrode and systems that have been reported for the production of 1 kg of  $\text{H}_2$ , (G) the UV-Vis spectra of the electrolyte, which were obtained at different time intervals during chronoamperometry experiment, (H) the XRD data, and (I) the FE-SEM data of the Sn that was extracted from the anodic solution following  $\text{H}_2\text{SO}_4$  neutralization.

Chronoamperometry investigations were used to evaluate the electrode's endurance under two-electrode electrochemical setups in both single-cell and H-type electrochemical cells. The durability was supported by the  $j$  value in both instances, which remained stable for the whole 90 h period (**Figure 2.7D**). Importantly, the  $j$  value for the single cell increased somewhat throughout the first 24 hours, suggesting possible electrode activation, this was not the case for the H-type cell. The H-cell and single cell's respective  $j$  values after 90 hours remained at 95 mA/cm<sup>2</sup> at 0.7 V and 260 mA/cm<sup>2</sup> at 0.8 V (**Figure 2.7D**). After comparing the actual and theoretical H<sub>2</sub> production data, the Faradaic efficiency value of around 96.7% was determined. This value may be suitable for future applications (**Figure 2.7E**).

The additional power consumption data likewise showed an ultralow value at  $j = 100$  mA/cm<sup>2</sup> of 11.8 kWh/kg of H<sub>2</sub>, indicating that the NiFeOOH-Co<sub>9</sub>S<sub>8</sub>-21 may perform better than the state-of-the-art systems that have been described (**Figure 2.7F** for power consumption calculation). [180] The H<sub>2</sub> generated has a 99.3% purity level, according to the GC analysis (**Figure A20**). After 90 hours of electrolysis, the FESEM data of the NiFeOOH-Co<sub>9</sub>S<sub>8</sub>-21 surface showed that the nanostructures had little change in shape, indicating that they were stable under the electrolysis conditions (**Figure A21**). Following the chronoamperometry test, the electrode's SOR trace matched that of the original sample, corroborating the previous findings (**Figure A22**). To determine the composition and purity, the Sn produced was characterized. The production of Sn<sup>2+</sup> in the solution during electrolysis was corroborated by the absorption peaks at 300 nm (**Figure 2.7G**). [181] The foregoing is further supported by the XRD data of the Sn recovered from the solution using H<sub>2</sub>SO<sub>4</sub> matching that of the S<sub>8</sub> JCPDS (**Figure 2.7H**). According to the FESEM data, the S<sub>n</sub> produced is in the form of granules of different diameters (**Figure 2.7I**). S<sub>n</sub> was the sole significant ingredient found by the EDS mapping (**Figure**

**A23**). In support of the aforementioned, the elemental analysis also showed that "S" was present in the sample in about 100%. (**Table A6**).

DFT simulations were used to investigate the oxidation routes of different sulfide ions on both pure and oxygen-doped 200 facets of  $\text{Co}_9\text{S}_8$  to get insight into the SOR activity of the material. **Figure 2.8A** displays the optimized structures for these facets together with the intermediates (**Figure A24**). Since the XRD and TEM analyses showed that the 200 facet was the predominant facet of the synthesized O-doped  $\text{Co}_9\text{S}_8$ , it was selected for the examination. Moreover, some well-known surfaces, like the 822 facet, have bigger atoms, which might greatly lengthen the computing time. For the progressive oxidation of  $\text{S}^{2-}$  to  $\text{S}_8$  ( $\text{S}^{2-} \rightarrow \text{S}^* \rightarrow \text{S}_2^* \rightarrow \text{S}_3^* \rightarrow \text{S}_4^* \rightarrow \text{S}_8^* \rightarrow \text{S}_8$ ) on  $\text{Co}_9\text{S}_8$ , we assessed the energy variation of elementary reactions (**Figure 2.8A**).

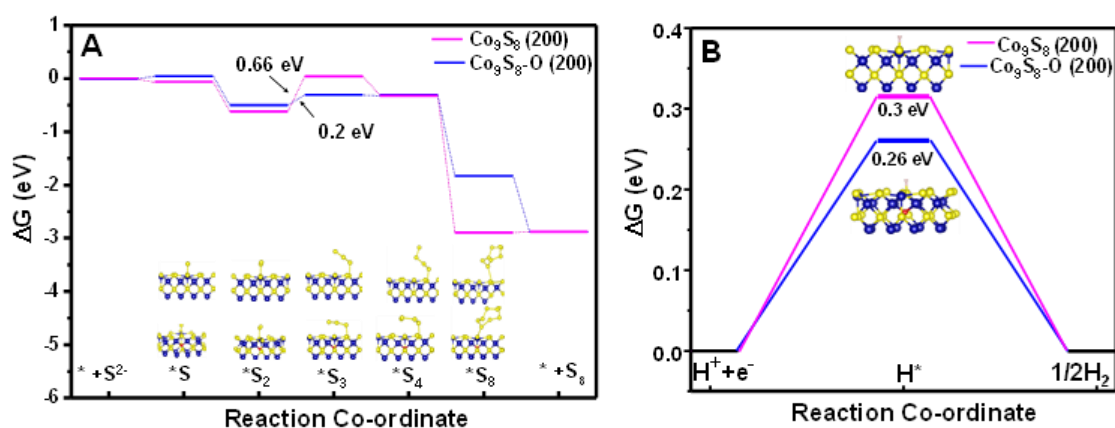


**Figure 2.8:** The findings of the DFT analysis (A) the energy levels of  $\text{Co}_9\text{S}_8$  and O-doped  $\text{Co}_9\text{S}_8$  for the HER process, and (B) the free energy levels of the final product and intermediate as calculated utilizing a step by step SOR procedure on the 200 facet of  $\text{Co}_9\text{S}_8$ .

The results of the study shed light on the energy barriers and reaction kinetics related to each stage. The transformation of  $\text{S}_2^*$  to  $\text{S}_3^*$  was the probable rate-determining step in the SOR process for both pristine and oxygen-doped  $\text{Co}_9\text{S}_8$  (200) facets. For this

phase, the energy barrier in the pure  $\text{Co}_9\text{S}_8$  (200) facet was 0.66 eV. It's interesting to note that the energy barrier dropped to 0.20 eV when oxygen doped into 200 facets. The reaction's kinetics may have been improved by this energy barrier decrease, improving SOR activity. The fact that the energy barrier was slightly lower than the values reported in earlier literature studies on some of the other cobalt sulfide systems highlights the increased SOR activity of  $\text{NiFeOOH-Co}_9\text{S}_8\text{-n}$ . The result of O-doping on the HER procedure was also calculated using DFT investigation. (**Figure 2.8B**). Following oxide doping, the  $\Delta G$  value for  $\text{Co}_9\text{S}_8$  dropped by 0.04 eV, providing more evidence for the doping process's ability to increase catalytic activity.

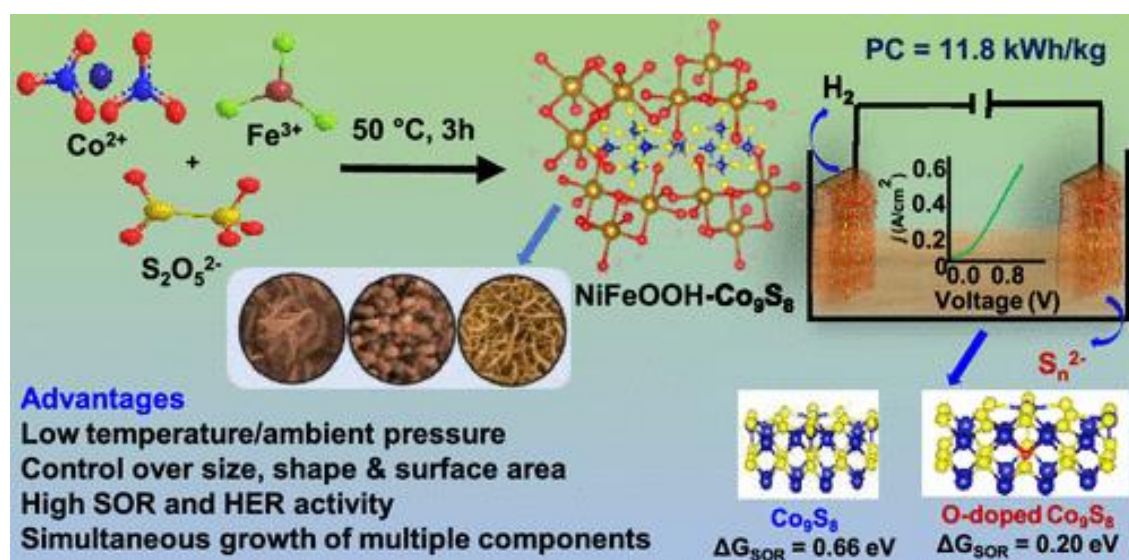
Overall, SOR and HER behavior were successfully improved by the  $\text{Co}_9\text{S}_8$  oxide doping and  $\text{NiFeOOH}$  intercalation, and the synthetic process allowed for the development of a range of nanostructures with the large surface area needed for  $\text{H}_2$  production at high  $j$  values, low total potential, and minimal power consumption responsibly. Due to its simple synthetic technique, this may also be used for large-scale electrode synthesis and future commercial applications. Future research may use this method of combining precursors with different levels of reactivity towards the reagent to create more hybrid nanostructures for related uses.

## 2.7 Conclusion

To fabricate intercalated nanostructures with enhanced catalytic activity in a single step, the relative reactivity of the two precursors might be one useful technique. A platform for the efficient production of green  $\text{H}_2$  in the presence of  $\text{S}^{2-}$  may be obtained by growing an intercalated nanostructure of  $\text{FeOOH}$  and  $\text{Co}_9\text{S}_8$  on NF. The combined operation of SOR and HER in an H-type or single cell is made possible by the developed  $\text{NiFeOOH-Co}_9\text{S}_8\text{-n}$  based catalytic system's bifunctionality. One useful parameter to regulate the potential-current connection is the inter-electrode distance. Without  $\text{NaOH}$ , the SOR

process was made possible by the catalyst's strong activity at a high  $j$  value. The DFT study showed that the SOR activity was enhanced by the oxide doping of  $\text{Co}_9\text{S}_8$  that occurs from the interface between  $\text{FeOOH}$  and  $\text{Co}_9\text{S}_8$ . All things considered, the present electrodes' significant power savings and low energy consumption in the generation of green  $\text{H}_2$  provide a feasible foundation for the technology's future commercialization.

### Table of Contents



## Chapter 3

# In situ Growth of $\text{Co}_3\text{O}_4@\text{NiCu}$ Alloy Nanocuboids assisted by Ni Surface and Polyacryloyl Hydrazide for Efficient Methanol Oxidation and Oxygen Evolution Reactions

(Adapted from DOI:10.1002/adsu.202400372, Copyright 2024 Wiley-VCH GmbH)

### 3.1 Abstract

A one-pot synthesis technique is used to grow  $\text{Co}_3\text{O}_4$  doped NiCu alloy nanocuboids on nickel foam under hydrothermal conditions. It uses polyacryloyl hydrazide (PAHz) as a composition-directing agent and a metallic nickel surface as a shape-directing agent. The size, shape, lattice configuration, doping, and heterostructure of the electrocatalysts may all be precisely controlled using this approach, which is essential for adjusting their catalytic activity. The resultant bi-functional electrodes exhibit superior performance in the HER and methanol oxidation reaction (MOR) and are suitable for high-energy coupled green hydrogen generation. The electrodes demonstrate remarkable longevity, continuing to operate at  $10 \text{ mA/cm}^2$  for 100 hours, while also displaying a low overall potential of 1.78 V, which allows for a current density of  $100 \text{ mA/cm}^2$  for the combined MOR and HER processes. The electrodes' selectivity in converting methanol to formate is another feature that confirms their suitability for the intended use. In the oxygen evolution reaction (OER), the NF-PAHz- $\text{Co}_3\text{O}_4@\text{NiCu}$  also shows promise, attaining a current density of  $100 \text{ mA/cm}^2$  at a potential of 1.65  $V_{\text{RHE}}$  with sufficient endurance. The wide implications of this synthetic approach for future developments in electrocatalyst design and synthesis emphasize its generality, scalability, and possible applicability to the creation of various metal oxide doped alloy nanostructures.

### 3.2 Introduction

When it comes to producing and using certain renewable energy sources as well as efficiently using greenhouse gases, electrocatalysis is crucial.[133,131] One of the main methods for producing green hydrogen ( $H_2$ ) is electrocatalysis, which is the primary mechanism that splits water into  $H_2$  and  $O_2$ . [182, 183] Recent research examines many half-cell reactions to improve the process's total energy efficiency, which is one of the main issues impeding the technology's commercial feasibility. [184, 185] The methanol oxidation reaction (MOR) is an important half-cell reaction that has been studied in the literature to increase the energy efficiency of the water splitting process because of its feasible side products and low theoretical starting potential. [24,186 ] Thus, MOR coupled with HER provides a feasible way to economically generate clean  $H_2$  energy, meeting one of the Sustainable Development Goals of the United Nations. In recent literature, many electrocatalysts with sufficient catalytic effectiveness towards MOR have been created and examined. [187,188] Periodically formed Pt-Au hetero nanostructures, for instance, showed better MOR activity in 0.1 M  $HClO_4$  solution than Pt/C. [189] Mn alloying of CoPt catalyst increased MOR's durability and activity in acidic conditions. [190] In particular, transition metal alloy-based nanostructures have shown competence in a range of electrochemical processes in published works. [191,192] For instance, under simple circumstances, CoNi alloy/CoNi layered double hydroxide activated  $MoS_2$  nanosheets demonstrated efficient  $H_2$  evolution activity. [193] NiCu alloy-based nanocatalysts have shown efficient MOR linked water splitting activities under varying pH settings, making them one of the active catalytic systems. [194,195] Cu/NiCu nanowires, for instance, with a mass  $j_{MOR}$  value of 867.1  $mA/mg_{metal}$  at 1.55  $V_{RHE}$  were manufactured in two steps. [85] In a similar vein, an alkaline system based on NiCu@C nanoparticles obtained a mass  $j_{MOR}$  value of 1028  $mA/mg_{metal}$  at 1.55  $V_{RHE}$ . [90] Even though the results were encouraging, further  $j$  value enhancement at a low

potential is preferred in order to fully use the system for commercial purposes. The benefits of both nanoscale metals and polymeric substrates have been combined in polymer-based metal nanoparticles, which have recently become an intriguing class of electrocatalysts. [196,197] The polymer matrix provides stability, resistance to chemicals, and an environment that can be adjusted to alter the shape of the nanoparticles, while the metal nanoparticles operate as active sites for efficient catalysis. [198, 199] It is also known that surface charges and hydrophobicity/hydrophilicity of polymeric coatings may be used to adjust the catalyst's surface electrical characteristics. [200] Metal nanocomposites based on conducting polymers or carbon-based supports, combined with earth-abundant metals, have been investigated recently. [201,202] It's significant that metal-polymer nanocomposites are ready to act as catalysts in the sustainable generation of H<sub>2</sub> from a variety of water sources. [203] For instance, in an alkaline environment, CoOx nanoparticles distributed in a poly(pyrrole-alkylammonium) system demonstrated efficient oxygen evolution reaction (OER) activity. [204] Nickel foam (NF) is a porous substance that exhibits strong electrical conductivity, resilience in alkaline solutions, and a suitable structure for the release of gas bubbles. To develop bimetallic alloy nanostructure on NF for MOR application, this method targets three aspects: metallic oxide doping, form orientation of nanostructures, and improvement of surface area in a one-pot synthetic operation. Given that the form of the nanocatalyst is known to regulate the activity, it is especially beneficial to develop alloy or multi-metallic nanostructures of a certain size and shape. [205] Since metal oxide doping is known to change the electronic structure and lead to band gap optimization, which is required for customizing catalytic activity, the prospect of doping the aforementioned alloy nanostructures with oxides is intended to improve the activity further. [206] To the best of our knowledge, there has been little research done in the literature on the function of active metal surfaces

as shape-directing agents in the development of bimetallic nanostructures. To create a nanocatalyst system with sufficient activity and durability, the composition-directing capacity of a polymeric reductant is also included in the design.

Here, hydrothermal conditions are used to in-situ generate NiCu alloy nanostructures from their salts using polyacryloyl hydrazide (PAHz) as the reducing and capping agent. [207] It has previously been shown in the literature that PAHz efficiently reduces a variety of metal salts to the matching nanoparticle in aqueous solution. [208,209,210] Size-controlled Ag and Au nanoparticles were synthesized in aqueous solutions using PAHz at ambient conditions. [211] We used a star polymer functionalized with carbonyl hydrazide to quickly convert different precious metal ions to the matching nanoparticles in solution. [212] Similarly, by the creation of matching nanoparticles, membranes based on CNT modified with PAHz were used to separate different metal ions from oil-water emulsion. [213] This method creates a metal oxide doped nanoalloy that may be used for electrocatalysis by taking use of PAHz's potential selective reduction capacity towards different metal ions. Additionally, the potential function of the NF surface as a nucleating site to control the geometry of the aforementioned nanostructure is investigated. [214, 215] The overall plan is to produce PAHz capped  $\text{Co}_3\text{O}_4@\text{NiCu}$  alloy nanocrystals on NF using a one-pot method, which will be used as active electrodes for MOR and OER activities in an alkaline medium. We study the effects of electrode structure, composition of the nanocatalyst, and material fabrication to maximize MOR and OER performances in membrane-less environments. By means of an in-depth electrochemical examination combined with physical and morphological description, we exhibit the generated electrodes' catalytic effectiveness and stability in alkaline media in comparison to the most advanced benchmark electrocatalysts. Overall, in order to fully realize the promise of polymer-based nanocomposite catalysts for effective and long-

lasting alkaline water splitting and MOR, our study offers important insights into the design principles for these materials.

### **3.3 Experimental Section**

#### **3.3.1 Material Required**

The following materials were used exactly as received: NF (99%, thickness 1.6 mm, Goodfellow), potassium hydroxide (98%, Qualigens), hydrazine hydrate (99%, Rankem), tetra-n-butylammonium bromide (98%, Merck), methanol (99%, Finar), tetrahydrofuran (99%, Finar Ltd.), ethanol (99%, Changshu HFCL), and hydrochloric acid (99%, SDFCL). The Millipore water filtration system provided the DI water.

#### **3.3.2 Material Characterization**

A Pananalytical Empyrean X-ray diffractometer was used to capture the XRD diffraction data in the  $2\theta$  range of 10-90°. To examine the surface electronic characteristics, a monochromatic Al K-Alpha analyzer (XPS, ThermoFisher) adjusted with C1s 284.8 eV was used. The material's surface morphology was examined using field emission scanning electron microscopy (FESEM JSM-7900F, Jeol Ltd.), and the energy dispersive X-ray spectroscopy (EDX) method (JSM-7900F, Jeol Ltd.) was used to study the elemental distribution. Together with the STEM-HAADF and SAED pictures, the high-resolution images were obtained using the HRTEM (JEM-F200 JEOL). Using an NMR JEOL 400 YH machine in the solvent D<sub>2</sub>O at 25 °C, the <sup>1</sup>H and <sup>13</sup>C NMR spectroscopic data were acquired. The PerkinElmer Spectrum Two instrument was used to capture the FT-IR spectroscopic data in ATR mode. X-ray absorption spectroscopy (XAS) was used at the INDUS beamline synchrotron facility (2.5 GeV, 100mA), BL-09, INDUS-2, to evaluate materials.

### 3.3.3 Synthesis of NF-PAHz-Co<sub>3</sub>O<sub>4</sub>@NiCu

The fabrication method of the NF-PAHz-Co<sub>3</sub>O<sub>4</sub>@NiCu electrode included the following steps. To remove any contaminants on the surface, the NF measuring  $2.5 \times 3 \text{ cm}^2$  was first washed with water, ethanol (20 mL), and hydrochloric acid (24 mL, 2 M). After that, a 50 mL, 16.55 mM Cu(NO<sub>3</sub>)<sub>2</sub>·3H<sub>2</sub>O solution was placed in a beaker at room temperature and continuously stirred at 700 rpm. Following this, 25 ml of a 2-weight percent PAHz solution was added, and the mixture was shake-free for 60 minutes. After adding a 50 mL (13.74% mM) solution of Co(NO<sub>3</sub>)<sub>2</sub>·6H<sub>2</sub>O, the mixture was stirred for 30 minutes. A further 25 milliliters of the 2-weight percent PAHz solution were added to this, and the whole mixture was stirred for 60 minutes. This homogenous liquid was then put into an autoclave, and the cleaned NF piece above was submerged in it. The autoclave was now placed in a 12-hour hot air oven set at 120°C. The system's temperature was then lowered to room temperature. After being taken out of the aqueous solution, the NF was cleaned with DI water. After that, the sample was dried for 12 hours at 50 °C in a vacuum oven.

### 3.3.4 Synthesis of NF-PAHz-NiCu

Using the mentioned method, 20 mL of ethanol, 24 mL of hydrochloric acid (2 M), and 20 mL of DI water, the surface of NF was activated. A 50 mL, 16.55 mM Cu(NO<sub>3</sub>)<sub>2</sub>·3H<sub>2</sub>O solution was added to a beaker and continuously swirled at room temperature at a speed of 700 rpm. After that, over an hour, 25 ml of a 2-weight percent PAHz solution was progressively added to the previously stated condition. After homogenizing the mixture, NF was added to an autoclave. For 12 hours, the autoclave was heated in a hot air oven to 120 °C to facilitate the formation of cubic nanoparticles on the nickel foam surface. Following a wash with DI water, the nickel foam was taken out of the solution, cleaned, and dried at 50 °C.

### 3.3.5 Synthesis of PAHz-Cu

Cu(NO<sub>3</sub>)<sub>2</sub>·3H<sub>2</sub>O solution (50 mL, 16.55 mM) was droppedwise added to 25 ml of 2 wt% PAHz aqueous solution over an hour at a continuous stirring rate of 700 rpm. The Co(NO<sub>3</sub>)<sub>2</sub>·6H<sub>2</sub>O (50 mL, 13.74 mM) solution was then added straight to the previous solution over the course of 30 minutes. The aforementioned solution was then mixed with 25 ml of 2 weight percent PAHz, added dropwise over the course of an hour. The above-mentioned solution was then mixed with 50 mL of Ni(NO<sub>3</sub>)<sub>2</sub>·6H<sub>2</sub>O solution (13.75% mM) over an hour. After that, the mixture was autoclaved and heated to 120 °C for 12 hours in a hot air oven. After that, the precipitate was filtered. After being repeatedly cleansed with deionized (DI) water, the filtrate was stored for 12 hours at 50 °C in a vacuum oven.

### 3.3.6 Electrochemical Measurements

An electrochemical workstation (M204 PGSTAT, Autolab) was used for all electrochemical analyses. A 25 mL mini gas-tight cell was used for the electrochemical tests. The NF-PAHz-Co<sub>3</sub>O<sub>4</sub>@NiCu electrode was used as the working electrode in a three-electrode system, the counter electrode was a graphite rod, and the reference electrode was Hg/HgO (1.0 M NaOH). Whereas a 1.0 M MeOH + 1.0 M KOH solution is used for MOR and HER, 1.0 M KOH was the electrolyte employed for OER and HER. Throughout the chronoamperometry test at 1.86 V, NMR spectroscopic data were taken at regular intervals of 24 hours to track changes throughout the production of formate from methanol. The potential on the RHE scale was transformed using the Nernst equation. The acquired current is transformed into *j* (current density) and normalized using the geometrical area of the working electrode.

$$E_{RHE} = E_{Hg/HgO}^0 + E_{Hg/HgO} + 0.0591 \times pH \quad \text{Equation 3.1}$$

### 3.3.7 Fabrication of PAHz-Cu Electrode

Initially, a solution was prepared by mixing 0.25 mL of methanol with 0.75 mL of deionized water. 20 mg of PAHz-Cu electrocatalyst material and 0.2 mL of a 5-weight percent Nafion solution were added to this solution. After that, the combination was treated with ultrasonic waves for an hour to break up the components and create a well-combined ink suspension. Next, 6  $\mu\text{L}$  of the previously described ink solution was drop cast onto a glassy carbon electrode that had a 5 mm diameter. The drop-cast film was left to dry overnight at 50 °C in a hot air oven.

### 3.3.8 Fabrication of IrO<sub>2</sub> and Pt/C electrode

To create homogenous inks, 6.25 mL of commercial Pt/C and IrO<sub>2</sub> were dissolved in 1.35 mL of a combination solution of isopropanol (0.80 mL), water (0.40 mL), and 5 weight percent Nafion (0.15 mL) separately. The mixture was then sonicated for 50 minutes. After that, 100  $\mu\text{L}$  of one of the catalyst inks was drop-coated onto the Ni foam electrodes' surface and allowed to dry overnight at 50 °C in a vacuum oven.

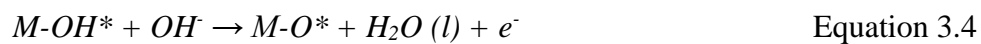
### 3.3.9 Computational Methods

The Vienna ab initio simulation (VASP) program was used to do first-principles calculations using the density functional theory (DFT) framework. [216,217] Projector-augmented wave (PAW) potentials were used to illustrate the interactions between electrons and ions. [218] In the Perdew–Burke–Ernzerh (PBE) form, the exchange-correlation functional was calculated using the generalized gradient approximation (GGA) [219]. An approach known as conjugate gradient (CG) was used to optimize the structure without symmetry constraints until the maximum force acting on each atom was less than 0.001 eV  $\text{\AA}^{-1}$ . The self-consistency loop iteration keeps on until the total energy difference between two successive iteration stages equals  $1 \times 10^{-5}$  eV. The Kohn–Sham electron wave function was extended using plane waves, with an energy threshold of 500

eV. For structural optimization, Brillouin zone (BZ) sampling was performed utilizing k-points on a  $3 \times 3 \times 1$  grid. The long-range van der Waals interactions were investigated using the DFT-D2 method. A  $10^{-15}$  Å vacuum layer has been taken in the z-direction. Two layers of Ni (111) and two further layers of Cu (111) plane were taken into consideration in this work to build the NiCu heterosystem. The first principles calculation technique states that to create a heterosystem, the lattice constants of several materials must agree. [220,221,222] The lattice constants for the Ni(111) and Cu(111) planes have been determined to be 2.55 Å and 2.53 Å, respectively, for this investigation.[223]. Because the lattice misfit between Ni(111) and Cu(111) surfaces is so modest (about 0.7%), we may produce their heterostructure by retaining two layers of Ni(111) surfaces on two layers of Cu(111) surfaces, or vice versa. The ideal Van der Waal's spacing between the layers of Ni-Ni, Cu-Cu, and Ni-Cu ranges from 2.00 to 2.03 Å.  $3 \times 3 \times 1$  supercell slabs of NiCu that were x- and y-directed were taken into consideration in order to prevent communication between adjacent pictures. The widely accepted OER process has four electron/proton transfer steps in both acidic and alkaline environments. OER is very sensitive to pH; in an acidic environment, water molecules ( $H_2O$ ) oxidize, releasing oxygen molecules ( $O_2$ ) as well as  $H^+$  and  $e^-$  pairs. In an alkaline environment, on the other hand, hydroxyl groups ( $OH^-$ ) oxidize to form  $H_2O$  and  $O_2$ , as well as the simultaneous release of electrons. [224] In an alkaline environment, the water oxidation process is given by [225]



This reaction generally proceeds through four steps:





In this case, M stands for the catalyst's active site, while M-OH, M-O, and M-OOH stand for the species OH, O, and OOH that are adsorbed on it. Equations 2 and 5 above have been used to calculate Gibb's free energy using the formula  $\Delta G = \Delta E + \Delta ZPE - T\Delta S$ , where  $\Delta E$  stands for the binding energy,  $\Delta ZPE$  for the change in zero-point energy,  $\Delta S$  for the entropy difference, and  $\Delta ZPE$  for the difference between the system's gas phase and adsorbed states. [226]

### 3.3.10 Detailed MOR Activity Calculation

#### 3.3.10.1 Step I: CH<sub>3</sub>OH adsorption

For methanol, the estimated bond lengths are 1.40 Å for C-O, 0.98 Å for O-H, and 1.10 Å for C-H. Methanol is adsorbed because of the weak adsorption state created when the lone pair of oxygen electrons attach to atoms or metallic surfaces. Methanol has a poor adsorption energy of -0.43 eV on the Cu site of the Co Oxide-doped Ni/Cu system. According to calculations, the chemical process has an energy of -0.43 eV and is exothermic.

#### 3.3.10.2 Step II: CH<sub>3</sub>OH→CH<sub>3</sub>O

Methanol undergoes oxidation to methoxy in this stage. For CH<sub>3</sub>O, the estimated bond lengths are 1.43 Å for C-O bonds and around 1.10 Å for C-H bonds. With an adsorption energy of -3.37 eV, CH<sub>3</sub>O is significantly adsorbed on the Cu site of the Co oxide doped Ni/Cu combination. However, the energy required to break the C-H bond is far more than that required to break the O-H bond. We thus ceased considering the conversion of CH<sub>3</sub>OH to CH<sub>2</sub>OH. According to calculations, the chemical process has an energy barrier of -0.27 eV and is exothermic by -0.71 eV.

### 3.3.10.3 Step III: CH<sub>3</sub>O→CH<sub>2</sub>O

CH<sub>3</sub>O is oxidized to CH<sub>2</sub>O in this phase. For CH<sub>2</sub>O, the estimated bond lengths are 1.32 Å for C-O bonds and around 1.11 Å for C-H bonds. CH<sub>2</sub>O has an adsorption value of -0.61 eV and is lightly adsorbed on the surface. It is calculated that the chemical process has an energy barrier of 1.02 eV and is endothermic by 0.31 eV.

### 3.3.10.4 Step IV: CH<sub>2</sub>O→HCO

CH<sub>2</sub>O undergoes oxidation to produce HCO in this phase. HCO's computed bond lengths for C-O and C-H bonds are 1.26 Å and over 1.11 Å, respectively. With an adsorption energy of -2.87 eV, HCO is highly adsorbed on the surface. It is calculated that the chemical process has an energy barrier of -0.35 eV and is exothermic by -0.03 eV.

### 3.3.10.5 Step V: HCO→HCOOH

The initial state in this phase is the adsorption of CHO, and the final state is the adsorption of CO. HCOOH's computed bond lengths are 1.01 Å for O-H bonds, 1.31 Å for C-O bonds, and around 1.10 Å for C-H bonds. With an adsorption energy of -0.81 eV, HCOOH is highly adsorbed on the surface. It is calculated that the chemical process has an energy barrier of 0.45 eV and is endothermic by 0.42 eV.

## 3.3.11 Electrochemical Measurements

### 3.3.11.1 Quantification of H<sub>2</sub> Gas

A chronoamperometric experiment was conducted to quantify H<sub>2</sub> gas using the water displacement technique. This experiment involves pouring 1.0 M KOH + 1M MeOH into an inverted burette. As the reaction proceeds, 1.0 M KOH + MeOH is replaced by H<sub>2</sub> gas. Faradic efficiency is computed for H<sub>2</sub> and O<sub>2</sub> using a similar procedure in the case of 1.0 M KOH.

$$FE(\%) = nF \times \frac{m}{Q} \times 100 \quad \text{Equation 3.7}$$

Where Q = Total Charge

n = No. electrons involved in the reaction, for OER (n = 4) or HER (n = 2)

m = moles of H<sub>2</sub> or O<sub>2</sub> produced

F = 96485 C/mol (Faraday's Constant)

### 3.3.12 ECSA Measurement

The electrochemical surface area (ECSA) of the catalyst in the presence of 1.0 M KOH electrolyte was determined using a three-electrode setup at various scan rates (30, 50, 90, 110, and 130 mV/s) and within the voltage range of 0.725 V to 0.925 V<sub>RHE</sub>. The ECSA was also computed using double-layer capacitance. The double-layer capacitance was determined using the  $\Delta j/2$  vs. scan rate plot; the  $C_{dl}$  value was the product of the slope of the curve and the electrode's area. By multiplying the  $C_{dl}$  value by the inverse of the electrode's specific capacitance ( $C_s$ ), ECSA was calculated. In this case, the standard value of  $C_s$  is 40  $\mu\text{F cm}^{-2}$ . [227]

$$ECSA = \frac{C_{dl}}{C_s} \quad \text{Equation 3.8}$$

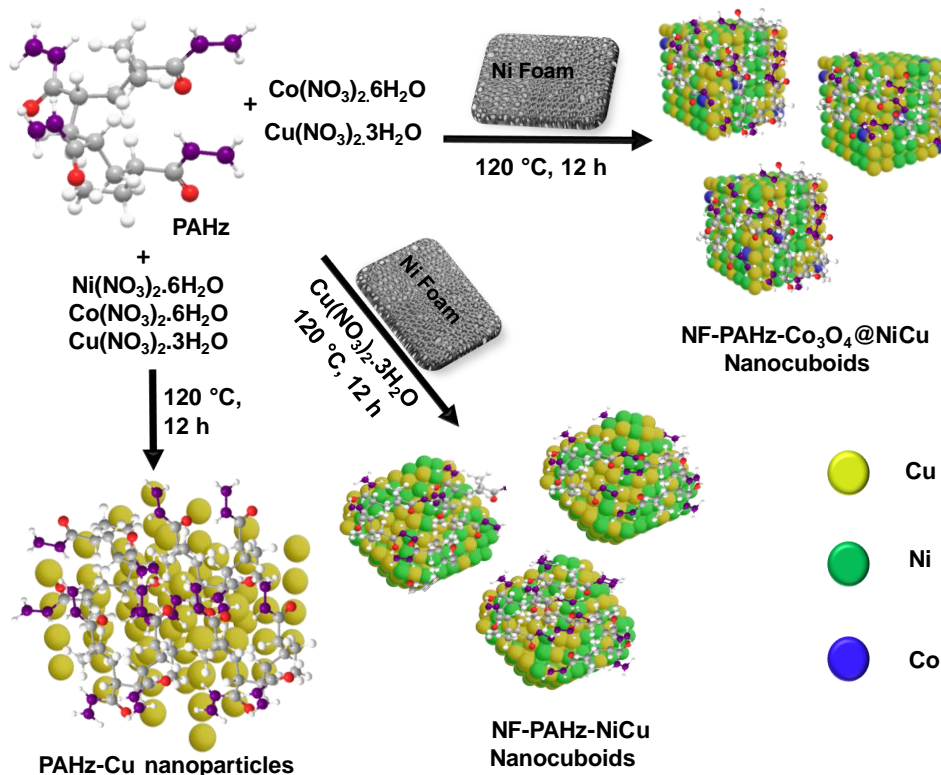
### 3.3.13 Product Analysis

200  $\mu\text{L}$  of electrolyte and 200  $\mu\text{L}$  of D<sub>2</sub>O were carefully mixed in an NMR tube to analyze the product in the electrolyte. After that, the mixture was well combined. The integration ratio of the signal ascribed to formate was then obtained by an NMR analysis.

## 3.4 Results and Discussion

The NF-PAHz-Co<sub>3</sub>O<sub>4</sub>@NiCu alloy nanocuboids were created by hydrothermally treating Cu(NO<sub>3</sub>)<sub>2</sub>·3H<sub>2</sub>O and Co(NO<sub>3</sub>)<sub>2</sub>·6H<sub>2</sub>O in equimolar amounts in PAHz aqueous solution with an NF piece (**Scheme 3.1**). As has been previously documented in the literature for other systems, NF acted as the Ni source to aid in the hydrothermal creation of the aforementioned alloy nanocuboids. [228,229] To comprehend the development process,

control samples, absence of NF (PAHz-Cu) and  $\text{Co}^{2+}$  (NF-PAHz-NiCu) were also produced.  $2\theta$  peaks at  $43.41^\circ$ ,  $50.56^\circ$ , and  $74.20^\circ$  on the X-ray diffraction (XRD) trace of NF-PAHz- $\text{Co}_3\text{O}_4$ @NiCu are attributed to the 111, 200, and 220 planes of Cu(0), respectively (**Figure 3.1A**). When compared to the Cu(0)-JCPDS, the  $2\theta$  value for 111 shifted by  $0.12^\circ$ , indicating a potential production of NiCu alloy (**Figure 3.1B**). [230] The XRD trace showed peaks at  $36.59^\circ$ ,  $38.49^\circ$ , and  $59.03^\circ$ , which were attributed to the  $\text{Co}_3\text{O}_4$  dopant's 311, 222, and 511 planes, respectively. In **Figure 3.1A**, the peaks corresponding to Ni(0) and the NF were located at  $44.51$  (111),  $51.86$  (200), and  $76.38^\circ$  (220). The NiCu alloy formation was supported by the  $2\theta$  peaks in the XRD data of the control (NF-PAHz-NiCu) produced without  $\text{Co}^{2+}$ , which corresponded to Cu(0) and Ni(0) in locations comparable to those of the NF-PAHz- $\text{Co}_3\text{O}_4$ @NiCu (**Figure A25**).



**Scheme 3.1:** The synthesis of different nanostructures with and without NF is shown in the schematic method.

Nevertheless, the PAHz-Cu sample that was synthesized without NF showed only two peaks, 2 $\theta$ , that corresponded to Cu(0). No peaks attributable to Co<sub>3</sub>O<sub>4</sub> or Ni(0) were visible, indicating that PAHz-Cu composite was formed and that Ni<sup>2+</sup> and Co<sup>2+</sup> may not have been able to participate in the formation of nanoparticles (**Figure A25**). A pair of peaks at 932.7 and 952.5 eV in the Cu 2p X-ray photoelectron spectroscopy (XPS) data indicated the existence of Cu(0) in the NF-PAHz-Co<sub>3</sub>O<sub>4</sub>@NiCu (**Figure 3.1C**). [231] Spectra also showed a small signal at 934.3 eV that corresponded to the oxidized form (CuO). Crucially, throughout the characterisation process, Cu(0) is known to oxidize in air. This oxidized peak was small in Cu 2p spectra. [232] Peaks at 852.8 and 870.1 eV were identified in the Ni 2p XPS data as being related to the Ni(0) found in the NF-PAHz-Co<sub>3</sub>O<sub>4</sub>@NiCu (**Figure 3.1D**). In addition, there were slight variations in the peak positions of the Cu 2p (-0.30 eV) and Ni 2p (0.17 eV) when compared to the pure single metal system that underpinned the alloy formation. [233,202] Prominent peaks in the Co 2p XPS spectra were seen at 781.8 and 779.3 eV, indicating the existence of Co<sup>2+</sup> and Co<sup>3+</sup> in Co<sub>3</sub>O<sub>4</sub>, respectively (**Figure 3.1E**). [234] The existence of Co<sub>3</sub>O<sub>4</sub> in the sample was corroborated by the O 1s signal at 531.2 eV. [235] The existence of PAHz in the sample was corroborated by the N 1s peaks at 399.0 (NH) and 400.1 eV (C-N), the C 1s peaks at 284.8 (C-C), 286.4 (C-N), and 288.3 eV (C=O), and the O 1s peak at 532.8 eV (C=O) (**Figures 3.1F, A26**). [236,237,238]

Ni 2p and Cu 2p peaks at 852.6 and 932.7 eV, corresponding to Ni(0) and Cu(0), respectively, were seen in the XPS data of NF-PAHz-NiCu, indicating a potential structural similarity with NF-PAHz-Co<sub>3</sub>O<sub>4</sub>@NiCu (**Figure A27**). The second control, PAHz-Cu, showed a Cu 2p peak at 932.9 eV, indicating that Cu<sup>2+</sup> may have been reduced to Cu(0) and that a PAHz-Cu nanocomposite may have formed (**Figure A28**). Remarkably, the Ni 2p peaks at 853.6 and 855.7 eV were seen, indicating the existence

of  $\text{Ni}^{2+}$  and  $\text{Ni}^{3+}$  as well as the potential for Ni oxide production under the given circumstances (**Figure A28**).

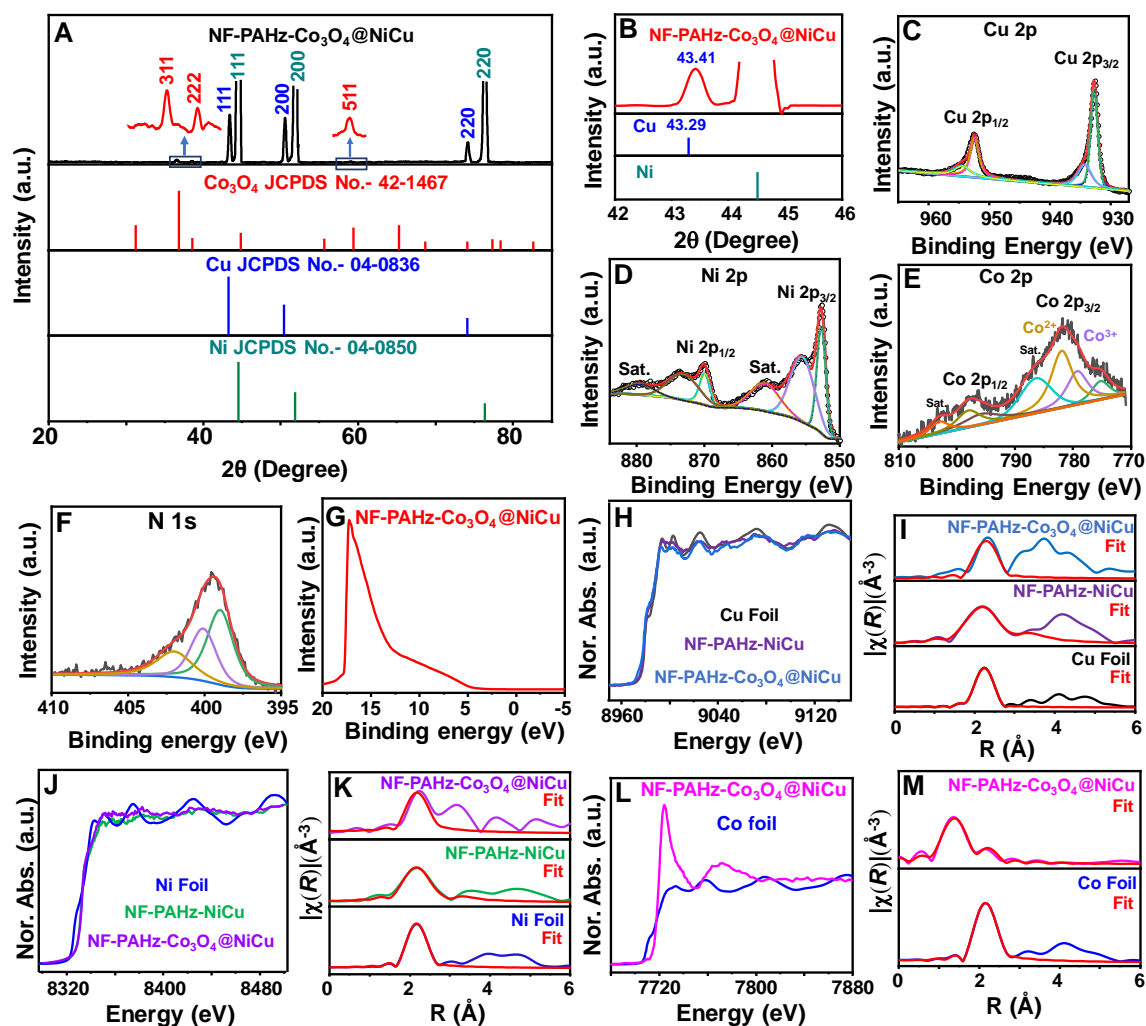


**Figure 3.1:** (A) The NF-PAHz- $\text{Co}_3\text{O}_4$ @NiCu XRD data and the associated JCPDS traces, (B) the XRD traces in "A" magnified in the  $42\text{--}46^\circ$   $2\theta$  region; (C) the Cu 2p, (D) Ni 2p, (E) Co 2p, and (F) N 1s XPS spectra of NF-PAHz- $\text{Co}_3\text{O}_4$ @NiCu, (G) the UPS spectra of NF-PAHz- $\text{Co}_3\text{O}_4$ @NiCu, the Cu K-edge (H) XANES and (I) Fourier transformed (FT)-EXAFS spectra; the Ni K-edge (J) XANES and (K) FT-EXAFS spectra; the Co K-edge (L) XANES and (M) FT-EXAFS spectra.

The work function values of the catalysts were determined by analyzing the data from Ultraviolet Photoelectron Spectroscopy (UPS) (**Figures 3.1G & A29**). The NF-

PAHz-Co<sub>3</sub>O<sub>4</sub>@NiCu and NF-PAHz-NiCu were found to have work function values of 4.19 and 5.02 eV, respectively. Work function values for already-active electrodes that demonstrate competency in OER and MOR activities are comparable in the literature. [239, 240] The curve coincided with the Cu foil's at the near edge area of the Cu K-Edge X-ray absorption near edge structure (XANES) data, indicating the existence of Cu(0) in NF-PAHz-Co<sub>3</sub>O<sub>4</sub>@NiCu. The Cu K-edge data of NF-PAHz-NiCu also showed a similar pattern, confirming the similarity in Cu oxidation state between the two samples mentioned above. Cu-Cu bond exists at 12 coordination with radial distances of 2.57 Å in NF-PAHz-Co<sub>3</sub>O<sub>4</sub>@NiCu and 2.54 Å in NF-PAHz-NiCu, which is near to that of the Cu foil (2.54 Å) according to the Cu K-edge Fourier transformed extended X-ray absorption fine structure (FT-EXAFS) data (**Figure 3.1H-1I**). [241] When compared to the Ni foil, the Ni K-edge location at half-maximum of absorption for NF-PAHz-Co<sub>3</sub>O<sub>4</sub>@NiCu and NF-PAHz-NiCu showed a little up-field shift, which may indicate a change in the oxidation state of Ni(0) (**Figure 3.1J**). The air oxidation of the Ni in the sample during handling might be the cause of the relatively tiny shift, which makes the change in oxidation state low (< +1). [242] The Ni-Ni bond is present at 12 coordination with a radial distance of 2.49 Å in NF-PAHz-Co<sub>3</sub>O<sub>4</sub>@NiCu and 2.48 Å in NF-PAHz-NiCu, which is comparable to that of the Ni foil (2.48 Å) (**Figure 3.1K**), according to the significant Ni K-edge FT-EXAFS data. [243] In contrast, the near edge area of the Co K-edge data showed a significant shift of 5.9 eV, indicating the existence of Co<sub>3</sub>O<sub>4</sub> in NF-PAHz-Co<sub>3</sub>O<sub>4</sub>@NiCu (**Figure 3.1L**). [244] The Co-O in NF-PAHz-Co<sub>3</sub>O<sub>4</sub>@NiCu was found to be present at 4 coordination with a radial distance of 1.98 Å, according to the Co K-edge FT-EXAFS data. This is 0.51 Å less than the Co foil's radial distance of 2.49 Å (**Figure 3.1M**). [245] Overall, the suggested structures of the NF-PAHz-Co<sub>3</sub>O<sub>4</sub>@NiCu and control samples were validated by the XRD, XPS, and XANES data. It's possible

that when a moderate reducing agent (PAHz) is present, the  $\text{Cu}^{2+}$  with a positive reduction potential ( $E^\circ$ ): ( $\text{Cu}^{2+}/\text{Cu} \approx +0.34 \text{ V}$ ) preferentially transforms into the corresponding  $\text{Cu}(0)$ , whereas the  $\text{Co}^{2+}$  with an oxidation-prone tendency ( $E^\circ$ :  $\text{Co}^{2+}/\text{Co} \approx -0.28 \text{ V}$ ) forms the corresponding oxide ( $\text{Co}_3\text{O}_4$ ). [246] Under moderate temperature conditions,  $\text{Cu}^{2+}$  and  $\text{Ni}^{2+}$  in the presence of hydrazine are known to produce  $\text{Cu}(0)$  and  $\text{Ni}(0)$ , respectively [247,248], however  $\text{Co}^{2+}$  needs a considerably stronger base, such as  $\text{NaOH}$ , in addition to hydrazine to form the equivalent  $\text{Co}(0)$ . [249] Whereas in the absence of NF the PAHz-Cu nanocomposite was separated and the amorphous oxides of Ni and Co that may have formed throughout the process stayed in the aqueous phase, the presence of NF allowed the  $\text{Ni}(0)$  from the NF surface to participate in the NiCu alloy nanocuboid production.

The result was followed by an examination utilizing Field Emission Scanning Electron Microscopy (FESEM) to investigate the morphology of NF-PAHz- $\text{Co}_3\text{O}_4@ \text{NiCu}$ . **Figure 3.2A–B** shows the irregular cuboid-type shape of the NF-PAHz- $\text{Co}_3\text{O}_4@ \text{NiCu}$ . These cuboids were found to have an average diameter of around 220 nm (**Figure A30**). To determine the repeatability of the size and form of these nanocrystals, another batch of NF-PAHz- $\text{Co}_3\text{O}_4@ \text{NiCu}$  was created. The next batch replicated the homogeneous cuboid forms well (**Figure A31**). According to the FESEM-EDX results, the Cu content of the NF-PAHz- $\text{Co}_3\text{O}_4@ \text{NiCu}$  is a little bit higher than the Ni content (8.8%). The sample included a comparatively small quantity of the Co (0.3%) dopant (**Figure A32**). The existence of PAHz chains in the sample was confirmed by the significant concentrations of C (53.7%), N (14.0%), and O (10.0%), which may have acted as a capping agent and encouraged the coalescence of NiCu alloy nanoparticles. With an average particle size ( $D_{\text{avg}}$ ) of 212 nm, the control sample (NF-PAHz-NiCu), which was produced without  $\text{Co}^{2+}$ , also showed cuboid shape of different sizes (**Figure**

**3.2C, Figure A33**). Nonetheless, the PAHz-Cu control, which was synthesized without NF and using distinct salts ( $\text{Cu}^{2+}$ ,  $\text{Ni}^{2+}$ , and  $\text{Co}^{2+}$ ) in the reaction medium, did not exhibit any distinct morphology. This suggests that, in experimental conditions, the NF surface may have served as a nucleating site and encouraged the formation of NiCu alloy cuboids (**Figure 3.2D, Figure A34**). NF-PAHz- $\text{Co}_3\text{O}_4$ @NiCu was then subjected to High-Resolution Transmission Electron Microscopic (HRTEM) data recording. The SEM findings were supported by images, which showed cuboids of various sizes ( $D_{\text{avg}} = 194$  nm) (**Figure 3.2E-F, Figure A35**). It's interesting to note that each of these cuboids had NiCu alloy nanocrystals ranging in size from 3 to 6.5 nm ( $D_{\text{avg}} = 5$  nm), which may have undergone segregation assisted by PAHz to take on their final form (**Figure A36**). The production of NiCu alloy was supported by the d spacing value of 0.205 nm, which corresponded to the [111] plane and was midway between Ni(0) (0.203 nm) and Cu(0) (0.209 nm) (**Figure 3.2G-H**). [250,251] The crystallinity of these PAHz- $\text{Co}_3\text{O}_4$ @NiCu nano-cuboids was supported by the well-resolved diffraction pattern shown in the selected area electron diffraction (SAED) picture. The picture showed the [111], [200], and [220] planes for the NiCu alloy and the [311] plane for the  $\text{Co}_3\text{O}_4$ . (**Figure 3.2I**). The NF-PAHz- $\text{Co}_3\text{O}_4$ @NiCu cuboids were found to contain a significant quantity of Cu, followed by Ni and Co, according to findings from high-angle annular dark-field scanning transmission electron microscopy (HAADF-STEM) (**Figure 3.2J-P**).

Significant amounts of N, C, and O provided further evidence that these cuboid matrices included PAHz chains. Overall, the characterization data points to the formation of NiCu alloy-based cuboids on the surface by both the PAHz chains and the Ni surface.

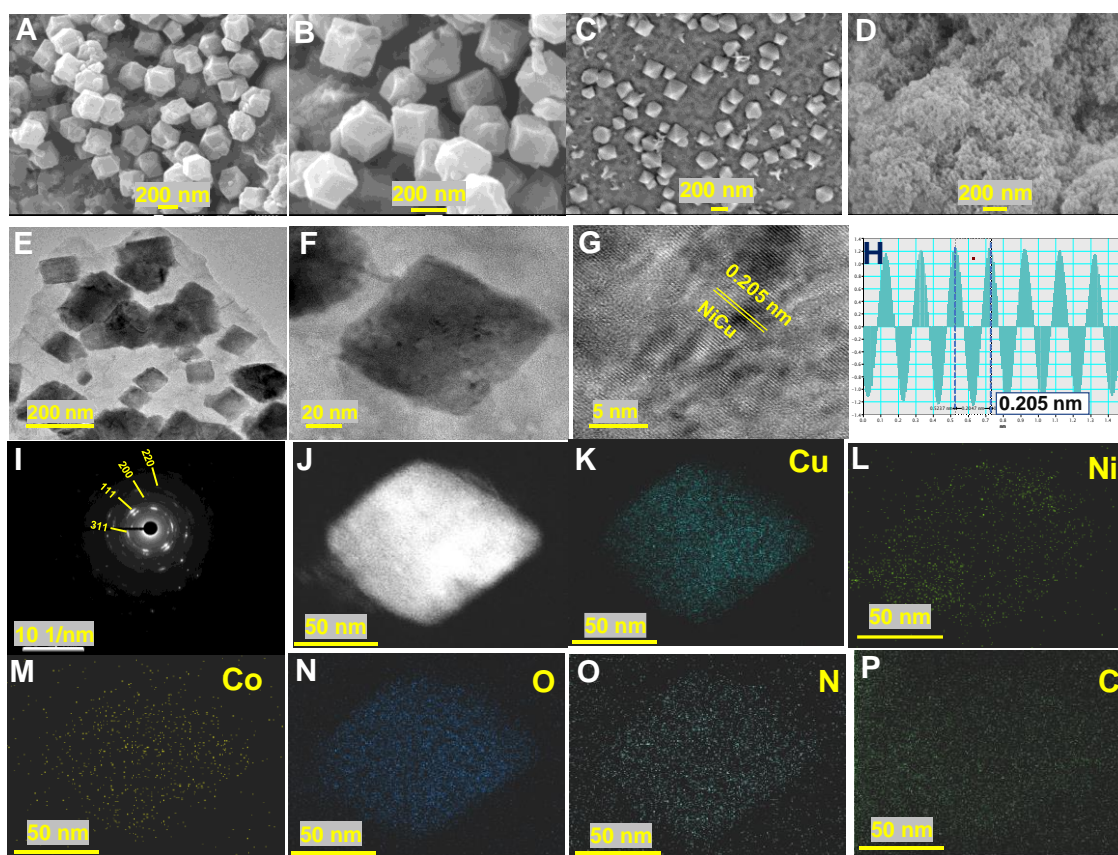


**Figure 3.2:** (A & B) NF-PAHz-Co<sub>3</sub>O<sub>4</sub>@NiCu FESEM images at various magnifications, (C) NF-PAHz-NiCu & (D) PAHz-Cu FESEM images, (E & F) NF-PAHz-Co<sub>3</sub>O<sub>4</sub>@NiCu TEM images at various magnifications, (G) the d spacing value of PAHz-Co<sub>3</sub>O<sub>4</sub>@NiCu and (H) the corresponding inverse fast fourier transform (IFFT) data, (I) the TEM diffraction pattern of PAHz-Co<sub>3</sub>O<sub>4</sub>@NiCu, and (J to P) the HAADF-STEM elemental mapping of PAHz-Co<sub>3</sub>O<sub>4</sub>@NiCu.

It is known that co-reduction of many metal salts results in the formation of alloy nanoparticles in aqueous solution. [252] Moreover, under hydrothermal circumstances, it is known that Ni(0) in the presence of Cu<sup>2+</sup> would undergo a redox reaction to generate Ni<sup>2+</sup> and Cu(0). [253] It is well known that PAHz can quickly convert different metal salts into the matching PAHz-capped metal nanoparticles in aqueous solution and self-assemble to form spherical aggregates in aqueous solution.[254] In light of the

aforementioned elements, a tenable mechanism for the potential creation of a NiCu alloy in the PAHz matrix is put forward, taking into account the reaction circumstances (**Figure A37**).<sup>[205,206,209]</sup> On the other hand, random-morphology PAHz-Cu composites were observed in the absence of NF. The NF-PAHz-Co<sub>3</sub>O<sub>4</sub>@NiCu was synthesized in the presence of 4 and 6wt% PAHz solutions to better understand the impact of PAHz concentration on the sizes and shapes of the resultant nanostructures. Similar to the 2wt% solution, cuboid structures were seen in the FESEM images in both instances (**Figures 3.2A, A38**). Nevertheless, it was found that in every instance, these cuboids' diameters varied. Additionally, the NF-PAHz-Co<sub>3</sub>O<sub>4</sub>@NiCu was produced with varying concentrations of [Cu<sup>2+</sup>]. The resultant sample had a cuboid form and an average size that slightly shrank to 208 nm when the concentration of [Cu<sup>2+</sup>] was increased from 16.5 to 24.8 mM in solution (**Figure A39**). Nevertheless, no cuboid shape development was seen at low [Cu<sup>2+</sup>] (8.2 mM) concentration in solution, and the resultant sample showed up as a cluster of nanoparticles with an average size of around 162.7 nm (**Figure A40**). It was predicted that the exposed conspicuous [111] plane and these sharply edged nanocuboids would demonstrate rapid electrocatalytic activity. <sup>[255,256]</sup>

Then, by examining MOR and OER processes, the electrodes' electrocatalytic activity was evaluated. The working and counter electrodes for the MOR activities were graphite and NF-PAHz-Co<sub>3</sub>O<sub>4</sub>@NiCu, respectively, in 1.0 M KOH and 1.0 M MeOH aqueous solutions. The electrode had exceptional MOR activity, and at a potential value of 1.41 V<sub>RHE</sub>, a *j* value of 100 mA/cm<sup>2</sup> was achieved (**Figure 3.3A**). While the PAHz-Cu failed to create a *j* value of 100 mA/cm<sup>2</sup> until 2.0 V<sub>RHE</sub>, the NF-PAHz-NiCu obtained a comparable *j*<sub>MOR</sub> value at a higher potential of 1.46 V<sub>RHE</sub>, indicating that the Co<sub>3</sub>O<sub>4</sub> doping and the nanocatalyst's structure may have encouraged the MOR activity. The value for NF-PAHz-Co<sub>3</sub>O<sub>4</sub>@NiCu (28.5 cm<sup>2</sup>) is superior to that of NF-PAHz-NiCu (16.8

cm<sup>2</sup>), indicating the higher activity of the former, according to the electrochemical active surface area (ECSA) data (**Figure A41-A42, Table A7**). Comparably, in 1.0 M KOH solution, the NF-PAHz-Co<sub>3</sub>O<sub>4</sub>@NiCu electrode showed sufficient OER activity, and at 1.65 V<sub>RHE</sub>, a  $j_{\text{OER}}$  value of 100 mA/cm<sup>2</sup> was noted. Significantly, at 100 mA/cm<sup>2</sup>, the potential value was 0.24 V lower than the  $j_{\text{MOR}}$ , indicating the higher energy efficiency of the MOR process (**Figure 3.3B**). At a high  $j$  value of 300 mA/cm<sup>2</sup>, the potential difference value (0.28 V) between MOR and OER was more noticeable. The MOR process achieved a  $j_{\text{MOR+HER}}$  value of 100 mA/cm<sup>2</sup> at 1.78 V<sub>RHE</sub> overall potential, whereas the OER-based process achieved the same value at 2.02 V. This indicates that the MOR process is a more energy-efficient choice for producing green H<sub>2</sub> (**Figure 3.3C**). The performance of the NF-PAHz-Co<sub>3</sub>O<sub>4</sub>@NiCu MOR ( $j_{10}$  at 1.37 V<sub>RHE</sub>) and OER ( $j_{10}$  at 1.52 V<sub>RHE</sub>) activities were similar to those of the benchmark IrO<sub>2</sub> ( $j_{10}$ , MOR at 1.37 V<sub>RHE</sub> and  $j_{10}$ , OER at 1.54 V<sub>RHE</sub>), indicating that the produced electrodes are effective for related applications (**Figure A43**). The  $j_{\text{MOR}}$  value achieved at 1.5 V<sub>RHE</sub> for many catalyst compositions published in the literature was compared to that of the NF-PAHz-Co<sub>3</sub>O<sub>4</sub>@NiCu. In comparison to some previously published systems, the current electrode's  $j_{\text{MOR}}$  value (448 mA/cm<sup>2</sup>) was higher (**Figure 3.3D, Table A8**). When the MOR activity stability of NF-PAHz-Co<sub>3</sub>O<sub>4</sub>@NiCu was evaluated, the chronoamperometry data at a potential value of 1.42 V<sub>RHE</sub> showed a little decline in activity (~20%) over 30 hours, indicating sufficient durability (**Figure 3.3E**). The slow drop in MeOH content in the electrolyte over time may be the cause of the aforesaid little reduction in  $j$  value. [257] Crucially, the OER durability data at potential = 1.62 V<sub>RHE</sub> showed that there was no change in  $j$  value over 30 hours, hence confirming the electrode's sustainability for both processes.

The greater activity of the former was confirmed by the low MOR Tafel slope value (36.1 mV/dec) of NF-PAHz-Co<sub>3</sub>O<sub>4</sub>@NiCu in comparison to that of PAHz-Cu (122.3 mV/dec) and NF-PAHz-NiCu (42.5 mV/dec) (**Figure 3.3F**). Comparing the NF-PAHz-Co<sub>3</sub>O<sub>4</sub>@NiCu Nyquist plots to that of NF-PAHz-NiCu (R<sub>s</sub> of MOR: 2.9 Ω), the latter showed solution resistance (R<sub>s</sub>) values of 2.8 and 3.3 Ω for MOR and OER activities, respectively. This suggests that Co<sub>3</sub>O<sub>4</sub> doping may play a role in enhancing conductivity (**Figure 3.3G**). According to the research, 1.92 V is the total voltage needed to complete the operation at  $j = 300 \text{ mA/cm}^2$  with MOR acting as the anode half reaction. This is 0.28 V more than what is needed for the traditional OER-based process (**Figure 3.3H**). These investigations clearly showed how the NF-PAHz-Co<sub>3</sub>O<sub>4</sub>@NiCu can efficiently generate MOR-promoted green H<sub>2</sub>. Additionally, the Co<sub>3</sub>O<sub>4</sub> doping, the form of the nanocuboids, and the Cu active site worked in concert to contribute to the above-mentioned enhanced catalytic activity of NF-PAHz-Co<sub>3</sub>O<sub>4</sub>@NiCu. In contrast to the 2 wt% electrode ( $j_{100, \text{MOR}} = 100 \text{ mA/cm}^2$  at 1.41 V<sub>RHE</sub>), no appreciable difference in the MOR activities of the NF-PAHz-Co<sub>3</sub>O<sub>4</sub>@NiCu electrodes synthesized in the presence of larger PAHz quantities (4 and 6 wt%) was seen (**Figure A44, Table A9**). The OER activities also showed a similar pattern for the electrodes that were manufactured with varying concentrations of PAHz in solution. It is noteworthy that the electrode produced using a 6-weight percent PAHz solution exhibited somewhat higher HER activity in comparison to the other compositions. After comparing the MOR, OER, and HER data of all the compositions, it was determined that the electrode that was created with 2 weight percent PAHz (NF-PAHz-Co<sub>3</sub>O<sub>4</sub>@NiCu) could be useful for further applications. Then, the catalytic activities of NF-PAHz-Co<sub>3</sub>O<sub>4</sub>@NiCu, which was produced with varying concentrations of Cu<sup>2+</sup>, were evaluated. NF-PAHz-Co<sub>3</sub>O<sub>4</sub>@NiCu exhibited

slightly stronger MOR and OER activities than the other compositions produced at lower (8.3 mM) and higher (24.8 mM)  $\text{Cu}^{2+}$  levels (**Figure A45, Table A10**).

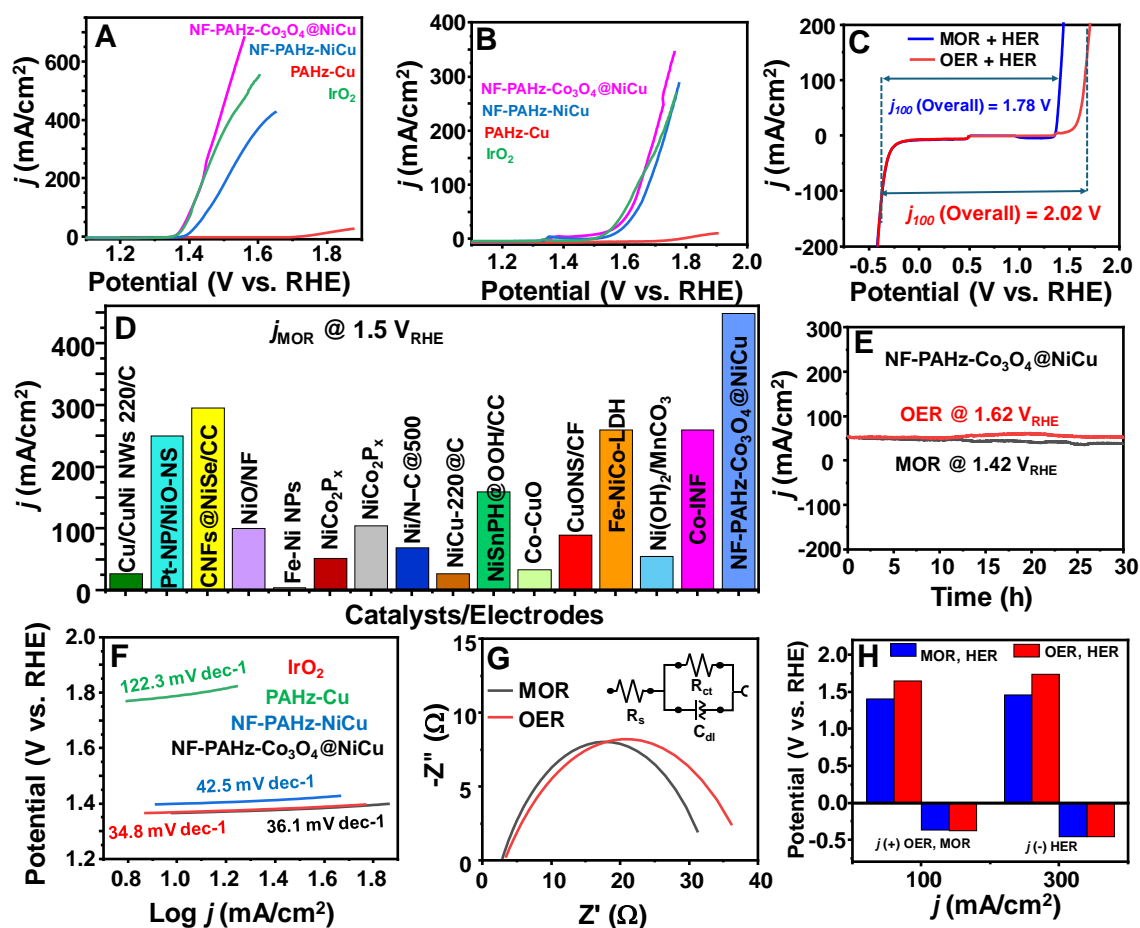


**Figure 3.3:** (A) The MOR and (B) OER lsv traces of NF-PAHz-Co<sub>3</sub>O<sub>4</sub>@NiCu, control, and reference electrodes in 1M KOH + 1M MeOH with 5 mV/s scan rate and electrode area of 0.25 cm<sup>2</sup> (C) the overall water splitting curves of NF-PAHz-Co<sub>3</sub>O<sub>4</sub>@NiCu MOR and OER-based processes, (D) the comparison of the MOR  $j$  value at 1.5 V<sub>RHE</sub> of NF-PAHz-Co<sub>3</sub>O<sub>4</sub>@NiCu with that of the recently reported systems, (E) the chronoamperometry traces of NF-PAHz-Co<sub>3</sub>O<sub>4</sub>@NiCu demonstrating the stability of MOR and OER; (F) the Tafel slope values of NF-PAHz-Co<sub>3</sub>O<sub>4</sub>@NiCu and controls recorded for MOR process, (G) the Nyquist fits of NF-PAHz-Co<sub>3</sub>O<sub>4</sub>@NiCu obtained

during MOR and OER operation; and (H) the comparison of  $j$  and potential values between MOR and OER operations for NF-PAHZ-Co<sub>3</sub>O<sub>4</sub>@NiCu.

Crucially, when compared to the other compositions, the electrode produced with 24.8 mM Cu<sup>2+</sup> exhibited higher HER activity. Overall, based on the overall catalytic activity and synthesis cost, the NF-PAHZ-Co<sub>3</sub>O<sub>4</sub>@NiCu produced with Cu<sup>2+</sup> = 16.5 mM was superior to the other compositions.

Subsequently, the procedures were executed in a two-electrode mode to replicate the electrolyzer configuration (**Figure 3.4A**). At 1.62 V, the  $j_{MOR}$  value of 10 mA/cm<sup>2</sup> was reached, whereas the OER-based approach achieved the same  $j$  value at 1.76 V (**Figure 3.4B**). The  $j_{MOR+HER}$  value (10 mA/cm<sup>2</sup>) over 100 hours showed no discernible change in the chronoamperometry data obtained at 1.62 V, indicating the electrode's durability (**Figure 3.4C**). NF-PAHZ-Co<sub>3</sub>O<sub>4</sub>@NiCu was used as the working and counter electrodes in a 2-electrode mode to test the stability of the OER-based process. The findings supported the statement by showing no discernible change in the  $j_{OER+HER}$  value for 100 hours (**Figure 3.4D**). Finally, it was determined that the generated H<sub>2</sub> in the two-electrode mode for MOR had a faradaic efficiency value of 93.2% (**Figure 3.4E**). The OER-based procedure's faradaic efficiencies for producing H<sub>2</sub> and O<sub>2</sub> were likewise successful (**Figure 3.4F**). <sup>1</sup>H Nuclear Magnetic Resonance (NMR) examination of the electrolyte in D<sub>2</sub>O was done in order to comprehend the product or products created during the MOR. The production of formate in the solution was corroborated by a new singlet for H-COO<sup>-</sup> at 8.3 ppm (**Figure 3.4G**). Upon analyzing the integrations of resonances at 3.1 ppm (H<sub>3</sub>C-OH) and 8.3 ppm, it was observed that about 71.6% conversion was achieved after 96 hours of MOR operation (**Figure A46**). [258] Crucially, the spectra showed no further peaks that would have supported the product

formation's selectivity. The generation of formate during the electrochemical process was corroborated by  $^{13}\text{C}$  NMR Peaks at 171 and 168 ppm, which correspond to  $\text{HCOO}^-$  and  $\text{HCOOH}$ , respectively. The formate formation was further corroborated by the Fourier-transform infrared (FT-IR) band at  $1639\text{ cm}^{-1}$  for  $\text{C}=\text{O}$ . (**Figure 3.4 H**).

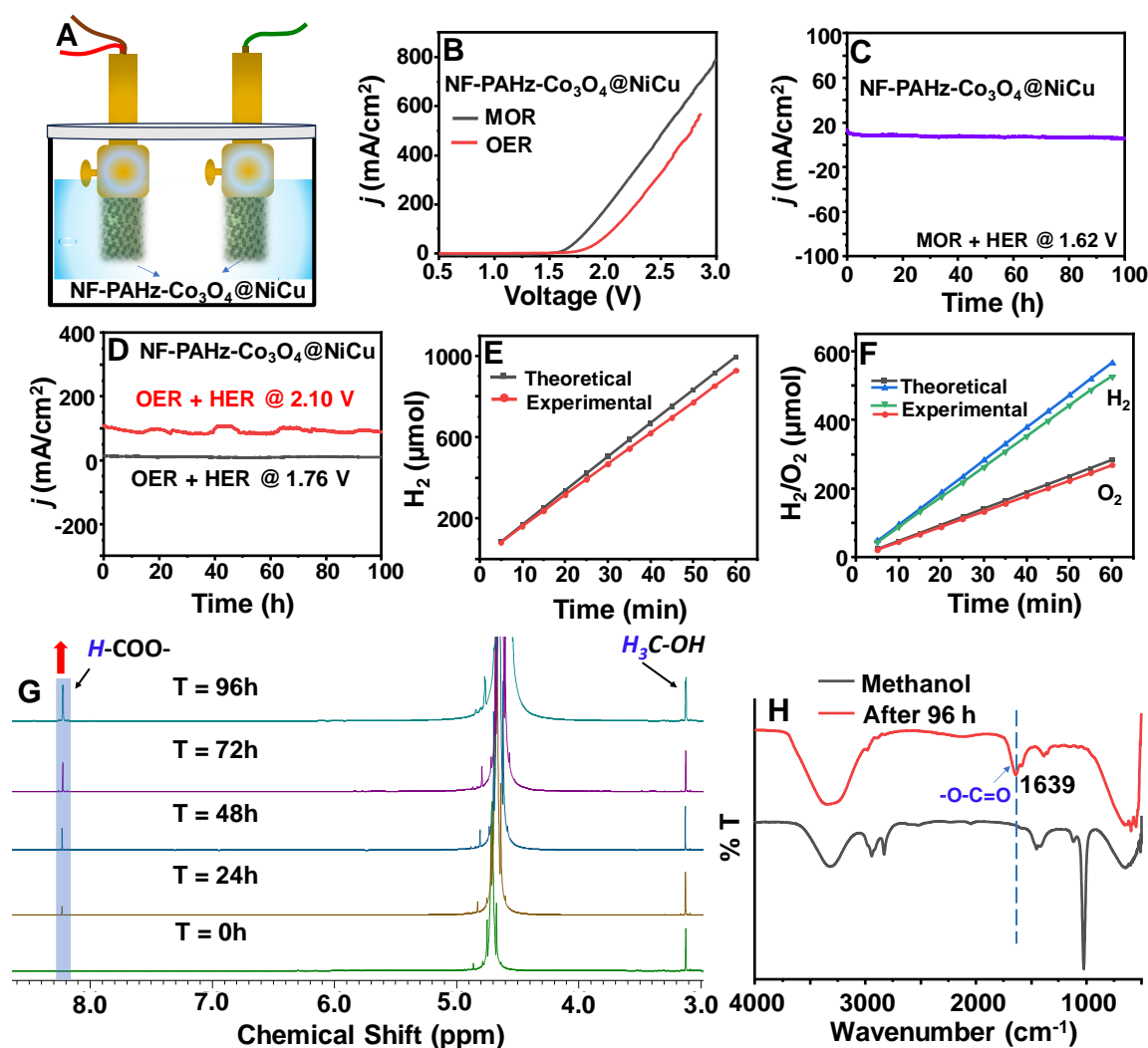


**Figure 3.4:** (A) The schematics of the two-electrode electrochemical setup for MOR coupled H<sub>2</sub> production using NF-PAHz-Co<sub>3</sub>O<sub>4</sub>@NiCu as the working and counter electrodes, (B) the linear sweep voltammetry (LSV) for OER and MOR based procedures in the two-electrode setup in 1M KOH + 1M MeOH with 5 mV/s scan rate and electrode area of 0.25 cm<sup>2</sup> (C) the chronoamperometry trace of the MOR based process recorded at 1.62 V and (D) the OER based process recorded at 1.76 and 2.10 V in the two-electrode

setup, (G) the electrolyte solution's  $^1\text{H}$  NMR and (H) FT-IR spectra recorded after regular intervals during MOR operation.

The electrolyte's  $^{13}\text{C}$  NMR spectra were obtained at various time intervals to investigate the probability of CO/CO<sub>2</sub> production throughout the procedure. Remarkably, the lack of resonance at 162 ppm most likely ruled out the chance that CO<sub>2</sub> was formed throughout the process (**Figure A47**). [259]

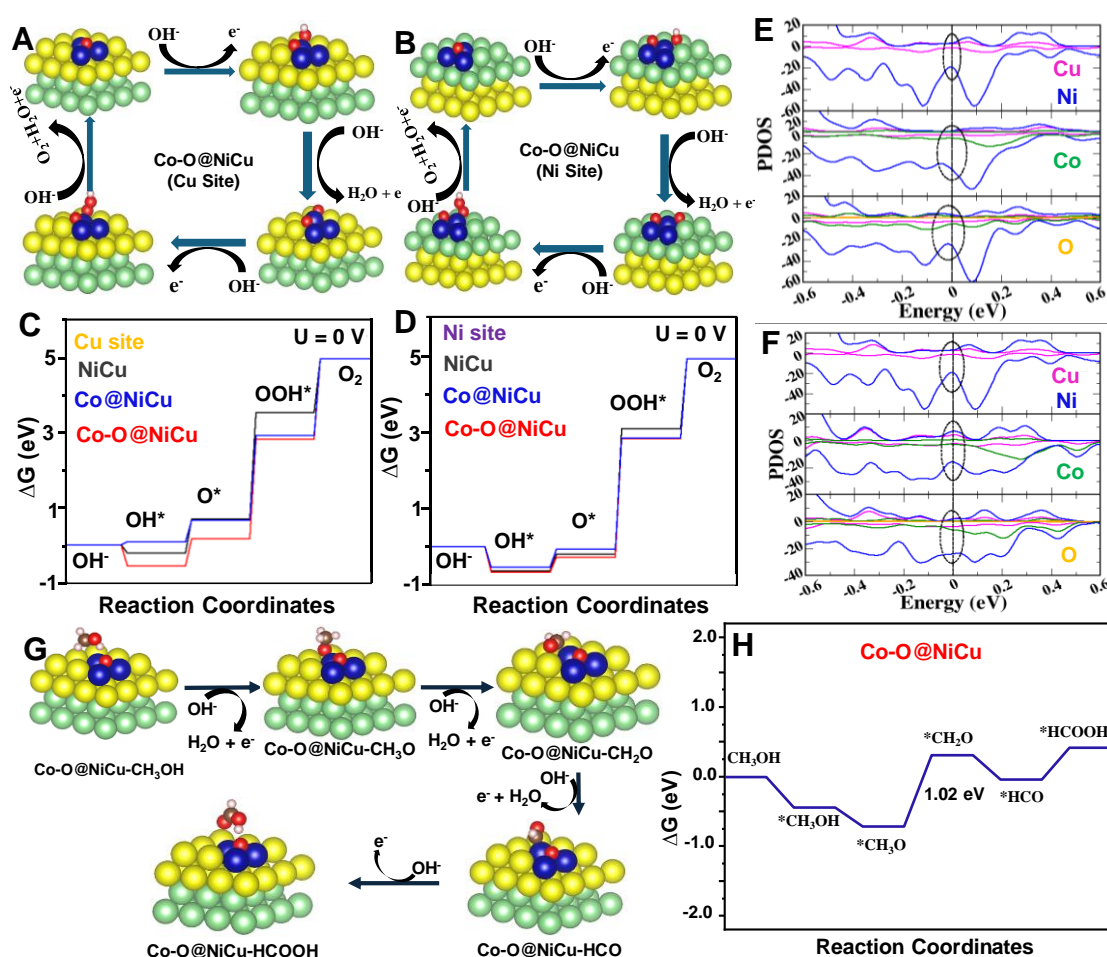


**Figure 3.5:** Diagrams of the OER activity of the Co-O doped on the (A) Cu and (B) Ni sites of Co-O@NiCu, Gibb's free energy diagrams for the OER activities of NiCu, Co@NiCu, and Co-O@NiCu calculated for (C) Cu site and (D) Ni site, respectively, PDOS of NiCu, Co@NiCu, and Co-O@NiCu obtained for (E) Cu site and (F) Ni site,

(G) illustrating the different steps of MOR activity on the Co-O@NiCu operated at Cu site, and (H) the Gibb's free energy diagrams for the MOR activities on Co-O@NiCu calculated on Cu site. The catalyst's active site is denoted by the symbol \*, and the species adsorbed on it are represented by the symbols \*CH<sub>3</sub>OH, \*CH<sub>3</sub>O, \*CH<sub>2</sub>O, \*HCO, and \*HCOOH.

Density Functional Theory (DFT) calculations were performed to determine the Gibbs free energy changes ( $\Delta G$ ) of the control electrode and NF-PAHz-Co<sub>3</sub>O<sub>4</sub>@NiCu to get more understanding of the superior activity. The literature-described procedure was used to calculate the  $\Delta G$  values for each of the primary stages at the equilibrium potential of OER. [224,225] To investigate the OER activity on the Ni and Cu sites in the NiCu alloy, Ni (111) and Cu (111) double layers were stacked on top of one another (**Figure A48**). Following the doping of Co and its oxide at the corresponding locations, the  $\Delta G$  profile was evaluated (**Figure 3.5A-B, Figure A49**). [260] **Figure 3.5C-D** displays the  $\Delta G$  profiles for various OER phases where NiCu, Co@NiCu, and Co-O@NiCu play catalytic roles. For every system under study, it was found that the M-O\* to M-OOH\* step determined the rate. The rate-determining step energy barrier of NiCu alloy in the case of OER activity at the Cu site was 2.80 eV; with Co and Co oxide doping, respectively, this value decreased to 2.63 and 2.24 eV (**Figure 3.5C**). Comparably, for OER activity at the Ni site, the  $\Delta G$  value for the rate-determining phase was 3.30 eV; however, with Co and Co oxide doping, it dropped to 2.91 eV and 3.09 eV, respectively (**Figure 3.5D**). Remarkably, the investigation showed that, in contrast to the Ni site, the activity at the Cu site in the NiCu alloy was linked to a reduced  $\Delta G$  value at the rate-determining step (RDS). Furthermore, the Co oxide doping reduced the  $\Delta G$  value even more, confirming the experimental finding and the enhanced OER activity of NF-PAHz-Co<sub>3</sub>O<sub>4</sub>@NiCu. The Co oxide doped at the Cu site had the lowest  $\Delta G$  value (2.24 eV),

suggesting that the Cu site in the NiCu alloy may have acted as the active site to start the OER and MOR processes.

The partial density of states (PDOS) of NiCu and Co & Co oxide doped NiCu were computed to confirm the findings. The inherent metallic properties of both pure and doped NiCu were confirmed by the continuous density of state (DOS) around the Fermi level. In contrast to pure NiCu, the DOS for the Co and Co oxide doped NiCu widened close to the Fermi level. The widening of the DOS at the Fermi level is highest for Co oxide doped NiCu catalyst for both the Ni and Cu active sites (**Figure 3.5E–F**). The charge carrier concentration rose as a result of the addition of Co and O atoms to NiCu, which improved the DOS close to the Fermi level. Therefore, in this case, Co oxide doped NiCu showed more conducting routes and facilitated much quicker electron transfer, giving them faster kinetics and enhanced OER activity. [261] Following that, the MOR activities were computed for Co-O@NiCu in an alkaline environment on the Cu site (**Figure 3.5G**). The rate-determining step (RDS) was found to be the conversion of  $*\text{CH}_3\text{O}$  to  $*\text{CH}_2\text{O}$ . The process was shown to be endothermic by 0.31 eV, with an energy barrier of 1.02 eV (**Figure 3.5H**). [81]

### 3.5 Conclusion

During the hydrothermal PAHz mediated in-situ reduction of Cu and Ni salts to the corresponding NiCu alloy nanocrystals, the metallic Ni surface acts as a shape-directing pathway. The process enables in-situ doping of metal oxides on the alloy surface and NiCu alloy formation in a single pot. The resultant electrodes are ideal for bi-functional MOR and OER coupled energy efficient green  $\text{H}_2$  generation and show rapid MOR and OER activities under alkaline conditions. It is possible that the sharp edges of the nanocuboids,  $\text{Co}_3\text{O}_4$  doping, and the active Cu site in the NiCu heterostructure work in concert to enhance electrocatalytic activity. Using methanol, the NF-PAHz-



This page was intentionally left

## Chapter 4

# Insitu Growth of CeFe doped CeO<sub>2</sub>/Ni<sub>3</sub>S<sub>2</sub> nanorod as highly stable bifunctional electrocatalyst for effective urea oxidation reaction

### 4.1 Abstract

A possible alternative to OER is the electrocatalytic urea oxidation process (UOR), which requires less thermodynamic potential. The lack of efficient catalysts that can get beyond the urea's sluggish kinetic constraints during electrolysis makes it an untapped potential energy source. It is especially crucial to develop inexpensive and highly effective catalysts to speed up the urea oxidation reaction (UOR), since this solves the problems of water pollution and energy constraint. In this study, we grew CeO<sub>2</sub> layered Ni<sub>3</sub>S<sub>2</sub> nanorods on nickel foam with the efficient doping of Fe and Co to create electrocatalysts. Experimental results confirm that Co and Fe doped CeO<sub>2</sub> layer has a major impact on the charge distribution within the Ni<sub>3</sub>S<sub>2</sub> structure. CF-CeO<sub>2</sub>/Ni<sub>3</sub>S<sub>2</sub> catalysts composition showed remarkable qualities, such as greater long-term stability and a reduced potential demand. When tested in a solution of 1.0 M KOH with 0.5 M urea, it obtained a current density of 100 mA cm<sup>-2</sup> at a voltage of just 1.38 V<sub>RHE</sub>. These remarkable results imply that our catalyst system has a lot of potential for real-world urea electrolysis applications, providing an effective way to clean wastewater and produce electricity.

## 4.2 Introduction

The global drive for sustainable energy solutions has accelerated the study of energy conversion and storage technologies that are both economical and ecologically benign. Among these, electrochemical processes have drawn a lot of interest because of their potential for producing useful chemical synthesis and clean energy. [262] In electrocatalysis, the UOR has shown great promise as a flexible and adaptable substitute for the OER process. It provides notable benefits in energy efficiency and real-world applications. The advantage of the UOR over the OER is that the former has a theoretical thermodynamic potential of  $0.37 V_{\text{RHE}}$ , whereas the other one has a potential of  $1.23 V_{\text{RHE}}$ . [263] This low-energy electrolysis method allows urea to break down into nitrogen and carbon dioxide while purifying urea-rich wastewater in an alkaline medium and producing hydrogen at the same time. [264] At first, noble metals were used to improve UOR performance, including ruthenium, iridium, and rhodium. However, there were substantial barriers to their widespread industrial use due to their scarcity and expensive cost. [265,266] Non-noble metal catalysts to overcome these obstacles and create high-performance, commercially viable electrocatalysts. [267] The customizable architecture and surface characteristics of these substitute materials provide new opportunities for improving electrocatalytic performance. To overcome the cost and availability issues with precious metal catalysts by precisely controlling electron transport and mass transfer in these non-noble metal catalysts to achieve equivalent or even better catalytic activity. [268] The study of UOR and OER presents interesting synergies and challenges. Both reactions involve complex multi-electron transfer processes and are sensitive to catalyst surface properties. Understanding the mechanisms of these reactions can lead to the development of bifunctional catalysts capable of efficiently performing both processes, which could be particularly valuable in integrated energy systems. The special characteristics of nickel-based catalysts with respect to UOR have attracted a lot of

interest.[269,270] Lately, many Ni-based materials have been investigated for improving UOR performance: metallic nickel hydroxide nanosheets,[271] porous nickel phosphide nanoflake arrays,[103] and low-dimensional Ni-MOFs.[272] The CeO<sub>2</sub>/CuO shows low overpotentials of 245 mV for HER and 410 mV for OER.[273] . To drive a current density of 100 mA cm<sup>-2</sup>, Ni-CuO NAs/CF needs just a low potential of 1.366 V<sub>RHE</sub> for UOR.[274] The 3D Nanostructured catalyst Ce-CoFe-LDH/NF has a low charge transfer impedance of 2.4 Ω in 1 M KOH electrolyte and an overpotential of 225 mV at 10 mA cm<sup>-2</sup> for OER.[275] hydroxyl-modified Ni<sub>3</sub>S<sub>2</sub> needs a low potential of 1.34 V<sub>RHE</sub> at current density of 100 mA cm<sup>-2</sup> for UOR and stable in alkaline media.[276] The distinct redox characteristics and oxygen-storing capacity of CeO<sub>2</sub> allow it to enhance the electrocatalytic activity of hybrid materials. It offers corrosion resistance and mechanical stability, which are essential for durability during electrocatalysis, particularly in alkaline conditions. The catalyst surface gains more active sites due to the reversible conversion between the Ce<sup>3+</sup> and Ce<sup>4+</sup> states, enhancing overall performance. Dopants such as Co and Fe were added to materials like Ni(OH)<sub>2</sub> and Ni<sub>3</sub>S<sub>2</sub>, which greatly enhanced conductivity and active sites and improved electrocatalytic performance. [277,278] Because of their abundance and catalytic efficiency, nickel-based materials especially nickel sulfides like Ni<sub>3</sub>S<sub>2</sub> show promise; nevertheless, more research is needed to see how well they work in UOR. In 1.0 M KOH with 0.5 M urea solution, Mn-Ni<sub>3</sub>S<sub>2</sub>/NF catalyst achieves a current density of 100 mA cm<sup>-2</sup> at a voltage of just 1.397 V<sub>RHE</sub>.[279] Mo-doped Ni<sub>3</sub>S<sub>2</sub> nanocluster arrays on Nickel foam (Mo-Ni<sub>3</sub>S<sub>2</sub>/NF) have been developed with a modified one-step solvothermal technique, needing just 212 and 291 mV of overpotential to provide OER current densities of 10 and 100 mA cm<sup>-2</sup> in alkaline seawater, respectively.[280] The Ni<sub>3</sub>S<sub>4</sub> electrocatalyst's Ni-S coordination is improved by CeO<sub>2</sub>, which results in stronger electronic contacts and better kinetics for the UOR.

Here electrocatalysts are created using the combination of two reducing agents. The material's catalytic activity is increased by the sulfide based reducing agent, while the reducing sugar used as a carbon source which helps to build a stable nanostructure and enhance the catalytic activity. [281]

### **4.3 Experimental Section**

#### **4.3.1 Material Requirements**

Cerium (III) nitrate hexahydrate (98% gma Aldrich), iron (III) nitrate nonahydrate (98% gma Aldrich), cobalt (II) nitrate hexahydrate (98% gma Aldrich), nickel foam (99%, thickness 1.6 mm, Goodfellow), potassium hydroxide (98%, Qualigens,), glucose (99%, qualigens), sodium thiosulphate (99%, qualigens), ethanol (99%, Changshu HFCL,), hydrochloric acid (99%, SDFCL). DI water obtained from the Millipore water purification system.

#### **4.3.2 Material Characterization**

XRD patterns were obtained using a Pananalytical Empyrean diffractometer, scanning a  $2\theta$  range of 10-90°. Surface electronic properties were examined via XPS using a ThermoFisher instrument with monochromatic Al K-Alpha radiation, calibrated to the C1s peak at 284.8 eV. Morphological analysis was conducted using a JEOL JSM-7900F FESEM, which also provided elemental distribution data through energy dispersive X-ray spectroscopy (EDS). For high-resolution imaging, including STEM-HAADF and SAED, a JEOL JEM-F200 high-resolution transmission electron microscope (HRTEM) was employed, equipped with an EDS detector for additional elemental analysis. The Raman spectra was recorded using confocal Raman spectrometer.

#### **4.3.3 Electrochemical Measurements:**

An electrochemical workstation (M204 PGSTAT, Autolab) with a three-electrode setup was used to perform all electrochemical measurements. A reference electrode of Hg/HgO (1.0 M NaOH) and a counter electrode of graphite rod were used in combination with the

CF-CeO<sub>2</sub>@Ni<sub>3</sub>S<sub>2</sub> material as the working electrode. The electrolyte used for the UOR and HER was 1.0 M KOH + 0.5 M urea. All reactions were conducted at a scan rate of 5 mV/s. The Nernst equation was used to change the observed potential to the reversible hydrogen electrode (RHE) scale. To calculate the current density values, the collected currents were normalized using the 0.5 × 0.5 cm<sup>2</sup> geometric area of the working electrode.

$$E_{RHE} = E_{Hg/HgO}^0 + E_{Hg/HgO} + 0.0591 \times pH \quad \text{Equation 4.1}$$

#### 4.3.4 Synthesis of CoFe doped CeO<sub>2</sub>@Ni<sub>3</sub>S<sub>2</sub>

First, clean the Ni foam in HCl, ethanol, and DI water. Then, prepare a 111 mM (20 mL) Glucose solution and stir it at 80°C. Add 137.44 mM (10 mL) cobalt nitrate to this solution, followed by 100.73 mM (10 mL) of Na<sub>2</sub>S<sub>2</sub>O<sub>3</sub>. Next, add 92.11 mM (10 mL) Cerium Nitrate to the mixture and subsequently, add a 99 mM (10 mL) solution of iron nitrate to the mixture. Allow this reaction to proceed for 1 hour. After 1 hour, transfer the homogeneous mixture to a 100 mL autoclave. Place a piece of the cleaned Ni foam in the autoclave and heat it to 160 °C for 12 hours. After cooling to room temperature, remove the Ni foam and wash it multiple times with DI water and dry it in hot air oven overnight.

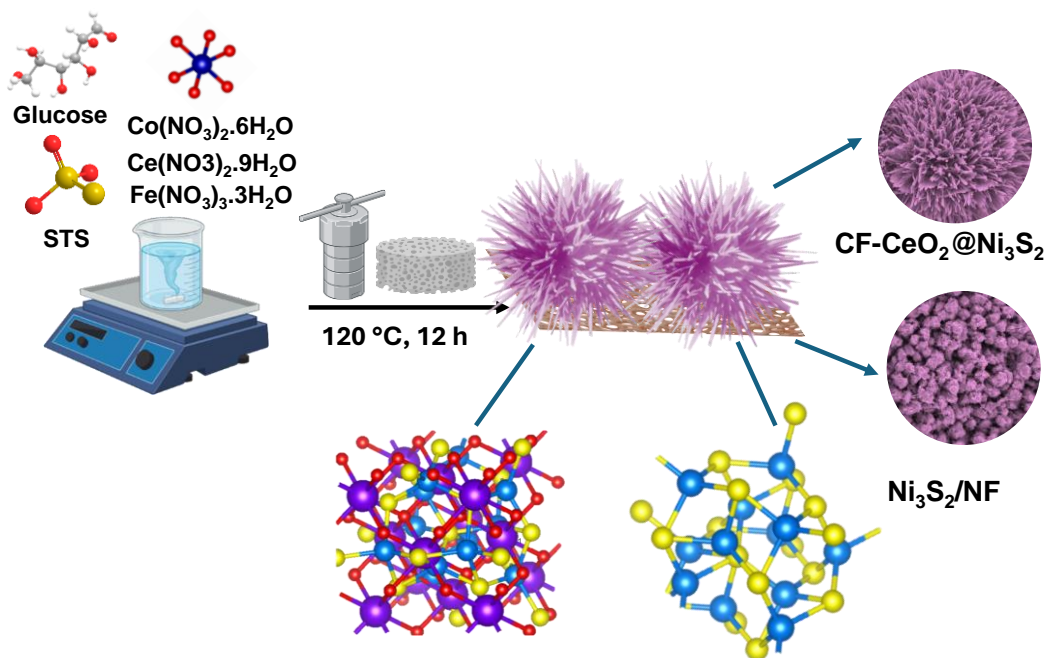
#### 4.3.5 Synthesis of Ni<sub>3</sub>S<sub>2</sub>/NF

First, use a solution of ethanol, HCl, and deionized (DI) water to clean the Ni foam. After that, take a 111 mM glucose solution in a beaker and stir at 80°C. To this solution, add 100.73 mM (10 mL) of Na<sub>2</sub>S<sub>2</sub>O<sub>5</sub>, and let the reaction run for an hour. Transfer the above homogenous mixture into a 100 mL autoclave after an hour. A piece of cleaned Ni foam should be placed into the autoclave and heated to 160°C for 12 hours. Let the autoclave cool to room temperature when the process is finished. After removing the Ni foam from the autoclave, thoroughly wash it several times with DI water and dry it in hot air oven overnight.

#### 4.4 Results and discussion

The target catalyst was synthesized by hydrothermally forming a CoFe-doped  $\text{CeO}_2@ \text{Ni}_3\text{S}_2$  nanorod structure on a cleaned NF substrate using one-step hydrothermal synthesis at  $120^\circ\text{C}$ , as shown in **Scheme 4.1**. In this method, the NF itself functions as the nickel source, [85] sodium thiosulfate as the sulfur source and glucose used as a carbon source and reducing agent. To alter the electronic structure and improve the material's catalytic qualities, cobalt ( $\text{Co}^{2+}$ ) and cerium ( $\text{Ce}^{3+}$ ) ions and  $\text{Fe}^{3+}$  salts were added. This material can nucleate and develop more easily under hydrothermal conditions, which enables it to create a layer of CoFe doped  $\text{CeO}_2$  outside the  $\text{Ni}_3\text{S}_2$  layer. Cobalt and Iron doping in  $\text{CeO}_2$  is probably accomplished by adding a cobalt and iron precursor to the reaction mixture, which is then integrated into the  $\text{CeO}_2$ . The same technique is used to make pure  $\text{Ni}_3\text{S}_2/\text{NF}$  for comparison, but dopants are not added.

Analysis of the produced products using powder X-ray diffraction (XRD) provided crucial crystallographic information. The XRD patterns, which showed three significant peaks at  $44.5^\circ$ ,  $51.8^\circ$ , and  $76.4^\circ$  that were attributable to the Ni foam substrate.  $\text{Ni}_3\text{S}_2$  was successfully formed and had good crystallinity in both the  $\text{Ni}_3\text{S}_2/\text{NF}$  and CF- $\text{CeO}_2@ \text{Ni}_3\text{S}_2/\text{NF}$  samples, as shown by the observed diffraction peaks closely matching the standard patterns of  $\text{Ni}_3\text{S}_2$  (JCPDS no. 044-1418). The peak at  $56.3$  showed the presence of  $\text{CeO}_2$  in the nanostructure. The CF- $\text{CeO}_2@ \text{Ni}_3\text{S}_2/\text{NF}$  sample had Co and Fe components, however, it's interesting to note that the XRD patterns did not show any diffraction peaks, showing the low content in the overall composition. [282,283] (**Figure 4.1A**)



**Scheme 4.1:** Synthetic scheme showing the formation of CoFe doped CeO<sub>2</sub>@Ni<sub>3</sub>S<sub>2</sub>.

The examination of Raman spectroscopy shows different vibrational modes that are indicative of different phases in the materials under study. According to its structure, Ni<sub>3</sub>S<sub>2</sub> has peaks at 188, 202, 224, 301, 304, 325 and 351 cm<sup>-1</sup> which are predominantly present in both samples Ni<sub>3</sub>S<sub>2</sub>/NF and CF-CeO<sub>2</sub>@Ni<sub>3</sub>S<sub>2</sub>. [284] The Ce–O vibrations bonds are responsible for the extra peaks in the CF-CeO<sub>2</sub>@Ni<sub>3</sub>S<sub>2</sub> sample, which are located at around 466 and 568 cm<sup>-1</sup>, respectively. [285] The effective integration of cerium oxide into the composite material is shown by these peaks, which validate the existence of a CeO<sub>2</sub> phase. Peaks at 537 and 633 cm<sup>-1</sup> are also seen in the spectra, they are typical of Co<sub>3</sub>O<sub>4</sub>. [286] This thorough Raman investigation shows the presence of nickel sulfide, cerium oxide, and cobalt oxide phases. **(figure 4.1B)** The Ni<sub>3</sub>S<sub>2</sub>/NF and CF-CeO<sub>2</sub>@Ni<sub>3</sub>S<sub>2</sub> sample's electronic states and surface chemical composition were thoroughly revealed by the X-ray photoelectron spectroscopy (XPS) study. All the targeted elements Fe, Co, Ni, and Ce were successfully incorporated into the sample surface as confirmed by the XPS survey. Ni 2p<sub>3/2</sub> and Ni 2p<sub>1/2</sub> were identified by the

spectrum's two primary peaks at 855.88 eV and 873.6 eV, respectively in case of CF-CeO<sub>2</sub>@Ni<sub>3</sub>S<sub>2</sub> (**Figure 4.1C**). The Ni<sub>3</sub>S<sub>2</sub>/NF shows the Ni 2p<sub>3/2</sub> and Ni 2p<sub>1/2</sub> peaks at 856.1 and 873.84 eV (**Figure A50**). Significantly, the CF-CeO<sub>2</sub>@Ni<sub>3</sub>S<sub>2</sub> sample showed a change in peak locations towards lower binding energies in contrast to the undoped Ni<sub>3</sub>S<sub>2</sub>/NF. This shift indicates that the presence of Co, Fe dopants and CeO<sub>2</sub> layer has significantly altered the local electronic structure of Ni atoms. [287,276]

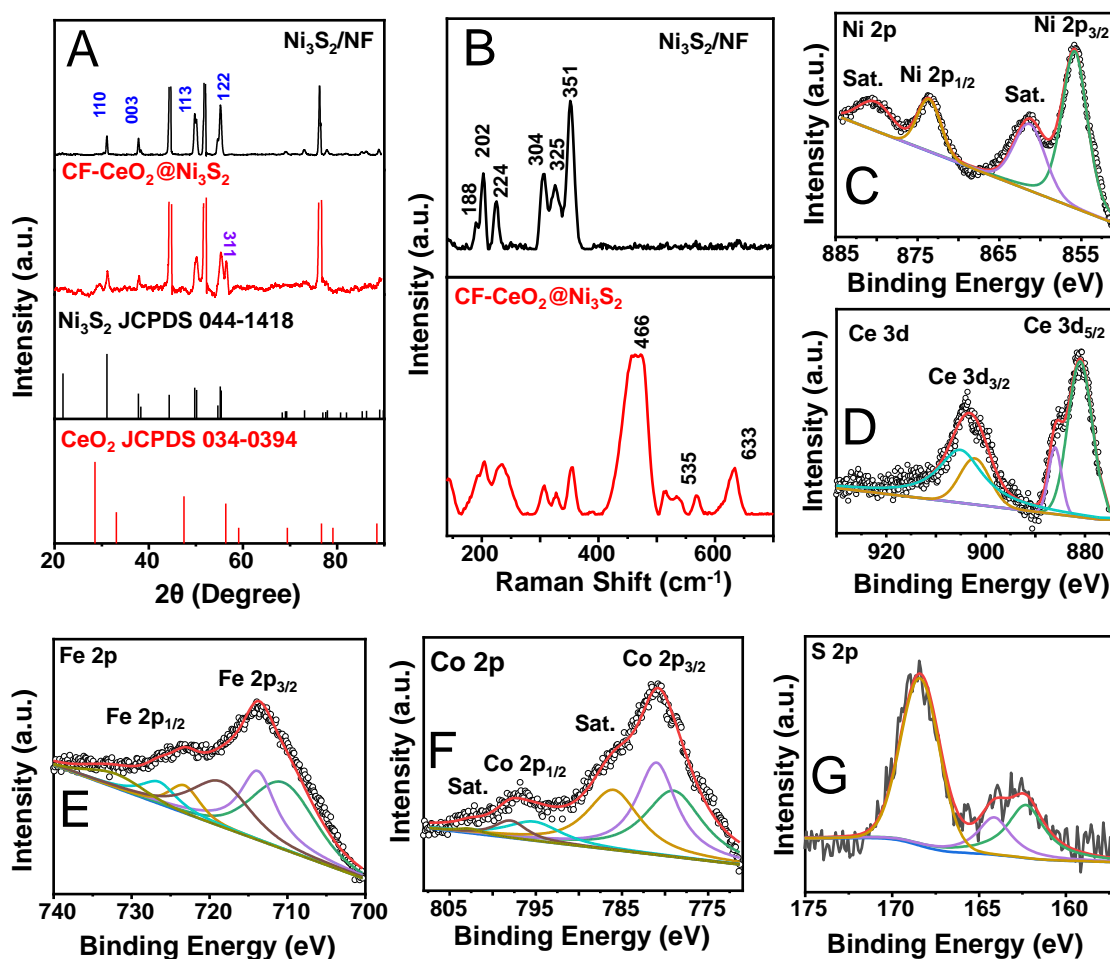


**Figure 4.1:** The XRD spectra of (A) CF-CeO<sub>2</sub>/Ni<sub>3</sub>S<sub>2</sub> and Ni<sub>3</sub>S<sub>2</sub>/NF with JCPDS correlations, the Raman spectra of (B) CF-CeO<sub>2</sub>/Ni<sub>3</sub>S<sub>2</sub> and Ni<sub>3</sub>S<sub>2</sub>/NF, the XPS spectra (C) Ni 2p, (D) Ce 3d, (E) Fe 2p, (F) Co 2p and (G) S 2p of CF-CeO<sub>2</sub>/Ni<sub>3</sub>S<sub>2</sub>.

Ce 3d<sub>5/2</sub> and Ce 3d<sub>3/2</sub> spin-orbit split components are represented by the two major areas of the high-resolution Ce 3d XPS spectra. The Ce 3d<sub>5/2</sub> transitions are assigned to the peaks in the 880-900 eV energy range, while the Ce 3d<sub>3/2</sub> transitions are assigned to the peaks in the 900-920 eV range in CF-CeO<sub>2</sub>@Ni<sub>3</sub>S<sub>2</sub> (**Figure 4.1D**).[288] Fe<sup>3+</sup> 2p<sub>3/2</sub> and Fe<sup>2+</sup> 2p<sub>1/2</sub> are separately represented by the distinctive peaks in the Fe 2p spectra, which are located at 710.9 eV and 713.88 eV, respectively (**Figure 4.1E**).[283] Similarly, Co 2p<sub>3/2</sub> is ascribed to the two primary peaks at 781.0 eV and 779.0 eV for +2 and +3 oxidation states, respectively in the Co 2p spectrum shows the presence of Co<sub>3</sub>O<sub>4</sub> (**Figure 4.1F**).[289] The S 2p<sub>3/2</sub> and S 2p<sub>1/2</sub> spin-orbit components are responsible for the two conspicuous peaks in the S 2p spectra, which are located at 162.32 eV and 164.12 eV, respectively (**Figure 4.1G** ).[290] The existence of S-O bonds is indicated by an extra peak at 168.45 eV, which is probably the product of surface oxidation or oxygen species adsorption during XPS analysis. [291] The Oxygen 1s spectra show three prominent peaks at 529.78, 531.30 and 532.48 eV corresponding to M-O bond, oxygen vacancies and oxygen species from physically absorbed water respectively (**Figure A51**). The successful integration of iron and cobalt into the material's lattice structure, which successfully modifies the electrical configuration around the nickel atoms, is strongly supported by this thorough XPS investigation.

The SEM images were used to analyze the nanostructure of the CF-CeO<sub>2</sub>@Ni<sub>3</sub>S<sub>2</sub> nanocomposite. The structure of the catalyst CF-CeO<sub>2</sub>@Ni<sub>3</sub>S<sub>2</sub> in the shape of nanorod-like structures with an average size of 55 nm (**Figure 4.2A-B, A52**). Similarly control sample Ni<sub>3</sub>S<sub>2</sub>/NF also show to nanorod type morphology with the average size of 318 nm (**Figure 4.2C-D, A53**). The two samples with different morphologies and size demonstrate how important the outside layer of Co, Fe doped CeO<sub>2</sub> on the Ni<sub>3</sub>S<sub>2</sub>/NF surface to increase the specific surface area and decrease the average size of a structure

which is advantageous for improving catalytic activity. The CF-CeO<sub>2</sub>@Ni<sub>3</sub>S<sub>2</sub> sample's elemental composition was revealed using FESEM-EDX. The CoFe doped CeO<sub>2</sub> layer outside the Ni<sub>3</sub>S<sub>2</sub> surface, formation was indicated by the results, which showed a greater concentration of Ni at 21.2% than Ce at 0.6 %. Although it was only found in a very modest quantity of 0.2%, the presence of Co and Fe as a dopants suggests that it plays a minor function in the composition. Significant levels of C at 55.3%, S at 11.4%, and O at 10.2% were seen in the sample, which is noteworthy and provides strong evidence for the existence of carbon based CF-CeO<sub>2</sub>@Ni<sub>3</sub>S<sub>2</sub> (**Figure A54**).

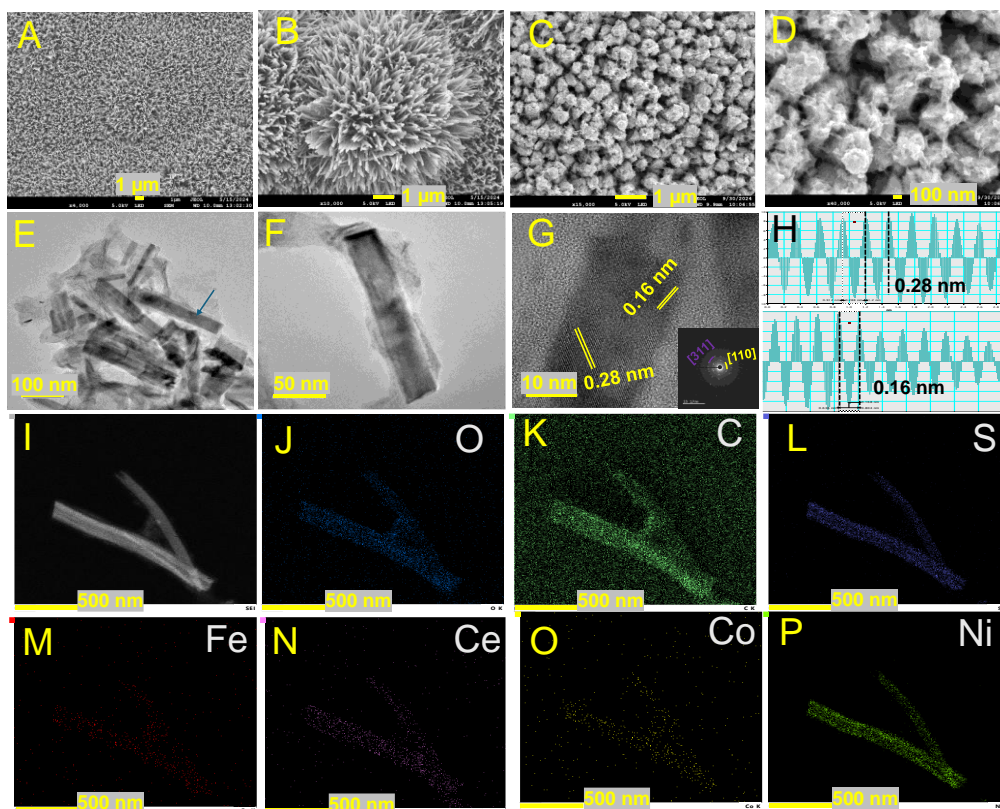


**Figure 4.2:** The FE-SEM images of (A & B) CF-CeO<sub>2</sub>/Ni<sub>3</sub>S<sub>2</sub> and (C & D) Ni<sub>3</sub>S<sub>2</sub>/NF at various magnifications, (E & F) TEM image of CF-CeO<sub>2</sub>/Ni<sub>3</sub>S<sub>2</sub>; (G) the d spacing values matching with Ni<sub>3</sub>S<sub>2</sub> and CeO<sub>2</sub> computed from digital micrographs software, the inset displays the SAED spectra of CF-CeO<sub>2</sub>/Ni<sub>3</sub>S<sub>2</sub> displaying the lattice planes, and (G) IFFT plot displaying the d spacing values, the (I-P) HAADF-STEM elemental mapping of CF-CeO<sub>2</sub>/Ni<sub>3</sub>S<sub>2</sub>.

Transmission electron microscopy (TEM) was used to characterize the nanorod, revealing complex information about its composition and structure. The nanoparticles after being separated from nickel foam was used for the analysis. The high-resolution HR-TEM images shows a similar structure of nanorod with an average size of 47 nm (**Figure 4.2E-F, A55**). The nanorod showed two separate lattice fringes with interplanar spacings of 0.28 nm inside the nanorod which confirms the formation of  $\text{Ni}_3\text{S}_2$  layer and 0.16 nm outside edges of the nanorod confirm the formation of  $\text{CeO}_2$  (**Figure 4.2G**). The existence of both materials in the composite structure is shown by these spacings, which correlate with the SAED pattern of the (110) plane of  $\text{Ni}_3\text{S}_2$  and the (311) plane of  $\text{CeO}_2$ . The existence of Co, Fe, Ni, Ce, C, O and S elements in the composite was validated by the HAADF-STEM mapping findings (**Figure 4.2I-P**). Interestingly, it was discovered that the Ni and S were equally distributed on the nanorod core surface and Fe, Ce, Ce, O and S elements were distributed outside the surface which provides support and enhances the catalytic activity of the catalyst. This TEM study highlights the effective integration of CoFe doped  $\text{CeO}_2$  layer on the  $\text{Ni}_3\text{S}_2$  surface and offers insightful information on the structural and compositional properties of the nanorod.

The acquired samples' electrocatalytic activity toward the urea oxidation process (UOR) was investigated in detail utilizing a wide range of electrochemical methods using a three-electrode setup. A 1 M potassium hydroxide (KOH) and 0.5 M urea electrolyte solution was used for all measurements. For both the control samples  $\text{Ni}_3\text{S}_2/\text{NF}$  and CoFe doped  $\text{CeO}_2@/\text{Ni}_3\text{S}_2$  electrocatalysts, polarization curves were produced using linear sweep voltammetry (LSV) at a scan rate of  $5 \text{ mV s}^{-1}$  for UOR and HER (**Figure 4.3A-B**). The CF- $\text{CeO}_2@/\text{Ni}_3\text{S}_2$  performs better as a catalyst for the UOR than  $\text{Ni}_3\text{S}_2/\text{NF}$ , CF- $\text{CeO}_2@/\text{Ni}_3\text{S}_2$  needed a potential of only 1.38  $\text{V}_{\text{RHE}}$  to get a current density of  $100 \text{ mA/cm}^2$ .

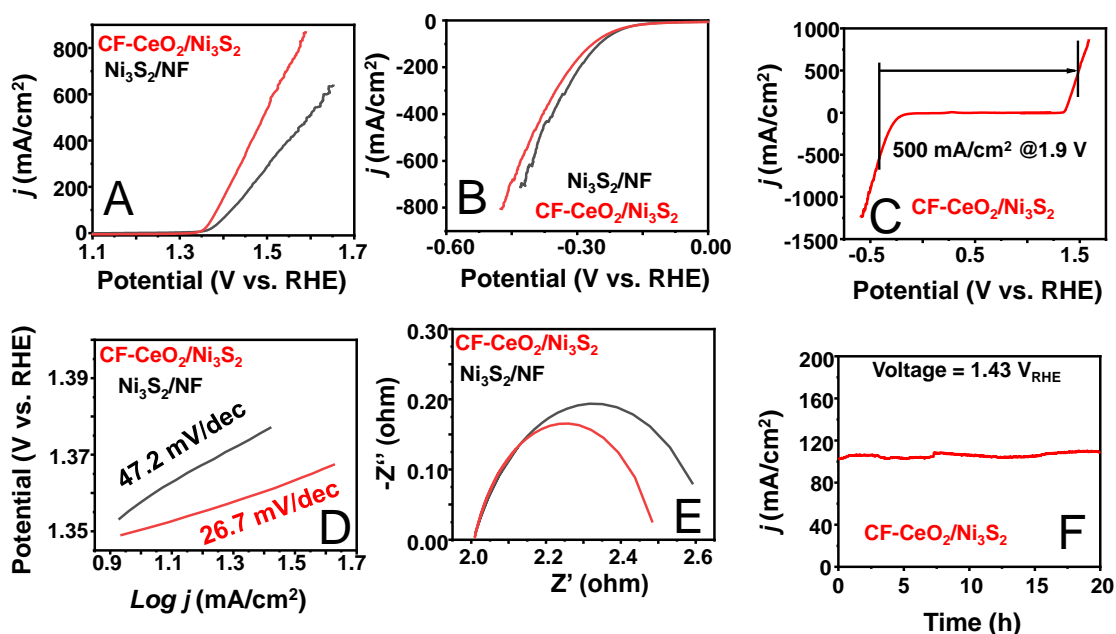


**Figure 4.3:** The LSV polarisation traces for (A) UOR, (B) HER, (C) the overall (UOR+HER) LSV traces of CF-CeO<sub>2</sub>/Ni<sub>3</sub>S<sub>2</sub> in 1 M KOH + 0.5 M Urea with 5 mV/s scan rate and electrode area of 0.25 cm<sup>2</sup> (D) Tafel slope, (E) EIS plot and (H) chronoamperometry trace of CF-CeO<sub>2</sub>/Ni<sub>3</sub>S<sub>2</sub>.

The positive impact of CeFe doped CeO<sub>2</sub> layer in Ni<sub>3</sub>S<sub>2</sub> surface for increased UOR catalytic activity was shown by CF-CeO<sub>2</sub>@Ni<sub>3</sub>S<sub>2</sub>, which demonstrated an 0.032 V lower potential required to achieve the 100 mA cm<sup>2</sup> current density when compared to Ni<sub>3</sub>S<sub>2</sub>/NF. Interestingly, Ni<sub>3</sub>S<sub>2</sub>/NF had a lower potential of 0.014 V compared to CF-CeO<sub>2</sub>@Ni<sub>3</sub>S<sub>2</sub> at 100 mA/cm<sup>2</sup> in case of HER (**Figure 4.3B**). The overall potential is required CF-CeO<sub>2</sub>@Ni<sub>3</sub>S<sub>2</sub> is 1.9 V which is 80 mV lower compared to the Ni<sub>3</sub>S<sub>2</sub>/NF at 500 mA/cm<sup>2</sup> (**Figure 4.3C**). The UOR kinetics for both catalysts were investigated in detail using Tafel plots and electrochemical impedance spectroscopy (EIS). With a much lower tafel slope of CF-CeO<sub>2</sub>@Ni<sub>3</sub>S<sub>2</sub> 26.7 mV dec<sup>-1</sup> compared to the considerably higher slope of 47.2 mV dec<sup>-1</sup> for Ni<sub>3</sub>S<sub>2</sub>/NF (**Figure 4.3D**). These results were further supported by the EIS analysis, which showed that a similar R<sub>s</sub> value with the lower charge transfer resistance (R<sub>ct</sub>) for CF-CeO<sub>2</sub>@Ni<sub>3</sub>S<sub>2</sub> compared to Ni<sub>3</sub>S<sub>2</sub>/NF (**Figure 4.3E**). This

significant decrease in  $R_{ct}$  for CF-CeO<sub>2</sub>@Ni<sub>3</sub>S<sub>2</sub> suggests a quicker UOR rate and more effective charge transfer at the interface between CF-CeO<sub>2</sub>@Ni<sub>3</sub>S<sub>2</sub> and electrolyte. For the UOR, the catalytic performance of CF-CeO<sub>2</sub>@Ni<sub>3</sub>S<sub>2</sub> was assessed and compared with other catalyst compositions documented in recent literature. The remarkable current density ( $j_{UOR}$ ) of 10 mA cm<sup>-2</sup> was shown by the CF-CeO<sub>2</sub>@Ni<sub>3</sub>S<sub>2</sub> electrode at a voltage of 1.35 V<sub>RHE</sub> (**Table A11**).

Two-electrode device schematics for total electrochemical urea electrolysis is presented in the **Figure 4.4A**. In this electrolyzer setup CF-CeO<sub>2</sub>@Ni<sub>3</sub>S<sub>2</sub> nanorod is used as the cathode and anode, both of which are submerged in a 1 M KOH + 0.5 M urea electrolyte. The CF-CeO<sub>2</sub>@Ni<sub>3</sub>S<sub>2</sub> electrode system attains current densities of 10 mA/cm<sup>2</sup> and 100 mA cm<sup>-2</sup> with relatively low working voltages of 1.55 V and 1.75 V respectively, indicating great efficiency in the case of total electrochemical urea electrolysis. To achieve the same current densities of 10 mA cm<sup>-2</sup> and 50 mA cm<sup>-2</sup>, respectively, the Ni<sub>3</sub>S<sub>2</sub>/NF electrode system requires 1.56 V and 1.8 V, demonstrating significantly lower performance compared to CF-CeO<sub>2</sub>@Ni<sub>3</sub>S<sub>2</sub> for urea electrolysis (**Figure 4.4B**).

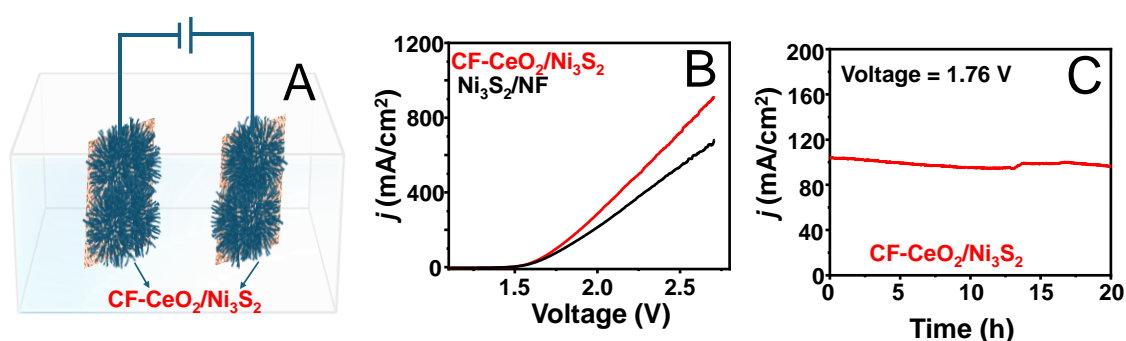


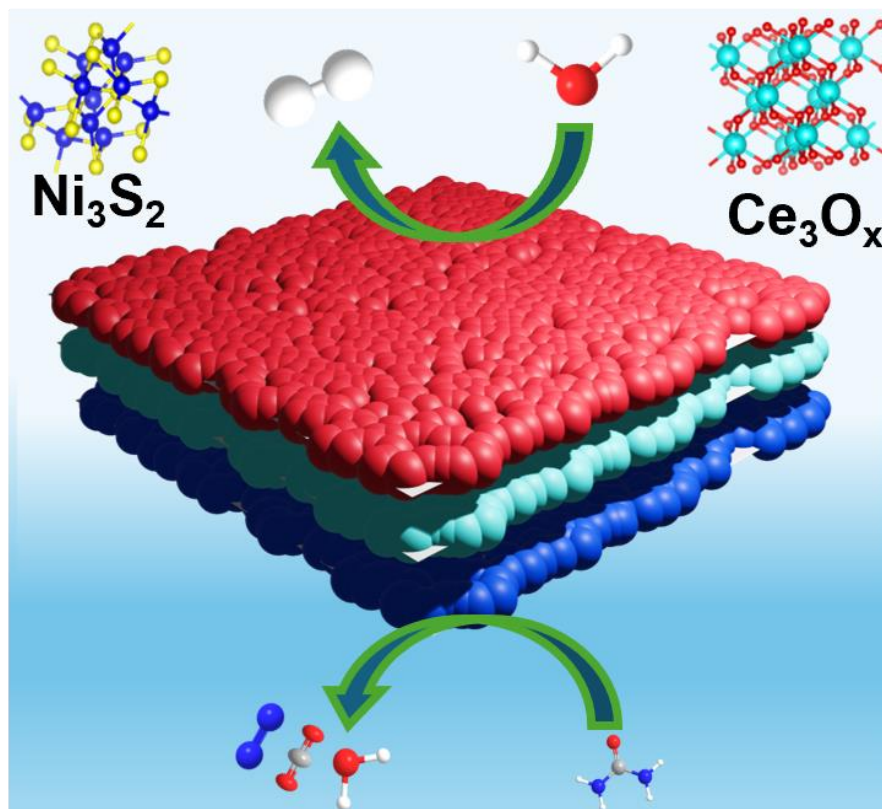
**Figure 4.4:** The (A) Schematic representation of two electrode device, (B) LSV polarisation traces of CF-CeO<sub>2</sub>/Ni<sub>3</sub>S<sub>2</sub> and Ni<sub>3</sub>S<sub>2</sub> 1 M KOH + 0.5 M Urea with 5 mV/s scan rate and electrode area of 0.25 cm<sup>2</sup> and (C) chronoamperometry trace of CF-CeO<sub>2</sub>/Ni<sub>3</sub>S<sub>2</sub>.

For two-electrode systems to continue to operate dependably and consistently over time, their prolonged operational stability is essential. The chronoamperometric (i-t) test used for the stability profile for the CF-CeO<sub>2</sub>@Ni<sub>3</sub>S<sub>2</sub> cell at 1.76 V for 20 h (**Figure 4.4C**). The cell exhibits a very consistent current production for the 20 h without degradation in the electrode system.

#### **4.5 Conclusion**

In this work, we developed a new method for an effective UOR electrocatalyst by growing CoFe-doped CeO<sub>2</sub>/Ni<sub>3</sub>S<sub>2</sub> nanorods on Ni foam using a simple, one-step hydrothermal process, this self-supported catalyst was created. The obtained CoFe-doped CeO<sub>2</sub>/Ni<sub>3</sub>S<sub>2</sub> catalyst showed outstanding endurance and low overpotential, which were characteristics of good UOR performance. According to experimental assessments, the dual doping of Co and Fe with the CeO<sub>2</sub> layer led to the optimization of electronic structures and an increase in accessible active sites, which were the main causes of the significant rise in UOR activity. The discovery offers new possibilities for research in the areas of energy conversion and other catalytic applications in addition to offering a workable and promising approach for the in-situ manufacture of affordable electrocatalysts including both transition and lanthanide elements.

## Table of Contents



This page was initially left blank.

# Chapter 5

## Summary and Future Perspectives

### 5.1 Summary

The development of transition metal-based electrodes and sustainable electrocatalysts for hybrid water electrolysis for green hydrogen production and valuable chemicals is the main objective of the thesis study. In place of the OER, we use anodic small molecule electrocatalytic oxidation to overcome several issues with conventional water splitting techniques. This alternate technique reduces the total energy consumption in electrolyzers and helps get around the sluggish kinetics of OER. Numerous electrocatalytic oxidation processes have been investigated in these studies, such as the oxidation of 5-hydroxymethylfurfural (HMFOR), hydrazine (HzOR), urea (UOR), and sulfur (SOR) and methanol oxidation reaction (MOR). A variety of catalysts have been studied, metal sulfides have shown appropriateness for SOR, while nickel-based catalysts have shown promise for urea oxidation and NiCu alloy-based catalysts are stable for MOR.

In the first chapter, we describe a comprehensive and in-depth analysis of the literature on hybrid water splitting, following its development from its beginnings to the present. This thorough review includes not just water splitting but also associated processes such as urea oxidation reactions, methanol oxidation, and sulfion oxidation. We explore the basic ideas behind water splitting, clarifying the thermodynamic factors that influence these procedures. The chapter discusses the discovery of new materials that have the potential to transform the area of advanced electrocatalysts. We also provide

a detailed explanation of the many structural and electrochemical characterisation methods used to examine and assess these electrocatalysts.

In chapter two by using the relative reactivity of the precursors, a one-step manufacturing approach combining FeOOH and Co<sub>9</sub>S<sub>8</sub> nanostructures on NF produces a highly efficient catalyst for the synthesis of green hydrogen. Effective hydrogen evolution is made possible by the increased catalytic activity of this intercalated nanostructure, especially when sulfide ions (S<sup>2-</sup>) are present. In either an H-type or single-cell configuration, the NiFeOOH-Co<sub>9</sub>S<sub>8</sub>-n-based system exhibits exceptional bifunctionality by enabling the HER and SOR at the same time. One important factor in maximizing the potential-current connection is the interelectrode distance. Notably, SOR may happen at high current densities without the need for sodium hydroxide (NaOH) because to the catalyst's strong activity. According to density functional theory the interface between FeOOH and Co<sub>9</sub>S<sub>8</sub> causes oxide doping, which greatly increases SOR activity. When producing green hydrogen, the combined impacts of these elements result in significant power savings and lower energy. An eco-friendly and energy-efficient substitute for traditional techniques, this novel catalytic system offers a viable foundation for the commercial and scalable synthesis of hydrogen. This technology's enhanced catalytic performance, bifunctionality, and energy efficiency make it a strong contender for future advancement and possible commercialization in the expanding area of sustainable energy generation.

In chapter third, a metallic Ni surface is treated as a shape-directing agent in the hydrothermal process of NiCu alloy nanocrystals, which enables the in-situ reduction of Cu and Ni salts by polyacryloyl hydrazide (PAHz). In addition to facilitating the formation of NiCu alloy nanocrystals, this one-pot technique permits the concurrent doping of metal oxides on the alloy surface. The resultant electrodes exhibit remarkable

performance in the alkaline methanol oxidation reaction (MOR) and OER, which qualifies them for dual-purpose uses in the manufacture of energy-efficient green hydrogen. A combination of the active Cu sites in the NiCu heterostructure, the doping of  $\text{Co}_3\text{O}_4$ , and the sharp edges of the nanocuboid shape are thought to have contributed to the increased electrocatalytic activity. Notably, when formate/formic acid is produced from methanol, the NF-PAHz- $\text{Co}_3\text{O}_4$ @NiCu electrode shows good yields. The Cu sites in the NiCu nanocrystals behave as active centers for OER and MOR activity, according to theoretical density functional theory (DFT) calculations, which corroborate the experimental results. This synthetic approach's adaptability indicates that it may be used to create different alloy nanocrystals for catalytic uses in electrochemical processes, creating new opportunities for the creation of effective and multipurpose electrocatalysts.

In chapter four, we synthesized CoFe-doped  $\text{CeO}_2/\text{Ni}_3\text{S}_2$  nanorods on nickel foam using a simple, one-step hydrothermal approach, which allowed us to create an efficient urea oxidation reaction (UOR) electrocatalyst. Excellent durability and a low overpotential two critical markers of outstanding UOR performance were shown by this self-supported catalyst. Our experimental analyses demonstrated that the Co and Fe dual doping in the  $\text{CeO}_2$  layer resulted in improved electronic structures and more accessible active sites, which were the main causes of the significant increase in UOR activity. This novel combination of a lanthanide element (Ce) and transition metals (Ni, Co, and Fe) in a single, in-situ fabricated electrocatalyst not only shows a viable and promising method for creating affordable UOR catalysts, but it also creates new opportunities for research in other catalytic processes and more general energy conversion applications. Combining the ease of the synthesis process with the exceptional performance of the final catalyst points to substantial potential for practical application and scaling up in a variety of

electrochemical systems, potentially transforming industries like fuel cells, hydrogen production, and other clean energy technologies.

Overall, we aimed to fabricate transition metal based robust and long-lasting electrodes for hybrid water electrolysis applications under different electrocatalytic conditions by developing novel methods to create non-noble, earth-abundant metal sulfide, oxyhydroxide and alloy-based nano catalysts. The significance of this study lies in its investigation of substitutes for costly noble metal catalysts and replacing the sluggish OER reactions by hybrid water electrolysis.

## **5.2 Future Scope**

The Future developments in hybrid water splitting of small molecule electrocatalytic oxidation provide several important research avenues that need in-depth study. Creating strong, selective, and reasonably priced electrocatalysts that can endure the harsh conditions of saltwater while retaining high activity and stability is still crucial from a catalytic standpoint. These catalysts must exhibit optimum binding energies for target compounds as well as effective charge transfer capabilities. The main technique for mechanistic study is an excessive dependence on Density Functional Theory (DFT) computations. Optimizing the process and enhancing selectivity requires an understanding of the intricate chemical processes, which include intermediate generation and electron transport routes. To improve mass transfer, lower ohmic losses, electrolyzer design and engineering need careful consideration of factors including electrode configuration, membrane choice, and cell layout. Since the integrated cell system is essential to determine the effectiveness of the cathode hydrogen generation and anode electrocatalytic oxidation processes, thorough investigation and optimization of the electrolyzer design are essential. The electrolyte solution's pH levels (whether acidic or alkaline) directly affect the reaction kinetics, the solute type affects conductivity and ion

transport, the diaphragm material selection affects ion selectivity and crossover prevention, the distance between electrodes influences ohmic resistance and mass transfer, the applied voltage determines the reaction rate and energy efficiency, and the electric current flow affects the overall reaction dynamics and production rates. A comprehensive understanding of these important parameters is necessary to achieve optimal performance. To overcome obstacles including gas crossing, product purification, and the selective recovery of important chemicals created during the oxidation process, it is essential to design effective product separation procedures. Achieving economic viability and environmental sustainability will also require optimizing operating parameters (pH, temperature, and pressure) and integrating these systems with renewable energy sources. To overcome present obstacles and move the area closer to useful applications in sustainable energy and chemical production, this multidisciplinary approach calls for cooperation across materials science, electrochemistry, and chemical engineering.

This page was initially left blank.

## Appendix

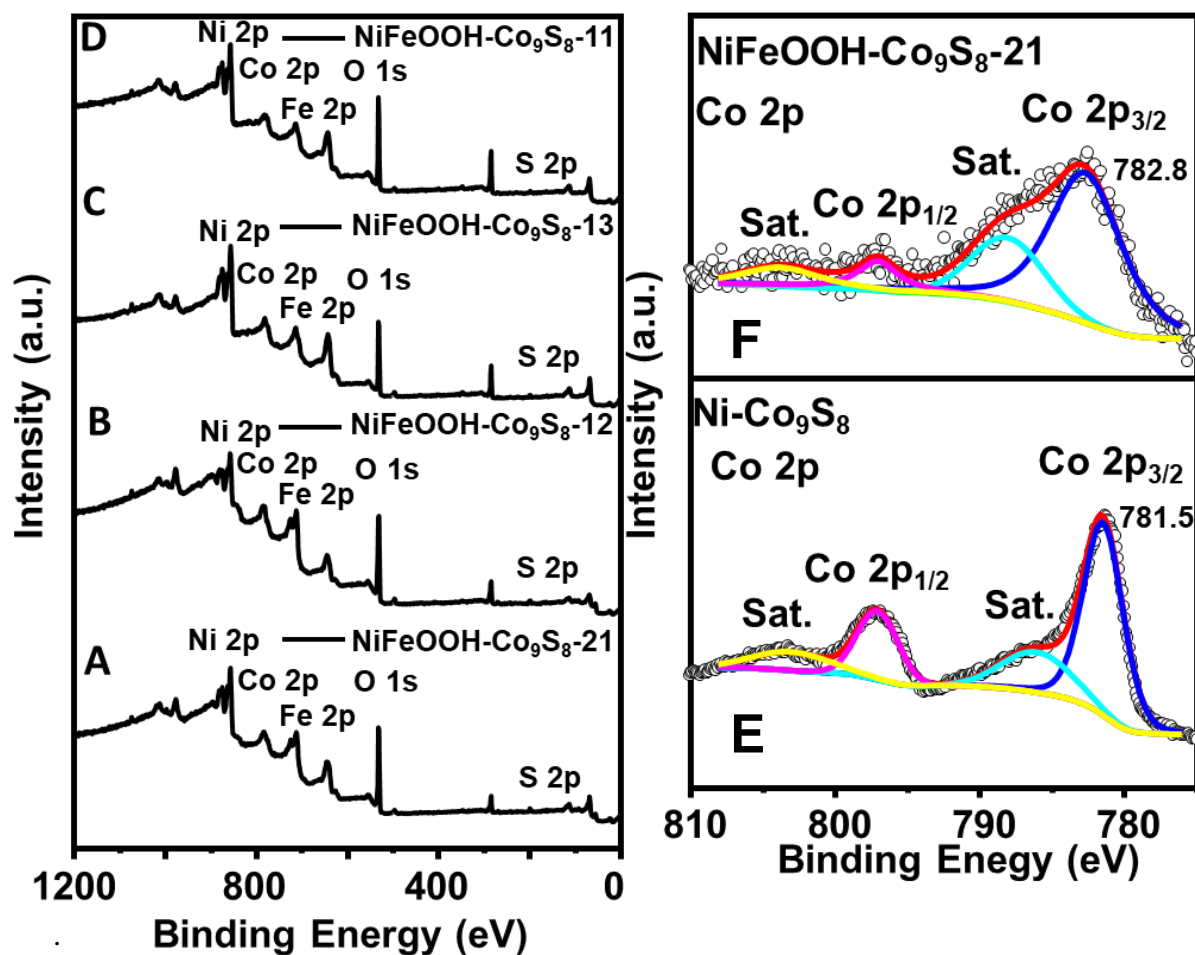


**Figure A 1:** The NiFeOOH-Co<sub>9</sub>S<sub>8</sub>-21, Co<sub>9</sub>S<sub>8</sub>-12, Co<sub>9</sub>S<sub>8</sub>-13, and Co<sub>9</sub>S<sub>8</sub>-11 XPS survey spectra are shown in (A), (B), (C), and (D) respectively. The Ni-Co<sub>9</sub>S<sub>8</sub> electrode's Co 2p XPS data and the NiFeOOH-Co<sub>9</sub>S<sub>8</sub>-21 electrode's Co 2p XPS data are shown in (E) and (F) respectively.

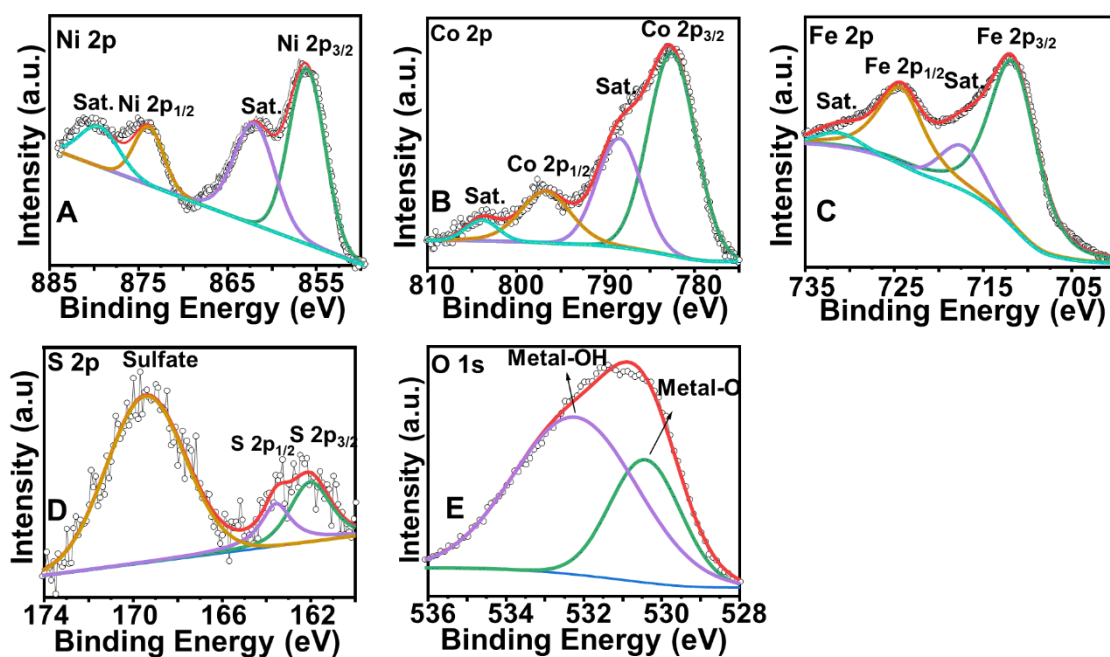


**Figure A 2:** The NiFeOOH-Co<sub>9</sub>S<sub>8</sub>-12 electrode's (A) Ni 2p, (B) Co 2p, (C) Fe 2p, (D) S 2p, and (E) O 1s XPS data.

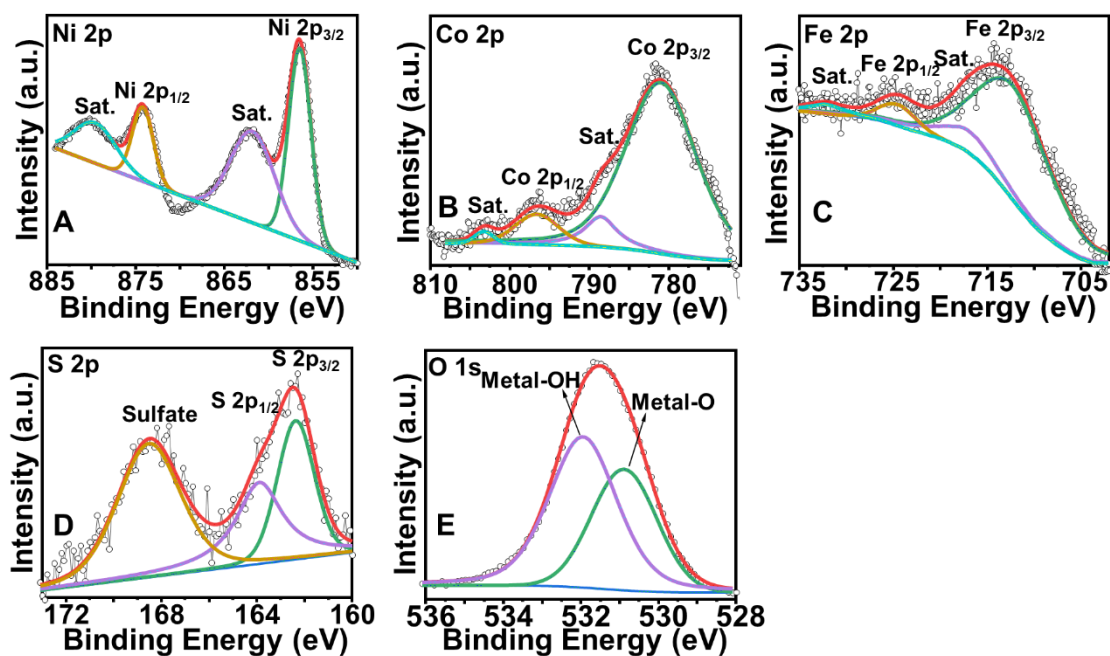


**Figure A 3:** The NiFeOOH-Co<sub>9</sub>S<sub>8</sub>-11 electrode's (A) Ni 2p, (B) Co 2p, (C) Fe 2p, (D) S 2p, and (E) O 1s XPS data.

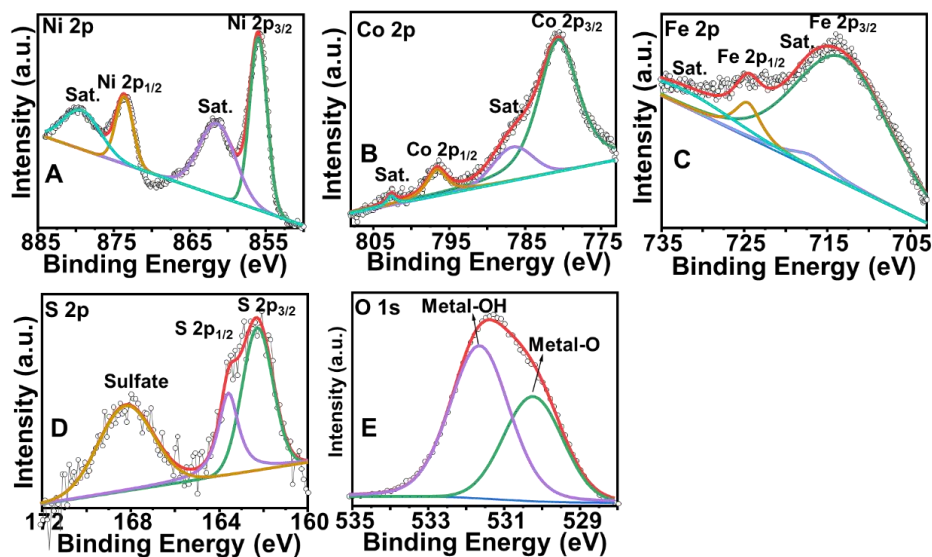


**Figure A 4:** The NiFeOOH-Co<sub>9</sub>S<sub>8</sub>-13 electrode's (A) Ni 2p, (B) Co 2p, (C) Fe 2p, (D) S 2p, and (E) O 1s XPS data.

**Table A 1:** SEM EDS and XPS data were used to compute the atomic ratio between Co and S.

Samples Code	EDS (Co/S Atomic Ratio)	XPS (Co/S Atomic Ratio)
NiFeOOH-Co <sub>9</sub> S <sub>8</sub> (11)	-	Co <sub>9</sub> S <sub>7.01</sub>
NiFeOOH-Co <sub>9</sub> S <sub>8</sub> (12)	Co <sub>9</sub> S <sub>8.86</sub>	Co <sub>9</sub> S <sub>7.84</sub>
NiFeOOH-Co <sub>9</sub> S <sub>8</sub> (21)	Co <sub>9</sub> S <sub>8</sub>	Co <sub>9</sub> S <sub>8.15</sub>
NiFeOOH-Co <sub>9</sub> S <sub>8</sub> (31)	Co <sub>9</sub> S <sub>8</sub>	Co <sub>9</sub> S <sub>8.2</sub>

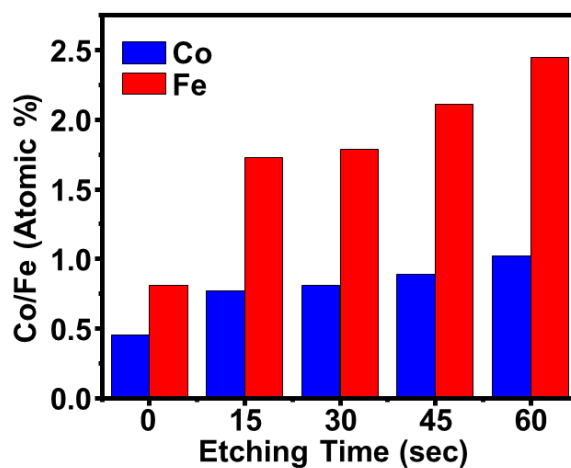


**Figure A 5:** The Co and Fe atomic percentages after various etching times.

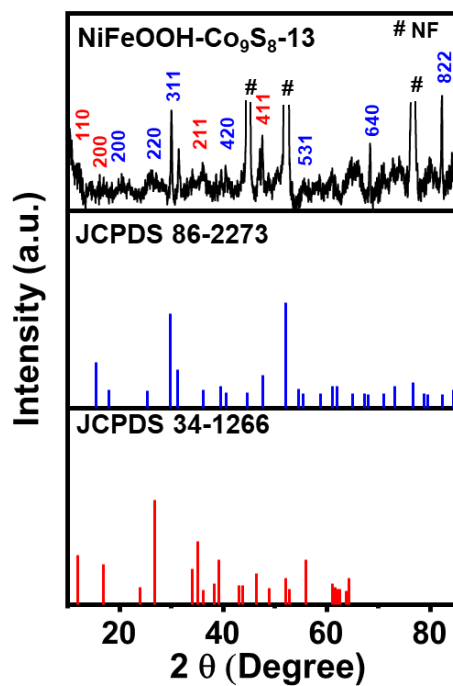


**Figure A 6:** NiFeOOH-Co<sub>9</sub>S<sub>8</sub>-13 electrode XRD data and JCPDS correlation.

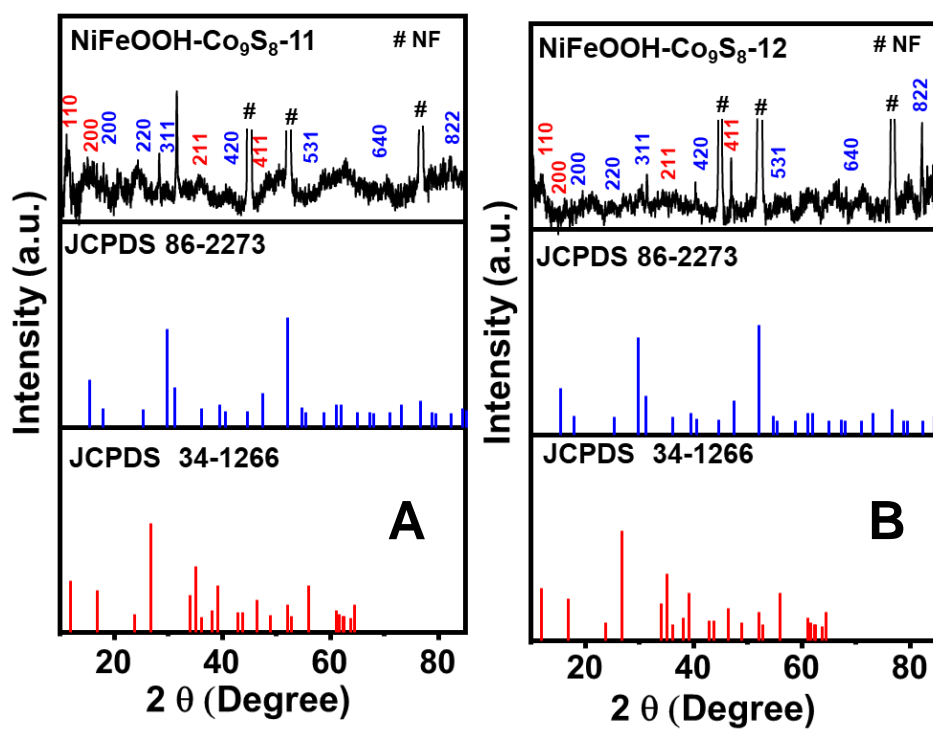


**Figure A 7:** The XRD data of A) NiFeOOH-Co<sub>9</sub>S<sub>8</sub>-11 electrode and JCPDS correlation and the (B) NiFeOOH-Co<sub>9</sub>S<sub>8</sub>-12 electrode and JCPDS correlation.

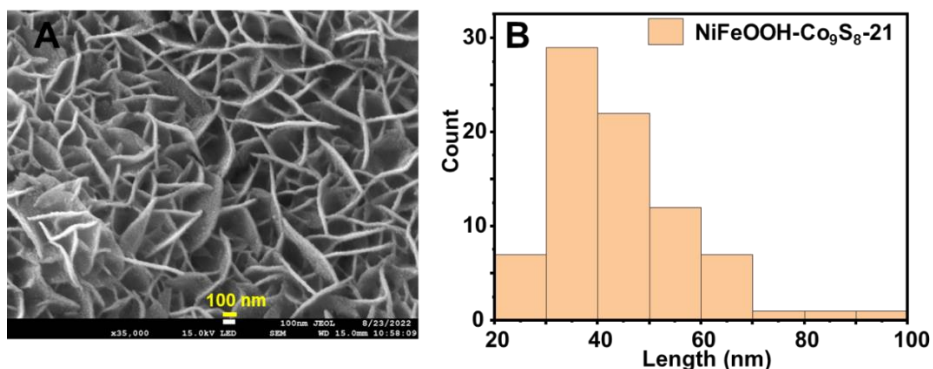


**Figure A 8:** The (A) FESEM image and (B) particle size distribution of NiFeOOH-Co<sub>9</sub>S<sub>8</sub>-21.

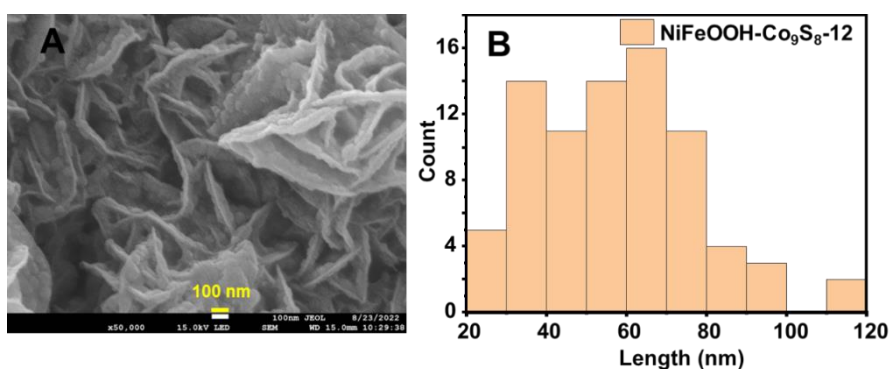


**Figure A 9:** The (A) FESEM image and (B) particle size distribution of NiFeOOH-Co<sub>9</sub>S<sub>8</sub>-12.

**Table A 2:** The FESEM-EDS studies on the electrode surface showed the Fe and Co atomic ratio.

Composition	NiFeOOH-Co <sub>9</sub> S <sub>8</sub> -21	NiFeOOH-Co <sub>9</sub> S <sub>8</sub> -12	NiFeOOH-Co <sub>9</sub> S <sub>8</sub> -11	NiFeOOH-Co <sub>9</sub> S <sub>8</sub> -13
EDS mapping Fe/Co (Atomic Ratio)	2.33:1.00	0.55:1.00	1.00:1.00	0.22:1.00

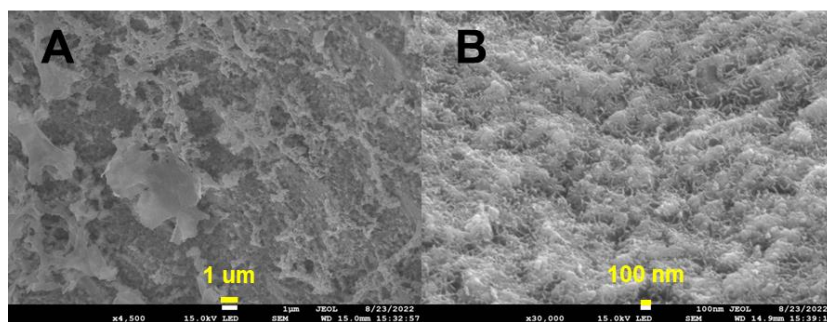


**Figure A 10:** The (A & B) FESEM image of NiFeOOH-Co<sub>9</sub>S<sub>8</sub>-31.

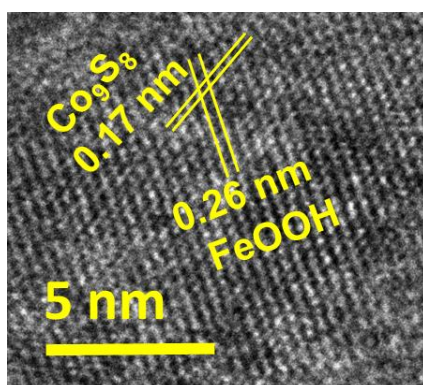


**Figure A 11:** The intercalated structure is supported by the lattice fringes of Co<sub>9</sub>S<sub>8</sub> and FeOOH.

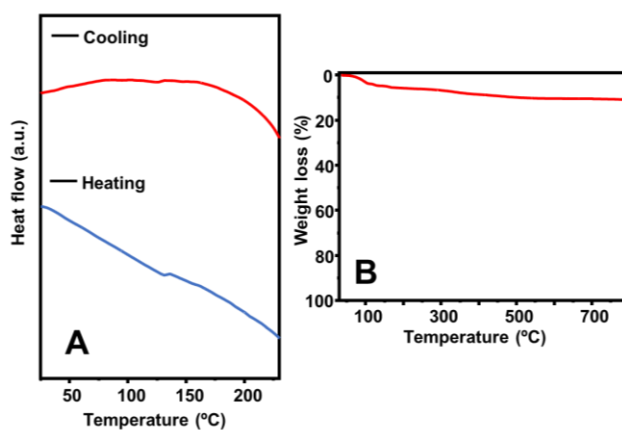


**Figure A 12:** The (A) DSC (B) TGA curves of the FeOOH-Co<sub>9</sub>S<sub>8</sub>-21.

**Table A 3:** The present electrodes' SOR efficiency is compared with current research.

Catalysts	Electrolyte	$j$ (mA cm <sup>-2</sup> )	Potential (V vs RHE)	Ref.
NiFeOOH-Co <sub>9</sub> S <sub>8</sub> -21	1 M NaOH +1M Na <sub>2</sub> S    1 M NaOH	1200	0.57	This Work
NiFeOOH-Co <sub>9</sub> S <sub>8</sub> -21	1 M Na <sub>2</sub> S    1 M NaOH	1000	0.7	This Work

Cu <sub>2</sub> S/NF	1 M NaOH +1M Na <sub>2</sub> S    1 M NaOH	290	0.8	1
CoNi@NGs	1 M NaOH +1M Na <sub>2</sub> S    1 M NaOH	155	0.6	53
NiCoOxCNTs	1 M NaOH +1M Na <sub>2</sub> S    1 M NaOH	50	0.50	53
IrO <sub>2</sub>	1 M NaOH +1M Na <sub>2</sub> S    1 M NaOH	10	0.43	53
CoS <sub>2</sub> @C/MXene/NF	1 M NaOH +1M Na <sub>2</sub> S    1 M NaOH	380	0.75	292
WS <sub>2</sub> NSs	1 M NaOH +1M Na <sub>2</sub> S    1 M NaOH	100	0.78	72
NiS <sub>2</sub>	1 M NaOH + 0.05 M Na <sub>2</sub> S    0.1 M NaOH	100	0.62	71
Co <sub>3</sub> S <sub>4</sub>	1 M NaOH +1M Na <sub>2</sub> S    1 M NaOH	400	0.32	148
Ni-Co-S/ NF	1 M NaOH +1M Na <sub>2</sub> S    1 M NaOH	370	0.6	180
CuCoS/CC	1 M NaOH +4M Na <sub>2</sub> S    1 M NaOH	400	0.415	22
VSe <sub>2</sub>	1 M NaOH +1M Na <sub>2</sub> S    1 M NaOH	1040	0.6	151

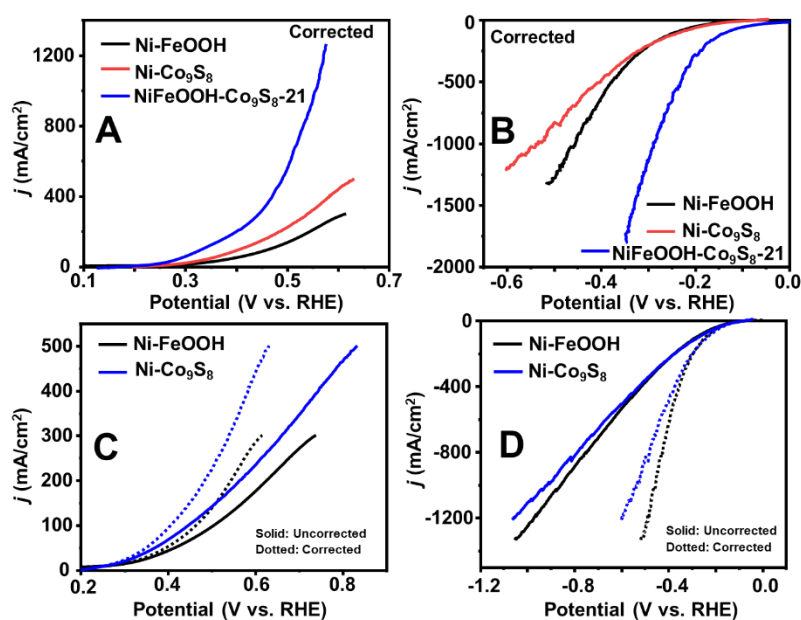


**Figure A 13:** The NiFeOOH-Co<sub>9</sub>S<sub>8</sub>-21 and control samples' (A) SOR and (B) HER traces, as well as the (C) SOR and (D) HER traces of the Ni-FeOOH and Ni-Co<sub>9</sub>S<sub>8</sub> control samples.

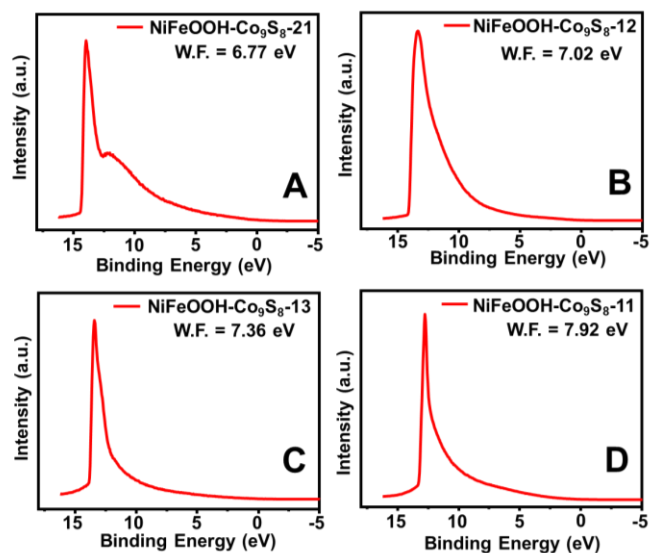


**Figure A 14:** The UPS spectra of NiFeOOH-Co<sub>9</sub>S<sub>8</sub>-21, Co<sub>9</sub>S<sub>8</sub>-12, Co<sub>9</sub>S<sub>8</sub>-13, and Co<sub>9</sub>S<sub>8</sub>-11 are shown in (A), (B),(C) and (D) respectively.

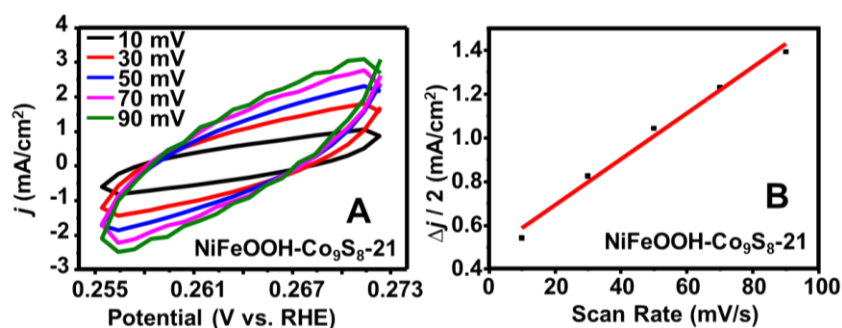


**Figure A 15** The non-faradaic potential region's cyclic voltammograms of (A) NiFeOOH-Co<sub>9</sub>S<sub>8</sub>-21 at different scan rates and (B) the average current density plotted against scan rate.

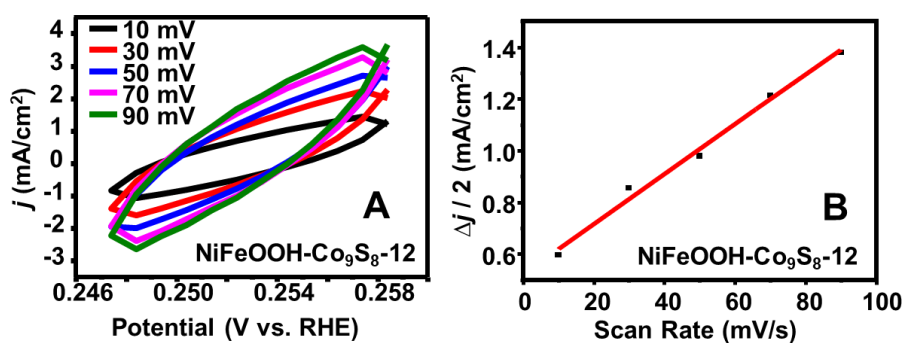


**Figure A 16:** The non-faradaic potential region's cyclic voltammograms of (A) NiFeOOH-Co<sub>9</sub>S<sub>8</sub>-12 at different scan rates and (B) the average current density plotted against scan rate.

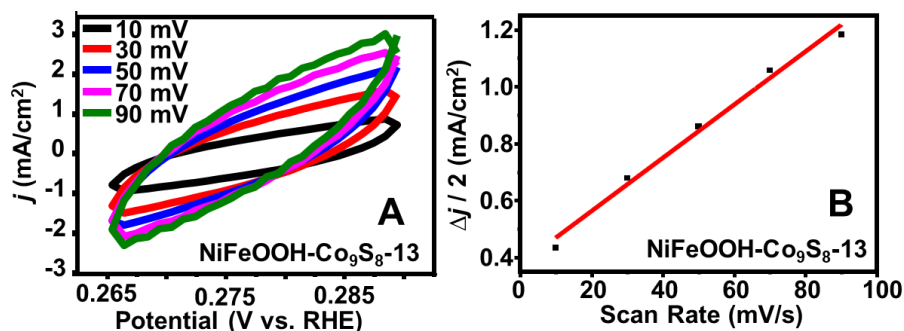


**Figure A 17:** The non-faradaic potential region's cyclic voltammograms of (A) NiFeOOH-Co<sub>9</sub>S<sub>8</sub>-13 at different scan rates and (B) the average current density plotted against scan rate.

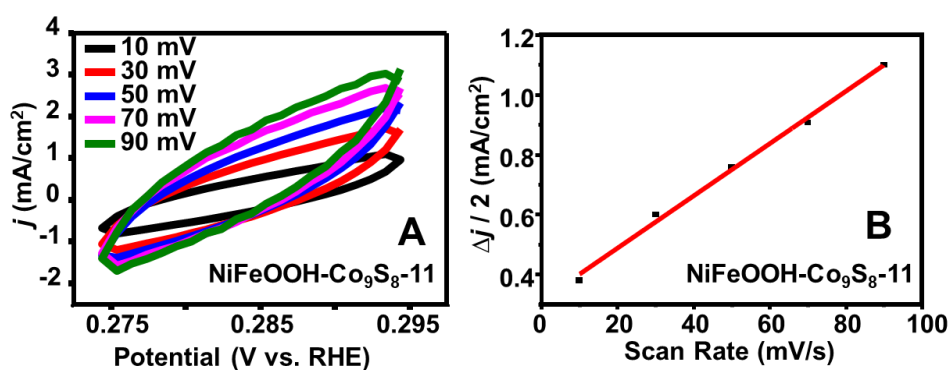


**Figure A 18:** The non-faradaic potential region's cyclic voltammograms of (A) NiFeOOH-Co<sub>9</sub>S<sub>8</sub>-11 at different scan rates and (B) the average current density plotted against scan rate.

**Table A 4:** The Co<sub>9</sub>S<sub>8</sub>-n NiFeOOH electrodes' electrochemical surface area (ECSA)

Catalyst	C <sub>dl</sub> (mF)	ECSA (cm <sup>2</sup> )
NiFeOOH- Co <sub>9</sub> S <sub>8</sub> -11	2.18	54.5

NiFeOOH- Co <sub>9</sub> S <sub>8</sub> -13	2.34	58.5
NiFeOOH- Co <sub>9</sub> S <sub>8</sub> -12	2.41	60.3
NiFeOOH- Co <sub>9</sub> S <sub>8</sub> -21	2.63	65.8

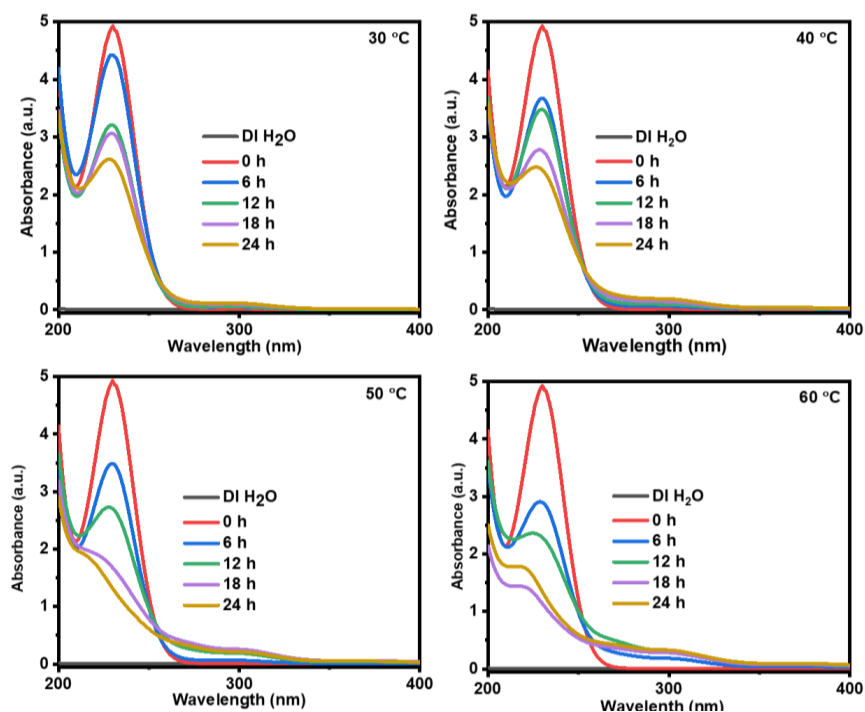
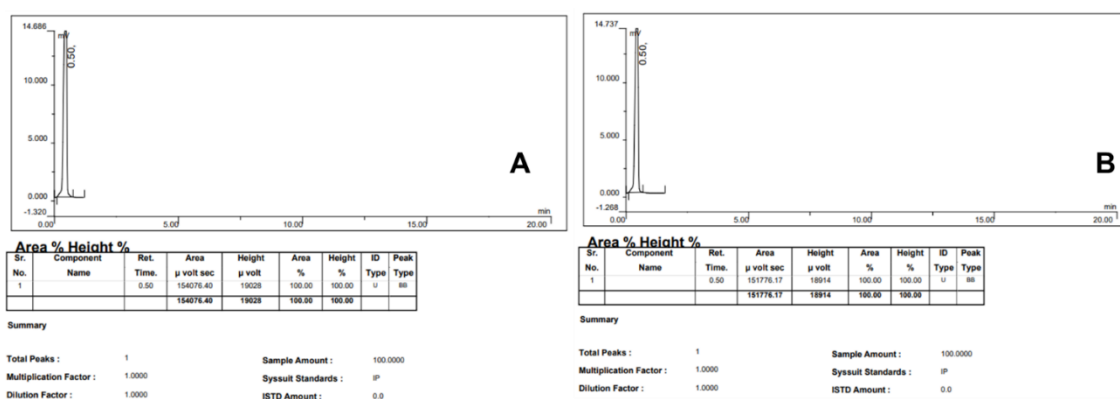


**Figure A 19:** The amount of S<sup>2-</sup> and Sn<sup>2-</sup> is shown by UV-Vis data of a 1M NaOH + 1M Na<sub>2</sub>S solution after varying electrolysis times and temperatures.

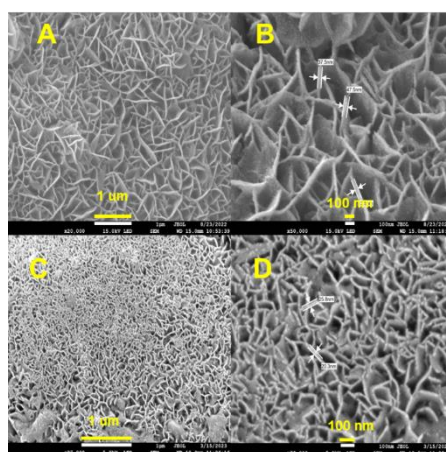
**Table A 5:** The total potential (SOR + HER) of the current electrodes in a two-electrode setup is compared with current research.

Catalyst	$j$ (mA/cm <sup>2</sup> )	Overall Potential (V)	Ref.
NiFeOOH- Co <sub>9</sub> S <sub>8</sub> -21	100	0.5 (iR Uncorrected)	This Work
CoS <sub>2</sub> @C/MXene/NF	100	0.58 (Corrected)	292
WS <sub>2</sub>	60	0.9 (Corrected)	72

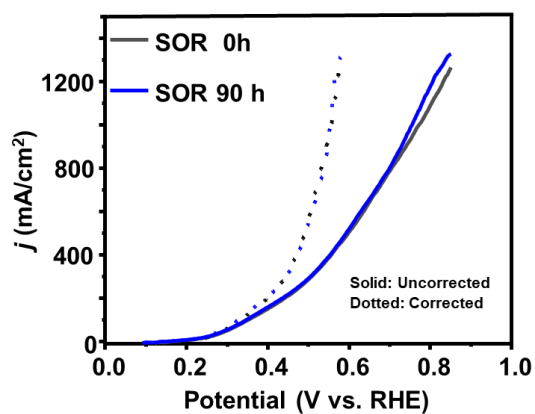
NiS <sub>2</sub>	100	0.76 (Corrected)	70
Co <sub>3</sub> S <sub>4</sub>	100	0.455 (Corrected)	148
Ni-Co-S/ NF	100	0.482 (Corrected)	180
CuCoS/CC	100	0.66 (Corrected)	22



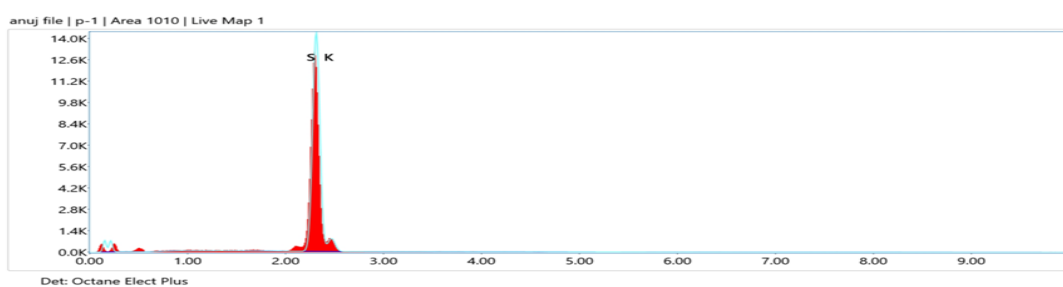
**Figure A 20:** Data of a gas chromatograph (GC) showing (A) pure hydrogen and (B) hydrogen sample.



**Figure A 21:** NiFeOOH-Co<sub>9</sub>S<sub>8</sub>-21 FESEM data taken before (A&B) and after (C&D) the stability study's 90-hour period.



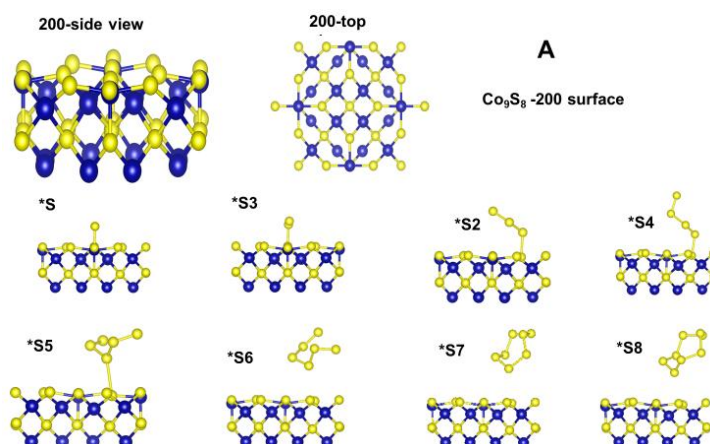
**Figure A 22:** The NiFeOOH-Co<sub>9</sub>S<sub>8</sub>-21 SOR data taken both before and after the stability study's 90-hour period.



**Figure A 23:** SOR-derived molecular sulfur elemental mapping.

**Table A 6:** CHNS data of elemental Sulfur.

Sample Code	Sample weight in mg	C/N Ratio	C%	H%	N%	S%
Sn	3.1	1.2274	0.07	0.187	0.06	99.68



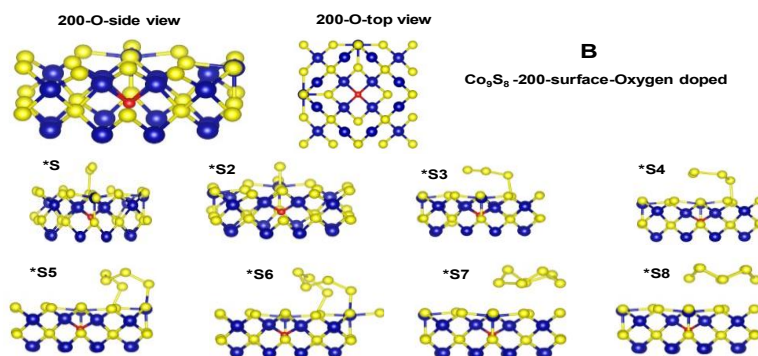


**Figure A 24:** The optimal intermediate and structure for (A) the  $\text{Co}_9\text{S}_8$ -200 surface and (B) the oxygen-doped  $\text{Co}_9\text{S}_8$ -200 surface.

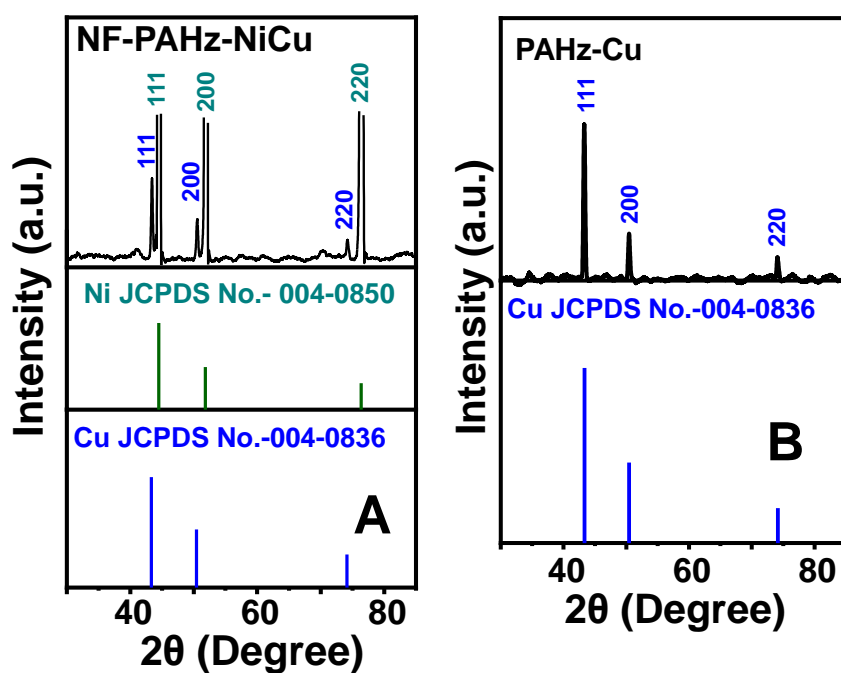


**Figure A 25:** The JCPDS correlation plots and the XRD data of the (A) NF-PAHz-NiCu electrode and the (B) PAHz-Cu electrode.

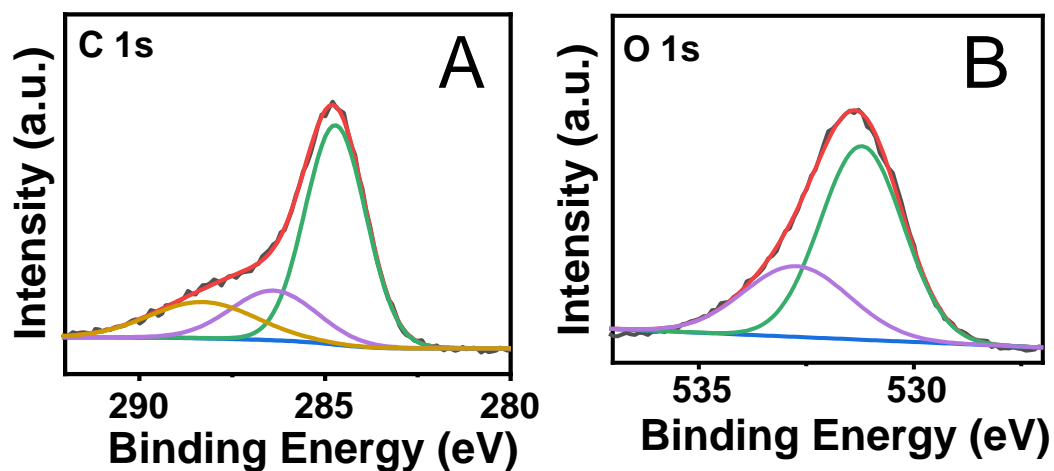


Figure A 26: The NF-PAHz-Co<sub>3</sub>O<sub>4</sub>@NiCu electrode XPS data (A) C 1s and (B) O 1s.

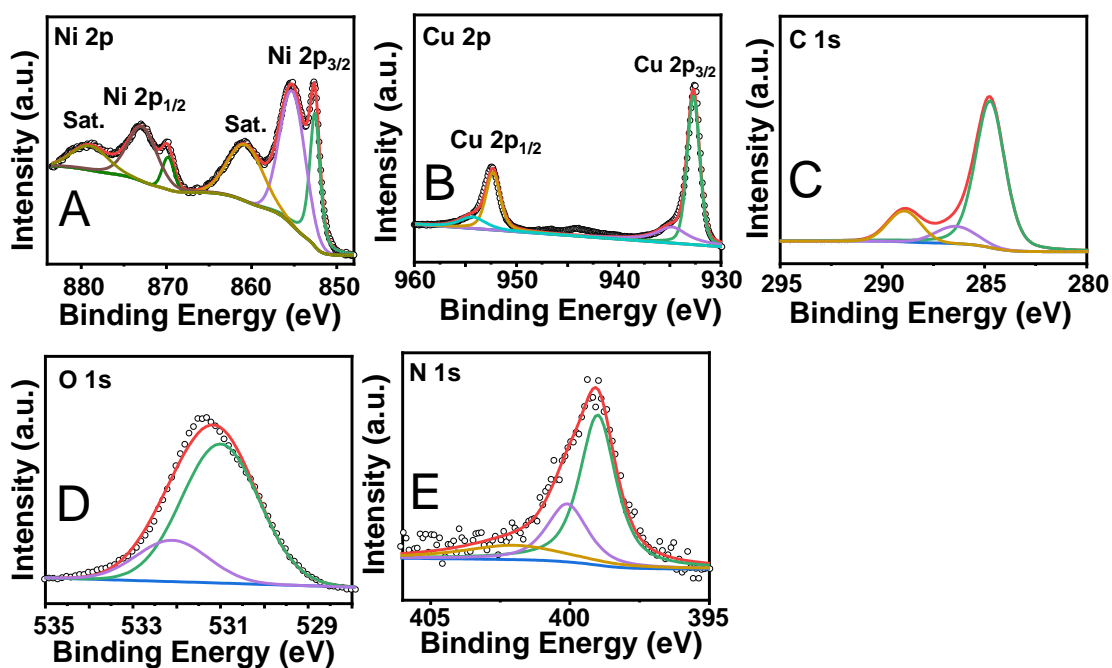
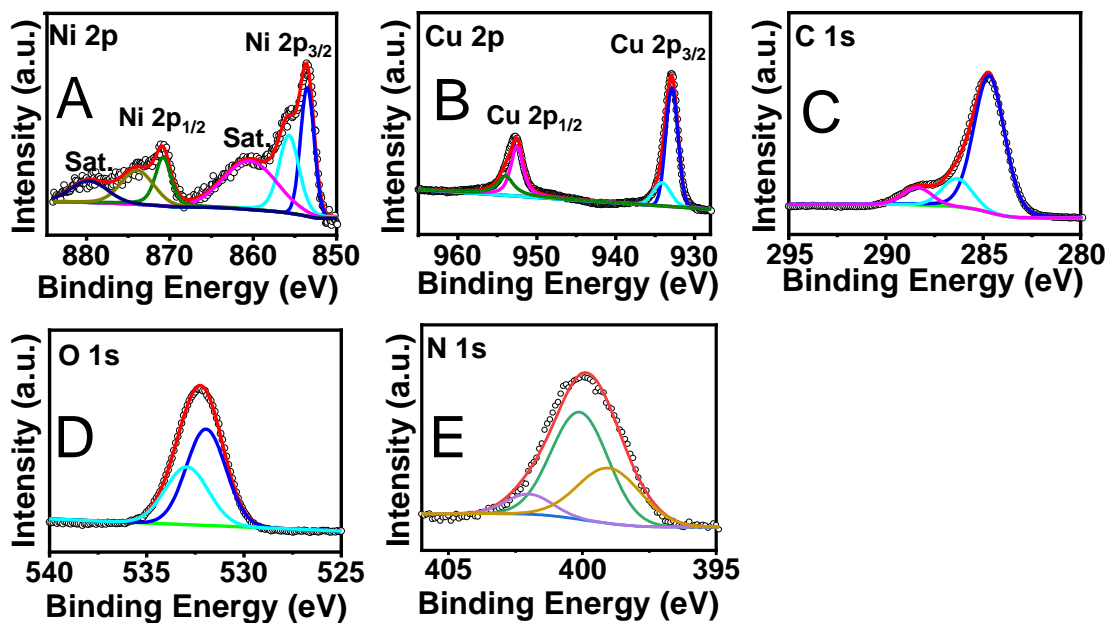
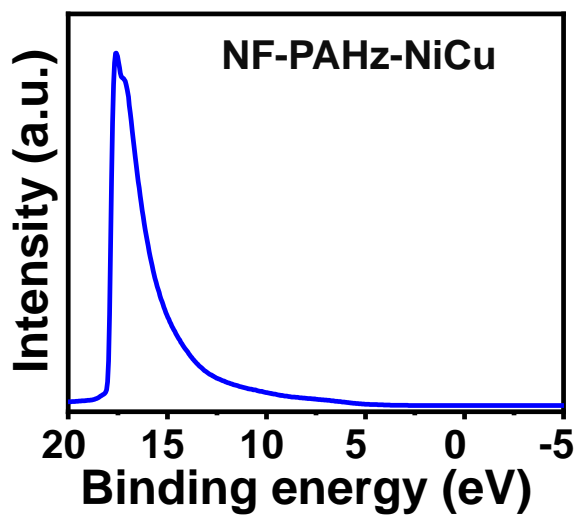


Figure A 27: The NF-PAHz-NiCu electrode's (A) Ni 2p, (B) Cu 2p, (C) C 1s, (D) O 1s, and (E) N 1s XPS traces.



**Figure A 28:** The PAHz-Cu electrode's (A) Ni 2p, (B) Cu 2p, (C) C 1s, (D) O 1s, and (E) N 1s XPS traces.



**Figure A 29:** The NF-PAHz-NiCu UPS spectrum.

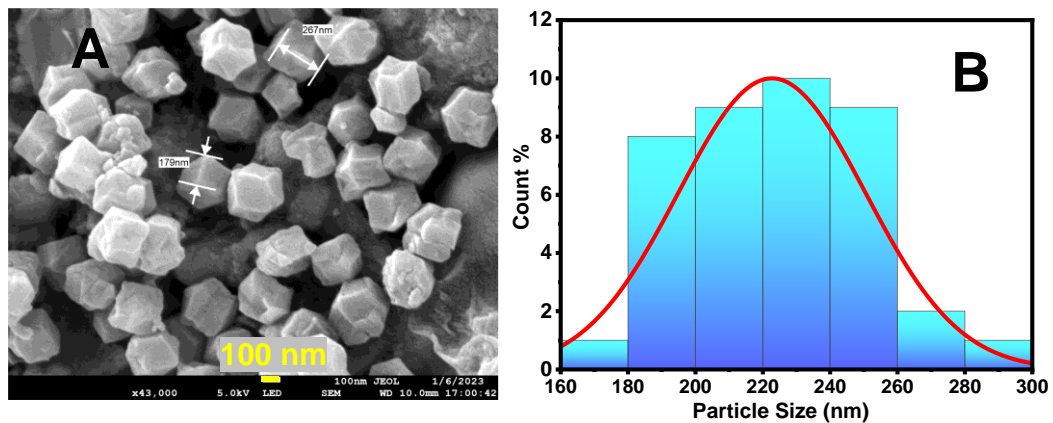


**Figure A 30:** The (A) FE-SEM image and (B) the corresponding average particle size distribution of NF-PAHz-Co<sub>3</sub>O<sub>4</sub>@NiCu.

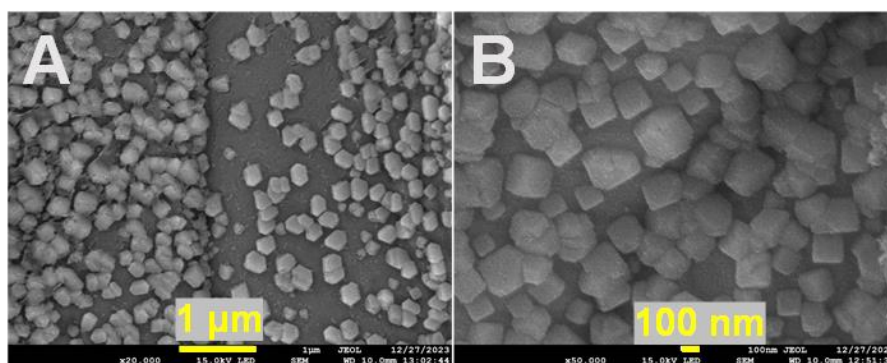


**Figure A 31:** The (A & B) BF-SEM images of Batch 2 of NF-PAHz-Co<sub>3</sub>O<sub>4</sub>@NiCu taken at various magnifications.

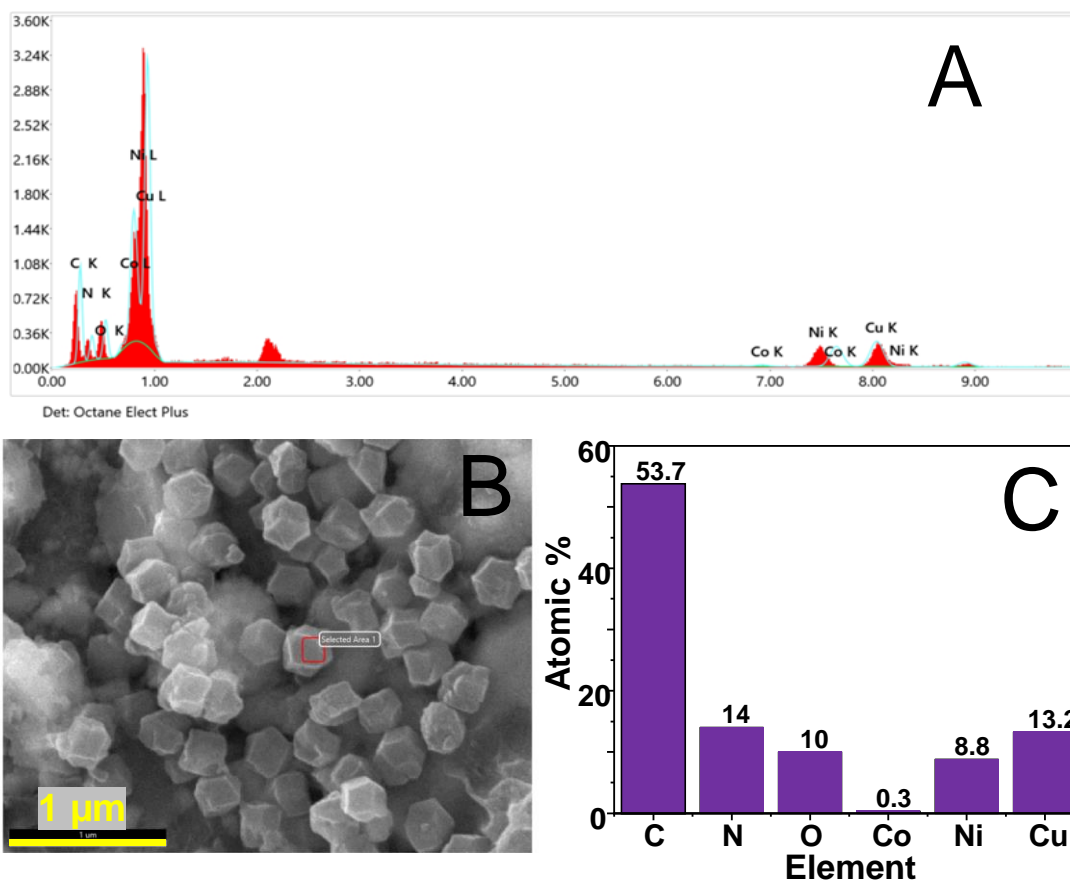


**Figure A 32:** The NF-PAHz- $\text{Co}_3\text{O}_4$ @NiCu nanocuboid EDX spectra (A), FESEM image (B), and atomic percentage distribution (C).

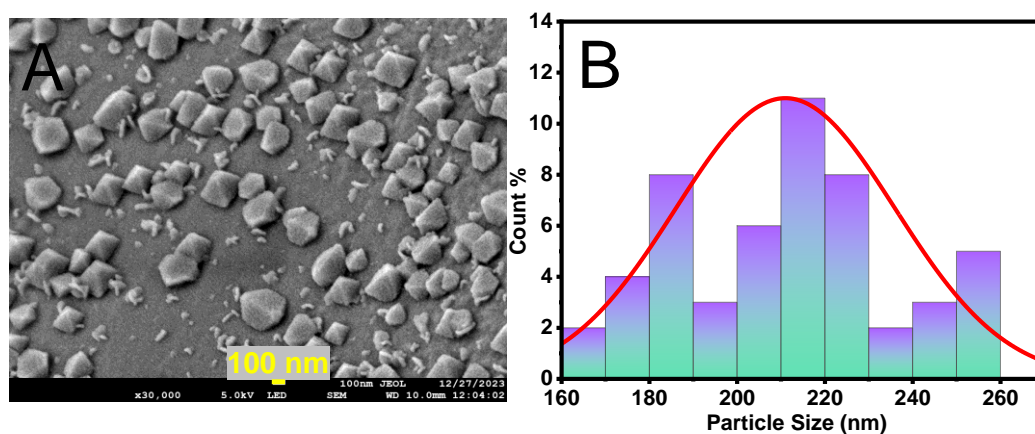


**Figure A 33:** The NF-PAHz-NiCu's (A) FE-SEM image and (B) average particle size distribution.

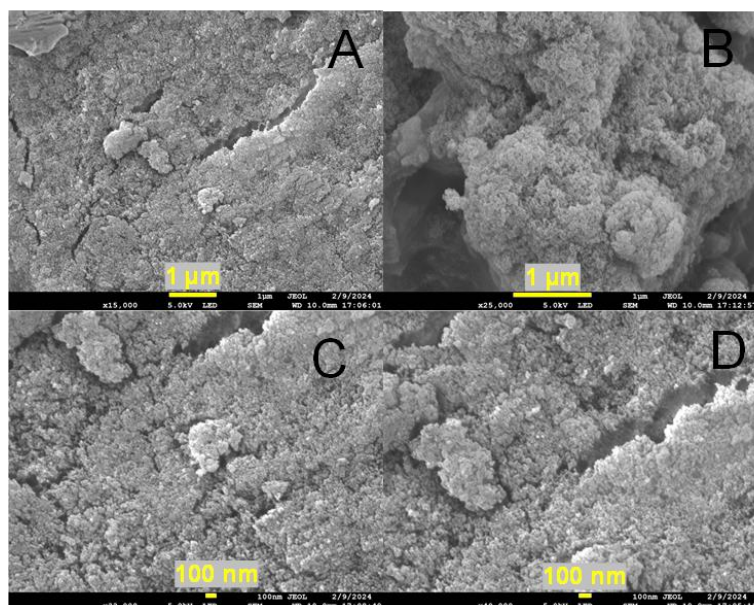


**Figure A 34:** (A-D) PAHz-Cu FE-SEM images taken at various magnifications.

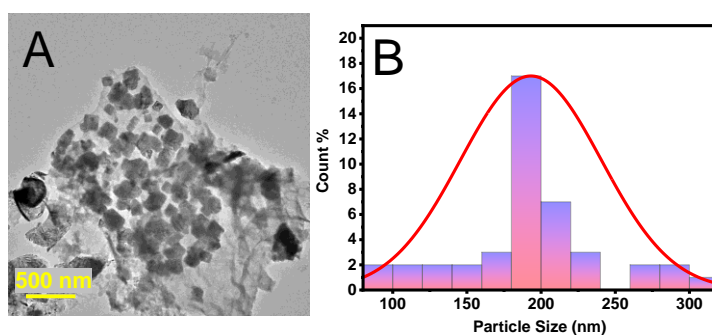


**Figure A 35:** The NF-PAHz-Co<sub>3</sub>O<sub>4</sub>@NiCu's (A) HR-TEM image and (B) average particle size distribution.

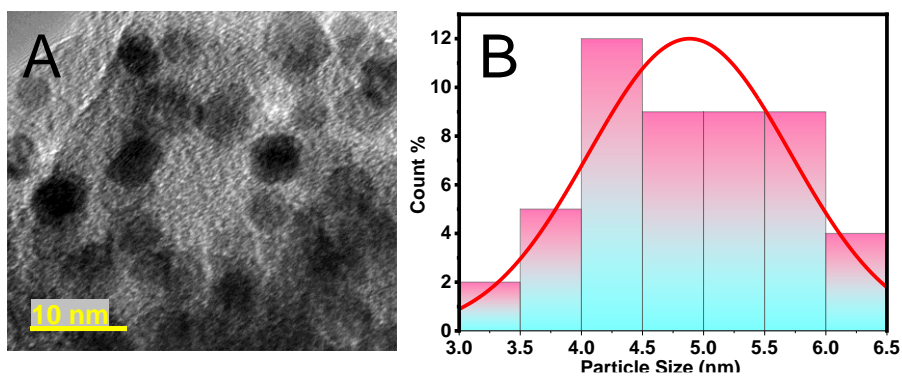


**Figure A 36:** The (A) HR-TEM image and (B) average particle size distribution of NiCu alloy nanoparticles depict inside one of the NF-PAHz-Co<sub>3</sub>O<sub>4</sub>@NiCu cubiod.

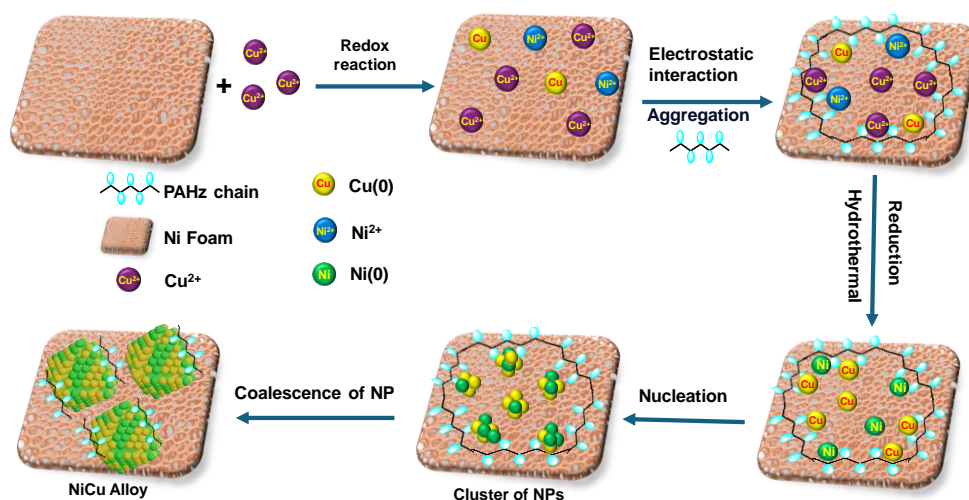


**Figure A 37:** The mechanism for the synthesis of NiCu alloy under specified reaction circumstances has been proposed.

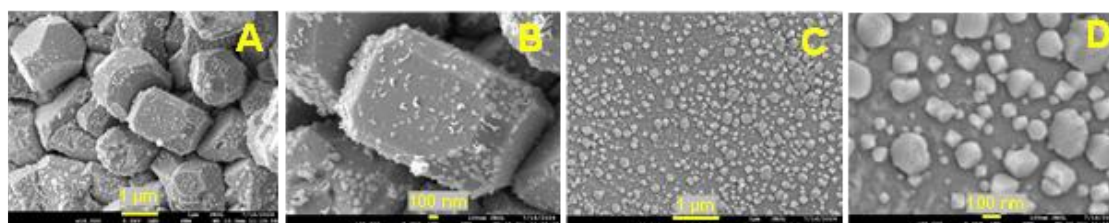


**Figure A 38:** The FE-SEM images of (A & B) NF-4PAHz-Co<sub>3</sub>O<sub>4</sub>@NiCu and (C & D) NF-6PAHz-Co<sub>3</sub>O<sub>4</sub>@NiCu.

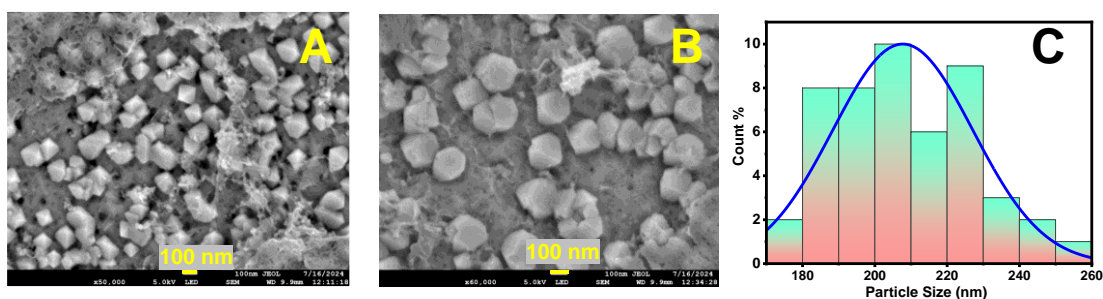


**Figure A 39:** The (A & B) FE-SEM images and (C) average particle size distribution of NF-PAHz-Co<sub>3</sub>O<sub>4</sub>@NiCu-25.

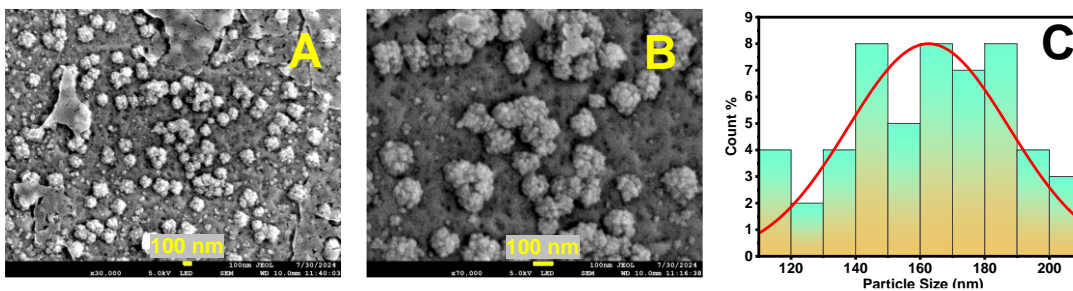


**Figure A 40:** The (A & B) FE-SEM image and (C) and average particle size distribution of NF-PAHz-Co<sub>3</sub>O<sub>4</sub>@NiCu-8.

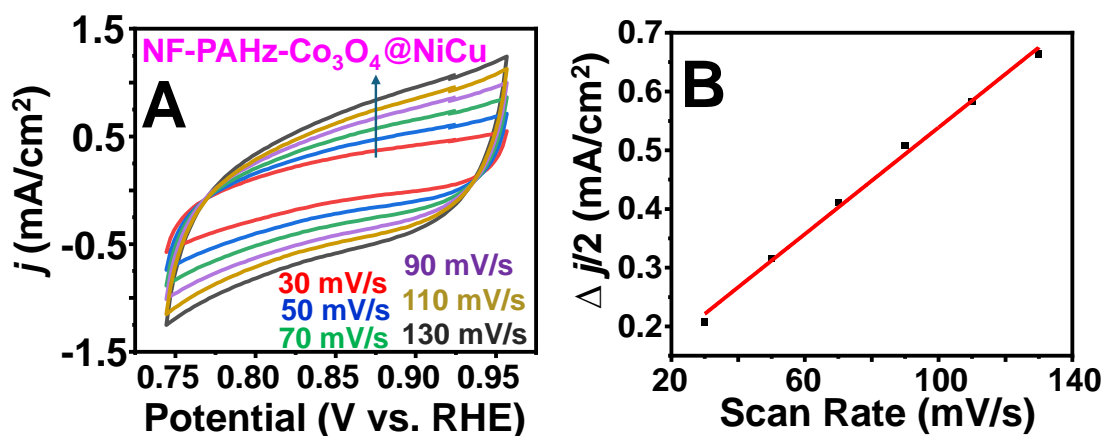


**Figure A 41:** (A) Cyclic voltammograms in the non-faradaic potential zone acquired at different scan rates, and (B) average current density plotted against scan rate of NF-PAHz-Co<sub>3</sub>O<sub>4</sub>@NiCu.

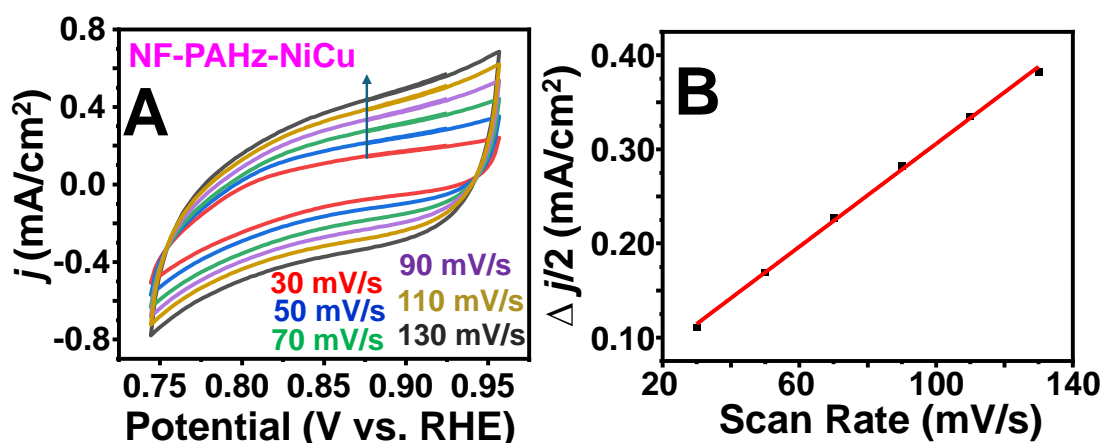


**Figure A 42:** (A) Cyclic voltammograms in the non-faradaic potential zone acquired at different scan rates, and (B) average current density plotted against scan rate of NF-PAHz-NiCu.

**Table A 7:** NF-PAHz-Co<sub>3</sub>O<sub>4</sub>@NiCu and NF-PAHz-NiCu electrodes' electrochemical surface area (ECSA).

Catalyst	C <sub>dl</sub> (mF)	ECSA (cm <sup>2</sup> )
NF-PAHz-NiCu	0.67	16.8
NF-PAHz-Co <sub>3</sub> O <sub>4</sub> @NiCu	1.14	28.5

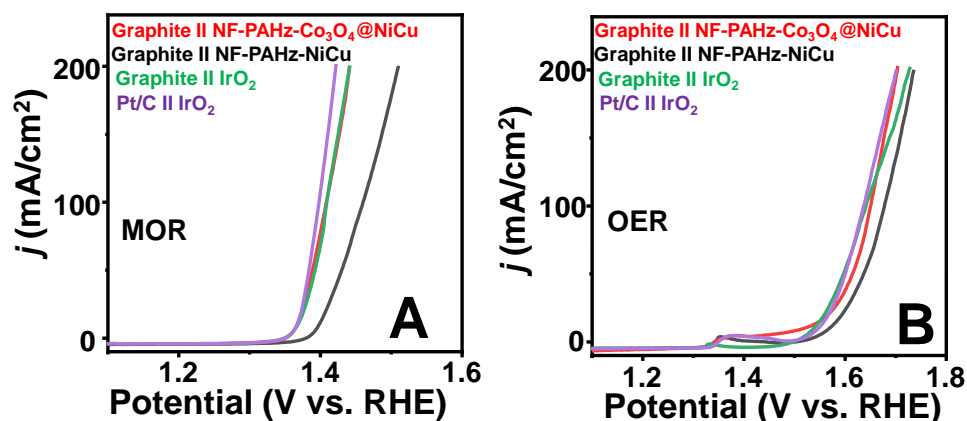


**Figure A 43:** The LSV traces for (A) MOR and (B) OER of NF-PAHz-Co<sub>3</sub>O<sub>4</sub>@NiCu, NF-PAHz-NiCu and benchmark IrO<sub>2</sub> recorded using a graphite or Pt/C as a counter electrode.

**Table A 8:** The  $j_{\text{MOR}}$  value achieved at 1.5 V<sub>RHE</sub> for several catalyst compositions reported in literature.

Catalyst	$j$ (mA/cm <sup>2</sup> )	Potential (V <sub>RHE</sub> )	Scan rate (mV/s)	Electrolyte	References
Cu/CuNi NWs 220/C	27	1.5	50	1 M MeOH + 1 M KOH	[85]
Pt-NP/NiO-NS	250	1.5	---	1 M MeOH + 1 M KOH	[293]
CNFs@NiSe/CC	295	1.5	5	1 M MeOH + 1 M KOH	[86]
NiO/NF	100	1.5 (without IR Corr.)	10	1 M MeOH + 1 M KOH	[87]
Fe-Ni NPs	5	1.5 V	20	1 M MeOH + 1 M NaOH	[88]
NiCo <sub>2</sub> Px	52	1.5	5	1 M MeOH + 1 M KOH	[294]

NiB-400	105	1.5	5	1 M MeOH + 1 M KOH	[81]
Ni/N-C@500	70	1.5	50	1 M MeOH + 1 M KOH	[89]
NiCu-220@C	27	1.5	---	1 M MeOH + 1 M KOH	[90]
NiSnPH@OOH/CC	160	1.5	5	1 M MeOH + 1 M KOH	[295]
Co-CuO	34	1.5	---	1 M MeOH + 1 M KOH	[296]
CuONS/CF	90	1.5	5	1 M MeOH + 1 M KOH	[297]
Fe-NiCo-LDH	260	1.5	5	1 M MeOH + 1 M KOH	[298]
Ni(OH) <sub>2</sub> / MnCO <sub>3</sub>	55	1.5	50	1 M MeOH + 1 M KOH	[91]
Co-INF	260	1.5	---	1 M MeOH + 1 M KOH	[299]
NF-PAHz- Co <sub>3</sub> O <sub>4</sub> @NiCu	448	1.5	5	1 M MeOH + 1 M KOH	THIS WORK

Note – The current density values are manually estimated from the literature in several cases.

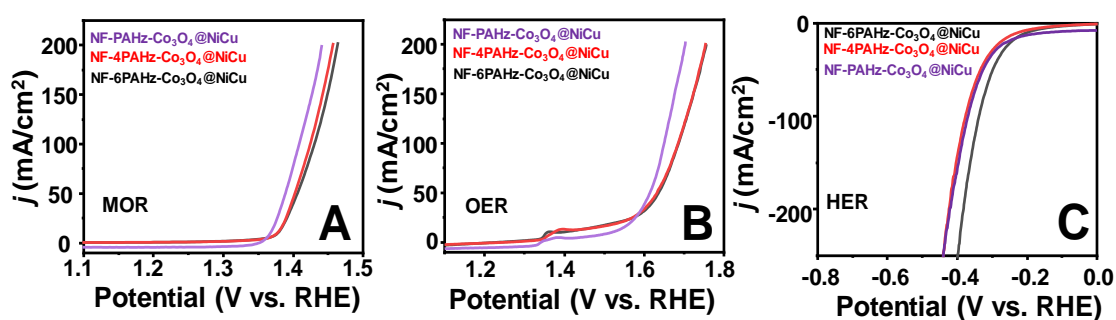


**Figure A 44:** The NF-PAHz-Co<sub>3</sub>O<sub>4</sub>@NiCu's (A) MOR, (B) OER, and (C) HER traces with varying PAHz concentrations.

**Table A 9:** The comparison of the NF-PAHz-Co<sub>3</sub>O<sub>4</sub>@NiCu electrocatalytic activity at 100 mA/cm<sup>2</sup> with varying PAHz concentrations.

Sample Code	PAHz (wt%)	Average Size	MOR@100 mA/cm <sup>2</sup>	OER@100 mA/cm <sup>2</sup>	HER@100 mA/cm <sup>2</sup>
NF-PAHz-Co <sub>3</sub> O <sub>4</sub> @NiCu	2	220 nm	1.41 V <sub>RHE</sub>	1.65 V <sub>RHE</sub>	-0.37 V <sub>RHE</sub>
NF-4PAHz-Co <sub>3</sub> O <sub>4</sub> @NiCu	4	1600 nm	1.43 V <sub>RHE</sub>	1.69 V <sub>RHE</sub>	-0.38 V <sub>RHE</sub>
NF-6PAHz-Co <sub>3</sub> O <sub>4</sub> @NiCu	6	175 nm	1.43 V <sub>RHE</sub>	1.69 V <sub>RHE</sub>	-0.34 V <sub>RHE</sub>

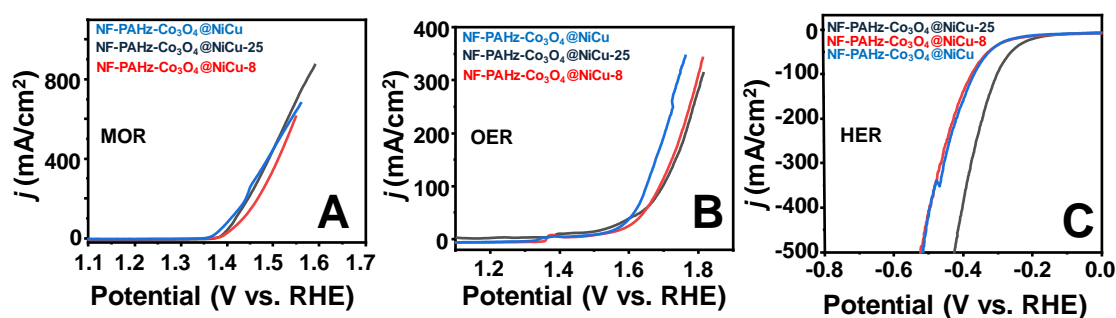


**Figure A 45:** The NF-PAHz-Co<sub>3</sub>O<sub>4</sub>@NiCu's (A) MOR, (B) OER, and (C) HER at varying Cu<sup>2+</sup> concentrations.

**Table A 10:** The comparison of the NF-PAHz-Co<sub>3</sub>O<sub>4</sub>@NiCu electrocatalytic activity at 100 mA/cm<sup>2</sup> with varying Cu<sup>2+</sup> concentrations.

Sample Code	[Cu <sup>2+</sup> ] (mM)	Average Size (nm)	MOR @100 mA/cm <sup>2</sup>	OER @100 mA/cm <sup>2</sup>	HER @100 mA/cm <sup>2</sup>
NF-PAHz-Co <sub>3</sub> O <sub>4</sub> @NiCu	16.55	220	1.41 V <sub>RHE</sub>	1.65 V <sub>RHE</sub>	-0.37 V <sub>RHE</sub>
NF-PAHz-Co <sub>3</sub> O <sub>4</sub> @NiCu-25	24.83	208	1.42 V <sub>RHE</sub>	1.70 V <sub>RHE</sub>	-0.30 V <sub>RHE</sub>
NF-PAHz-Co <sub>3</sub> O <sub>4</sub> @NiCu-8	8.27	162.7	1.44 V <sub>RHE</sub>	1.69 V <sub>RHE</sub>	-0.38 V <sub>RHE</sub>

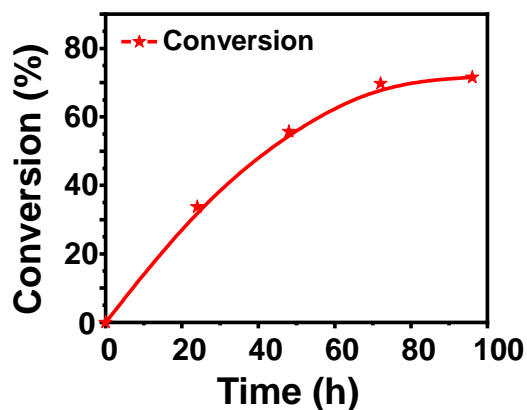


**Figure A 46:** The conversion values from  $^1\text{H}$  NMR spectroscopy were determined by comparing the peak integrations in the conversion plot of methanol to formate at various time intervals.

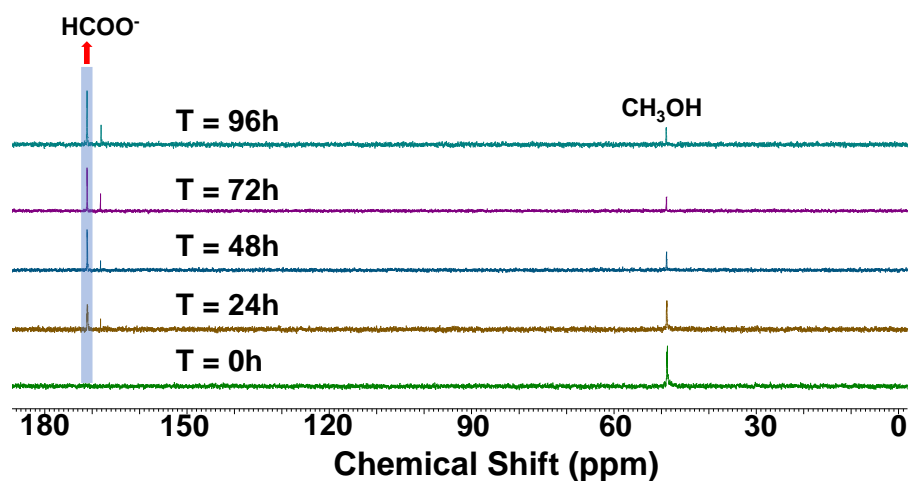


**Figure A 47:** The electrolyte's  $^{13}\text{C}$  NMR spectra were acquired at various electrolysis time intervals using 1.0 M KOH + 1.0 M MeOH.

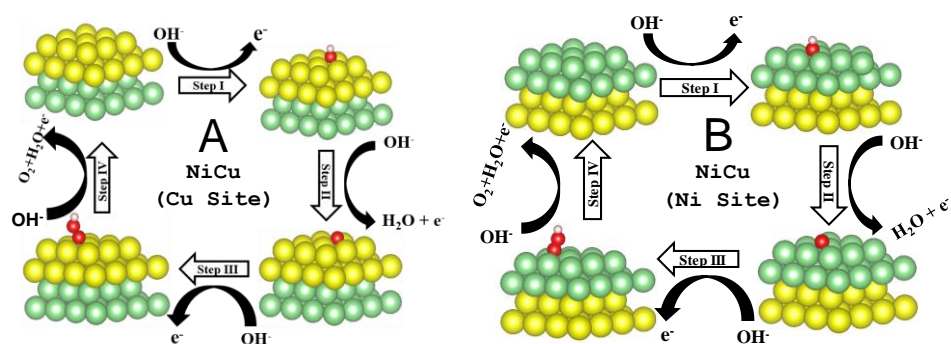


**Figure A 48:** A schematic representation of the OER activity on the NiCu alloy's (A) Cu and (B) Ni sites.

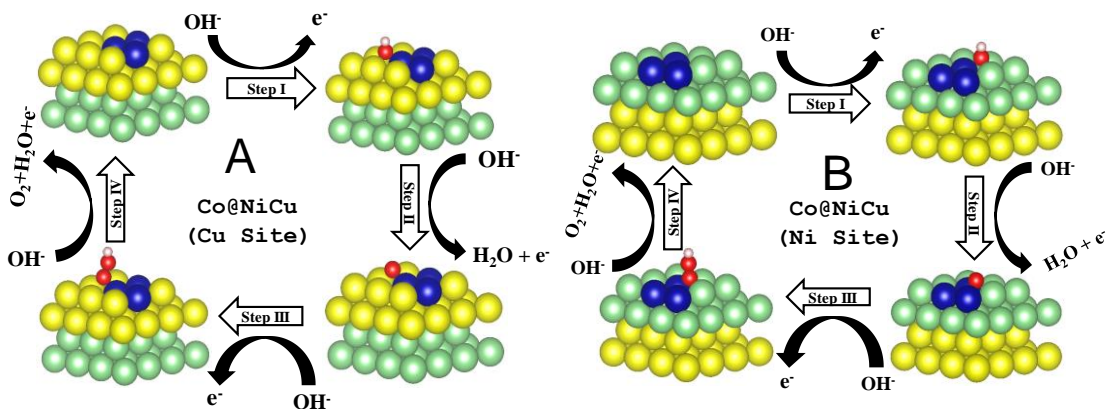


**Figure A 49:** A schematic representation of the OER activity of the Co doped on the Co@NiCu alloy's (A) Cu and (B) Ni sites.

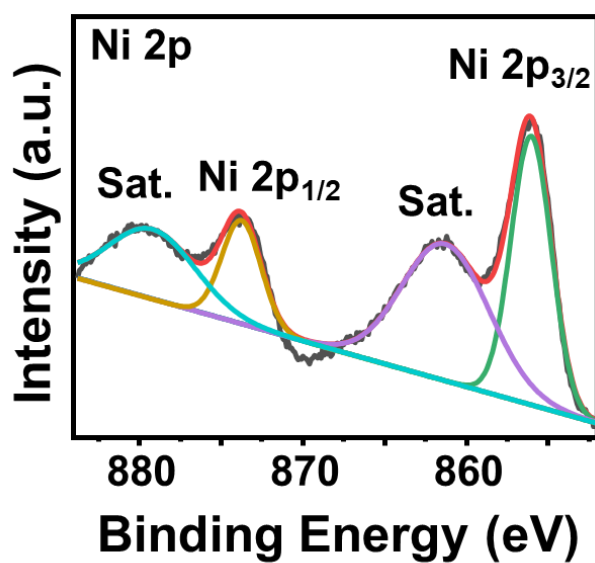


**Figure A 50:** The Ni 2p XPS spectra of Ni<sub>3</sub>S<sub>2</sub>/NF.

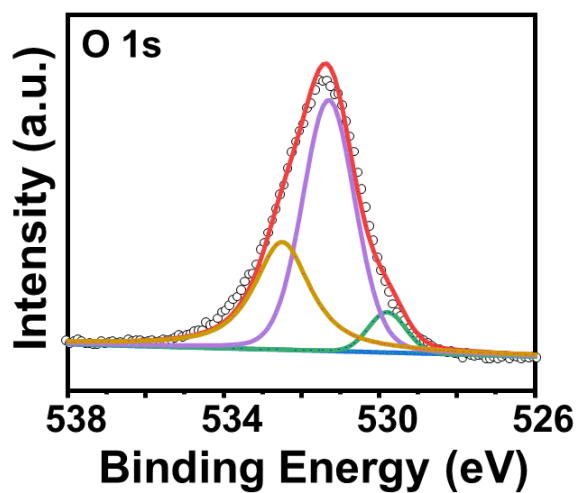


**Figure A 51:** The O 1s XPS spectra of CF-CeO<sub>2</sub>/Ni<sub>3</sub>S<sub>2</sub>.

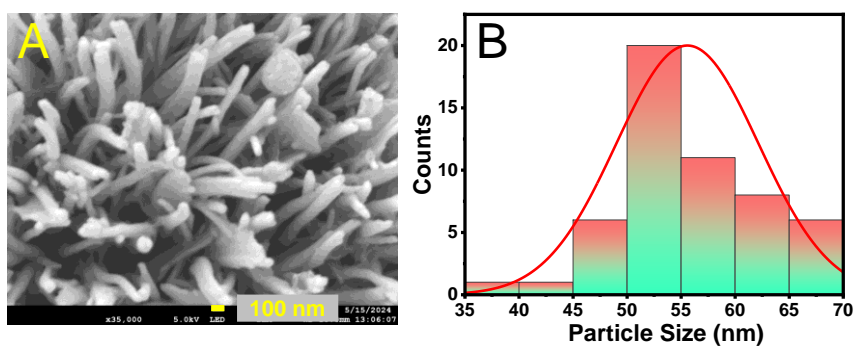


**Figure A 52:**The (A) FE-SEM image and (B) the corresponding average particle size distribution of CF-CeO<sub>2</sub>/Ni<sub>3</sub>S<sub>2</sub>.

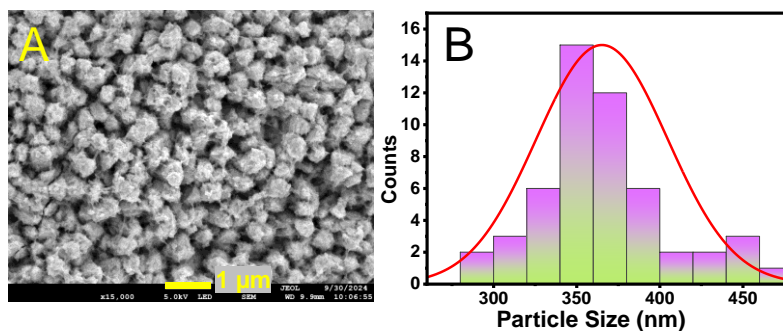


**Figure A 53:**The (A) FE-SEM image and (B) the corresponding average particle size distribution of Ni<sub>3</sub>S<sub>2</sub>/NF.

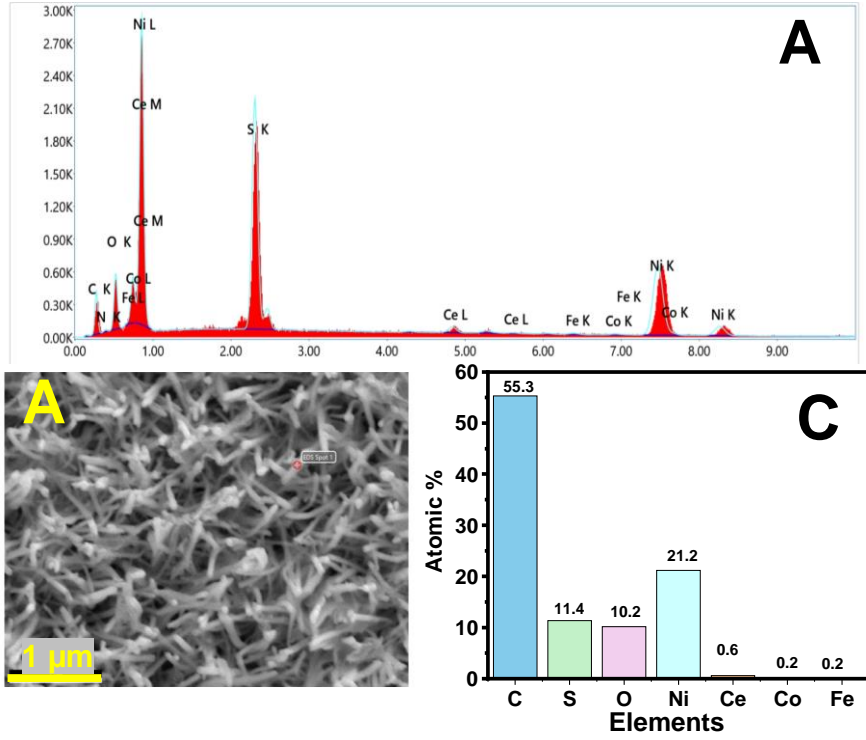


**Figure A 54:** The (A) FE-SEM EDX spectra (B) the corresponding FE-SEM image and (C) Atomic % obtained from EDX spectra of CF-CeO<sub>2</sub>/Ni<sub>3</sub>S<sub>2</sub>.

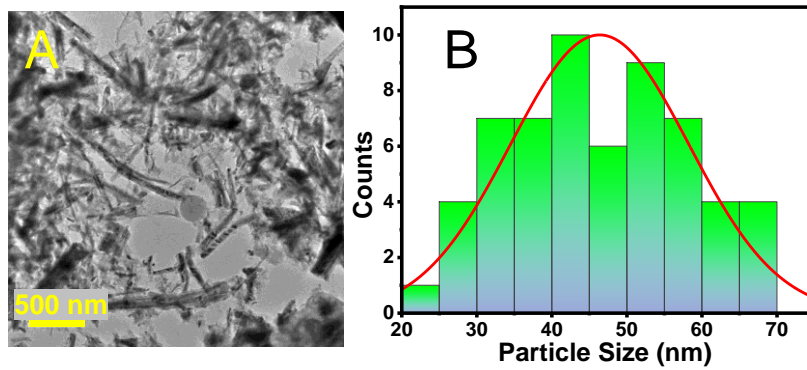


**Figure A 55:** The (A) HR-TEM image and (B) the corresponding average particle size distribution of CF-CeO<sub>2</sub>/Ni<sub>3</sub>S<sub>2</sub>.

**Table A 11:** The  $10 \text{ mA/cm}^2$   $j_{\text{UOR}}$  value comparison for several catalyst compositions reported in literature.

S. No.	Catalysts	$V_{\text{RHE}}$ at $10 \text{ mA/cm}^2$	Electrolyte	Ref.
1.	NF/NiMoO-Ar	1.37	1M KOH + 0.5 M Urea	125
2.	Zn <sub>0.08</sub> Co <sub>0.92</sub> P/TM	1.38	1M KOH + 0.5 M Urea	300
3.	Ni-CoP/HPFs	1.43	1M KOH + 0.5 M Urea	301
4.	NF-G-Mn CoPx-NF	1.41	1M KOH + 0.5 M Urea	302
5.	P-NTS-0.5	1.36	1M KOH + 0.33 M Urea	303
6.	MOF-Ni@MOF-Fe	1.35	1M KOH + 0.5 M Urea	304
7.	CoNi-LDH	1.38	1M KOH + 0.5 M Urea	305
8.	Ni (OH) <sub>2</sub> /MnO <sub>2</sub>	1.46	1M KOH + 0.5 M Urea	306
9.	CeO <sub>2</sub> -NiMoO <sub>4</sub>	1.35	1M KOH + 0.5 M Urea	307
10.	NiO-NiPi	1.35	1M KOH + 0.5 M Urea	308
11.	Amorphous Ni-S-Se	1.38	1M KOH + 0.5 M Urea	309
12.	Ni <sub>2</sub> P nanoflakes	1.430	1 M KOH + 0.5 M urea	310
13.	V-Doped Ni <sub>3</sub> N/NF	1.36	1 M KOH + 0.5 M urea	311
14.	Ni/N-Doped CNT	1.38	1 M KOH + 0.5 M urea	312
15.	NiFe(OH) <sub>x</sub> @Ni <sub>3</sub> N/NF	1.36	1 M KOH + 1.0 M urea	313
16.	Ni <sub>3</sub> S <sub>2</sub> /NF	1.36	1M KOH + 0.5 M urea	This work
17.	CF-CeO <sub>2</sub> @Ni <sub>3</sub> S <sub>2</sub> /NF	1.35	1 M KOH + 0.5 M urea	This work

## References

---

1. Chu, S.; Majumdar, A. Opportunities and challenges for a sustainable energy future. *Nature* **2012**, *488*, 294.
2. Sherif, S. A.; Barbir, F.; Veziroglu, T. N. Towards a hydrogen economy. *The Electricity Journal* **2005**, *18*, 62.
3. Staffell, I.; Scamman, D.; Abad, A. V.; Balcombe, P.; Dodds, P. E.; Ekins, P.; Shah, N.; Ward, K. R. The role of hydrogen and fuel cells in the global energy system. *Energy & Environmental Science* **2018**, *12*, 463.
4. Song, G.; Wei, M.; Zhou, J.; Mu, L.; Song, S. Modulation of the Phase Transformation of Fe<sub>2</sub>O<sub>3</sub> for Enhanced Water Oxidation under a Magnetic Field. *ACS Catalysis* **2024**, *14*, 846.
5. Kong, S.; Li, A.; Long, J.; Adachi, K.; Hashizume, D.; Jiang, Q.; Fushimi, K.; Ooka, H.; Xiao, J.; Nakamura, R. Acid-stable manganese oxides for proton exchange membrane water electrolysis. *Nature Catalysis* **2024**, *7*, 252.
6. Chen, Y.; Zheng, D. J.; Xu, Z. J.; Shao-Horn, Y. Best practices for oxygen electrocatalysis. *Nature Sustainability* **2024**, *7*, 371.
7. Zhang, W.; Liu, M.; Gu, X.; Shi, Y.; Deng, Z.; Cai, N. Water Electrolysis toward Elevated Temperature: Advances, Challenges and Frontiers. *Chemical Reviews* **2023**, *123*, 7119.
8. Wang, T.; Cao, X.; Jiao, L. Progress in Hydrogen Production Coupled with Electrochemical Oxidation of Small Molecules. *Angewandte Chemie International Edition* **2022**, *61*, 202213328.
9. Abdelghafar, F.; Xu, X.; Jiang, S. P.; Shao, Z. Perovskite for electrocatalytic oxygen evolution at elevated temperatures. *ChemSusChem* **2024**, *17*, e202301534.

10. Sun, H.; Xu, X.; Kim, H.; Shao, Z.; Jung, W. Advanced electrocatalysts with unusual active sites for electrochemical water splitting. *InfoMat* **2023**, *6*, 12494.
11. Lei, X.; Jiang, C.; Han, Q.; Zhang, X.; Zhao, K.; Yan, N.; Guo, H.; Tang, B.; Li, Y.; Cui, Y.; Fu, X.-Z.; Li, J.; Sun, Y. Unraveling the oxygen vacancy site mechanism of a Self-Assembly hybrid catalyst for efficient alkaline water oxidation. *ACS Catalysis* **2024**, *14*, 4523.
12. Hua, D.; Huang, J.; Fabbri, E.; Rafique, M.; Song, B. Development of anion Exchange Membrane Water Electrolysis and the Associated Challenges: A review. *ChemElectroChem* **2022**, *10*, e202200999.
13. Park, E. J.; Arges, C. G.; Xu, H.; Kim, Y. S. Membrane Strategies for water electrolysis. *ACS Energy Letters* **2022**, *7*, 3447.
14. Slobodkin, I.; Davydova, E.; Sananis, M.; Breytus, A.; Rothschild, A. Electrochemical and chemical cycle for high-efficiency decoupled water splitting in a near-neutral electrolyte. *Nature Materials* **2024**, *23*, 398.
15. Mathur, A.; Diesendruck, C. E. Advanced Device Architecture Strategies for Decoupled Water Splitting: A review. *ACS Materials Letters* **2024**, *6*, 2725.
16. Yao, D.; Zhang, Y.; Zhang, S.; Wan, J.; Yu, H.; Jin, H. Hybrid water electrolysis with integrated and cascading reactions using two-dimensional electrocatalysts. *Journal of Materials Chemistry A* **2023**, *11*, 16433.
17. Roh, H.; Oh, S.; Lim, C.; Yong, K. Recent Progress and Challenges in Hybrid Water Electrolysis through Economic Evaluation. *ACS Materials Letters* **2024**, *6*, 3080.
18. Xu, Y.; Zhang, B. Recent Advances in Electrochemical Hydrogen Production from Water Assisted by Alternative Oxidation Reactions. *ChemElectroChem* **2019**, *6*, 3214.

19. Fan, L.; Wang, D.; Ma, K.; Zhou, C.; Yue, H. Recent Advances in Hydrogen Production from Hybrid Water Electrolysis through Alternative Oxidation Reactions. *ChemCatChem* **2024**, *16*, e202301332.
20. Zhang, R.; Jiang, S.; Rao, Y.; Chen, S.; Yue, Q.; Kang, Y. Electrochemical biomass upgrading on CoOOH nanosheets in a hybrid water electrolyzer. *Green Chemistry* **2021**, *23*, 2525.
21. Li, T.; Wang, B.; Cao, Y.; Liu, Z.; Wang, S.; Zhang, Q.; Sun, J.; Zhou, G. Energy-saving hydrogen production by seawater electrolysis coupling tip-enhanced electric field promoted electrocatalytic sulfion oxidation. *Nature Communications* **2024**, *15*, 6173.
22. Yu, H.; Wang, W.; Mao, Q.; Deng, K.; Xu, Y.; Wang, Z.; Li, X.; Wang, H.; Wang, L. Electrocatalytic sulfion recycling assisted energy-saving hydrogen production using CuCo-based nanosheet arrays. *Journal of Materials Chemistry A* **2023**, *11*, 2218.
23. Li, Y.; Wei, X.; Han, S.; Chen, L.; Shi, J. MnO<sub>2</sub> electrocatalysts coordinating alcohol oxidation for Ultra-Durable hydrogen and chemical productions in acidic solutions. *Angewandte Chemie* **2021**, *133*, 21634.
24. Li, J.; Li, L.; Wang, J.; Cabot, A.; Zhu, Y. Boosting hydrogen evolution by methanol Oxidation reaction on Ni-Based Electrocatalysts: From Fundamental Electrochemistry to Perspectives. *ACS Energy Letters* **2024**, *9*, 853.
25. Zhu, L.; Huang, J.; Meng, G.; Wu, T.; Chen, C.; Tian, H.; Chen, Y.; Kong, F.; Chang, Z.; Cui, X.; Shi, J. Active site recovery and N-N bond breakage during hydrazine oxidation boosting the electrochemical hydrogen production. *Nature Communications* **2023**, *14*, 1997.
26. Liu, Y.; Zhang, J.; Li, Y.; Qian, Q.; Li, Z.; Zhang, G. Realizing the Synergy of Interface Engineering and Chemical Substitution for Ni<sub>3</sub>N Enables its Bifunctionality

Toward Hydrazine Oxidation Assisted Energy-Saving Hydrogen Production. *Advanced Functional Materials* **2021**, *31*, 2103673.

27. Wang, T.; Miao, L.; Zheng, S.; Qin, H.; Cao, X.; Yang, L.; Jiao, L. Interfacial engineering of Ni<sub>3</sub>N/Mo<sub>2</sub>N heterojunctions for Urea-Assisted Hydrogen Evolution Reaction. *ACS Catalysis* **2023**, *13*, 4091.

28. Wang, C.; Lu, H.; Mao, Z.; Yan, C.; Shen, G.; Wang, X. Bimetal Schottky Heterojunction Boosting Energy-Saving Hydrogen Production from Alkaline Water via Urea Electrocatalysis. *Advanced Functional Materials* **2020**, *30*, 2000556.

29. Xie, Y.; Zhou, Z.; Yang, N.; Zhao, G. An Overall Reaction Integrated with Highly Selective Oxidation of 5-Hydroxymethylfurfural and Efficient Hydrogen Evolution. *Advanced Functional Materials* **2021**, *31*, 2102886.

30. Fu, G.; Kang, X.; Zhang, Y.; Guo, Y.; Li, Z.; Liu, J.; Wang, L.; Zhang, J.; Fu, X.-Z.; Luo, J.-L. Capturing critical gem-diol intermediates and hydride transfer for anodic hydrogen production from 5-hydroxymethylfurfural. *Nature Communications* **2023**, *14*, 8395.

31. Hassan, N. S.; Jalil, A. A.; Saravanan, R.; Izzuddin, N. M.; Bahari, M. B.; Prasetyoko, D.; Nugraha, R. E. Recent progress on electrocatalysts in ammonia electrooxidation reaction for clean hydrogen production. *Journal of Materials Chemistry A* **2024**, *12*, 23202.

32. Liu, H.; Xu, X.; Guan, D.; Shao, Z. Minireview on the electrocatalytic ammonia oxidation reaction for hydrogen production and sewage treatment. *Energy & Fuels* **2023**, *38*, 919.

33. Ren, J.-T.; Chen, L.; Wang, H.-Y.; Tian, W.-W.; Yuan, Z.-Y. Water electrolysis for hydrogen production: from hybrid systems to self-powered/catalyzed devices. *Energy & Environmental Science* **2023**, *17*, 49.

34. De Levie, R. The electrolysis of water. *Journal of Electroanalytical Chemistry* **1999**, 476, 92.
35. Kreuter, W. Electrolysis: The important energy transformer in a world of sustainable energy. *International Journal of Hydrogen Energy* **1998**, 23, 661.
36. Zoulias, E.; Varkaraki, E.; Lymberopoulos, N.; Christodoulou, C.N.; Karagiorgis, G.N. A review on water electrolysis. *Tcjsst* **2004**, 4, 41.
37. Zeng, K.; Zhang, D. Recent progress in alkaline water electrolysis for hydrogen production and applications. *Progress in Energy and Combustion Science* **2009**, 36, 307.
38. Chen, L.; Dong, X.; Wang, Y.; Xia, Y. Separating hydrogen and oxygen evolution in alkaline water electrolysis using nickel hydroxide. *Nature Communications* **2016**, 7, 11741.
39. Bin, S.; Chen, Z.; Zhu, Y.; Zhang, Y.; Xia, Y.; Gong, S.; Zhang, F.; Shi, L.; Duan, X.; Sun, Z. High-pressure proton exchange membrane water electrolysis: Current status and challenges in hydrogen production. *International Journal of Hydrogen Energy* **2024**, 67, 390.
40. Li, Y.; Sun, Y.; Qin, Y.; Zhang, W.; Wang, L.; Luo, M.; Yang, H.; Guo, S. Recent advances on Water-Splitting electrocatalysis mediated by Noble-Metal-Based nanostructured materials. *Advanced Energy Materials* **2020**, 10, 1903120.
41. Li, W.; Tian, H.; Ma, L.; Wang, Y.; Liu, X.; Gao, X. Low-temperature water electrolysis: fundamentals, progress, and new strategies. *Materials Advances* **2022**, 3, 5598.
42. Choudhury, D.; Das, R.; Maurya, R.; Kumawat, H.; Neergat, M. Kinetics of the oxygen evolution Reaction (OER) on amorphous and crystalline iridium oxide surfaces in acidic medium. *Langmuir* **2023**, 39, 13748.

43. Becker, H.; Murawski, J.; Shinde, D. V.; Stephens, I. E. L.; Hinds, G.; Smith, G. Impact of impurities on water electrolysis: a review. *Sustainable Energy & Fuels* **2023**, *7*, 1565.
44. Fan, C.; Piron, D. L.; Sleb, A.; Paradis, P. Study of electrodeposited Nickel-Molybdenum, Nickel-Tungsten, Cobalt-Molybdenum, and Cobalt-Tungsten as hydrogen electrodes in alkaline water electrolysis. *Journal of the Electrochemical Society* **1994**, *141*, 382.
45. Tian, X.; Zhao, P.; Sheng, W. Hydrogen evolution and oxidation: mechanistic studies and material advances. *Advanced Materials* **2019**, *31*, 1808066.
46. Jiang, Y.; Sun, P.; Sharma, L.; Mao, B.; Kakkar, R.; Meng, T.; Zheng, L.; Cao, M. Further insights into bifunctional mechanism in alkaline hydrogen evolution for hybridized nanocatalysts and general route toward mechanism-oriented synthesis. *Nano Energy* **2020**, *81*, 105645.
47. Cheng, T.; Wang, L.; Merinov, B. V.; Goddard, W. A. Explanation of dramatic pH-Dependence of hydrogen binding on noble metal electrode: Greatly weakened water adsorption at high pH. *Journal of the American Chemical Society* **2018**, *140*, 7787.
48. Zheng, J.; Sheng, W.; Zhuang, Z.; Xu, B.; Yan, Y. Universal dependence of hydrogen oxidation and evolution reaction activity of platinum-group metals on pH and hydrogen binding energy. *Science Advances* **2016**, *2*, e1501602.
49. Mahmood, N.; Yao, Y.; Zhang, J.; Pan, L.; Zhang, X.; Zou, J. Electrocatalysts for hydrogen Evolution in alkaline electrolytes: Mechanisms, challenges, and Prospective solutions. *Advanced Science* **2017**, *5*, 1700464.
50. Shi, Z.; Wang, X.; Ge, J.; Liu, C.; Xing, W. Fundamental understanding of the acidic oxygen evolution reaction: mechanism study and state-of-the-art catalysts. *Nanoscale* **2020**, *12*, 13249.

51. Hagiwara, S.; Kuroda, F.; Kondo, T.; Otani, M. Electrocatalytic mechanisms for an oxygen evolution reaction at a rhombohedral boron monosulfide Electrode/Alkaline Medium Interface. *ACS Applied Materials & Interfaces* **2023**, *15*, 50174.
52. Zeng, Z.; Li, W.; Wang, Q.; Liu, X. Programmed design of a Lithium–Sulfur battery Cathode by integrating functional units. *Advanced Science* **2019**, *6*, 1900711.
53. Zhang, M.; Guan, J.; Tu, Y.; Chen, S.; Wang, Y.; Wang, S.; Yu, L.; Ma, C.; Deng, D.; Bao, X. Highly efficient H<sub>2</sub> production from H<sub>2</sub>S via a robust graphene-encapsulated metal catalyst. *Energy & Environmental Science* **2019**, *13*, 119.
54. Chung, W. J.; Griebel, J. J.; Kim, E. T.; Yoon, H.; Simmonds, A. G.; Ji, H. J.; Dirlam, P. T.; Glass, R. S.; Wie, J. J.; Nguyen, N. A.; Guralnick, B. W.; Park, J.; Somogyi, Á.; Theato, P.; Mackay, M. E.; Sung, Y.-E.; Char, K.; Pyun, J. The use of elemental sulfur as an alternative feedstock for polymeric materials. *Nature Chemistry* **2013**, *5*, 518.
55. Du, X.; Liu, J.; Chen, H.; Zhang, Z. Study on the electrochemical oxidation desulfurization behavior of model diesel on anodic alumina oxide and Ceria nanotubes. *Energy & Fuels* **2018**, *32*, 2612.
56. Szpyrkowicz, L.; Kaul, S. N.; Neti, R. N.; Satyanarayan, S. Influence of anode material on electrochemical oxidation for the treatment of tannery wastewater. *Water Research* **2005**, *39*, 1601.
57. Pokhrel, D.; Viraraghavan, T. Treatment of pulp and paper mill wastewater—a review. *The Science of the Total Environment* **2004**, *333*, 37.
58. Wei, X.; Zhang, S.; Han, Y.; Wolfe, F. A. Treatment of petrochemical wastewater and produced water from oil and gas. *Water Environment Research* **2019**, *91*, 1025.
59. Parangusan, H.; Bhadra, J.; Al-Thani, N. A review of passivity breakdown on metal surfaces: influence of chloride- and sulfide-ion concentrations, temperature, and pH. *Emergent Materials* **2021**, *4*, 1187.

60. Piccardo, M. T.; Geretto, M.; Pulliero, A.; Izzotti, A. Odor emissions: A public health concern for health risk perception. *Environmental Research* **2021**, *204*, 112121.
61. Fazzo, L.; Minichilli, F.; Santoro, M.; Ceccarini, A.; Della Seta, M.; Bianchi, F.; Comba, P.; Martuzzi, M. Hazardous waste and health impact: a systematic review of the scientific literature. *Environmental Health* **2017**, *16*, 107.
62. Lin, S.; Mackey, H. R.; Hao, T.; Guo, G.; Van Loosdrecht, M. C. M.; Chen, G. Biological sulfur oxidation in wastewater treatment: A review of emerging opportunities. *Water Research* **2018**, *143*, 399.
63. Patel, A.; Arkatkar, A.; Singh, S.; Rabbani, A.; Medina, J. D. S.; Ong, E. S.; Habashy, M. M.; Jadhav, D. A.; Rene, E. R.; Mungray, A. A.; Mungray, A. K. Physico-chemical and biological treatment strategies for converting municipal wastewater and its residue to resources. *Chemosphere* **2021**, *282*, 130881.
64. Liu, X.; Han, Y.; Guo, Y.; Zhao, X.; Pan, D.; Li, K.; Wen, Z. Electrochemical hydrogen generation by oxygen evolution Reaction-Alternative anodic oxidation reactions. *Advanced Energy and Sustainability Research* **2022**, *3*, 2200005.
65. Z. Jin and A. Bard, Surface Interrogation of Electrodeposited MnO<sub>x</sub> and CaMnO<sub>3</sub> Perovskites by Scanning Electrochemical Microscopy: Probing Active Sites and Kinetics for the Oxygen Evolution Reaction, *Angew. Chem., Int. Ed.*, **2021**, *60*, 794.
66. Mefford, J. T.; Akbashev, A. R.; Kang, M.; Bentley, C. L.; Gent, W. E.; Deng, H. D.; Alsem, D. H.; Yu, Y.-S.; Salmon, N. J.; Shapiro, D. A.; Unwin, P. R.; Chueh, W. C. Correlative operando microscopy of oxygen evolution electrocatalysts. *Nature* **2021**, *593*, 67.
67. Yu, W.; Yu, J.; Wang, Y.; Li, X.; Wang, Y.; Yuan, H.; Zhang, X.; Liu, H.; Zhou, W. Electrocatalytic upcycling of nitrate and hydrogen sulfide via a nitrogen-doped carbon

nanotubes encapsulated iron carbide electrode. *Applied Catalysis B Environment and Energy* **2022**, *310*, 121291.

68. Eow, J. S. Recovery of sulfur from sour acid gas: A review of the technology. *Environmental Progress* **2002**, *21*, 143.

69. Zhang, X.; Xu, C.; Li, S.; Liu, X.; Liu, Y. N-doped porous carbocatalyst engineering via modulating the crystalline size of ZIF-8 for continuous H<sub>2</sub>S selective oxidation. *Applied Materials Today* **2021**, *25*, 101228.

70. Jangam, K.; Chen, Y.-Y.; Qin, L.; Fan, L.-S. Perspectives on reactive separation and removal of hydrogen sulfide. *Chemical Engineering Science X* **2021**, *11*, 100105.

71. Zhang, S.; Zhou, Q.; Shen, Z.; Jin, X.; Zhang, Y.; Shi, M.; Zhou, J.; Liu, J.; Lu, Z.; Zhou, Y.; Zhang, H. Sulfophobic and Vacancy Design Enables Self-Cleaning Electrodes for Efficient Desulfurization and Concurrent Hydrogen Evolution with Low Energy Consumption. *Advanced Functional Materials* **2021**, *31*, 2101922.

72. Yi, L.; Ji, Y.; Shao, P.; Chen, J.; Li, J.; Li, H.; Chen, K.; Peng, X.; Wen, Z. Scalable synthesis of tungsten disulfide nanosheets for Alkali-Acid electrocatalytic sulfion recycling and H<sub>2</sub> generation. *Angewandte Chemie International Edition* **2021**, *60*, 21550.

73. Deka, T. J.; Osman, A. I.; Baruah, D. C.; Rooney, D. W. Methanol fuel production, utilization, and techno-economy: a review. *Environmental Chemistry Letters* **2022**, *20*, 3525.

74. Clausen, L. R.; Houbak, N.; Elmgaard, B. Technoeconomic analysis of a methanol plant based on gasification of biomass and electrolysis of water. *Energy* **2010**, *35*, 2338.

75. Ravaghi-Ardebili, Z.; Manenti, F. Unified modeling and feasibility study of novel green pathway of biomass to methanol/dimethylether. *Applied Energy* **2015**, *145*, 278.

76. Santos, R. O. D.; De Sousa Santos, L.; Prata, D. M. Simulation and optimization of a methanol synthesis process from different biogas sources. *Journal of Cleaner Production* **2018**, *186*, 821.
77. Supronowicz, W.; Ignatyev, I. A.; Lolli, G.; Wolf, A.; Zhao, L.; Mleczko, L. Formic acid: a future bridge between the power and chemical industries. *Green Chemistry* **2015**, *17*, 2904.
78. Sarangi, P. K.; Nanda, S.; Vo, D.-V. N. Technological advancements in the production and application of biomethanol: Biorefinery of Alternative Resources: Targeting Green Fuels and Platform Chemicals, 1<sup>st</sup> Edition, *Springer Nature Singapore Pte Ltd.* **2020**; 127–139. ISBN: 9789811518041
79. Xu, Y.; Liu, M.; Wang, S.; Ren, K.; Wang, M.; Wang, Z.; Li, X.; Wang, L.; Wang, H. Integrating electrocatalytic hydrogen generation with selective oxidation of glycerol to formate over bifunctional nitrogen-doped carbon coated nickel-molybdenum-nitrogen nanowire arrays. *Applied Catalysis B Environment and Energy* **2021**, *298*, 120493.
80. Li, J.; Li, L.; Ma, X.; Han, X.; Xing, C.; Qi, X.; He, R.; Arbiol, J.; Pan, H.; Zhao, J.; Deng, J.; Zhang, Y.; Yang, Y.; Cabot, A. Selective Ethylene Glycol Oxidation to Formate on Nickel Selenide with Simultaneous Evolution of Hydrogen. *Advanced Science* **2023**, *10*, 2300841.
81. Qi, Y.; Zhang, Y.; Yang, L.; Zhao, Y.; Zhu, Y.; Jiang, H.; Li, C. Insights into the activity of nickel boride/nickel heterostructures for efficient methanol electrooxidation. *Nature Communications* **2022**, *13*, 4602.
82. Lu, S.; Eid, K.; Ge, D.; Guo, J.; Wang, L.; Wang, H.; Gu, H. One-pot synthesis of PtRu nanodendrites as efficient catalysts for methanol oxidation reaction. *Nanoscale* **2016**, *9*, 1033.

83. Kamyabi, M. A.; Jadali, S.; Khangheshlaghi, L. S.; Heris, M. K. H. A high-performance Pt-based catalyst for the methanol oxidation reaction: effect of electrodeposition mode and cocatalyst on electrocatalytic activity. *New Journal of Chemistry* **2022**, *47*, 1209.
84. Semwal, S.; Samal, A.; Nayak, S. K.; Urkude, R. R.; Sinha, A. S. K.; Ojha, U. Ni Surface & Polyacryloyl Hydrazide Mediated Growth of Co<sub>3</sub>O<sub>4</sub>@NiCu Alloy Nanocuboids for Effective Methanol Oxidation and Oxygen Evolution Reactions. *Advanced Sustainable Systems* **2024**, 202400372.
85. Wu, D.; Zhang, W.; Cheng, D. Facile synthesis of Cu/NiCu electrocatalysts integrating alloy, Core–Shell, and One-Dimensional structures for efficient methanol oxidation reaction. *ACS Applied Materials & Interfaces* **2017**, *9*, 19843.
86. Zhao, B.; Liu, J.-W.; Yin, Y.-R.; Wu, D.; Luo, J.-L.; Fu, X.-Z. Carbon nanofibers@NiSe core/sheath nanostructures as efficient electrocatalysts for integrating highly selective methanol conversion and less-energy intensive hydrogen production. *Journal of Materials Chemistry A* **2019**, *7*, 25878.
87. Abdullah, M. I.; Hameed, A.; Zhang, N.; Islam, M. H.; Ma, M.; Pollet, B. G. Ultrasonically Surface-Activated nickel foam as a highly efficient monolith electrode for the catalytic oxidation of methanol to formate. *ACS Applied Materials & Interfaces* **2021**, *13*, 30603.
88. Candelaria, S. L.; Bedford, N. M.; Woehl, T. J.; Rentz, N. S.; Showalter, A. R.; Pylypenko, S.; Bunker, B. A.; Lee, S.; Reinhart, B.; Ren, Y.; Ertem, S. P.; Coughlin, E. B.; Sather, N. A.; Horan, J. L.; Herring, A. M.; Greenlee, L. F. Multi-Component Fe–Ni Hydroxide Nanocatalyst for Oxygen Evolution and Methanol Oxidation Reactions under Alkaline Conditions. *ACS Catalysis* **2016**, *7*, 365.

89. Wu, N.; Zhai, M.; Chen, F.; Zhang, X.; Guo, R.; Hu, T.; Ma, M. Nickel nanocrystal/nitrogen-doped carbon composites as efficient and carbon monoxide-resistant electrocatalysts for methanol oxidation reactions. *Nanoscale* **2020**, *12*, 21687.
90. An, Y.; Ijaz, H.; Huang, M.; Qu, J.; Hu, S. The one-pot synthesis of CuNi nanoparticles with a Ni-rich surface for the electrocatalytic methanol oxidation reaction. *Dalton Transactions* **2020**, *49*, 1646.
91. Liu, C.; Yang, F.; Yang, Y.; Wang, S.; Feng, L. An active Ni(OH)<sub>2</sub>/MnCO<sub>3</sub> catalyst with efficient synergism for alkaline methanol oxidation. *Chemical Communications* **2024**, *60*, 1591.
92. Gaikwad, M. A.; Burungale, V. V.; Malavekar, D. B.; Ghorpade, Uma. V.; Suryawanshi, U. P.; Jang, S.; Guo, X.; Shin, S. W.; Ha, J.; Suryawanshi, M. P.; Kim, J. H. Self-Supported Fe-Based nanostructured electrocatalysts for water splitting and selective oxidation reactions: past, present, and future. *Advanced Energy Materials* **2024**, *14*, 2303730.
93. Hao, Y.; Yu, D.; Zhu, S.; Kuo, C.-H.; Chang, Y.-M.; Wang, L.; Chen, H.-Y.; Shao, M.; Peng, S. Methanol upgrading coupled with hydrogen product at large current density promoted by strong interfacial interactions. *Energy & Environmental Science* **2023**, *16*, 1100.
94. Fearon, W. R. The Biochemistry of Urea. *Physiological Reviews* **1926**, *6*, 399.
95. Song, M.; Zhang, Z.; Li, Q.; Jin, W.; Wu, Z.; Fu, G.; Liu, X. Ni-foam supported Co(OH)F and Co-P nanoarrays for energy-efficient hydrogen production via urea electrolysis. *Journal of Materials Chemistry A* **2019**, *7*, 3697.

96. Xie, J.; Qu, H.; Lei, F.; Peng, X.; Liu, W.; Gao, L.; Hao, P.; Cui, G.; Tang, B. Partially amorphous nickel–iron layered double hydroxide nanosheet arrays for robust bifunctional electrocatalysis. *Journal of Materials Chemistry A* **2018**, *6*, 16121.
97. Li, J.; Li, J.; Liu, T.; Chen, L.; Li, Y.; Wang, H.; Chen, X.; Gong, M.; Liu, Z.; Yang, X. Deciphering and suppressing Over-Oxidized nitrogen in Nickel-Catalyzed urea electrolysis. *Angewandte Chemie International Edition* **2021**, *60*, 26656.
98. Sun, W.; Li, J.; Gao, W.; Kang, L.; Lei, F.; Xie, J. Recent advances in the pre-oxidation process in electrocatalytic urea oxidation reactions. *Chemical Communications* **2022**, *58*, 2430.
99. Wang, Z.; Wang, C.; Ye, L.; Liu, X.; Xin, L.; Yang, Y.; Wang, L.; Hou, W.; Wen, Y.; Zhan, T. MnO<sub>x</sub> Film-Coated NiFe-LDH nanosheets on Ni Foam as selective oxygen evolution electrocatalysts for alkaline seawater oxidation. *Inorganic Chemistry* **2022**, *61*, 15256.
100. Zhang, J.-J.; Bao, W.-W.; Li, M.-Y.; Yang, C.-M.; Zhang, N.-N. Ultrafast formation of an FeOOH electrocatalyst on Ni for efficient alkaline water and urea oxidation. *Chemical Communications* **2020**, *56*, 14713.
101. Xu, H.; Liao, Y.; Gao, Z.; Qing, Y.; Wu, Y.; Xia, L. A branch-like Mo-doped Ni<sub>3</sub>S<sub>2</sub> nanoforest as a high-efficiency and durable catalyst for overall urea electrolysis. *Journal of Materials Chemistry A* **2020**, *9*, 3418.
102. Bera, K.; Karmakar, A.; Kumaravel, S.; Sankar, S. S.; Madhu, R.; Dhandapani, H. N.; Nagappan, S.; Kundu, S. Vanadium-Doped Nickel Cobalt Layered Double Hydroxide: a High-Performance Oxygen Evolution Reaction electrocatalyst in alkaline medium. *Inorganic Chemistry* **2022**, *61*, 4502.

103. Liu, D.; Liu, T.; Zhang, L.; Qu, F.; Du, G.; Asiri, A. M.; Sun, X. High-performance urea electrolysis towards less energy-intensive electrochemical hydrogen production using a bifunctional catalyst electrode. *Journal of Materials Chemistry A* **2017**, *5*, 3208.
104. Ge, W.; Lin, L.; Wang, S.-Q.; Wang, Y.; Ma, X.; An, Q.; Zhao, L. Electrocatalytic urea oxidation: advances in mechanistic insights, nanocatalyst design, and applications. *Journal of Materials Chemistry A* **2023**, *11*, 15100.
105. Li, C.; Baek, J.-B. Recent advances in noble Metal (Pt, Ru, and Ir)-Based electrocatalysts for efficient hydrogen evolution reaction. *ACS Omega* **2019**, *5*, 31.
106. Udayakumar, A.; Dhandapani, P.; Ramasamy, S.; Yan, C.; Angaiah, S. Recent developments in noble metal-based hybrid electrocatalysts for overall water splitting. *Ionics* **2023**, *30*, 61.
107. Tian, L.; Li, Z.; Song, M.; Li, J. Recent progress in water-splitting electrocatalysis mediated by 2D noble metal materials. *Nanoscale* **2021**, *13*, 12088.
108. Anantharaj, S.; Kundu, S.; Noda, S. Progress in nickel chalcogenide electrocatalyzed hydrogen evolution reaction. *Journal of Materials Chemistry A* **2020**, *8*, 4174.
109. Sun, Y.; Zhang, T.; Li, C.; Xu, K.; Li, Y. Compositional engineering of sulfides, phosphides, carbides, nitrides, oxides, and hydroxides for water splitting. *Journal of Materials Chemistry A* **2020**, *8*, 13415.
110. Semwal, S.; Shakir, R.; Karthikeyan, J.; Sinha, A. S. K.; Ojha, U. NiFeOOH-Co<sub>9</sub>S<sub>8</sub>-Intercalated nanostructure arrays for Energy-Efficient H<sub>2</sub> production and sulfion oxidation at high current density. *ACS Applied Nano Materials* **2023**, *6*, 18945.
111. Ghosh, S.; Mondal, B.; Roy, S.; Shalom, M.; Sadan, M. B. Alcohol oxidation with high efficiency and selectivity by nickel phosphide phases. *Journal of Materials Chemistry A* **2022**, *10*, 8238.

112. Bo, X.; Hocking, R. K.; Zhou, S.; Li, Y.; Chen, X.; Zhuang, J.; Du, Y.; Zhao, C. Capturing the active sites of multimetallic (oxy)hydroxides for the oxygen evolution reaction. *Energy & Environmental Science* **2020**, *13*, 4225.
113. Song, F.; Bai, L.; Moysiadou, A.; Lee, S.; Hu, C.; Liardet, L.; Hu, X. Transition metal oxides as electrocatalysts for the oxygen evolution reaction in alkaline Solutions: An Application-Inspired Renaissance. *Journal of the American Chemical Society* **2018**, *140*, 7748.
114. Fan, C.; Yue, X.; Shen, X.; Cheng, J.; Ke, W.; Ji, Z.; Yuan, A.; Zhu, G. One-Pot hydrothermal synthesis of Ni<sub>3</sub>S<sub>2</sub>/MoS<sub>2</sub>/FeOOH hierarchical microspheres on Ni Foam as a High-Efficiency and durable Dual-Function electrocatalyst for overall water splitting. *ChemElectroChem* **2020**, *8*, 665.
115. Liu, S.; Gao, R.-T.; Sun, M.; Wang, Y.; Nakajima, T.; Liu, X.; Zhang, W.; Wang, L. In situ construction of hybrid Co(OH)<sub>2</sub> nanowires for promoting long-term water splitting. *Applied Catalysis B Environment and Energy* **2021**, *292*, 120063.
116. Jing, Z.; Zhao, Q.; Zheng, D.; Sun, L.; Geng, J.; Zhou, Q.; Lin, J. Nickel-doped pyrrhotite iron sulfide nanosheets as a highly efficient electrocatalyst for water splitting. *Journal of Materials Chemistry A* **2020**, *8*, 20323.
117. Wang, J.; Han, L.; Huang, B.; Shao, Q.; Xin, H. L.; Huang, X. Amorphization activated ruthenium-tellurium nanorods for efficient water splitting. *Nature Communications* **2019**, *10*, 5692.
118. Jamesh, M.; Kuang, Y.; Sun, X. Constructing earth-abundant 3D nanoarrays for efficient overall water splitting – a review. *ChemCatChem* **2019**, *11*, 1550.
119. Jothi, V. R.; Karuppasamy, K.; Maiyalagan, T.; Rajan, H.; Jung, C.; Yi, S. C. Corrosion and alloy engineering in rational design of high current density electrodes for efficient water splitting. *Advanced Energy Materials* **2020**, *10*, 1904020.

120. Liu, J.; Zhu, D.; Zheng, Y.; Vasileff, A.; Qiao, S.-Z. Self-Supported Earth-Abundant nanoarrays as efficient and robust electrocatalysts for Energy-Related reactions. *ACS Catalysis* **2018**, *8*, 6707.
121. Murthy, R.; Neelakantan, S. C. Graphitic Carbon Cloth-Based Hybrid Molecular Catalyst: a non-conventional, synthetic strategy of the drop casting method for a stable and bifunctional electrocatalyst for enhanced hydrogen and oxygen evolution reactions. *ACS Omega* **2022**, *7*, 32604.
122. Yu, P.; Ma, J.; Zhang, R.; Zhang, J. Z.; Botte, G. G. Novel Pd–Co Electrocatalyst Supported on Carbon Fibers with Enhanced Electrocatalytic Activity for Coal Electrolysis To Produce Hydrogen. *ACS Applied Energy Materials* **2018**, *1*, 267.
123. Pei, Y.; Cheng, J.; Zhong, H.; Pi, Z.; Zhao, Y.; Jin, F. Sulfide-oxidation-assisted electrochemical water splitting for H<sub>2</sub> production on a bifunctional Cu<sub>2</sub>S/nickel foam catalyst. *Green Chemistry* **2021**, *23*, 6975.
124. Li, P.; Wang, J.; Cai, N.; Wang, L.; Tong, J.; Yu, F. Self-Supported Electrocatalysts for Efficient oxygen Evolution Reaction: Hierarchical CuOx@CoO nanorods grown on cu foam. *ChemCatChem* **2020**, *12*, 1639.
125. Yu, Z.-Y.; Lang, C.-C.; Gao, M.-R.; Chen, Y.; Fu, Q.-Q.; Duan, Y.; Yu, S.-H. Ni–Mo–O nanorod-derived composite catalysts for efficient alkaline water-to-hydrogen conversion via urea electrolysis. *Energy & Environmental Science* **2018**, *11*, 1890.
126. Raveendran, A.; Chandran, M.; Dhanusuraman, R. A comprehensive review on the electrochemical parameters and recent material development of electrochemical water splitting electrocatalysts. *RSC Advances* **2023**, *13*, 3843.
127. Li, S.; Li, E.; An, X.; Hao, X.; Jiang, Z.; Guan, G. Transition metal-based catalysts for electrochemical water splitting at high current density: current status and perspectives. *Nanoscale* **2021**, *13*, 12788.

128. Zou, X.; Zhang, Y. Noble metal-free hydrogen evolution catalysts for water splitting. *Chemical Society Reviews* **2015**, *44*, 5148.
129. Wu, Z.; Lu, X. F.; Zang, S.; Lou, X. W. Non-Noble-Metal-Based Electrocatalysts toward the Oxygen Evolution Reaction. *Advanced Functional Materials* **2020**, *30*, 1910274.
130. Quarton, C. J.; Tlili, O.; Welder, L.; Mansilla, C.; Blanco, H.; Heinrichs, H.; Leaver, J.; Samsatli, N. J.; Lucchese, P.; Robinius, M.; Samsatli, S. The curious case of the conflicting roles of hydrogen in global energy scenarios. *Sustainable Energy & Fuels* **2020**, *4*, 80.
131. Luo, Y.; Zhang, Z.; Chhowalla, M.; Liu, B. Recent advances in design of electrocatalysts for High-Current-Density water splitting. *Advanced Materials* **2021**, *34*, 2108133.
132. Jin, M.; Zhang, X.; Niu, S.; Wang, Q.; Huang, R.; Ling, R.; Huang, J.; Shi, R.; Amini, A.; Cheng, C. Strategies for Designing High-Performance Hydrogen Evolution Reaction Electrocatalysts at Large Current Densities above  $1000 \text{ mA cm}^{-2}$ . *ACS Nano* **2022**, *16*, 11577.
133. Van Der Spek, M.; Banet, C.; Bauer, C.; Gabrielli, P.; Goldthorpe, W.; Mazzotti, M.; Munkejord, S. T.; Røkke, N. A.; Shah, N.; Sunny, N.; Sutter, D.; Trusler, J. M.; Gazzani, M. Perspective on the hydrogen economy as a pathway to reach net-zero CO<sub>2</sub> emissions in Europe. *Energy & Environmental Science* **2022**, *15*, 1034.
134. Anantharaj, S.; Ede, S. R.; Karthick, K.; Sankar, S. S.; Sangeetha, K.; Karthik, P. E.; Kundu, S. Precision and correctness in the evaluation of electrocatalytic water splitting: revisiting activity parameters with a critical assessment. *Energy & Environmental Science* **2018**, *11*, 744.

135. Masa, J.; Andronesco, C.; Schuhmann, W. Electrocatalysis as the nexus for sustainable renewable energy: the Gordian knot of activity, stability, and selectivity. *Angewandte Chemie International Edition* **2020**, *59*, 15298.
136. Chen, G.; Tu, X.; Homm, G.; Weidenkaff, A. Plasma pyrolysis for a sustainable hydrogen economy. *Nature Reviews Materials* **2022**, *7*, 333.
137. Liu, W.-J.; Xu, Z.; Zhao, D.; Pan, X.-Q.; Li, H.-C.; Hu, X.; Fan, Z.-Y.; Wang, W.-K.; Zhao, G.-H.; Jin, S.; Huber, G. W.; Yu, H.-Q. Efficient electrochemical production of glucaric acid and H<sub>2</sub> via glucose electrolysis. *Nature Communications* **2020**, *11*, 265.
138. Yu, J. M.; Lee, J.; Kim, Y. S.; Song, J.; Oh, J.; Lee, S. M.; Jeong, M.; Kim, Y.; Kwak, J. H.; Cho, S.; Yang, C.; Jang, J.-W. High-performance and stable photoelectrochemical water splitting cell with organic-photoactive-layer-based photoanode. *Nature Communications* **2020**, *11*, 5509.
139. Dong, W. J.; Xiao, Y.; Yang, K. R.; Ye, Z.; Zhou, P.; Navid, I. A.; Batista, V. S.; Mi, Z. Pt nanoclusters on GaN nanowires for solar-assisted seawater hydrogen evolution. *Nature Communications* **2023**, *14*, 179.
140. Zhou, P.; Navid, I. A.; Ma, Y.; Xiao, Y.; Wang, P.; Ye, Z.; Zhou, B.; Sun, K.; Mi, Z. Solar-to-hydrogen efficiency of more than 9% in photocatalytic water splitting. *Nature* **2023**, *613*, 66.
141. Riahi, S.; Rowley, C. N. Why can hydrogen sulfide permeate cell membranes? *Journal of the American Chemical Society* **2014**, *136*, 15111.
142. Lee, T.; Dirlam, P. T.; Njardarson, J. T.; Glass, R. S.; Pyun, J. Polymerizations with Elemental Sulfur: From Petroleum Refining to Polymeric Materials. *Journal of the American Chemical Society* **2021**, *144*, 5.
143. Lou, M.; Bao, J. L.; Zhou, L.; Naidu, G. N.; Robotjazi, H.; Bayles, A. I.; Everitt, H. O.; Nordlander, P.; Carter, E. A.; Halas, N. J. Direct H<sub>2</sub>S Decomposition by Plasmonic

Photocatalysis: Efficient Remediation plus Sustainable Hydrogen Production. *ACS Energy Letters* **2022**, *7*, 3666.

144. Yu, S.; Wu, F.; Zou, P.; Fan, X.-B.; Duan, C.; Dan, M.; Xie, Z.; Zhang, Q.; Zhang, F.; Zheng, H.; Zhou, Y. Highly value-added utilization of H<sub>2</sub>S in Na<sub>2</sub>SO<sub>3</sub> solution over Ca–CdS nanocrystal photocatalysts. *Chemical Communications* **2020**, *56*, 14227.

145. Zhou, W.; Teo, W. L.; Phua, S. Z. F.; Xi, S.; Chen, B.; Jana, D.; Wang, D.; Qian, C.; Wang, H.; Zhang, H.; Zhao, Y. Impeding catalyst sulfur poisoning in aqueous solution by Metal–Organic framework composites. *Small Methods* **2020**, *4*, 201900890.

146. Kim, K.; Lee, C. Recent progress in electrochemical hydrogen sulfide splitting: Strategies for enabling Sulfur-tolerant anodic reactions. *Chemical Engineering Journal* **2023**, *469*, 143861.

147. Garg, K.; Kumar, M.; Kaur, S.; Nagaiah, T. C. Electrochemical Production of Hydrogen from Hydrogen Sulfide Using Cobalt Cadmium Sulfide. *ACS Applied Materials & Interfaces* **2023**, *15*, 27845.

148. Xiao, Z.; Lu, C.; Wang, J.; Qian, Y.; Wang, B.; Zhang, Q.; Tang, A.; Yang, H. Bifunctional Co<sub>3</sub>S<sub>4</sub> Nanowires for Robust Sulfion Oxidation and Hydrogen Generation with Low Power Consumption. *Advanced Functional Materials* **2022**, *33*, 2212183.

149. Kumar, M.; Nagaiah, T. C. Efficient production of hydrogen from H<sub>2</sub>S via electrolysis using a CoFeS<sub>2</sub> catalyst. *Journal of Materials Chemistry A* **2022**, *10*, 7048.

150. Wang, H.; Wang, B.; Yu, H.; Deng, K.; Xu, Y.; Li, X.; Wang, Z.; Wang, L. Bifunctional Cobalt–Nickel sulfide nanoflowers as electrocatalysts for concurrent Energy-Efficient hydrogen production and sulfur recycling. *ACS Applied Nano Materials* **2023**, *6*, 10863.

151. Feng, W.; Cheng, M.; Du, R.; Wang, Y.; Wang, P.; Li, H.; Song, L.; Wen, X.; Yang, J.; Li, X.; He, J.; Shi, J. Gram-Scale synthesized Two-Dimensional VSe<sub>2</sub> and SnSe<sub>2</sub> for ultrahigh electrocatalytic sulfion recycling. *Advanced Materials Interfaces* **2022**, *9*, 2200060.
152. Lei, G.; Tong, Y.; Shen, L.; Liu, F.; Xiao, Y.; Lin, W.; Zhang, Y.; Au, C.; Jiang, L. Highly Active and Sulfur-Resistant Fe–N<sub>4</sub> Sites in Porous Carbon Nitride for the Oxidation of H<sub>2</sub>S into Elemental Sulfur. *Small* **2020**, *16*, 2003904.
153. Lei, G.; Tong, Y.; Shen, L.; Zheng, Y.; Liang, S.; Lin, W.; Liu, F.; Cao, Y.; Xiao, Y.; Jiang, L. Highly Poison-Resistant Single-Atom Co–N<sub>4</sub> Active Sites with Superior Operational Stability over 460 h for H<sub>2</sub>S Catalytic Oxidation. *Small* **2021**, *17*, 2104939.
154. Mao, Q.; Mu, X.; Deng, K.; Yu, H.; Wang, Z.; Xu, Y.; Li, X.; Wang, L.; Wang, H. Sulfur Vacancy-Rich Amorphous Rh Metallene Sulfide for Electrocatalytic Selective Synthesis of Aniline Coupled with Efficient Sulfion Degradation. *ACS Nano* **2022**, *17*, 790.
155. Voiry, D.; Yamaguchi, H.; Li, J.; Silva, R.; Alves, D. C. B.; Fujita, T.; Chen, M.; Asefa, T.; Shenoy, V. B.; Eda, G.; Chhowalla, M. Enhanced catalytic activity in strained chemically exfoliated WS<sub>2</sub> nanosheets for hydrogen evolution. *Nature Materials* **2013**, *12*, 850.
156. Pascuzzi, M. E. C.; Man, A. J. W.; Goryachev, A.; Hofmann, J. P.; Hensen, E. J. M. Investigation of the stability of NiFe-(oxy)hydroxide anodes in alkaline water electrolysis under industrially relevant conditions. *Catalysis Science & Technology* **2020**, *10*, 5593.
157. Hao, Y.; Li, Y.; Wu, J.; Meng, L.; Wang, J.; Jia, C.; Liu, T.; Yang, X.; Liu, Z.-P.; Gong, M. Recognition of surface oxygen intermediates on NiFe oxyhydroxide Oxygen-Evolving catalysts by homogeneous oxidation reactivity. *Journal of the American Chemical Society* **2021**, *143*, 1493.

158. Sk, S.; Madhu, R.; Gavali, D. S.; Bhasin, V.; Thapa, R.; Jha, S. N.; Bhattacharyya, D.; Kundu, S.; Pal, U. An ultrathin 2D NiCo-LDH nanosheet decorated NH<sub>2</sub>-UiO-66 MOF-nanocomposite with exceptional chemical stability for electrocatalytic water splitting. *Journal of Materials Chemistry A* **2023**, *11*, 10309.
159. Woo, J.; Moon, B. C.; Lee, U.; Oh, H.-S.; Chae, K. H.; Jun, Y.; Min, B. K.; Lee, D. K. Collaborative electrochemical oxidation of the alcohol and aldehyde groups of 5-Hydroxymethylfurfural by NiOOH and Cu(OH)<sub>2</sub> for superior 2,5-Furandicarboxylic acid production. *ACS Catalysis* **2022**, *12*, 4078.
160. Konkena, B.; Masa, J.; Botz, A. J. R.; Sinev, I.; Xia, W.; Koßmann, J.; Drautz, R.; Muhler, M.; Schuhmann, W. Metallic NiPS<sub>3</sub>@NiOOH Core–Shell heterostructures as highly efficient and stable electrocatalyst for the oxygen evolution reaction. *ACS Catalysis* **2016**, *7*, 229.
161. Zhang, H.; Zhou, Y.; Xu, M.; Chen, A.; Ni, Z.; Akdim, O.; Wågberg, T.; Huang, X.; Hu, G. Interface engineering on Amorphous/Crystalline Hydroxides/Sulfides heterostructure nanoarrays for enhanced solar water splitting. *ACS Nano* **2022**, *17*, 636.
162. Kresse, G.; Joubert, D. From ultrasoft pseudopotentials to the projector augmented-wave method. *Physical Review. B, Condensed Matter* **1999**, *59*, 1758.
163. Nørskov, J. K.; Rossmeisl, J.; Logadottir, A.; Lindqvist, L.; Kitchin, J. R.; Bligaard, T.; Jónsson, H. Origin of the overpotential for oxygen reduction at a Fuel-Cell Cathode. *The Journal of Physical Chemistry B* **2004**, *108*, 17886.
164. Li, J.; Xu, Y.; Zhang, Y.; He, C.; Li, T. Enhanced redox kinetics of polysulfides by nano-rod FeOOH for ultrastable lithium–sulfur batteries. *Journal of Materials Chemistry A* **2020**, *8*, 19544.

165. Lin, Z.; Bu, P.; Xiao, Y.; Gao, Q.; Diao, P.  $\beta$ - and  $\gamma$ -NiFeOOH electrocatalysts for an efficient oxygen evolution reaction: an electrochemical activation energy aspect. *Journal of Materials Chemistry A* **2022**, *10*, 20847.
166. Tian, B.; Kolodziejczyk, W.; Saloni, J.; Cheah, P.; Qu, J.; Han, F.; Cao, D.; Zhu, X.; Zhao, Y. Intercalation of cobalt cations into Co<sub>9</sub>S<sub>8</sub> interlayers for highly efficient and stable electrocatalytic hydrogen evolution. *Journal of Materials Chemistry A* **2022**, *10*, 3522.
167. Glover, E. N. K.; Ellington, S. G.; Sankar, G.; Palgrave, R. G. The nature and effects of rhodium and antimony dopants on the electronic structure of TiO<sub>2</sub>: towards design of Z-scheme photocatalysts. *Journal of Materials Chemistry A* **2016**, *4*, 6946.
168. Cai, P.; Huang, J.; Chen, J.; Wen, Z. Oxygen-Containing amorphous cobalt sulfide porous nanocubes as High-Activity electrocatalysts for the oxygen evolution reaction in an Alkaline/Neutral medium. *Angewandte Chemie International Edition* **2017**, *56*, 4858.
169. Wang, H.; Liu, J.; Wang, H.; Cai, X.; Ye, X.; Zhang, L.; Chen, Z.; Shen, Z. X. Cobalt sulfide nanoflakes grown on graphite foam for Na-ion batteries with ultrahigh initial coulombic efficiency. *Journal of Materials Chemistry A* **2020**, *8*, 14900.
170. Huang, S.; Meng, Y.; He, S.; Goswami, A.; Wu, Q.; Li, J.; Tong, S.; Asefa, T.; Wu, M. N-, O-, and S-Tridoped Carbon-Encapsulated Co<sub>9</sub>S<sub>8</sub> nanomaterials: efficient bifunctional electrocatalysts for overall water splitting. *Advanced Functional Materials* **2017**, *27*, 1606585.
171. Ma, X.; Zhang, W.; Deng, Y.; Zhong, C.; Hu, W.; Han, X. Phase and composition controlled synthesis of cobalt sulfide hollow nanospheres for electrocatalytic water splitting. *Nanoscale* **2018**, *10*, 4816.

172. Xie, L.; Wang, J.; Shi, C.; Huang, J.; Zhang, H.; Liu, Q.; Liu, Q.; Zeng, H. Probing surface interactions of electrochemically active galena mineral surface using atomic force microscopy. *The Journal of Physical Chemistry C* **2016**, *120*, 22433.
173. Ratcliff, E. L.; Meyer, J.; Steirer, K. X.; Garcia, A.; Berry, J. J.; Ginley, D. S.; Olson, D. C.; Kahn, A.; Armstrong, N. R. Evidence for Near-Surface NiOOH species in Solution-Processed NiO<sub>x</sub> Selective Interlayer Materials: Impact on energetics and the performance of polymer bulk heterojunction photovoltaics. *Chemistry of Materials* **2011**, *23*, 4988.
174. Ma, D.; Hu, B.; Wu, W.; Liu, X.; Zai, J.; Shu, C.; Tsega, T. T.; Chen, L.; Qian, X.; Liu, T. L. Highly active nanostructured CoS<sub>2</sub>/CoS heterojunction electrocatalysts for aqueous polysulfide/iodide redox flow batteries. *Nature Communications* **2019**, *10*, 3367.
175. Mujtaba, J.; He, L.; Zhu, H.; Xiao, Z.; Huang, G.; Solovev, A. A.; Mei, Y. Co<sub>9</sub>S<sub>8</sub> nanoparticles for hydrogen evolution. *ACS Applied Nano Materials* **2021**, *4*, 1776.
176. Zhai, Y.; Ma, X.; Mao, H.; Shao, W.; Xu, L.; He, Y.; Qian, Y. Mn-Doped  $\alpha$ -FeOOH nanorods and  $\alpha$ -Fe<sub>2</sub>O<sub>3</sub> mesoporous nanorods: facile synthesis and applications as high-performance anodes for LiBs. *Advanced Electronic Materials* **2015**, *1*, 1400057.
177. Lyu, D.; Yao, S.; Ali, A.; Tian, Z. Q.; Tsiakaras, P.; Shen, P. K. N, S Codoped Carbon Matrix-Encapsulated Co<sub>9</sub>S<sub>8</sub> nanoparticles as a highly efficient and durable bifunctional oxygen Redox electrocatalyst for rechargeable Zn–Air batteries. *Advanced Energy Materials* **2021**, *11*, 2101249.
178. Zeradjanin, A. R.; Narangoda, P.; Masa, J.; Schlögl, R. What controls activity trends of electrocatalytic hydrogen evolution Reaction? —Activation energy versus frequency factor. *ACS Catalysis* **2022**, *12*, 11597.

179. Suermann, M.; Schmidt, T. J.; Büchi, F. N. Comparing the kinetic activation energy of the oxygen evolution and reduction reactions. *Electrochimica Acta* **2018**, *281*, 466.
180. Gao, T.; Tang, X.; Li, X.; Lan, H.; Yu, S.; Wu, S.; Yue, Q.; Xiao, D. Surface reconstructing hierarchical structures as robust sulfion oxidation catalysts to produce hydrogen with ultralow energy consumption. *Inorganic Chemistry Frontiers* **2023**, *10*, 1447.
181. Kumar, M.; Nagaiah, T. C. Pure hydrogen and sulfur production from H<sub>2</sub>S by an electrochemical approach using a NiCu–MoS<sub>2</sub> catalyst. *Journal of Materials Chemistry A* **2022**, *10*, 13031.
182. Yu, Z.; Duan, Y.; Feng, X.; Yu, X.; Gao, M.; Yu, S. Clean and Affordable Hydrogen Fuel from Alkaline Water Splitting: Past, Recent Progress, and Future Prospects. *Advanced Materials* **2021**, *33*, 2007100.
183. Tewary, A.; Mandal, S.; Alam, Z.; Sinha, A. S. K.; Ojha, U. Scalable green synthesis of Ni<sub>3</sub>N-Encapsulated NC-Layered FeOOH heterostructures: bifunctional electrodes for sustainable electrocatalytic seawater splitting. *ACS Sustainable Chemistry & Engineering* **2023**, *11*, 6556.
184. Lin, L.; Zhou, W.; Gao, R.; Yao, S.; Zhang, X.; Xu, W.; Zheng, S.; Jiang, Z.; Yu, Q.; Li, Y.-W.; Shi, C.; Wen, X.-D.; Ma, D. Low-temperature hydrogen production from water and methanol using Pt/ $\alpha$ -MoC catalysts. *Nature* **2017**, *544*, 80.
185. Han, X.; Sheng, H.; Yu, C.; Walker, T. W.; Huber, G. W.; Qiu, J.; Jin, S. Electrocatalytic oxidation of glycerol to formic acid by CuCo<sub>2</sub>O<sub>4</sub> spinel oxide nanostructure catalysts. *ACS Catalysis* **2020**, *10*, 6741.
186. Paredes-Salazar, E. A.; Calderón-Cárdenas, A.; Varela, H. Microkinetic modeling of the methanol electro-oxidation reaction on platinum. *ACS Catalysis* **2023**, *13*, 9366.

187. Wang, J.; Zhang, B.; Guo, W.; Wang, L.; Chen, J.; Pan, H.; Sun, W. Toward Electrocatalytic methanol oxidation Reaction: longstanding debates and emerging catalysts. *Advanced Materials* **2023**, *35*, 2211099.
188. Li, M.; Deng, X.; Xiang, K.; Liang, Y.; Zhao, B.; Hao, J.; Luo, J.; Fu, X. Value-Added Formate Production from Selective Methanol Oxidation as Anodic Reaction to Enhance Electrochemical Hydrogen Cogeneration. *ChemSusChem* **2019**, *13*, 914.
189. Liu, Y.; Zhu, E.; Huang, J.; Zhang, A.; Shah, A. H.; Jia, Q.; Xu, M.; Liu, E.; Sun, Q.; Duan, X.; Huang, Y. Periodic assembly of diblock Pt–Au heteronanowires for the methanol oxidation reaction. *Nano Letters* **2023**, *23*, 2758.
190. Deshpande, P.; Prasad, B. L. V. Alloying with Mn Enhances the Activity and Durability of the CoPt Catalyst toward the Methanol Oxidation Reaction. *ACS Applied Materials & Interfaces* **2023**, *15*, 26554.
191. Liu, K.; Zhang, C.; Sun, Y.; Zhang, G.; Shen, X.; Zou, F.; Zhang, H.; Wu, Z.; Wegener, E. C.; Taubert, C. J.; Miller, J. T.; Peng, Z.; Zhu, Y. High-Performance Transition Metal phosphide alloy catalyst for oxygen evolution reaction. *ACS Nano* **2017**, *12*, 158.
192. Ma, S.; Yang, P.; Chen, J.; Wu, Z.; Li, X.; Zhang, H. NiCu alloys anchored Co<sub>3</sub>O<sub>4</sub> nanowire arrays as efficient hydrogen evolution electrocatalysts in alkaline and neutral media. *Journal of Colloid and Interface Science* **2023**, *642*, 604.
193. Dong, J.; Zhang, X.; Huang, J.; Hu, J.; Chen, Z.; Lai, Y. In-situ formation of unsaturated defect sites on converted CoNi alloy/Co-Ni LDH to activate MoS<sub>2</sub> nanosheets for pH-universal hydrogen evolution reaction. *Chemical Engineering Journal* **2021**, *412*, 128556.

194. Fu, Y.; Yu, H.; Jiang, C.; Zhang, T.; Zhan, R.; Li, X.; Li, J.; Tian, J.; Yang, R. NiCo alloy nanoparticles decorated on N-Doped carbon nanofibers as highly active and durable oxygen electrocatalyst. *Advanced Functional Materials* **2017**, *28*, 1705094.
195. Zhou, Z.; Ng, Y. H.; Xu, S.; Yang, S.; Gao, Q.; Cai, X.; Liao, J.; Fang, Y.; Zhang, S. A CuNi Alloy–Carbon Layer Core–Shell catalyst for highly efficient conversion of aqueous formaldehyde to hydrogen at room temperature. *ACS Applied Materials & Interfaces* **2021**, *13*, 37299.
196. Qu, R.; Zhang, W.; Liu, N.; Zhang, Q.; Liu, Y.; Li, X.; Wei, Y.; Feng, L. Antioil Ag<sub>3</sub>PO<sub>4</sub> Nanoparticle/Polydopamine/Al<sub>2</sub>O<sub>3</sub> Sandwich Structure for Complex Wastewater Treatment: Dynamic Catalysis under Natural Light. *ACS Sustainable Chemistry & Engineering* **2018**, *6*, 8019.
197. Mileo, P. G. M.; Yuan, S.; Ayala, S.; Duan, P.; Semino, R.; Cohen, S. M.; Schmidt-Rohr, K.; Maurin, G. Structure of the polymer backbones in polyMOF materials. *Journal of the American Chemical Society* **2020**, *142*, 10863.
198. Bronstein, L. M.; Goerigk, G.; Kostylev, M.; Pink, M.; Khotina, I. A.; Valetsky, P. M.; Matveeva, V. G.; Sulman, E. M.; Sulman, M. G.; Bykov, A. V.; Lakina, N. V.; Spontak, R. J. Structure and catalytic properties of Pt-Modified Hyper-Cross-Linked polystyrene exhibiting hierarchical porosity. *The Journal of Physical Chemistry B* **2004**, *108*, 18234.
199. Gu, Y.; Huang, M.; Zhang, W.; Pearson, M. A.; Johnson, J. A. PolyMOF nanoparticles: dual roles of a multivalent polyMOF ligand in size control and surface functionalization. *Angewandte Chemie International Edition* **2019**, *58*, 16676.
200. Venugopal, A.; Egberts, L. H. T.; Meeprasert, J.; Pidko, E. A.; Dam, B.; Burdyny, T.; Sinha, V.; Smith, W. A. Polymer modification of surface electronic properties of electrocatalysts. *ACS Energy Letters* **2022**, *7*, 1586.

201. Alsharabasy, A. M.; Pandit, A.; Farràs, P. Recent advances in the design and sensing applications of Hemin/Coordination Polymer-Based nanocomposites. *Advanced Materials* **2020**, *33*, 2003883.
202. Rana, S. M. S.; Zahed, M. A.; Rahman, M. T.; Salauddin, M.; Lee, S. H.; Park, C.; Maharjan, P.; Bhatta, T.; Shrestha, K.; Park, J. Y. Cobalt-Nanoporous Carbon functionalized Nanocomposite-Based triboelectric nanogenerator for contactless and sustainable Self-Powered sensor systems. *Advanced Functional Materials* **2021**, *31*, 2105110.
203. Abdelazeez, A. A. A.; Rabia, M.; Hasan, F.; Mahanta, V.; Adly, E. R. Polymer Nanocomposites: Catalysts for Sustainable Hydrogen Production from Challenging Water Sources. *Advanced Energy and Sustainability Research* **2024**, 2400077.
204. Morales, D. V.; Astudillo, C. N.; Anastasoie, V.; Dautreppe, B.; Urbano, B. F.; Rivas, B. L.; Gondran, C.; Aldakov, D.; Chovelon, B.; André, D.; Putaux, J.-L.; Lancelon-Pin, C.; Sirach, S.; Ungureanu, E.-M.; Costentin, C.; Collomb, M.-N.; Fortage, J. A cobalt oxide–polypyrrole nanocomposite as an efficient and stable electrode material for electrocatalytic water oxidation. *Sustainable Energy & Fuels* **2021**, *5*, 4710.
205. Rizo, R.; Cuenya, B. R. Shape-Controlled nanoparticles as anodic catalysts in Low-Temperature fuel cells. *ACS Energy Letters* **2019**, *4*, 1484.
206. Al-Naggar, A. H.; Shinde, N. M.; Kim, J.-S.; Mane, R. S. Water splitting performance of metal and non-metal-doped transition metal oxide electrocatalysts. *Coordination Chemistry Reviews* **2022**, *474*, 214864.
207. Ujjwal, R. R.; Purohit, M. P.; Patnaik, S.; Ojha, U. General Reagent free route to pH responsive polyacryloyl hydrazide capped metal nanogels for synergistic anticancer therapeutics. *ACS Applied Materials & Interfaces* **2015**, *7*, 11497.

208. Ujjwal, R. R.; Sona, C.; Debnath, S.; Yadav, P. N.; Ojha, U. Dye-Labeled Polyacryloyl Hydrazide–Ag nanoparticle fluorescent probe for ultrasensitive and selective detection of Au ion. *ACS Omega* **2017**, *2*, 4278.
209. Yuan, S.; Ge, F.; Chen, Y.; Cai, Z. Tunable metal-enhanced fluorescence by pH-responsive polyacryloyl hydrazide capped Ag nanoparticles. *RSC Advances* **2017**, *7*, 6358.
210. Mandal, S.; Seth, A.; Yadav, V.; Kumari, S.; Kumar, M.; Ojha, U. Nanocomposite grafted stretchable and conductive ionic hydrogels for use as soft electrode in a wearable electrocardiogram monitoring device. *ACS Applied Polymer Materials* **2019**, *2*, 618.
211. Shin, S. S.; Jung, Y.; Jeon, S.; Park, S.-J.; Yoon, S.-J.; Jung, K.-W.; Choi, J.-W.; Lee, J.-H. Efficient recovery and recycling/upcycling of precious metals using hydrazide-functionalized star-shaped polymers. *Nature Communications* **2024**, *15*, 3889.
212. Jo, J. H.; Shin, S. S.; Jeon, S.; Park, S.-J.; Park, H.; Park, Y.-I.; Lee, J.-H. Star polymer-assembled adsorptive membranes for effective Cr(VI) removal. *Chemical Engineering Journal* **2022**, *449*, 137883.
213. Zhang, L.; Zha, X.; Zhang, G.; Gu, J.; Zhang, W.; Huang, Y.; Zhang, J.; Chen, T. Designing a reductive hybrid membrane to selectively capture noble metallic ions during oil/water emulsion separation with further function enhancement. *Journal of Materials Chemistry A* **2018**, *6*, 10217.
214. Tang, P.-Y.; Zhao, Y.-Q.; Wang, Y.-M.; Xu, C.-L. A metal-decorated nickel foam-inducing regulatable manganese dioxide nanosheet array architecture for high-performance supercapacitor applications. *Nanoscale* **2013**, *5*, 8156.
215. Gopalakrishnan, A.; Durai, L.; Ma, J.; Kong, C. Y.; Badhulika, S. Vertically Aligned Few-Layer Crumpled MoS<sub>2</sub> Hybrid Nanostructure on Porous Ni Foam toward Promising Binder-Free Methanol Electro-Oxidation Application. *Energy & Fuels* **2021**, *35*, 10169.

216. Wang, J.; Fan, Y.; Qi, S.; Li, W.; Zhao, M. Bifunctional HER/OER or OER/ORR Catalytic Activity of Two-Dimensional  $\text{TM}_3(\text{HITP})_2$  with  $\text{TM} = \text{Fe-Zn}$ . *The Journal of Physical Chemistry C* **2020**, *124*, 9350.
217. Liu, Y.; Koza, J. A.; Switzer, J. A. Conversion of electrodeposited  $\text{Co}(\text{OH})_2$  to  $\text{CoOOH}$  and  $\text{Co}_3\text{O}_4$ , and comparison of their catalytic activity for the oxygen evolution reaction. *Electrochimica Acta* **2014**, *140*, 359.
218. Blöchl, P. E. Projector augmented-wave method. *Physical Review. B, Condensed Matter* **1994**, *50*, 17953.
219. Perdew, J. P.; Burke, K.; Ernzerhof, M. Generalized gradient approximation made simple. *Physical Review Letters* **1996**, *77*, 3865.
220. Samal, A.; Kushwaha, A. K.; Das, D.; Sahoo, M. R.; Lanzillo, N. A.; Nayak, S. K. Thermal and electrical conductivity of Copper-Graphene heterosystem: an effect of strain and thickness. *Advanced Engineering Materials* **2023**, *25*, 2201192.
221. Khomyakov, P. A.; Giovannetti, G.; Rusu, P. C.; Brocks, G.; Van Den Brink, J.; Kelly, P. J. First-principles study of the interaction and charge transfer between graphene and metals. *Physical Review B* **2009**, *79*, 195425.
222. Giovannetti, G.; Khomyakov, P. A.; Brocks, G.; Karpan, V. M.; Van Den Brink, J.; Kelly, P. J. Doping Graphene with Metal Contacts. *Physical Review Letters* **2008**, *101*, 026803.
223. Sahoo, M. R.; Kushwaha, A. K.; Pati, R.; Ajayan, P. M.; Nayak, S. K. First-principles study of a vertical spin switch in atomic scale two-dimensional platform. *Journal of Magnetism and Magnetic Materials* **2019**, *484*, 462.
224. Liang, Q.; Brocks, G.; Bieberle-Hütter, A. Oxygen evolution reaction (OER) mechanism under alkaline and acidic conditions. *Journal of Physics Energy* **2021**, *3*, 026001.

225. Aashi, N.; Alagar, S.; Krishankant, N.; Gaur, A.; Bera, C.; Bagchi, V. Rapid synthesis of a CuZn-MOF via controlled electrodeposition: manifesting enhanced overall electrocatalytic water splitting. *Sustainable Energy & Fuels* **2023**, *7*, 3692.
226. Kwon, N. H.; Kim, M.; Jin, X.; Lim, J.; Kim, I. Y.; Lee, N.-S.; Kim, H.; Hwang, S.-J. A rational method to kinetically control the rate-determining step to explore efficient electrocatalysts for the oxygen evolution reaction. *NPG Asia Materials* **2018**, *10*, 659.
227. Luan, C.; Liu, G.; Liu, Y.; Yu, L.; Wang, Y.; Xiao, Y.; Qiao, H.; Dai, X.; Zhang, X. Structure effects of 2D materials on A-Nickel hydroxide for oxygen evolution reaction. *ACS Nano* **2018**, *12*, 3875.
228. Jiang, H.; Ai, L.; Chen, M.; Jiang, J. Broadband Nickel Sulfide/Nickel Foam-Based solar evaporator for highly efficient water purification and electricity generation. *ACS Sustainable Chemistry & Engineering* **2020**, *8*, 10833.
229. Bhat, K. S.; Nagaraja, H. S. In situ synthesis of Copper Sulfide-Nickel sulfide arrays on Three-Dimensional nickel foam for overall water splitting. *ChemistrySelect* **2020**, *5*, 2455.
230. Gioria, E.; Li, S.; Mazheika, A.; D'Alnoncourt, R. N.; Thomas, A.; Rosowski, F. CuNi Nanoalloys with Tunable Composition and Oxygen Defects for the Enhancement of the Oxygen Evolution Reaction. *Angewandte Chemie International Edition* **2023**, *62*, e202217888.
231. Ahsan, M. A.; Santiago, A. R. P.; Hong, Y.; Zhang, N.; Cano, M.; Rodriguez-Castellon, E.; Echegoyen, L.; Sreenivasan, S. T.; Noveron, J. C. Tuning of Trifunctional NiCu Bimetallic Nanoparticles Confined in a Porous Carbon Network with Surface Composition and Local Structural Distortions for the Electrocatalytic Oxygen Reduction, Oxygen and Hydrogen Evolution Reactions. *Journal of the American Chemical Society* **2020**, *142*, 14688.

232. Yen, H.; Seo, Y.; Kaliaguine, S.; Kleitz, F. Role of Metal–Support interactions, particle size, and Metal–Metal synergy in CuNi nanocatalysts for H<sub>2</sub> Generation. *ACS Catalysis* **2015**, *5*, 5505.
233. Yu, L.; Wu, L.; McElhenny, B.; Song, S.; Luo, D.; Zhang, F.; Yu, Y.; Chen, S.; Ren, Z. Ultrafast room-temperature synthesis of porous S-doped Ni/Fe (oxy)hydroxide electrodes for oxygen evolution catalysis in seawater splitting. *Energy & Environmental Science* **2020**, *13*, 3439.
234. He, D.; Song, X.; Li, W.; Tang, C.; Liu, J.; Ke, Z.; Jiang, C.; Xiao, X. Active Electron Density Modulation of Co<sub>3</sub>O<sub>4</sub>-Based Catalysts Enhances their Oxygen Evolution Performance. *Angewandte Chemie International Edition* **2020**, *59*, 6929.
235. Harilal, M.; Vidyadharan, B.; Misnon, I. I.; Anilkumar, G. M.; Lowe, A.; Ismail, J.; Yusoff, M. M.; Jose, R. One-Dimensional assembly of conductive and capacitive metal oxide electrodes for High-Performance asymmetric supercapacitors. *ACS Applied Materials & Interfaces* **2017**, *9*, 10730.
236. Dietrich, F.; Fernandez, J.; Hevia, S.; Cisternas, E.; Flores, M. Determination of the conformational preference of para-Aminobenzoic acid on vanadium pentoxide surface: an XPS and DFT study. *The Journal of Physical Chemistry C* **2021**, *125*, 20450.
237. Thangavel, P.; Ha, M.; Kumaraguru, S.; Meena, A.; Singh, A. N.; Harzandi, A. M.; Kim, K. S. Graphene-nanoplatelets-supported NiFe-MOF: high-efficiency and ultra-stable oxygen electrodes for sustained alkaline anion exchange membrane water electrolysis. *Energy & Environmental Science* **2020**, *13*, 3447.
238. Carroll, K. J.; Reveles, J. U.; Shultz, M. D.; Khanna, S. N.; Carpenter, E. E. Preparation of elemental Cu and Ni nanoparticles by the Polyol Method: an experimental and theoretical approach. *The Journal of Physical Chemistry C* **2011**, *115*, 2656.

239. Zhang, H.; Zhang, D.; Lu, X.; Liu, C.; Zhou, G.; Ma, X.; Wang, L.; Jiang, P.; Xue, Q.-K.; Bao, X. Origin of charge transfer and enhanced electron–phonon coupling in single unit-cell FeSe films on SrTiO<sub>3</sub>. *Nature Communications* **2017**, *8*, 214.
240. Oh, N. K.; Seo, J.; Lee, S.; Kim, H.-J.; Kim, U.; Lee, J.; Han, Y.-K.; Park, H. Highly efficient and robust noble-metal free bifunctional water electrolysis catalyst achieved via complementary charge transfer. *Nature Communications* **2021**, *12*, 4606.
241. Liu, B.; Liu, X.; Liu, J.; Feng, C.; Li, Z.; Li, C.; Gong, Y.; Pan, L.; Xu, S.; Sun, C. Q. Efficient charge separation between UiO-66 and ZnIn<sub>2</sub>S<sub>4</sub> flowerlike 3D microspheres for photoelectronchemical properties. *Applied Catalysis B Environment and Energy* **2017**, *226*, 234.
242. Woolley, R. J.; Illy, B. N.; Ryan, M. P.; Skinner, S. J. In situ determination of the nickel oxidation state in La<sub>2</sub>NiO<sub>4+δ</sub> and La<sub>4</sub>Ni<sub>3</sub>O<sub>10-δ</sub> using X-ray absorption near-edge structure. *Journal of Materials Chemistry* **2011**, *21*, 18592.
243. Heilmann, M.; Prinz, C.; Bienert, R.; Wendt, R.; Kunkel, B.; Radnik, J.; Hoell, A.; Wohlrab, S.; Buzanich, A. G.; Emmerling, F. Size-Tunable Ni–Cu Core–Shell Nanoparticles—Structure, composition, and catalytic activity for the reverse Water–Gas shift reaction. *Advanced Engineering Materials* **2022**, *24*, 2101308.
244. Wang, H.-Y.; Hung, S.-F.; Chen, H.-Y.; Chan, T.-S.; Chen, H. M.; Liu, B. In operando identification of Geometrical-Site-Dependent water oxidation activity of spinel CO<sub>3</sub>O<sub>4</sub>. *Journal of the American Chemical Society* **2015**, *138*, 36.
245. Gajdek, D.; Olsson, P. a. T.; Blomberg, S.; Gustafson, J.; Carlsson, P.-A.; Haase, D.; Lundgren, E.; Merte, L. R. Structural Changes in Monolayer Cobalt Oxides under Ambient Pressure CO and O<sub>2</sub> Studied by In Situ Grazing-Incidence X-ray Absorption Fine Structure Spectroscopy. *The Journal of Physical Chemistry C* **2022**, *126*, 3411.

246. Shi, H.; Dai, X.; Liu, Q.; Zhang, T.; Zhang, Y.; Shi, Y.; Wang, T. Magnetic CuNi alloy nanoparticles for catalytic transfer hydrogenation of nitroarene. *Industrial & Engineering Chemistry Research* **2021**, *60*, 16011.
247. Boudjahem, A. G.; Serge, M.; Michel, M.; Mohammed, M. B. Study of support effects on the reduction of Ni<sup>2+</sup> ions in aqueous hydrazine. *Langmuir* **2004**, *20*, 208.
248. Gawande, M. B.; Goswami, A.; Felpin, F.-X.; Asefa, T.; Huang, X.; Silva, R.; Zou, X.; Zboril, R.; Varma, R. S. Cu and Cu-Based Nanoparticles: Synthesis and Applications in Catalysis. *Chemical Reviews* **2016**, *116*, 3722.
249. Qu, P.; Yang, S.; Wang, C.; Han, H. Two-Step hydrometallurgical preparation of ultrafine cobalt powders. *ACS Omega* **2022**, *7*, 8840.
250. Ren, Y.; Bai, Y.; Wang, G.; Liu, Y.; Mou, C.; Chen, J.; Wei, B.; Wang, H.; Sun, Y. Cu–Ni alloy nanoparticles anchored on Nitrogen-Doped carbon nanotubes for efficient CO<sub>2</sub> electroreduction to CO. *Energy & Fuels* **2023**, *37*, 9289.
251. Zhang, X.; Ju, S.; Li, C.; Hao, J.; Sun, Y.; Hu, X.; Chen, W.; Chen, J.; He, L.; Xia, G.; Fang, F.; Sun, D.; Yu, X. Atomic reconstruction for realizing stable solar-driven reversible hydrogen storage of magnesium hydride. *Nature Communications* **2024**, *15*, 2815.
252. Amiri, A.; Yurkiv, V.; Phakatkar, A. H.; Shokuhfar, T.; Shahbazian-Yassar, R. Insights into Formation and Growth of Colloidal Multielement Alloy Nanoparticles in Solution through In Situ Liquid Cell TEM Study. *Advanced Functional Materials* **2024**, *34*, 2304685.
253. Liang, Y.; Zeng, Y.; Tang, X.; Xia, W.; Song, B.; Yao, F.; Yang, Y.; Chen, Y.; Peng, C.; Zhou, C.; Lai, C. One-step synthesis of Cu(OH)<sub>2</sub>-Cu/Ni foam cathode for electrochemical reduction of nitrate. *Chemical Engineering Journal* **2022**, *451*, 138936.

254. Mandal, S.; Pandey, N.; Singh, S.; Ranjan, A.; Ojha, U. Polyacryloyl hydrazide incorporation into ionic hydrogels improves toughness, elasticity, self-healability, adhesive & strain sensing properties. *Materials Chemistry Frontiers* **2019**, *3*, 690.
255. Xiao, L.; Mou, S.; Dai, W.; Yang, W.; Cheng, Q.; Liu, S.; Dong, F. Identification of Cu(111) as Superior Active Sites for Electrocatalytic NO Reduction to NH<sub>3</sub> with High Single-Pass Conversion Efficiency. *Angewandte Chemie International Edition* **2024**, *63*, e202319135.
256. Mahmoud, M. A.; Narayanan, R.; El-Sayed, M. A. Enhancing colloidal metallic nanocatalysis: sharp edges and corners for solid nanoparticles and cage effect for hollow ones. *Accounts of Chemical Research* **2013**, *46*, 1795.
257. Rao, C.; Wang, H.; Chen, K.; Chen, H.; Ci, S.; Xu, Q.; Wen, Z. Hybrid Acid/Base electrolytic cell for hydrogen generation and methanol conversion implemented by bifunctional Ni/MoN Nanorod Electrocatalyst. *Small* **2023**, *20*, 2303300.
258. Li, J.; Wei, R.; Wang, X.; Zuo, Y.; Han, X.; Arbiol, J.; Llorca, J.; Yang, Y.; Cabot, A.; Cui, C. Selective Methanol-to-Formate electrocatalytic conversion on branched nickel carbide. *Angewandte Chemie International Edition* **2020**, *59*, 20826.
259. Zhu, B.; Dong, B.; Wang, F.; Yang, Q.; He, Y.; Zhang, C.; Jin, P.; Feng, L. Unraveling a bifunctional mechanism for methanol-to-formate electro-oxidation on nickel-based hydroxides. *Nature Communications* **2023**, *14*, 1686.
260. Li, G.; Yu, J.; Yu, W.; Yang, L.; Zhang, X.; Liu, X.; Liu, H.; Zhou, W. Phosphorus-Doped Iron Nitride Nanoparticles Encapsulated by Nitrogen-Doped Carbon Nanosheets on Iron Foam In Situ Derived from *Saccharomyces Cerevisiae* for Electrocatalytic Overall Water Splitting. *Small* **2020**, *16*, 2001980.

261. Li, Q.; Wang, X.; Tang, K.; Wang, M.; Wang, C.; Yan, C. Electronic modulation of electrocatalytically active center of Cu<sub>7</sub>S<sub>4</sub> nanodisks by Cobalt-Doping for highly efficient oxygen evolution reaction. *ACS Nano* **2017**, *11*, 12230.
262. Rößner, L.; Armbrüster, M. Electrochemical Energy Conversion on Intermetallic Compounds: A review. *ACS Catalysis* **2019**, *9*, 2018.
263. Zemtsova, V. M.; Oshchepkov, A. G.; Savinova, E. R. Unveiling the role of iron in the Nickel-Catalyzed urea oxidation reaction. *ACS Catalysis* **2023**, *13*, 13466.
264. Zhang, L.; Wang, L.; Lin, H.; Liu, Y.; Ye, J.; Wen, Y.; Chen, A.; Wang, L.; Ni, F.; Zhou, Z.; Sun, S.; Li, Y.; Zhang, B.; Peng, H. A Lattice-Oxygen-Involved reaction pathway to boost urea oxidation. *Angewandte Chemie International Edition* **2019**, *58*, 16820.
265. Miller, A. T.; Hassler, B. L.; Botte, G. G. Rhodium electrodeposition on nickel electrodes used for urea electrolysis. *Journal of Applied Electrochemistry* **2012**, *42*, 925.
266. Boggs, B. K.; King, R. L.; Botte, G. G. Urea electrolysis: direct hydrogen production from urine. *Chemical Communications* **2009**, *32*, 4859.
267. Zhu, B.; Liang, Z.; Zou, R. Designing advanced catalysts for energy conversion based on urea oxidation reaction. *Small* **2020**, *16*, 1906133.
268. King, R. L.; Botte, G. G. Investigation of multi-metal catalysts for stable hydrogen production via urea electrolysis. *Journal of Power Sources* **2011**, *196*, 9579.
269. Forslund, R. P.; Alexander, C. T.; Abakumov, A. M.; Johnston, K. P.; Stevenson, K. J. Enhanced electrocatalytic activities by substitutional tuning of Nickel-Based Ruddlesden–Popper catalysts for the oxidation of urea and small alcohols. *ACS Catalysis* **2019**, *9*, 2664.

270. Periyasamy, S.; Subramanian, P.; Levi, E.; Aurbach, D.; Gedanken, A.; Schechter, A. Exceptionally active and stable spinel nickel manganese oxide electrocatalysts for urea oxidation reaction. *ACS Applied Materials & Interfaces* **2016**, *8*, 12176.
271. Patil, S. J.; Chodankar, N. R.; Hwang, S.; Raju, G. S. R.; Huh, Y.; Han, Y. Fluorine engineered Self-Supported ultrathin 2D nickel hydroxide nanosheets as highly robust and stable bifunctional electrocatalysts for oxygen evolution and urea oxidation reactions. *Small* **2021**, *18*, 2103326.
272. Yuan, M.; Wang, R.; Sun, Z.; Lin, L.; Yang, H.; Li, H.; Nan, C.; Sun, G.; Ma, S. Morphology-Controlled Synthesis of Ni-MOFs with Highly Enhanced Electrocatalytic Performance for Urea Oxidation. *Inorganic Chemistry* **2019**, *58*, 11449.
273. Ghosh, D.; Pradhan, D. Effect of cooperative redox property and oxygen vacancies on bifunctional OER and HER activities of solvothermally synthesized CeO<sub>2</sub>/CuO composites. *Langmuir* **2023**, *39*, 3358.
274. Sun, H.; Liu, J.; Kim, H.; Song, S.; Fei, L.; Hu, Z.; Lin, H.; Chen, C.; Ciucci, F.; Jung, W. Ni-Doped CuO nanoarrays activate urea adsorption and stabilizes reaction intermediates to achieve High-Performance urea oxidation catalysts. *Advanced Science* **2022**, *9*, 2204800.
275. Wang, L.; Liu, Y.; Liu, X.; Chen, W. 3D nanostructured Ce-doped CoFe-LDH/NF self-supported catalyst for high-performance OER. *Dalton Transactions* **2023**, *52*, 12038.
276. Xiao, Z.; Qian, Y.; Tan, T.; Lu, H.; Liu, C.; Wang, B.; Zhang, Q.; Sarwar, M. T.; Gao, R.; Tang, A.; Yang, H. Energy-saving hydrogen production by water splitting coupling urea decomposition and oxidation reactions. *Journal of Materials Chemistry A* **2022**, *11*, 259.

277. Song, X.; Zhu, W.; Wang, X.; Tan, Z. Recent Advances of CeO<sub>2</sub>-Based Electrocatalysts for Oxygen and Hydrogen Evolution as well as Nitrogen Reduction. *ChemElectroChem* **2021**, *8*, 996.
278. Gao, W.; Ma, F.; Wang, C.; Wen, D. Ce dopant significantly promotes the catalytic activity of Ni foam-supported Ni<sub>3</sub>S<sub>2</sub> electrocatalyst for alkaline oxygen evolution reaction. *Journal of Power Sources* **2020**, *450*, 227654.
279. Yang, H.; Yuan, M.; Sun, Z.; Wang, D.; Lin, L.; Li, H.; Sun, G. In Situ Construction of a Mn<sup>2+</sup>-Doped Ni<sub>3</sub>S<sub>2</sub> Electrode with Highly Enhanced Urea Oxidation Reaction Performance. *ACS Sustainable Chemistry & Engineering* **2020**, *8*, 8348.
280. Lan, C.; Xie, H.; Wu, Y.; Chen, B.; Liu, T. Nanoengineered, Mo-Doped, Ni<sub>3</sub>S<sub>2</sub> Electrocatalyst with Increased Ni–S Coordination for Oxygen Evolution in Alkaline Seawater. *Energy & Fuels* **2022**, *36*, 2910.
281. Babu, K. J.; Kumar, T. R.; Yoo, D. J.; Phang, S.-M.; Kumar, G. G. Electrodeposited nickel cobalt sulfide flowerlike architectures on disposable cellulose filter paper for Enzyme-Free glucose sensor applications. *ACS Sustainable Chemistry & Engineering* **2018**, *6*, 16982.
282. Wu, X.; Zhang, T.; Wei, J.; Feng, P.; Yan, X.; Tang, Y. Facile synthesis of Co and Ce dual-doped Ni<sub>3</sub>S<sub>2</sub> nanosheets on Ni foam for enhanced oxygen evolution reaction. *Nano Research* **2020**, *13*, 2130.
283. Wang, S.; Li, H.; Li, S.; Ni, Y. Fe,Ce Co-Doped Ni<sub>3</sub>S<sub>2</sub>/NiS Polymorphism Nanosheets with Improved Electrocatalytic Activity and Stability for Water Oxidation. *ChemSusChem* **2024**, e202400896.
284. Cheng, Z.; Abernathy, H.; Liu, M. Raman Spectroscopy of Nickel Sulfide Ni<sub>3</sub>S<sub>2</sub>. *The Journal of Physical Chemistry C* **2007**, *111*, 17997.

285. Yu, W.; Zhou, Q.; Wang, H.; Liu, Y.; Chu, W.; Cai, R.; Yang, W. Selective removal of CO from hydrocarbon-rich industrial off-gases over CeO<sub>2</sub>-supported metal oxides. *Journal of Materials Science* **2019**, *55*, 2321.
286. Liu, B.; Kong, D.; Zhang, J.; Wang, Y.; Chen, T.; Cheng, C.; Yang, H. Y. 3D hierarchical Co<sub>3</sub>O<sub>4</sub>@Co<sub>3</sub>S<sub>4</sub> nanoarrays as cathode materials for asymmetric pseudocapacitors. *Journal of Materials Chemistry A* **2016**, *4*, 3287.
287. Ai, T.; Wang, H.; Bao, W.; Feng, L.; Zou, X.; Wei, X.; Ding, L.; Deng, Z.; Rao, B. Fe-V synergistic doping effect of hierarchical Ni<sub>3</sub>S<sub>2</sub> oblate-nanorod arrays for efficient electrocatalytic oxygen evolution reaction. *Chemical Engineering Journal* **2022**, *450*, 138358.
288. Sun, Q.; Liu, Y.; Li, X.; Guo, X.; Huang, W.-H.; Zhu, Y.; Wang, Z.; Chueh, C.-C.; Chen, C.-L.; Peng, Y.-K.; Zhu, Z. Highly Disordered Fe-Doped CeO<sub>2</sub> with Oxygen Vacancies Facilitates Electrocatalytic Water Oxidation. *Energy & Fuels* **2023**, *37*, 9434.
289. He, D.; Song, X.; Li, W.; Tang, C.; Liu, J.; Ke, Z.; Jiang, C.; Xiao, X. Active Electron Density Modulation of Co<sub>3</sub>O<sub>4</sub>-Based Catalysts Enhances their Oxygen Evolution Performance. *Angewandte Chemie* **2020**, *132*, 6996.
290. Long, N.; Peng, J.; Jiang, Y.; Shen, W.; He, R.; Li, M. Synergy of interface coupling and sulfur vacancies in Ni<sub>3</sub>S<sub>2</sub>/Fe<sub>2</sub>P for water splitting. *Inorganic Chemistry* **2024**, *63*, 16382.
291. Zhang, B.; Zhang, J.; Zhang, H.; Jiang, H.; Li, C. Surface covalent sulfur enriching Ni active sites of Ni<sub>3</sub>S<sub>2</sub> nanoparticles for efficient oxygen evolution. *New Journal of Chemistry* **2021**, *45*, 3210.
292. Zhang, L.; Wang, Z.; Qiu, J. Energy-Saving hydrogen production by seawater electrolysis coupling sulfion degradation. *Advanced Materials* **2022**, *34*, 2109321.

293. Ma, G.; Zhang, X.; Zhou, G.; Wang, X. Hydrogen production from methanol reforming electrolysis at NiO nanosheets supported Pt nanoparticles. *Chemical Engineering Journal* **2021**, *411*, 128292.
294. Chen, S.; Yang, X.; Tong, X.; Zhang, F.; Zou, H.; Qiao, Y.; Dong, M.; Wang, J.; Fan, W. Design of 3D hollow porous heterogeneous Nickel–Cobalt phosphides for synergistically enhancing catalytic performance for electrooxidation of methanol. *ACS Applied Materials & Interfaces* **2020**, *12*, 34971.
295. Shao, J.; Fang, Y.; Wu, X.; Abdullah, M. I.; Tao, Y. Unraveling the role of NiSnPH@OOH/CC perovskite hydroxide for efficient electrocatalytic oxidation of methanol to formate. *Nano Research* **2023**, *17*, 2388.
296. Jung, S.; Senthil, R. A.; Min, A.; Kumar, A.; Moon, C. J.; Choi, M. Y. Laser-Synthesized Co-Doped CuO Electrocatalyst: Unveiling boosted methanol oxidation kinetics for enhanced hydrogen production efficiency by In Situ/Operando Raman and theoretical analyses. *Small Methods* **2024**, *8*, 2301628.
297. Wei, X.; Li, Y.; Chen, L.; Shi, J. Formic acid Electro-Synthesis by concurrent cathodic CO<sub>2</sub> reduction and anodic CH<sub>3</sub>OH oxidation. *Angewandte Chemie International Edition* **2020**, *60*, 3148.
298. Shi, J.; He, H.; Zhou, S.; Li, J.; Cai, W. Fe-based “electron pump” involving NiCo-LDH enables robust and highly selective electrocatalytic methanol oxidation to formic acid. *Green Chemistry* **2024**, *26*, 2638.
299. Dang, J.; Chen, G.; Yuan, B.; Liu, F.; Wang, Q.; Wang, F.; Miao, H.; Yuan, J. Promoting the four electrocatalytic reactions of OER/ORR/HER/MOR using a multi-component metal sulfide heterostructure for zinc-air batteries and water-splitting. *Nanoscale* **2024**, *16*, 4710.

300. Liu, T.; Liu, D.; Qu, F.; Wang, D.; Zhang, L.; Ge, R.; Hao, S.; Ma, Y.; Du, G.; Asiri, A. M.; Chen, L.; Sun, X. Enhanced Electrocatalysis for Energy-Efficient Hydrogen Production over CoP Catalyst with Nonelectroactive Zn as a Promoter. *Advanced Energy Materials* **2017**, *7*, 1700020.
301. Pan, Y.; Sun, K.; Lin, Y.; Cao, X.; Cheng, Y.; Liu, S.; Zeng, L.; Cheong, W.-C.; Zhao, D.; Wu, K.; Liu, Z.; Liu, Y.; Wang, D.; Peng, Q.; Chen, C.; Li, Y. Electronic structure and d-band center control engineering over M-doped CoP (M = Ni, Mn, Fe) hollow polyhedron frames for boosting hydrogen production. *Nano Energy* **2018**, *56*, 411.
302. Chen, S.; Duan, J.; Vasileff, A.; Qiao, S. Z. Size Fractionation of Two-Dimensional Sub-Nanometer Thin Manganese Dioxide Crystals towards Superior Urea Electrocatalytic Conversion. *Angewandte Chemie International Edition* **2016**, *55*, 3804.
303. Ji, Z.; Liu, J.; Deng, Y.; Zhang, S.; Zhang, Z.; Du, P.; Zhao, Y.; Lu, X. Accurate synergy effect of Ni–Sn dual active sites enhances electrocatalytic oxidation of urea for hydrogen evolution in alkaline medium. *Journal of Materials Chemistry A* **2020**, *8*, 14680.
304. Xu, H.; Ye, K.; Zhu, K.; Yin, J.; Yan, J.; Wang, G.; Cao, D. Efficient bifunctional catalysts synthesized from three-dimensional Ni/Fe bimetallic organic frameworks for overall urea electrolysis. *Dalton Transactions* **2020**, *49*, 5646.
305. Feng, Y.; Wang, X.; Huang, J.; Dong, P.; Ji, J.; Li, J.; Cao, L.; Feng, L.; Jin, P.; Wang, C. Decorating CoNi layered double hydroxides nanosheet arrays with fullerene quantum dot anchored on Ni foam for efficient electrocatalytic water splitting and urea electrolysis. *Chemical Engineering Journal* **2020**, *390*, 124525.
306. Meng, J.; Chernev, P.; Mohammadi, M. R.; Klingan, K.; Loos, S.; Pasquini, C.; Kubella, P.; Jiang, S.; Yang, X.; Cui, Z.; Zhu, S.; Li, Z.; Liang, Y.; Dau, H. Self-supported

Ni(OH)<sub>2</sub>/MnO<sub>2</sub> on CFP as a flexible anode towards electrocatalytic urea conversion: The role of composition on activity, redox states and reaction dynamics. *Electrochimica Acta* **2019**, *318*, 32.

307. Gao, W.; Wang, C.; Ma, F.; Wen, D. Highly active electrocatalysts of CeO<sub>2</sub> modified NiMoO<sub>4</sub> nanosheet arrays towards water and urea oxidation reactions. *Electrochimica Acta* **2019**, *320*, 134608.

308. Xu, X.; Guo, T.; Xia, J.; Zhao, B.; Su, G.; Wang, H.; Huang, M.; Toghan, A. Modulation of the crystalline/amorphous interface engineering on Ni-P-O-based catalysts for boosting urea electrolysis at large current densities. *Chemical Engineering Journal* **2021**, *425*, 130514.

309. Chen, N.; Du, Y.-X.; Zhang, G.; Lu, W.-T.; Cao, F.-F. Amorphous nickel sulfoselenide for efficient electrochemical urea-assisted hydrogen production in alkaline media. *Nano Energy* **2020**, *81*, 105605.

310. Liu, H.; Zhu, S.; Cui, Z.; Li, Z.; Wu, S.; Liang, Y. Ni<sub>2</sub>P nanoflakes for the high-performing urea oxidation reaction: linking active sites to a UOR mechanism. *Nanoscale* **2020**, *13*, 1759.

311. Li, R.-Q.; Liu, Q.; Zhou, Y.; Lu, M.; Hou, J.; Qu, K.; Zhu, Y.; Fontaine, O. 3D self-supported porous vanadium-doped nickel nitride nanosheet arrays as efficient bifunctional electrocatalysts for urea electrolysis. *Journal of Materials Chemistry A* **2021**, *9*, 4159.

312. Zhang, Q.; Kazim, F. Md.; Ma, S.; Qu, K.; Li, M.; Wang, Y.; Hu, H.; Cai, W.; Yang, Z. Nitrogen dopants in nickel nanoparticles embedded carbon nanotubes promote overall urea oxidation. *Applied Catalysis B Environment and Energy* **2020**, *280*, 119436.

313. Zhang, H.; Meng, X.; Zhang, J.; Huang, Y. Hierarchical NiFe Hydroxide/Ni<sub>3</sub>N Nanosheet-on-Nanosheet heterostructures for bifunctional oxygen evolution and urea oxidation reactions. *ACS Sustainable Chemistry & Engineering* **2021**, *9*, 12584.

## List of Publications

1. **Semwal, S.**; Shakir, R.; Karthikeyan, J.; Sinha, A. S. K.; Ojha, U. NiFeOOH-Co<sub>9</sub>S<sub>8</sub>-Intercalated Nanostructure Arrays for Energy-Efficient H<sub>2</sub> Production and Sulfion Oxidation at High Current Density. *ACS Appl. Nano Mater.* **2023**, *6*, 18945-18956.
2. Tewary, A.; **Semwal, S.**; Sinha, A. S. K.; Ojha, U. Hydroxyl Amine Promoted in-situ Growth of Fe<sub>2</sub>O<sub>3</sub>-Ni<sub>3</sub>N Nanospikes on Ni Surface for Effective Hydrogen Evolution Reaction *ACS Appl. Nano Mater.* **2024**, *7*, 5923.
3. **Semwal, S.**; Samal, A.; Nayak, S. K.; Urkude, R. R.; Sinha, A. S. K.; Ojha, U. Surface Mediated Growth of Polyacryloyl Hydrazide Promoted Co<sub>3</sub>O<sub>4</sub>@NiCu Alloy Nanocuboids for Effective Methanol Oxidation & Oxygen Evolution Reactions. *Adv. Sustainable Syst.* **2024**, 2400372.
4. Setia, Y.; **Semwal, S.**; Sinha, A. S. K.; Ojha, U. NH<sub>2</sub>NH<sub>2</sub> Mediated Hydrothermal Growth of Ultra-small Ni<sub>2</sub>O<sub>3</sub>/NiOOH Nanoparticle based Nanoflakes for Electrocatalytic Hydrogen Evolution Reaction. (Manuscript Under Preparation)
5. **Semwal, S.**; Sinha, A. S. K.; Ojha, U. In-situ Growth of CeFe doped CeO<sub>2</sub>/Ni<sub>3</sub>S<sub>2</sub> nanorod as highly stable bifunctional electrocatalyst for effective urea oxidation reaction (Manuscript Under Preparation)

This page was initially left blank.

## Conferences/Workshops/Webinars

1. Presented Poster at “International Conference on Science and Technology of Polymers and Advanced Materials through Innovation, Entrepreneurship and Industry” – SPSI-MACRO-2022, NCL Pune, Maharashtra (2-4 November 2022).
2. Presented Poster at “International Conference on “Macromolecules: Synthesis, Morphology, Processing, Structure, Properties and Applications ICM-2024 Mahatma Gandhi University, Kottayam, Kerala, India. (12-14 January 2024).
3. Workshop on Rietveld Refinement; Organised by the Department of Physics, M. A. M. O. college, Mukkam (10-27 March 2024).
4. Workshop on Quantum Leap: DFT Code Mastery; Organised by AIP and Janardan Sing Foundation (11-12 May 2024).
5. NeW IPR 2021 e-Workshop; Organized by Innovative Technology Enabling Centre (InTEC), CSIR- IMMT, Bhubaneswar 14-19 June 2021.
6. Webinar on Scholarly Publishing in Energy Research; Organised by- ACS Energy Letters, ACS Energy & Fuels (27-28 June 2024).
7. ACS Science Talks: Designing a greener energy conversion system for a sustainable future; Organised by- American Chemical Society (25 Aug 2023).
8. Workshop on Electrochemical Data Analysis: Organized by SIAS Research Centre in Association with Metrohm India (7-18 October 2024)

This page was initially left blank.

# Copyright Clearance



## Marketplace

This is a License Agreement between Santosh Semwal ("User") and Copyright Clearance Center, Inc. ("CCC") on behalf of the Rightsholder identified in the order details below. The license consists of the order details, the Marketplace Permissions General Terms and Conditions below, and any Rightsholder Terms and Conditions which are included below.

All payments must be made in full to CCC in accordance with the Marketplace Permissions General Terms and Conditions below.

<b>Order Date</b>	07-Nov-2024	<b>Type of Use</b>	Republish in a thesis/dissertation
<b>Order License ID</b>	1543688-1	<b>Publisher Portion</b>	RSC Publishing Image/photo/illustration
<b>ISSN</b>	1754-5706		

### LICENSED CONTENT

<b>Publication Title</b>	Energy & environmental science	<b>Publication Type</b>	e-Journal
<b>Article Title</b>	Water electrolysis for hydrogen production: from hybrid systems to self-powered/catalyzed devices	<b>Start Page</b>	49
<b>Author / Editor</b>	Royal Society of Chemistry (Great Britain)	<b>End Page</b>	113
<b>Date</b>	01/01/2008	<b>Issue</b>	1
<b>Language</b>	English	<b>Volume</b>	17
<b>Country</b>	United Kingdom of Great Britain and Northern Ireland	<b>URL</b>	<a href="http://www.rsc.org/Publishing/Journals/EE/Index.asp">http://www.rsc.org/Publishing/Journals/EE/Index.asp</a>
<b>Rightsholder</b>	Royal Society of Chemistry		

### REQUEST DETAILS

<b>Portion Type</b>	Image/photo/illustration	<b>Distribution</b>	Worldwide
<b>Number of Images / Photos / Illustrations</b>	1	<b>Translation</b>	Original language of publication
<b>Format (select all that apply)</b>	Print, Electronic	<b>Copies for the Disabled?</b>	No
<b>Who Will Republish the Content?</b>	Publisher, not-for-profit	<b>Minor Editing Privileges?</b>	No
<b>Duration of Use</b>	Life of current edition	<b>Incidental Promotional Use?</b>	No
<b>Lifetime Unit Quantity</b>	More than 2,000,000	<b>Currency</b>	USD
<b>Rights Requested</b>	Main product		

### NEW WORK DETAILS

<b>Title</b>	Synthesis and Characterization of Transition Metal based Nanocatalysts for Energy Efficient Electrochemical H2 production	<b>Institution Name</b>	RAJIV GANDHI INSTITUTE OF PETROLEUM TECHNOLOGY JAIS, INDIA – 229304
<b>Instructor Name</b>	Santosh Semwal	<b>Expected Presentation Date</b>	2025-01-01

## ADDITIONAL DETAILS

---

<b>Order Reference Number</b>	N/A	<b>The Requesting Person / Organization to Appear on the License</b>	Santosh Semwal
-------------------------------	-----	--	----------------

## REQUESTED CONTENT DETAILS

---

<b>Title, Description or Numeric Reference of the Portion(s)</b>	Fig. 1 (a)	<b>Title of the Article / Chapter the Portion Is From</b>	Water electrolysis for hydrogen production: from hybrid systems to self-powered/catalyzed devices
<b>Editor of Portion(s)</b>	Ren, Jin-Tao; Chen, Lei; Wang, Hao-Yu; Tian, Wen-Wen; Yuan, Zhong-Yong	<b>Author of Portion(s)</b>	Ren, Jin-Tao; Chen, Lei; Wang, Hao-Yu; Tian, Wen-Wen; Yuan, Zhong-Yong
<b>Volume / Edition</b>	17	<b>Issue, if Republishing an Article From a Serial</b>	1
<b>Page or Page Range of Portion</b>	49-113	<b>Publication Date of Portion</b>	2024-01-01

## Marketplace Permissions General Terms and Conditions

The following terms and conditions (“General Terms”), together with any applicable Publisher Terms and Conditions, govern User’s use of Works pursuant to the Licenses granted by Copyright Clearance Center, Inc. (“CCC”) on behalf of the applicable Rightsholders of such Works through CCC’s applicable Marketplace transactional licensing services (each, a “Service”).

1) **Definitions.** For purposes of these General Terms, the following definitions apply:

“License” is the licensed use the User obtains via the Marketplace platform in a particular licensing transaction, as set forth in the Order Confirmation.

“Order Confirmation” is the confirmation CCC provides to the User at the conclusion of each Marketplace transaction. “Order Confirmation Terms” are additional terms set forth on specific Order Confirmations not set forth in the General Terms that can include terms applicable to a particular CCC transactional licensing service and/or any Rightsholder-specific terms.

“Rightsholder(s)” are the holders of copyright rights in the Works for which a User obtains licenses via the Marketplace platform, which are displayed on specific Order Confirmations.

“Terms” means the terms and conditions set forth in these General Terms and any additional Order Confirmation Terms collectively.

“User” or “you” is the person or entity making the use granted under the relevant License. Where the person accepting the Terms on behalf of a User is a freelancer or other third party who the User authorized to accept the General Terms on the User’s behalf, such person shall be deemed jointly a User for purposes of such Terms.

“Work(s)” are the copyright protected works described in relevant Order Confirmations.

2) **Description of Service.** CCC's Marketplace enables Users to obtain Licenses to use one or more Works in accordance with all relevant Terms. CCC grants Licenses as an agent on behalf of the copyright rightsholder identified in the relevant Order Confirmation.

3) **Applicability of Terms.** The Terms govern User's use of Works in connection with the relevant License. In the event of any conflict between General Terms and Order Confirmation Terms, the latter shall govern. User acknowledges that Rightsholders have complete discretion whether to grant any permission, and whether to place any limitations on any grant, and that CCC has no right to supersede or to modify any such discretionary act by a Rightsholder.

4) **Representations; Acceptance.** By using the Service, User represents and warrants that User has been duly authorized by the User to accept, and hereby does accept, all Terms.

5) **Scope of License; Limitations and Obligations.** All Works and all rights therein, including copyright rights, remain the sole and exclusive property of the Rightsholder. The License provides only those rights expressly set forth in the terms and conveys no other rights in any Works

6) **General Payment Terms.** User may pay at time of checkout by credit card or choose to be invoiced. If the User chooses to be invoiced, the User shall: (i) remit payments in the manner identified on specific invoices, (ii) unless otherwise specifically stated in an Order Confirmation or separate written agreement, Users shall remit payments upon receipt of the relevant invoice from CCC, either by delivery or notification of availability of the invoice via the Marketplace platform, and (iii) if the User does not pay the invoice within 30 days of receipt, the User may incur a service charge of 1.5% per month or the maximum rate allowed by applicable law, whichever is less. While User may exercise the rights in the License immediately upon receiving the Order Confirmation, the License is automatically revoked and is null and void, as if it had never been issued, if CCC does not receive complete payment on a timely basis.

7) **General Limits on Use.** Unless otherwise provided in the Order Confirmation, any grant of rights to User (i) involves only the rights set forth in the Terms and does not include subsequent or additional uses, (ii) is non-exclusive and non-transferable, and (iii) is subject to any and all limitations and restrictions (such as, but not limited to, limitations on duration of use or circulation) included in the Terms. Upon completion of the licensed use as set forth in the Order Confirmation, User shall either secure a new permission for further use of the Work(s) or immediately cease any new use of the Work(s) and shall render inaccessible (such as by deleting or by removing or severing links or other locators) any further copies of the Work. User may only make alterations to the Work if and as expressly set forth in the Order Confirmation. No Work may be used in any way that is unlawful, including without limitation if such use would violate applicable sanctions laws or regulations, would be defamatory, violate the rights of third parties (including such third parties' rights of copyright, privacy, publicity, or other tangible or intangible property), or is otherwise illegal, sexually explicit, or obscene. In addition, User may not conjoin a Work with any other material that may result in damage to the reputation of the Rightsholder. Any unlawful use will render any licenses hereunder null and void. User agrees to inform CCC if it becomes aware of any infringement of any rights in a Work and to cooperate with any reasonable request of CCC or the Rightsholder in connection therewith.

8) **Third Party Materials.** In the event that the material for which a License is sought includes third party materials (such as photographs, illustrations, graphs, inserts and similar materials) that are identified in such material as having been used by permission (or a similar indicator), User is responsible for identifying, and seeking separate licenses (under this Service, if available, or otherwise) for any of such third party materials; without a separate license, User may not use such third party materials via the License.

9) **Copyright Notice.** Use of proper copyright notice for a Work is required as a condition of any License granted under the Service. Unless otherwise provided in the Order Confirmation, a proper copyright notice will read substantially as follows: "Used with permission of [Rightsholder's name], from [Work's title, author, volume, edition number and year of copyright]; permission conveyed through Copyright Clearance Center, Inc." Such notice must be provided in a reasonably legible font size and must be placed either on a cover page or in another location that any person, upon gaining access to the material which is the subject of a permission, shall see, or in the case of republication Licenses, immediately adjacent to the Work as used (for example, as part of a by-line or footnote) or in the place where substantially all other credits or notices for the new work containing the republished Work are located. Failure to include the required notice results in loss to the Rightsholder and CCC, and the User shall be liable to pay liquidated damages for each such failure equal to twice the use fee specified in the Order Confirmation, in addition to the use fee itself and any other fees and charges specified.

10) **Indemnity.** User hereby indemnifies and agrees to defend the Rightsholder and CCC, and their respective employees and directors, against all claims, liability, damages, costs, and expenses, including legal fees and expenses, arising out of

any use of a Work beyond the scope of the rights granted herein and in the Order Confirmation, or any use of a Work which has been altered in any unauthorized way by User, including claims of defamation or infringement of rights of copyright, publicity, privacy, or other tangible or intangible property.

11) **Limitation of Liability.** UNDER NO CIRCUMSTANCES WILL CCC OR THE RIGHTSHOLDER BE LIABLE FOR ANY DIRECT, INDIRECT, CONSEQUENTIAL, OR INCIDENTAL DAMAGES (INCLUDING WITHOUT LIMITATION DAMAGES FOR LOSS OF BUSINESS PROFITS OR INFORMATION, OR FOR BUSINESS INTERRUPTION) ARISING OUT OF THE USE OR INABILITY TO USE A WORK, EVEN IF ONE OR BOTH OF THEM HAS BEEN ADVISED OF THE POSSIBILITY OF SUCH DAMAGES. In any event, the total liability of the Rightsholder and CCC (including their respective employees and directors) shall not exceed the total amount actually paid by User for the relevant License. User assumes full liability for the actions and omissions of its principals, employees, agents, affiliates, successors, and assigns.

12) **Limited Warranties.** THE WORK(S) AND RIGHT(S) ARE PROVIDED "AS IS." CCC HAS THE RIGHT TO GRANT TO USER THE RIGHTS GRANTED IN THE ORDER CONFIRMATION DOCUMENT. CCC AND THE RIGHTSHOLDER DISCLAIM ALL OTHER WARRANTIES RELATING TO THE WORK(S) AND RIGHT(S), EITHER EXPRESS OR IMPLIED, INCLUDING WITHOUT LIMITATION IMPLIED WARRANTIES OF MERCHANTABILITY OR FITNESS FOR A PARTICULAR PURPOSE. ADDITIONAL RIGHTS MAY BE REQUIRED TO USE ILLUSTRATIONS, GRAPHS, PHOTOGRAPHS, ABSTRACTS, INSERTS, OR OTHER PORTIONS OF THE WORK (AS OPPOSED TO THE ENTIRE WORK) IN A MANNER CONTEMPLATED BY USER; USER UNDERSTANDS AND AGREES THAT NEITHER CCC NOR THE RIGHTSHOLDER MAY HAVE SUCH ADDITIONAL RIGHTS TO GRANT.

13) **Effect of Breach.** Any failure by User to pay any amount when due, or any use by User of a Work beyond the scope of the License set forth in the Order Confirmation and/or the Terms, shall be a material breach of such License. Any breach not cured within 10 days of written notice thereof shall result in immediate termination of such License without further notice. Any unauthorized (but licensable) use of a Work that is terminated immediately upon notice thereof may be liquidated by payment of the Rightsholder's ordinary license price therefor; any unauthorized (and unlicensable) use that is not terminated immediately for any reason (including, for example, because materials containing the Work cannot reasonably be recalled) will be subject to all remedies available at law or in equity, but in no event to a payment of less than three times the Rightsholder's ordinary license price for the most closely analogous licensable use plus Rightsholder's and/or CCC's costs and expenses incurred in collecting such payment.

14) **Additional Terms for Specific Products and Services.** If a User is making one of the uses described in this Section 14, the additional terms and conditions apply:

a) ***Print Uses of Academic Course Content and Materials (photocopies for academic coursepacks or classroom handouts).*** For photocopies for academic coursepacks or classroom handouts the following additional terms apply:

i) The copies and anthologies created under this License may be made and assembled by faculty members individually or at their request by on-campus bookstores or copy centers, or by off-campus copy shops and other similar entities.

ii) No License granted shall in any way: (i) include any right by User to create a substantively non-identical copy of the Work or to edit or in any other way modify the Work (except by means of deleting material immediately preceding or following the entire portion of the Work copied) (ii) permit "publishing ventures" where any particular anthology would be systematically marketed at multiple institutions.

iii) Subject to any Publisher Terms (and notwithstanding any apparent contradiction in the Order Confirmation arising from data provided by User), any use authorized under the academic pay-per-use service is limited as follows:

A) any License granted shall apply to only one class (bearing a unique identifier as assigned by the institution, and thereby including all sections or other subparts of the class) at one institution;

B) use is limited to not more than 25% of the text of a book or of the items in a published collection of essays, poems or articles;

C) use is limited to no more than the greater of (a) 25% of the text of an issue of a journal or other periodical or (b) two articles from such an issue;

D) no User may sell or distribute any particular anthology, whether photocopied or electronic, at more than one institution of learning;

E) in the case of a photocopy permission, no materials may be entered into electronic memory by User except in order to produce an identical copy of a Work before or during the academic term (or analogous period) as to which any particular permission is granted. In the event that User shall choose to retain materials that are the subject of a photocopy permission in electronic memory for purposes of producing identical copies more than one day after such retention (but still within the scope of any permission granted), User must notify CCC of such fact in the applicable permission request and such retention shall constitute one copy actually sold for purposes of calculating permission fees due; and

F) any permission granted shall expire at the end of the class. No permission granted shall in any way include any right by User to create a substantively non-identical copy of the Work or to edit or in any other way modify the Work (except by means of deleting material immediately preceding or following the entire portion of the Work copied).

iv) Books and Records; Right to Audit. As to each permission granted under the academic pay-per-use Service, User shall maintain for at least four full calendar years books and records sufficient for CCC to determine the numbers of copies made by User under such permission. CCC and any representatives it may designate shall have the right to audit such books and records at any time during User's ordinary business hours, upon two days' prior notice. If any such audit shall determine that User shall have underpaid for, or underreported, any photocopies sold or by three percent (3%) or more, then User shall bear all the costs of any such audit; otherwise, CCC shall bear the costs of any such audit. Any amount determined by such audit to have been underpaid by User shall immediately be paid to CCC by User, together with interest thereon at the rate of 10% per annum from the date such amount was originally due. The provisions of this paragraph shall survive the termination of this License for any reason.

b) **Digital Pay-Per-Uses of Academic Course Content and Materials (e-coursepacks, electronic reserves, learning management systems, academic institution intranets).** For uses in e-coursepacks, posts in electronic reserves, posts in learning management systems, or posts on academic institution intranets, the following additional terms apply:

i) The pay-per-uses subject to this Section 14(b) include:

A) **Posting e-reserves, course management systems, e-coursepacks for text-based content**, which grants authorizations to import requested material in electronic format, and allows electronic access to this material to members of a designated college or university class, under the direction of an instructor designated by the college or university, accessible only under appropriate electronic controls (e.g., password);

B) **Posting e-reserves, course management systems, e-coursepacks for material consisting of photographs or other still images not embedded in text**, which grants not only the authorizations described in Section 14(b)(i)(A) above, but also the following authorization: to include the requested material in course materials for use consistent with Section 14(b)(i)(A) above, including any necessary resizing, reformatting or modification of the resolution of such requested material (provided that such modification does not alter the underlying editorial content or meaning of the requested material, and provided that the resulting modified content is used solely within the scope of, and in a manner consistent with, the particular authorization described in the Order Confirmation and the Terms), but not including any other form of manipulation, alteration or editing of the requested material;

C) **Posting e-reserves, course management systems, e-coursepacks or other academic distribution for audiovisual content**, which grants not only the authorizations described in Section 14(b)(i)(A) above, but also the following authorizations: (i) to include the requested material in course materials for use consistent with Section 14(b)(i)(A) above; (ii) to display and perform the requested material to such members of such class in the physical classroom or remotely by means of streaming media or other video formats; and (iii) to "clip" or reformat the requested material for purposes of time or content management or ease of delivery, provided that such "clipping" or reformatting does not alter the underlying editorial content or meaning of the requested material and that the resulting material is used solely within the scope of, and in a manner consistent with, the particular authorization described in the Order Confirmation and the Terms. Unless expressly set forth in the relevant Order Confirmation, the License does not authorize any other form of manipulation, alteration or editing of the requested material.

ii) Unless expressly set forth in the relevant Order Confirmation, no License granted shall in any way: (i) include any right by User to create a substantively non-identical copy of the Work or to edit or in any other way modify the Work (except by means of deleting material immediately preceding or following the entire portion of the Work

copied or, in the case of Works subject to Sections 14(b)(1)(B) or (C) above, as described in such Sections) (ii) permit "publishing ventures" where any particular course materials would be systematically marketed at multiple institutions.

iii) Subject to any further limitations determined in the Rightsholder Terms (and notwithstanding any apparent contradiction in the Order Confirmation arising from data provided by User), any use authorized under the electronic course content pay-per-use service is limited as follows:

A) any License granted shall apply to only one class (bearing a unique identifier as assigned by the institution, and thereby including all sections or other subparts of the class) at one institution;

B) use is limited to not more than 25% of the text of a book or of the items in a published collection of essays, poems or articles;

C) use is limited to not more than the greater of (a) 25% of the text of an issue of a journal or other periodical or (b) two articles from such an issue;

D) no User may sell or distribute any particular materials, whether photocopied or electronic, at more than one institution of learning;

E) electronic access to material which is the subject of an electronic-use permission must be limited by means of electronic password, student identification or other control permitting access solely to students and instructors in the class;

F) User must ensure (through use of an electronic cover page or other appropriate means) that any person, upon gaining electronic access to the material, which is the subject of a permission, shall see:

- a proper copyright notice, identifying the Rightsholder in whose name CCC has granted permission,
- a statement to the effect that such copy was made pursuant to permission,
- a statement identifying the class to which the material applies and notifying the reader that the material has been made available electronically solely for use in the class, and
- a statement to the effect that the material may not be further distributed to any person outside the class, whether by copying or by transmission and whether electronically or in paper form, and User must also ensure that such cover page or other means will print out in the event that the person accessing the material chooses to print out the material or any part thereof.

G) any permission granted shall expire at the end of the class and, absent some other form of authorization, User is thereupon required to delete the applicable material from any electronic storage or to block electronic access to the applicable material.

iv) Uses of separate portions of a Work, even if they are to be included in the same course material or the same university or college class, require separate permissions under the electronic course content pay-per-use Service. Unless otherwise provided in the Order Confirmation, any grant of rights to User is limited to use completed no later than the end of the academic term (or analogous period) as to which any particular permission is granted.

v) Books and Records; Right to Audit. As to each permission granted under the electronic course content Service, User shall maintain for at least four full calendar years books and records sufficient for CCC to determine the numbers of copies made by User under such permission. CCC and any representatives it may designate shall have the right to audit such books and records at any time during User's ordinary business hours, upon two days' prior notice. If any such audit shall determine that User shall have underpaid for, or underreported, any electronic copies used by three percent (3%) or more, then User shall bear all the costs of any such audit; otherwise, CCC shall bear the costs of any such audit. Any amount determined by such audit to have been underpaid by User shall immediately be paid to CCC by User, together with interest thereon at the rate of 10% per annum from the date such amount was originally due. The provisions of this paragraph shall survive the termination of this license for any reason.

**c) Pay-Per-Use Permissions for Certain Reproductions (Academic photocopies for library reserves and interlibrary loan reporting) (Non-academic internal/external business uses and commercial document**

**delivery).** The License expressly excludes the uses listed in Section (c)(i)-(v) below (which must be subject to separate license from the applicable Rightsholder) for: academic photocopies for library reserves and interlibrary loan reporting; and non-academic internal/external business uses and commercial document delivery.

- i) electronic storage of any reproduction (whether in plain-text, PDF, or any other format) other than on a transitory basis;
- ii) the input of Works or reproductions thereof into any computerized database;
- iii) reproduction of an entire Work (cover-to-cover copying) except where the Work is a single article;
- iv) reproduction for resale to anyone other than a specific customer of User;
- v) republication in any different form. Please obtain authorizations for these uses through other CCC services or directly from the rightsholder.

Any license granted is further limited as set forth in any restrictions included in the Order Confirmation and/or in these Terms.

d) **Electronic Reproductions in Online Environments (Non-Academic-email, intranet, internet and extranet).** For “electronic reproductions”, which generally includes e-mail use (including instant messaging or other electronic transmission to a defined group of recipients) or posting on an intranet, extranet or Intranet site (including any display or performance incidental thereto), the following additional terms apply:

- i) Unless otherwise set forth in the Order Confirmation, the License is limited to use completed within 30 days for any use on the Internet, 60 days for any use on an intranet or extranet and one year for any other use, all as measured from the “republication date” as identified in the Order Confirmation, if any, and otherwise from the date of the Order Confirmation.
- ii) User may not make or permit any alterations to the Work, unless expressly set forth in the Order Confirmation (after request by User and approval by Rightsholder); provided, however, that a Work consisting of photographs or other still images not embedded in text may, if necessary, be resized, reformatted or have its resolution modified without additional express permission, and a Work consisting of audiovisual content may, if necessary, be “clipped” or reformatted for purposes of time or content management or ease of delivery (provided that any such resizing, reformatting, resolution modification or “clipping” does not alter the underlying editorial content or meaning of the Work used, and that the resulting material is used solely within the scope of, and in a manner consistent with, the particular License described in the Order Confirmation and the Terms.

#### 15) **Miscellaneous.**

a) User acknowledges that CCC may, from time to time, make changes or additions to the Service or to the Terms, and that Rightsholder may make changes or additions to the Rightsholder Terms. Such updated Terms will replace the prior terms and conditions in the order workflow and shall be effective as to any subsequent Licenses but shall not apply to Licenses already granted and paid for under a prior set of terms.

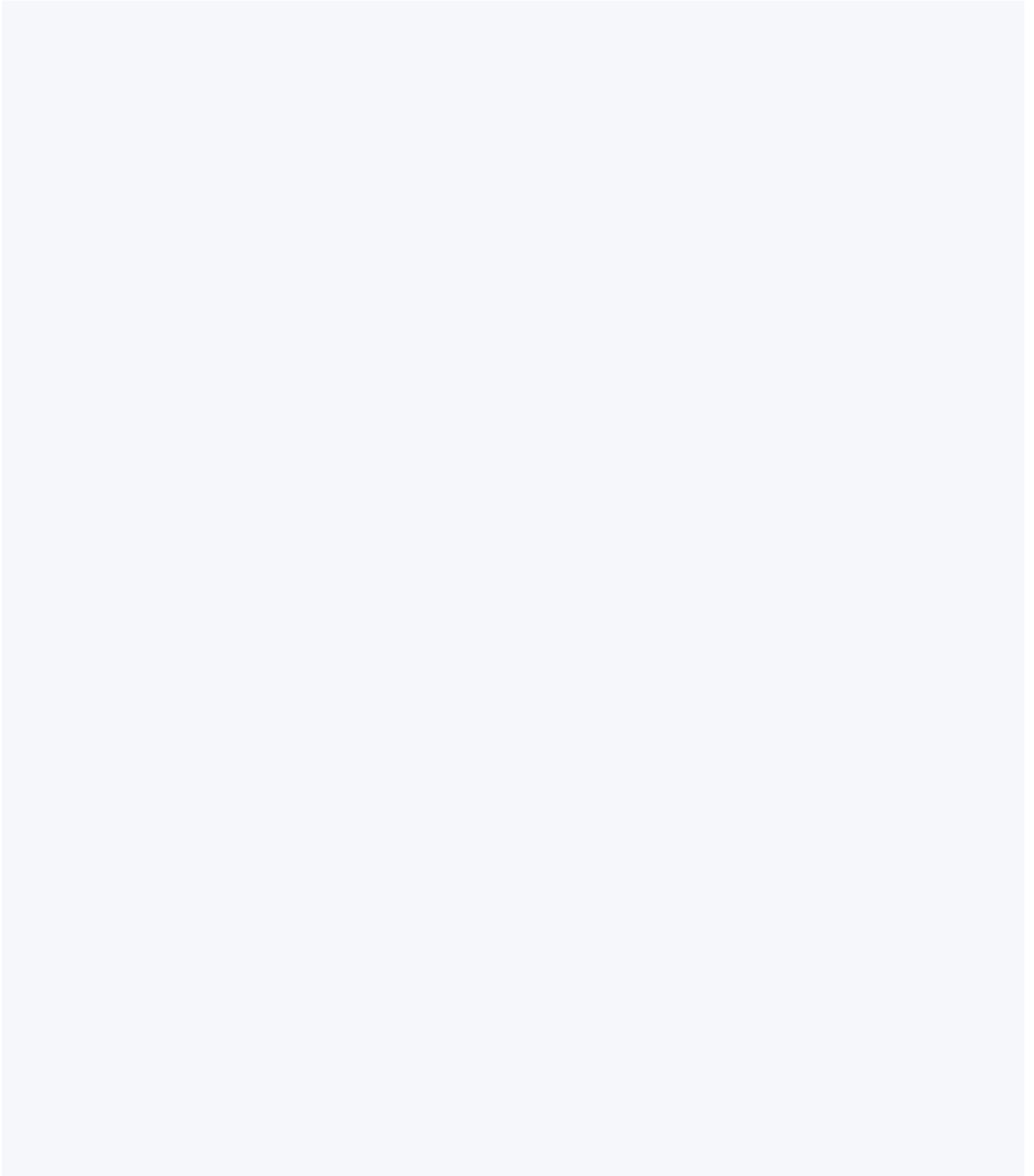
b) Use of User-related information collected through the Service is governed by CCC’s privacy policy, available online at [www.copyright.com/about/privacy-policy/](http://www.copyright.com/about/privacy-policy/).

c) The License is personal to User. Therefore, User may not assign or transfer to any other person (whether a natural person or an organization of any kind) the License or any rights granted thereunder; provided, however, that, where applicable, User may assign such License in its entirety on written notice to CCC in the event of a transfer of all or substantially all of User’s rights in any new material which includes the Work(s) licensed under this Service.

d) No amendment or waiver of any Terms is binding unless set forth in writing and signed by the appropriate parties, including, where applicable, the Rightsholder. The Rightsholder and CCC hereby object to any terms contained in any writing prepared by or on behalf of the User or its principals, employees, agents or affiliates and purporting to govern or otherwise relate to the License described in the Order Confirmation, which terms are in any way inconsistent with any Terms set forth in the Order Confirmation, and/or in CCC’s standard operating procedures, whether such writing is prepared prior to, simultaneously with or subsequent to the Order Confirmation, and whether such writing appears on a copy of the Order Confirmation or in a separate instrument.

e) The License described in the Order Confirmation shall be governed by and construed under the law of the State of New York, USA, without regard to the principles thereof of conflicts of law. Any case, controversy, suit, action, or proceeding arising out of, in connection with, or related to such License shall be brought, at CCC's sole discretion, in any federal or state court located in the County of New York, State of New York, USA, or in any federal or state court whose geographical jurisdiction covers the location of the Rightsholder set forth in the Order Confirmation. The parties expressly submit to the personal jurisdiction and venue of each such federal or state court.

*Last updated October 2022*





## Toward Electrocatalytic Methanol Oxidation Reaction: Longstanding Debates and Emerging Catalysts

**Author:** Wenping Sun, Hongge Pan, Jian Chen, et al

**Publication:** Advanced Materials

**Publisher:** John Wiley and Sons

**Date:** May 28, 2023

© 2023 Wiley-VCH GmbH

### Order Completed

Thank you for your order.

This Agreement between Santosh Semwal ("You") and John Wiley and Sons ("John Wiley and Sons") consists of your order details and the terms and conditions provided by John Wiley and Sons and Copyright Clearance Center.

**License number** Reference confirmation email for license number

**License date** Nov, 04 2024

#### 📄 Licensed Content

<b>Licensed Content Publisher</b>	John Wiley and Sons
<b>Licensed Content Publication</b>	Advanced Materials
<b>Licensed Content Title</b>	Toward Electrocatalytic Methanol Oxidation Reaction: Longstanding Debates and Emerging Catalysts
<b>Licensed Content Author</b>	Wenping Sun, Hongge Pan, Jian Chen, et al
<b>Licensed Content Date</b>	May 28, 2023
<b>Licensed Content Volume</b>	35
<b>Licensed Content Issue</b>	26
<b>Licensed Content Pages</b>	20

#### 📄 Order Details

<b>Type of use</b>	Dissertation/Thesis
<b>Requestor type</b>	University/Academic
<b>Format</b>	Print and electronic
<b>Portion</b>	Figure/table
<b>Number of figures/tables</b>	1
<b>Will you be translating?</b>	No

#### 📄 About Your Work

<b>Title of new work</b>	SYNTHESIS AND CHARACTERIZATION OF TRANSITION METAL BASED ELECTROCATALYST FOR EFFICIENT HYDROGEN PRODUCTION
<b>Institution name</b>	RAJIV GANDHI INSTITUTE OF PETROLEUM TECHNOLOGY JAIS, INDIA - 229304
<b>Expected presentation date</b>	Jan 2025

#### 📄 Additional Data

<b>Portions</b>	Figure 2: A dual-pathway mechanism for electrocatalytic MOR, where * represents the adsorption site on the catalyst surface, the red arrows indicate the CO pathway, and the others the CO-free pathway.
<b>The Requesting Person / Organization to Appear on the License</b>	Santosh Semwal

 Requestor Location

 Tax Details

**Requestor Location**  
Mr. Santosh Semwal  
Jais  
Amethi  
Raebareli, Uttar Pradesh  
229305  
India

**Publisher Tax ID** EU826007151

 Billing Information

**Billing Type** Invoice  
Mr. Santosh Semwal  
Jais  
**Billing address** Amethi  
Raebareli, India 229305

Would you like to purchase the full text of this article? If so, please continue on to the content ordering system located here: [Purchase PDF](#)  
If you click on the buttons below or close this window, you will not be able to return to the content ordering system.

**Total: 0.00 USD**

[CLOSE WINDOW](#)

## JOHN WILEY AND SONS ORDER DETAILS

Nov 04, 2024

---

This Agreement between Santosh Semwal ("You") and John Wiley and Sons ("John Wiley and Sons") consists of your order details and the terms and conditions provided by John Wiley and Sons and Copyright Clearance Center.

Order Number	501943812
Order date	Nov 04, 2024
Licensed Content Publisher	John Wiley and Sons
Licensed Content Publication	Advanced Materials
Licensed Content Title	Toward Electrocatalytic Methanol Oxidation Reaction: Longstanding Debates and Emerging Catalysts
Licensed Content Author	Wenping Sun, Hongge Pan, Jian Chen, et al
Licensed Content Date	May 28, 2023
Licensed Content Volume	35
Licensed Content Issue	26
Licensed Content Pages	20
Type of use	Dissertation/Thesis
Requestor type	University/Academic
Format	Print and electronic
Portion	Figure/table
Number of figures/tables	1
Will you be translating?	No
Title of new work	SYNTHESIS AND CHARACTERIZATION OF TRANSITION METAL BASED ELECTROCATALYST FOR EFFICIENT HYDROGEN PRODUCTION
Institution name	RAJIV GANDHI INSTITUTE OF PETROLEUM TECHNOLOGY JAIS, INDIA – 229304
Expected presentation date	Jan 2025
Portions	Figure 2: A dual-pathway mechanism for electrocatalytic MOR, where * represents the adsorption site on the catalyst surface, the red arrows indicate the CO pathway, and the others the CO-free pathway.
The Requesting Person / Organization to Appear on the License	Santosh Semwal
Requestor Location	Mr. Santosh Semwal Jais Amethi Raebareli, Uttar Pradesh 229305 India
Publisher Tax ID	EU826007151

Billing Type	Invoice
	Mr. Santosh Semwal
	Jais
Billing Address	Amethi
	Raebareli, India 229305
Total	0.00 USD
Terms and Conditions	

### TERMS AND CONDITIONS

This copyrighted material is owned by or exclusively licensed to John Wiley & Sons, Inc. or one of its group companies (each a "Wiley Company") or handled on behalf of a society with which a Wiley Company has exclusive publishing rights in relation to a particular work (collectively "WILEY"). By clicking "accept" in connection with completing this licensing transaction, you agree that the following terms and conditions apply to this transaction (along with the billing and payment terms and conditions established by the Copyright Clearance Center Inc., ("CCC's Billing and Payment terms and conditions"), at the time that you opened your RightsLink account (these are available at any time at <http://myaccount.copyright.com>).

#### Terms and Conditions

- The materials you have requested permission to reproduce or reuse (the "Wiley Materials") are protected by copyright.
- You are hereby granted a personal, non-exclusive, non-sub licensable (on a stand-alone basis), non-transferable, worldwide, limited license to reproduce the Wiley Materials for the purpose specified in the licensing process. This license, **and any CONTENT (PDF or image file) purchased as part of your order**, is for a one-time use only and limited to any maximum distribution number specified in the license. The first instance of republication or reuse granted by this license must be completed within two years of the date of the grant of this license (although copies prepared before the end date may be distributed thereafter). The Wiley Materials shall not be used in any other manner or for any other purpose, beyond what is granted in the license. Permission is granted subject to an appropriate acknowledgement given to the author, title of the material/book/journal and the publisher. You shall also duplicate the copyright notice that appears in the Wiley publication in your use of the Wiley Material. Permission is also granted on the understanding that nowhere in the text is a previously published source acknowledged for all or part of this Wiley Material. Any third party content is expressly excluded from this permission.
- With respect to the Wiley Materials, all rights are reserved. Except as expressly granted by the terms of the license, no part of the Wiley Materials may be copied, modified, adapted (except for minor reformatting required by the new Publication), translated, reproduced, transferred or distributed, in any form or by any means, and no derivative works may be made based on the Wiley Materials without the prior permission of the respective copyright owner. **For STM Signatory Publishers clearing permission under the terms of the [STM Permissions Guidelines](#) only, the terms of the license are extended to include subsequent editions and for editions in other languages, provided such editions are for the work as a whole in situ and does not involve the separate exploitation of the permitted figures**

**or extracts,** You may not alter, remove or suppress in any manner any copyright, trademark or other notices displayed by the Wiley Materials. You may not license, rent, sell, loan, lease, pledge, offer as security, transfer or assign the Wiley Materials on a stand-alone basis, or any of the rights granted to you hereunder to any other person.

- The Wiley Materials and all of the intellectual property rights therein shall at all times remain the exclusive property of John Wiley & Sons Inc, the Wiley Companies, or their respective licensors, and your interest therein is only that of having possession of and the right to reproduce the Wiley Materials pursuant to Section 2 herein during the continuance of this Agreement. You agree that you own no right, title or interest in or to the Wiley Materials or any of the intellectual property rights therein. You shall have no rights hereunder other than the license as provided for above in Section 2. No right, license or interest to any trademark, trade name, service mark or other branding ("Marks") of WILEY or its licensors is granted hereunder, and you agree that you shall not assert any such right, license or interest with respect thereto
- NEITHER WILEY NOR ITS LICENSORS MAKES ANY WARRANTY OR REPRESENTATION OF ANY KIND TO YOU OR ANY THIRD PARTY, EXPRESS, IMPLIED OR STATUTORY, WITH RESPECT TO THE MATERIALS OR THE ACCURACY OF ANY INFORMATION CONTAINED IN THE MATERIALS, INCLUDING, WITHOUT LIMITATION, ANY IMPLIED WARRANTY OF MERCHANTABILITY, ACCURACY, SATISFACTORY QUALITY, FITNESS FOR A PARTICULAR PURPOSE, USABILITY, INTEGRATION OR NON-INFRINGEMENT AND ALL SUCH WARRANTIES ARE HEREBY EXCLUDED BY WILEY AND ITS LICENSORS AND WAIVED BY YOU.
- WILEY shall have the right to terminate this Agreement immediately upon breach of this Agreement by you.
- You shall indemnify, defend and hold harmless WILEY, its Licensors and their respective directors, officers, agents and employees, from and against any actual or threatened claims, demands, causes of action or proceedings arising from any breach of this Agreement by you.
- IN NO EVENT SHALL WILEY OR ITS LICENSORS BE LIABLE TO YOU OR ANY OTHER PARTY OR ANY OTHER PERSON OR ENTITY FOR ANY SPECIAL, CONSEQUENTIAL, INCIDENTAL, INDIRECT, EXEMPLARY OR PUNITIVE DAMAGES, HOWEVER CAUSED, ARISING OUT OF OR IN CONNECTION WITH THE DOWNLOADING, PROVISIONING, VIEWING OR USE OF THE MATERIALS REGARDLESS OF THE FORM OF ACTION, WHETHER FOR BREACH OF CONTRACT, BREACH OF WARRANTY, TORT, NEGLIGENCE, INFRINGEMENT OR OTHERWISE (INCLUDING, WITHOUT LIMITATION, DAMAGES BASED ON LOSS OF PROFITS, DATA, FILES, USE, BUSINESS OPPORTUNITY OR CLAIMS OF THIRD PARTIES), AND WHETHER OR NOT THE PARTY HAS BEEN ADVISED OF THE POSSIBILITY OF SUCH DAMAGES. THIS LIMITATION SHALL APPLY NOTWITHSTANDING ANY FAILURE OF ESSENTIAL PURPOSE OF ANY LIMITED REMEDY PROVIDED HEREIN.
- Should any provision of this Agreement be held by a court of competent jurisdiction to be illegal, invalid, or unenforceable, that provision shall be deemed amended to

achieve as nearly as possible the same economic effect as the original provision, and the legality, validity and enforceability of the remaining provisions of this Agreement shall not be affected or impaired thereby.

- The failure of either party to enforce any term or condition of this Agreement shall not constitute a waiver of either party's right to enforce each and every term and condition of this Agreement. No breach under this agreement shall be deemed waived or excused by either party unless such waiver or consent is in writing signed by the party granting such waiver or consent. The waiver by or consent of a party to a breach of any provision of this Agreement shall not operate or be construed as a waiver of or consent to any other or subsequent breach by such other party.
- This Agreement may not be assigned (including by operation of law or otherwise) by you without WILEY's prior written consent.
- Any fee required for this permission shall be non-refundable after thirty (30) days from receipt by the CCC.
- These terms and conditions together with CCC's Billing and Payment terms and conditions (which are incorporated herein) form the entire agreement between you and WILEY concerning this licensing transaction and (in the absence of fraud) supersedes all prior agreements and representations of the parties, oral or written. This Agreement may not be amended except in writing signed by both parties. This Agreement shall be binding upon and inure to the benefit of the parties' successors, legal representatives, and authorized assigns.
- In the event of any conflict between your obligations established by these terms and conditions and those established by CCC's Billing and Payment terms and conditions, these terms and conditions shall prevail.
- WILEY expressly reserves all rights not specifically granted in the combination of (i) the license details provided by you and accepted in the course of this licensing transaction, (ii) these terms and conditions and (iii) CCC's Billing and Payment terms and conditions.
- This Agreement will be void if the Type of Use, Format, Circulation, or Requestor Type was misrepresented during the licensing process.
- This Agreement shall be governed by and construed in accordance with the laws of the State of New York, USA, without regards to such state's conflict of law rules. Any legal action, suit or proceeding arising out of or relating to these Terms and Conditions or the breach thereof shall be instituted in a court of competent jurisdiction in New York County in the State of New York in the United States of America and each party hereby consents and submits to the personal jurisdiction of such court, waives any objection to venue in such court and consents to service of process by registered or certified mail, return receipt requested, at the last known address of such party.

## **WILEY OPEN ACCESS TERMS AND CONDITIONS**

Wiley Publishes Open Access Articles in fully Open Access Journals and in Subscription journals offering Online Open. Although most of the fully Open Access journals publish open access articles under the terms of the Creative Commons Attribution (CC BY)

License only, the subscription journals and a few of the Open Access Journals offer a choice of Creative Commons Licenses. The license type is clearly identified on the article.

### **The Creative Commons Attribution License**

The [Creative Commons Attribution License \(CC-BY\)](#) allows users to copy, distribute and transmit an article, adapt the article and make commercial use of the article. The CC-BY license permits commercial and non-

### **Creative Commons Attribution Non-Commercial License**

The [Creative Commons Attribution Non-Commercial \(CC-BY-NC\)License](#) permits use, distribution and reproduction in any medium, provided the original work is properly cited and is not used for commercial purposes.(see below)

### **Creative Commons Attribution-Non-Commercial-NoDerivs License**

The [Creative Commons Attribution Non-Commercial-NoDerivs License](#) (CC-BY-NC-ND) permits use, distribution and reproduction in any medium, provided the original work is properly cited, is not used for commercial purposes and no modifications or adaptations are made. (see below)

### **Use by commercial "for-profit" organizations**

Use of Wiley Open Access articles for commercial, promotional, or marketing purposes requires further explicit permission from Wiley and will be subject to a fee.

Further details can be found on Wiley Online Library  
<http://olabout.wiley.com/WileyCDA/Section/id-410895.html>

### **Other Terms and Conditions:**

**v1.10 Last updated September 2015**

---

---

101. HyUnder, Assessment of the Potential, the Actors and Relevant Business Cases for Large Scale and Long Term Storage of Renewable Electricity by Hydrogen Underground Storage in Europe, <http://hyunder.eu/publications/>, 2014.
102. L. Welder, P. Stenzel, N. Ebersbach, P. Markewitz, M. Robinius, B. Emonts and D. Stolten, Design and evaluation of hydrogen electricity reconversion pathways in national energy systems using spatially and temporally resolved energy system optimization, *Int. J. Hydrogen Energy*, 2019, **44**, 9594–9607 [CrossRef](#) [CAS](#) .
103. C. Azar and B. A. Sandén, The elusive quest for technology-neutral policies, *Environmental Innovation and Societal Transitions*, 2011, **1**, 135–139 [CrossRef](#) .
104. S. de Mello and H. Paulo, Cost-effectiveness as energy policy mechanisms: The paradox of technology-neutral and technology-specific policies in the short and long term, *Renewable Sustainable Energy Rev.*, 2016, **58**, 1216–1222 [CrossRef](#) .
105. S. Pfenninger, L. Hirth, I. Schlecht, E. Schmid, F. Wiese, T. Brown, C. Davis, M. Gidden, H. Heinrichs, C. Heuberger, S. Hilpert, U. Krien, C. Matke, A. Nebel, R. Morrison and B. Müller, *et al.*, Opening the black box of energy modelling: Strategies and lessons learned, *Energy Strategy Reviews*, 2018, **19**, 63–71 [CrossRef](#) .
106. International Institute for Applied Systems Analysis, Global Energy Assessment Scenario Database, 11 November 2013, <http://www.iiasa.ac.at/web/home/research/researchPrograms/Energy/Global-Energy-Assessment-Database.en.html>, accessed 6 September 2019.

This journal is © The Royal Society of Chemistry 2020

About

Cited by

Related



## The curious case of the conflicting roles of hydrogen in global energy scenarios

C. J. Quarton, O. Tlili, L. Welder, C. Mansilla, H. Blanco, H. Heinrichs, J. Leaver, N. J. Samsatli, P. Lucchese, M. Robinius and S. Samsatli, *Sustainable Energy Fuels*, 2020, **4**, 80 DOI: 10.1039/C9SE00833K

This article is licensed under a [Creative Commons Attribution 3.0 Unported Licence](#). You can use material from this article in other publications without requesting further permissions from the RSC, provided that the correct acknowledgement is given.

Read more about [how to correctly acknowledge RSC content](#).

## NiFeOOH-Co9S8-Intercalated Nanostructure Arrays for Energy-Efficient H<sub>2</sub> Production and Sulfion Oxidation at High Current Density



**Author:** Santosh Semwal, Renna Shakir, Jeyakumar Karthikeyan, et al

**Publication:** ACS Applied Nano Materials

**Publisher:** American Chemical Society

**Date:** Oct 1, 2023

*Copyright © 2023, American Chemical Society*

### PERMISSION/LICENSE IS GRANTED FOR YOUR ORDER AT NO CHARGE

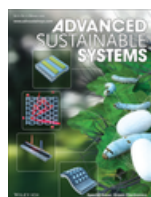
This type of permission/license, instead of the standard Terms and Conditions, is sent to you because no fee is being charged for your order. Please note the following:

- Permission is granted for your request in both print and electronic formats, and translations.
- If figures and/or tables were requested, they may be adapted or used in part.
- Please print this page for your records and send a copy of it to your publisher/graduate school.
- Appropriate credit for the requested material should be given as follows: "Reprinted (adapted) with permission from {COMPLETE REFERENCE CITATION}. Copyright {YEAR} American Chemical Society." Insert appropriate information in place of the capitalized words.
- One-time permission is granted only for the use specified in your RightsLink request. No additional uses are granted (such as derivative works or other editions). For any uses, please submit a new request.

If credit is given to another source for the material you requested from RightsLink, permission must be obtained from that source.

[BACK](#)

[CLOSE WINDOW](#)



## Ni Surface & Polyacryloyl Hydrazide Mediated Growth of Co<sub>3</sub>O<sub>4</sub>@NiCu Alloy Nanocuboids for Effective Methanol Oxidation and Oxygen Evolution Reactions

**Author:** Umaprasana Ojha, Akhoury Sudhir Kumar Sinha, Rajashri R. Urkude, et al

**Publication:** Advanced Sustainable Systems

**Publisher:** John Wiley and Sons

**Date:** Sep 5, 2024

© 2024 Wiley-VCH GmbH

### Order Completed

Thank you for your order.

This Agreement between Santosh Semwal ("You") and John Wiley and Sons ("John Wiley and Sons") consists of your license details and the terms and conditions provided by John Wiley and Sons and Copyright Clearance Center.

Your confirmation email will contain your order number for future reference.

**License Number** 5897530091564

[Printable Details](#)

**License date** Oct 28, 2024

#### ✓ Licensed Content

<b>Licensed Content Publisher</b>	John Wiley and Sons
<b>Licensed Content Publication</b>	Advanced Sustainable Systems
<b>Licensed Content Title</b>	Ni Surface & Polyacryloyl Hydrazide Mediated Growth of Co <sub>3</sub> O <sub>4</sub> @NiCu Alloy Nanocuboids for Effective Methanol Oxidation and Oxygen Evolution Reactions
<b>Licensed Content Author</b>	Umaprasana Ojha, Akhoury Sudhir Kumar Sinha, Rajashri R. Urkude, et al
<b>Licensed Content Date</b>	Sep 5, 2024
<b>Licensed Content Volume</b>	0
<b>Licensed Content Issue</b>	0
<b>Licensed Content Pages</b>	11

#### 📄 Order Details

<b>Type of use</b>	Dissertation/Thesis
<b>Requestor type</b>	Author of this Wiley article
<b>Format</b>	Print and electronic
<b>Portion</b>	Figure/table
<b>Number of figures/tables</b>	6
<b>Will you be translating?</b>	No

#### 📄 About Your Work

<b>Title of new work</b>	SYNTHESIS AND CHARACTERIZATION OF TRANSITION METAL BASED ELECTROCATALYST FOR EFFICIENT HYDROGEN PRODUCTION
<b>Institution name</b>	RAJIV GANDHI INSTITUTE OF PETROLEUM TECHNOLOGY JAIS, INDIA – 229304
<b>Expected presentation date</b>	Jan 2025

#### 📄 Additional Data

<b>Portions</b>	Scheme 1, Figure 1 to 5
<b>The Requesting Person / Organization to Appear on the License</b>	Santosh Semwal

 Requestor Location

 Tax Details

Mr. Santosh Semwal  
Jais  
Amethi

**Publisher Tax ID**

EU826007151

**Requestor Location**

Raebareli, Uttar Pradesh  
229305  
India  
Attn: Rajiv Gandhi Institute of  
Petroleum Technology

**Would you like to purchase the full text of this article? If so, please continue on to the content ordering system located here: [Purchase PDF](#)**  
**If you click on the buttons below or close this window, you will not be able to return to the content ordering system.**

**Total: 0.00 USD**

[CLOSE WINDOW](#)

[ORDER MORE](#)

JOHN WILEY AND SONS LICENSE  
TERMS AND CONDITIONS

Nov 04, 2024

---

---

This Agreement between Santosh Semwal ("You") and John Wiley and Sons ("John Wiley and Sons") consists of your license details and the terms and conditions provided by John Wiley and Sons and Copyright Clearance Center.

License Number 5897530091564

License date Oct 28, 2024

Licensed Content Publisher John Wiley and Sons

Licensed Content Publication Advanced Sustainable Systems

Licensed Content Title Ni Surface & Polyacryloyl Hydrazide Mediated Growth of Co<sub>3</sub>O<sub>4</sub>@NiCu Alloy Nanocuboids for Effective Methanol Oxidation and Oxygen Evolution Reactions

Licensed Content Author Umapasana Ojha, Akhoury Sudhir Kumar Sinha, Rajashri R. Urkude, et al

Licensed Content Date Sep 5, 2024

Licensed Content Volume 0

Licensed Content Issue 0

Licensed Content Pages 11

Type of use Dissertation/Thesis

Requestor type	Author of this Wiley article
Format	Print and electronic
Portion	Figure/table
Number of figures/tables	6
Will you be translating?	No
Title of new work	SYNTHESIS AND CHARACTERIZATION OF TRANSITION METAL BASED ELECTROCATALYST FOR EFFICIENT HYDROGEN PRODUCTION
Institution name	RAJIV GANDHI INSTITUTE OF PETROLEUM TECHNOLOGY JAIS, INDIA – 229304
Expected presentation date	Jan 2025
Portions	Scheme 1, Figure 1 to 5
The Requesting Person / Organization to Appear on the License	Santosh Semwal
Requestor Location	Mr. Santosh Semwal Jais Amethi  Raebareli, Uttar Pradesh 229305 India
Publisher Tax ID	EU826007151
Total	0.00 USD
Terms and Conditions	

**TERMS AND CONDITIONS**

This copyrighted material is owned by or exclusively licensed to John Wiley & Sons, Inc. or one of its group companies (each a "Wiley Company") or handled on behalf of a society with which a Wiley Company has exclusive publishing rights in relation to a particular work (collectively "WILEY"). By clicking "accept" in connection with completing this licensing transaction, you agree that the following terms and conditions apply to this transaction (along with the billing and payment terms and conditions established by the Copyright Clearance Center Inc., ("CCC's Billing and Payment terms and conditions"), at the time that you opened your RightsLink account (these are available at any time at <http://myaccount.copyright.com>).

## Terms and Conditions

- The materials you have requested permission to reproduce or reuse (the "Wiley Materials") are protected by copyright.
- You are hereby granted a personal, non-exclusive, non-sub licensable (on a stand-alone basis), non-transferable, worldwide, limited license to reproduce the Wiley Materials for the purpose specified in the licensing process. This license, **and any CONTENT (PDF or image file) purchased as part of your order**, is for a one-time use only and limited to any maximum distribution number specified in the license. The first instance of republication or reuse granted by this license must be completed within two years of the date of the grant of this license (although copies prepared before the end date may be distributed thereafter). The Wiley Materials shall not be used in any other manner or for any other purpose, beyond what is granted in the license. Permission is granted subject to an appropriate acknowledgement given to the author, title of the material/book/journal and the publisher. You shall also duplicate the copyright notice that appears in the Wiley publication in your use of the Wiley Material. Permission is also granted on the understanding that nowhere in the text is a previously published source acknowledged for all or part of this Wiley Material. Any third party content is expressly excluded from this permission.
- With respect to the Wiley Materials, all rights are reserved. Except as expressly granted by the terms of the license, no part of the Wiley Materials may be copied, modified, adapted (except for minor reformatting required by the new Publication), translated, reproduced, transferred or distributed, in any form or by any means, and no derivative works may be made based on the Wiley Materials without the prior permission of the respective copyright owner. **For STM Signatory Publishers clearing permission under the terms of the [STM Permissions Guidelines](#) only, the terms of the license are extended to include subsequent editions and for editions in other languages, provided such editions are for the work as a whole in situ and does not involve the separate exploitation of the permitted figures or extracts**, You may not alter, remove or suppress in any manner any copyright, trademark or other notices displayed by the Wiley Materials. You may not license, rent, sell, loan, lease, pledge, offer as security, transfer or assign the Wiley Materials on a stand-alone basis, or any of the rights granted to you hereunder to any other person.
- The Wiley Materials and all of the intellectual property rights therein shall at all times remain the exclusive property of John Wiley & Sons Inc, the Wiley Companies, or their respective licensors, and your interest therein is only that of having possession of and the right to reproduce the Wiley Materials pursuant to Section 2 herein during the continuance of this Agreement. You agree that you own

no right, title or interest in or to the Wiley Materials or any of the intellectual property rights therein. You shall have no rights hereunder other than the license as provided for above in Section 2. No right, license or interest to any trademark, trade name, service mark or other branding ("Marks") of WILEY or its licensors is granted hereunder, and you agree that you shall not assert any such right, license or interest with respect thereto

- NEITHER WILEY NOR ITS LICENSORS MAKES ANY WARRANTY OR REPRESENTATION OF ANY KIND TO YOU OR ANY THIRD PARTY, EXPRESS, IMPLIED OR STATUTORY, WITH RESPECT TO THE MATERIALS OR THE ACCURACY OF ANY INFORMATION CONTAINED IN THE MATERIALS, INCLUDING, WITHOUT LIMITATION, ANY IMPLIED WARRANTY OF MERCHANTABILITY, ACCURACY, SATISFACTORY QUALITY, FITNESS FOR A PARTICULAR PURPOSE, USABILITY, INTEGRATION OR NON-INFRINGEMENT AND ALL SUCH WARRANTIES ARE HEREBY EXCLUDED BY WILEY AND ITS LICENSORS AND WAIVED BY YOU.
- WILEY shall have the right to terminate this Agreement immediately upon breach of this Agreement by you.
- You shall indemnify, defend and hold harmless WILEY, its Licensors and their respective directors, officers, agents and employees, from and against any actual or threatened claims, demands, causes of action or proceedings arising from any breach of this Agreement by you.
- IN NO EVENT SHALL WILEY OR ITS LICENSORS BE LIABLE TO YOU OR ANY OTHER PARTY OR ANY OTHER PERSON OR ENTITY FOR ANY SPECIAL, CONSEQUENTIAL, INCIDENTAL, INDIRECT, EXEMPLARY OR PUNITIVE DAMAGES, HOWEVER CAUSED, ARISING OUT OF OR IN CONNECTION WITH THE DOWNLOADING, PROVISIONING, VIEWING OR USE OF THE MATERIALS REGARDLESS OF THE FORM OF ACTION, WHETHER FOR BREACH OF CONTRACT, BREACH OF WARRANTY, TORT, NEGLIGENCE, INFRINGEMENT OR OTHERWISE (INCLUDING, WITHOUT LIMITATION, DAMAGES BASED ON LOSS OF PROFITS, DATA, FILES, USE, BUSINESS OPPORTUNITY OR CLAIMS OF THIRD PARTIES), AND WHETHER OR NOT THE PARTY HAS BEEN ADVISED OF THE POSSIBILITY OF SUCH DAMAGES. THIS LIMITATION SHALL APPLY NOTWITHSTANDING ANY FAILURE OF ESSENTIAL PURPOSE OF ANY LIMITED REMEDY PROVIDED HEREIN.
- Should any provision of this Agreement be held by a court of competent jurisdiction to be illegal, invalid, or unenforceable, that provision shall be deemed amended to achieve as nearly as possible the same economic effect as the original provision, and the legality, validity and enforceability of the remaining provisions of this Agreement shall not be affected or impaired thereby.
- The failure of either party to enforce any term or condition of this Agreement shall not constitute a waiver of either party's right to enforce each and every term and condition of this Agreement. No breach under this agreement shall be deemed waived or excused by either party unless such waiver or consent is in writing signed by the party granting such waiver or consent. The waiver by or consent of a party to a breach of any provision of this Agreement shall not operate or be construed as a

waiver of or consent to any other or subsequent breach by such other party.

- This Agreement may not be assigned (including by operation of law or otherwise) by you without WILEY's prior written consent.
- Any fee required for this permission shall be non-refundable after thirty (30) days from receipt by the CCC.
- These terms and conditions together with CCC's Billing and Payment terms and conditions (which are incorporated herein) form the entire agreement between you and WILEY concerning this licensing transaction and (in the absence of fraud) supersedes all prior agreements and representations of the parties, oral or written. This Agreement may not be amended except in writing signed by both parties. This Agreement shall be binding upon and inure to the benefit of the parties' successors, legal representatives, and authorized assigns.
- In the event of any conflict between your obligations established by these terms and conditions and those established by CCC's Billing and Payment terms and conditions, these terms and conditions shall prevail.
- WILEY expressly reserves all rights not specifically granted in the combination of (i) the license details provided by you and accepted in the course of this licensing transaction, (ii) these terms and conditions and (iii) CCC's Billing and Payment terms and conditions.
- This Agreement will be void if the Type of Use, Format, Circulation, or Requestor Type was misrepresented during the licensing process.
- This Agreement shall be governed by and construed in accordance with the laws of the State of New York, USA, without regards to such state's conflict of law rules. Any legal action, suit or proceeding arising out of or relating to these Terms and Conditions or the breach thereof shall be instituted in a court of competent jurisdiction in New York County in the State of New York in the United States of America and each party hereby consents and submits to the personal jurisdiction of such court, waives any objection to venue in such court and consents to service of process by registered or certified mail, return receipt requested, at the last known address of such party.

## **WILEY OPEN ACCESS TERMS AND CONDITIONS**

Wiley Publishes Open Access Articles in fully Open Access Journals and in Subscription journals offering Online Open. Although most of the fully Open Access journals publish open access articles under the terms of the Creative Commons Attribution (CC BY) License only, the subscription journals and a few of the Open Access Journals offer a choice of Creative Commons Licenses. The license type is clearly identified on the article.

### **The Creative Commons Attribution License**

The [Creative Commons Attribution License \(CC-BY\)](#) allows users to copy, distribute and transmit an article, adapt the article and make commercial use of the article. The CC-BY license permits commercial and non-

### **Creative Commons Attribution Non-Commercial License**

The [Creative Commons Attribution Non-Commercial \(CC-BY-NC\) License](#) permits use, distribution and reproduction in any medium, provided the original work is properly cited and is not used for commercial purposes.(see below)

### **Creative Commons Attribution-Non-Commercial-NoDerivs License**

The [Creative Commons Attribution Non-Commercial-NoDerivs License](#) (CC-BY-NC-ND) permits use, distribution and reproduction in any medium, provided the original work is properly cited, is not used for commercial purposes and no modifications or adaptations are made. (see below)

### **Use by commercial "for-profit" organizations**

Use of Wiley Open Access articles for commercial, promotional, or marketing purposes requires further explicit permission from Wiley and will be subject to a fee.

Further details can be found on Wiley Online Library  
<http://olabout.wiley.com/WileyCDA/Section/id-410895.html>

### **Other Terms and Conditions:**

**v1.10 Last updated September 2015**

Questions? [customercare@copyright.com](mailto:customercare@copyright.com).

---

---